CRADA No. 00-F039

DOE/NETL-2005/1218

Follow-On Cooperative Research and Development Agreement: MFIX to FLUENT Technology Transfer and Validation Studies

Final Report

Madhava Syamlal, Chris Guenther, and Thomas J. O'Brien
U.S. Department of Energy

Sofiane Benyahia and Shaoping Shi
Fluent Inc.

for the

National Energy Technology Laboratory
3610 Collins Ferry Rd., PO Box 880, Morgantown, WV 26507-0880

March 2005

Disclaimer

Contents

Executive Summary 1
Introduction 2
Summary of Studies 2
Fluid Dynamic Simulation of O_3 Decomposition in a Bubbling Fluidized Bed 2
Hydrodynamics of Particle Segregation in Fluidized Beds 3
Simulation of Chemically Reactive Fluidized Beds 3
Two-Fluid Model of an Industrial Scale Transpoer Gasifier 3
The Effect of Model Parameters on the Predictions of Core Annular Flow Behavior in a Fast-Fluidized Gas/Solids Bed 3
Presentation of the Comparison of MFIX and Fluent results in a 2-D Riser 3
Evaluation of Boundary Conditions Used to Model Dilute, Turbulent Gas/Solids Flows in a Pipe 4
Transport Gasifier Simulation Testing Fluent's Eulerian-Eulerian Model 4
Transport Gasifier Simulation Testing Fluent's Eulerian-Eulerian Model 4
Extension of Koch and Hill Drag Correlation Over All Ranges of Reynolds Number and Solids Volume Fraction 4
A Comparison of Experimental and CFD Values for Granular Temperature, Turbulent Kinetic Energy and Solids Fraction of Core Particles at the Wall in the Riser of a CFB 4
Related Presentations and Publications 5
Publications 5
Conference Presentations 5
Appendix A 9
Appendix B 10
Appendix C 11
Appendix D 12
Appendix E 13
Appendix F 14
Appendix G 15
Appendix H 16
Appendix I 17

Appendix J 18
Appendix K 19

Executive Summary

This report summarizes the effort by NETL and Fluent on the Cooperative Research and Development Agreement No. 00-F039 signed in May 2000. The objective of the CRADA was to transfer technology from NETL's MFIX code into the commercial software FLUENT so as to increase the computational speed, accuracy, and utility of FLUENT. During the period of this CRADA MFIX was used to develop granular flow theories and used for simulating gas-solids chemical reactors. The FLUENT and MFIX predictions were compared with each other and with experimental data generated at NETL. The granular kinetic theory in FLUENT was improved as a result of this work, and a gas-solids reaction (ozone decomposition) was used as a test case for the gas-solids chemical reaction capability in FLUENT. Also, under a separate project, work has begun to transfer the coal combustion and gasification model in MFIX to FLUENT.

Introduction

This CRADA is a follow on of an earlier CRADA between NETL and Fluent, Inc. In the earlier CRADA, which started in 1995, the gas-solids multiphase flow model in MFIX was transferred to the commercial computational fluid dynamic (CFD) software, FLUENT. The objective of the follow-on CRADA was to continue the transfer of technology from MFIX to FLUENT, and to apply and validate FLUENT. The end goal was to increase the computational speed, accuracy, and utility of FLUENT, thereby making it more valuable in practical applications. Four CRADA tasks were identified to accomplish this goal; the work accomplished under the four CRADA tasks is given below.

As reported in the next section, FLUENT was benchmarked by running the code on NETL's Beowulf system to evaluate its speed and search for programming errors. The results were compared with MFIX results (Task 1).

The circulating fluidized-bed in at NETL's B-22 Laboratory in Morgantown was simulated with both MFIX and FLUENT, and results were compared to benchmark both the codes. The specific simulation conditions and results are reported in the next section (Task 2).

The CRADA also called for exploring new multiphase physics related to dense granular flow in a downcomer. A new model was developed for binary particle flow, and turbulence models and boundary conditions were evaluated. Together, NETL and Fluent, Inc. have published articles describing these models (Task 3).

Task 4 called for exploring new multiphase physics related to flowing cohesive particles. NETL and Fluent were partners in the Group-C of Multiphase Fluid Dynamic Research Consortium, and collaborated with Dow-Corning on the task of model development. Because of the great difficulty in developing a proper mathematical framework for describing Group-C particles, this effort was terminated. Instead, work focused on the description of chemically reacting gas-solids flows. Together, NETL and Fluent, Inc. have published articles describing chemically reacting gas-solids flows (Task 4).

This report fulfills the CRADA report requirement under Task 5. The report has been generated by compiling papers relevant to the CRADA. The next section gives a brief summary of the papers, and shows the relevance of the results to the CRADA.

Summary of Studies

A brief summary of various studies relevant to this CRADA are given below in chronological order. The complete papers and presentations are given in the Appendices at the end of this report.

Fluid Dynamic Simulation of O3 Decomposition in a Bubbling Fluidized Bed

This paper describes the use of catalytic decomposition of O_3 in a bubbling fluidized bed to validate the gas solids reaction capability of a multiphase flow code. The simulations were completed with MFIX. Results were compared with experimental data. This problem was later used as a test case for FLUENT. The complete paper can be found in Appendix A.

Hydrodynamics of Particle Segregation in Fluidized Beds

This paper describes the development of a new gas-solids constitutive equation for the drag between different solids phases. The proposed equation defines a "hinderance" effect, which accounts for the hindrance to the movement of small particles trapped in the interstices of close-packed large particles. The complete paper can be found in Appendix B.

Simulation of Chemically Reactive Fluidized Beds

This report summarizes the results of five simulation studies involving gas-solids chemical reactions: ozone decomposition, silane pyrolysis, silicon hydrochlorination, methane combustion, and coal gasification. These studies were conducted using MFIX. The complete paper can be found in Appendix C.

Two-Fluid Model of an Industrial Scale Transport Gasifier

The modeling of an industrial scale transport gasifier is described in this paper. MFIX simulations were conducted to model the Kellogg, Brown & Root Transport Gasifier in operation at the Power Systems Development Facility in Wilsonville, Alabama. The chemistry model in MFIX uses global reaction rates to account for devolitization, tar cracking, water-gas shift reaction, gasification and combustion. The gas phase consists of eight species O_2, CO, CO2, CH_4, H_2, H_2O, N_2, and tar, and the solids phase consists of four species carbon, volatile matter, ash, and moisture. Simulation results of a western sub-bituminous and a western bituminous coal are presented, which show excellent agreement with experimental data. Furthermore, results are presented comparing oxygen and air blown gasification conditions. Work is ongoing to transfer this MFIX chemistry model to FLUENT. The complete paper can be found in Appendix D.

The Effect of Model Parameters on the Predictions of Core Annular Flow Behavior in a Fast-Fluidized Gas/Solids Bed

There are several gas-solids turbulence models and boundary conditions reported in the literature. In this study, MFIX was used to evaluate four different boundary conditions when used in conjunction with Simonin's turbulence model. The model predictions were compared with experimental data of Jones and Sinclair. The experimental data fall between the large-friction/no-sliding and small-friction/all-sliding limits of Jenkins and Louge boundary conditions. However, the physical behavior of the particle-wall interactions is close to the small-friction/all-sliding limit of Jenkins and Louge boundary conditions, or the Johnson and Jackson boundary conditions with a small specularity coefficient, or simply the free-slip boundary conditions. A new wall function for gas-solids flow was also developed in this study. The complete paper can be found in Appendix E.

Presentation of the Comparison of MFIX and Fluent Results in a 2-D Riser

These slides summarize the comparison of MFIX and Fluent results in a 2-D riser simulation. This comparative study resulted in improvements of both MFIX and FLUENT. Excerpt slides of this presentation can be found in Appendix F.

Evaluation of Boundary Conditions Used to Model Dilute, Turbulent Gas/Solids Flows in a Pipe

The main purpose of this study was to investigate the ability of three gas-solids flow models: standard granular kinetic theory, and two gas-solids turbulence models (Simonin and Ahmadi) to predict core-annular flow behavior commonly observed in dense gas/solids flows (>3% solids volume fraction). The effect of three types of boundary conditions, Johnson and Jackson, and the free-slip condition, was also investigated. This study has demonstrated that the granular kinetic theory and the two turbulence models gave similar predictions for a dense, fully developed flow in a vertical channel. It also showed that the gas turbulence may not have a dominant effect in relatively dense gas/solids flows. The complete paper can be found in Appendix G.

Transport Gasifier Simulation Testing Fluent's Eulerian-Eulerian Model

Comparison of results of FLUENT and MFIX simulations of a circulating fluidized bed are reported in this presentation. This study was done to determine the feasibility of including detailed chemistry into the latest version of FLUENT with gas-solids chemistry capability. For a given time step FLUENT was found to be 2.4 times faster than MFIX; FLUENT was also able to use much larger time steps than MFIX. The complete presentation can be found in Appendix H.

Transport Gasifier Simulation Testing Fluent's Eulerian-Eulerian Model

The algebraic and partial differential equation models for granular temperature in FLUENT are compared with experimental data in this presentation. The experimental data were taken from the circulating fluidized bed experimental facility at NETL. This study was undertaken to validate the granular stress model in FLUENT. The complete presentation can be found in Appendix I.

Extension of Koch and Hill Drag Correlation Over All Ranges of Reynolds Number and Solids Volume Fraction

An important constitutive relation in multiphase flow models flows is the gas-solids drag formula. Recently, Koch and Hill proposed a set of drag correlations, based on data from Lattice-Boltzmann simulations. These correlations, while very accurate within the range of void fractions and Reynolds numbers used in the Lattice-Boltzmann simulations, do not cover the full range of void fractions and Reynolds numbers encountered in fluidized bed simulations. In this paper a drag correlation applicable to the full range of void fractions and Reynolds numbers is developed by blending the Koch and Hill drag correlation with known limiting forms of the gas-solids drag function, such that the blended function is continuous with respect to Reynolds number and void fraction. The complete paper can be found in Appendix J.

A Comparison of Experimental and CFD Values for Granular Temperature, Turbulent Kinetic Energy and Solids Fraction of Core Particles at the Wall in the Riser of a CFB

In gases, the differences in time scales between molecular collisions in which fluctuations in molecular velocities represent temperature, and those that represent turbulence spans five to 10 orders of magnitude. However, in the granular continuum, the time scales for particle collisions is only one or two orders of magnitude smaller than that of turbulent

velocity fluctuations. In this paper, a method is presented to distinguish between particle velocity fluctuations that contribute to granular temperature and those that contribute to turbulent kinetic energy. Comparisons are made for both granular temperature and turbulent kinetic energy between computational fluid dynamic simulations (using MFIX and FLUENT) and experiments using 812 μm cork particles measured near the wall in the core annular flow regime of a circulating fluidized bed riser. The complete paper can be found in Appendix K.

Related Presentations and Publications

Publications

Agrawal, K., Loezos,P.N., Syamlal, M., and Sundaresan, S. 2001. "The Role of Meso-Scale Structures in Rapid Gas-Solids Flows." *J. Fluid Mech*., 445, pp.151-185.

Benyahia, S., Syamlal, M., and O'Brien, T.J., 2004. "Numerical Analysis of a Turbulent Gas/Solids Flow in a Pipe." *Powder Technology*, forthcoming.

Cizmas, P.G., Palacios, A., O'Brien, T., and Syamlal, T. 2003. "Proper-Orthogonal Decomposition of Spatio-Temporal Patterns in Fuidized Beds." *Chemical Engineering Science*, 58, pp. 4,417– 4,427.

Gera, D., Syamlal, M., and O'Brien, T.J. 2004. "Hydrodynamics of Multiple Size Particles Segregation in Fluidized Beds." *Int. J. Multiphase Flow*, 30, pp. 419-428.

Guenther, C. and Syamlal, M. 2001. "The Effect of Numerical Diffusion on Isolated Bubbles in a Gas-Solid Fluidized Bed." *Powder Technology*, 116, pp. 142-154.

Guenther, C., and Syamlal, M. 2001. "The Effect of Numerical Diffusion on Gas-Solids Fluidized Beds and the Use of Deferred Correction in Finite Volume Methods to Stabilize High-Order Discretization of Convective Terms." *Advances in Computation: Theory and Practice*. P. Minev and Y. Lin, Eds. Nova Science, New York, pp. 201-209.

Loth, E., O'Brien,T.J., Syamlal, M., and Cantero, M. 2004. "Effective Diameter for Group Motion of Polydisperse Particle Mixtures." *Powder Technology,* 142, pp. 209-218.

Syamlal, M., and O'Brien,T.J. 2003. "Fluid Dynamic Simulation of O3 Decomposition in a Bubbling Fluidized Bed." *AIChE J.*, 49, pp. 2,793-2,801.

Conference Presentations

Benyahia, S., Syamlal, M., and O'Brien, T.J. 2003. "Numerical Computation of a Turbulent Gas/Solids Flow in a Pipe." Paper Presented at the AIChE Annual Meeting, November 16-21, 2003, San Francisco, CA.

Cizmas, P., O'Brien, T., Palacios, A., and Syamlal, M. 2002. "Reduced Order Models for Fluidized Beds." Paper Presented at the 7th Experimental Chaos Conference August 2002, San Diego, CA.

Cizmas, P., O'Brien, T., and Palacios, A. 2001. "Symmetry-Breaking Bifurcations in Spatio-Temporal Patterns." Paper Presented at the PIMS-MITACS Workshop on Computational Fuel Cell Dynamics, June 2001, Vancouver, Canada.

D'Azevedo, E., Pannala, S., Syamlal, M., Gel, A., Prinkey, M., and O'Brien, T. 2001. "Parallelization of MFIX: A Multiphase CFD Code for Modeling Fluidized Beds." Paper Presented at Tenth SIAM Conference on Parallel Processing for Scientific Computing, March 12-14, 2001, Portsmith, VA.

Gera, D. 2003. "Discrete Element Simulation of Gas-Particle Flows." Paper Presented at the SIAM Conference on Computational Science and Engineering (CSE03), February 10-13, 2003, San Diego, CA.

Gera, D. 2001. "On the Computation of Granular Temperature and Effective Normal Stresses in Fluidized Beds: Kinetic Theory Approach vs. DEM Formulations." Paper Presented at the International Conference of Fluidization-X, May 14-18, 2001, Beijing, China.

Gera, D., Syamlal, M., and O'Brien, T.J. 2003. "Hydrodynamics of Multiple Size Particles in a Liquid Fluidized Bed Classifier." Paper Presented at the 4th ASME/JSME Joint Fluids Engineering Conference (FEDSM2003), July 2003, Honolulu, Hawaii.

Gera, D., Syamlal, M., and O'Brien, T. 2004. "Transport Equation for Modeling Particle Contacts." Paper Presented at the 11th International Conference on Fluidization, May 9-13, 2004, Napoli, Italy.

Guenther, C. 2002. "A Critical Investigation of High-Order Flux Limiters In Multiphase Flow Problems." In *Proceedings of the 3rd International Symposium on Finite Volumes for Complex Applications*, June 24-28, 2002, Porquerolles, France.

Guenther, C., O'Brien, T., and Syamlal, M. 2001. "A Numerical Model of Silane Pyrolysis in a Gas-solids Fluidized Bed." In *Proceedings of the International Conference on Multiphase Flow*, May 27-June 1, 2001, New Orleans, LA.

Guenther, C., Shahnam, M., Syamlal, M., Longanbach, J., Cicero, D., and Smith, P. 2002. "CFD Modeling of a Transport Gasifier." In *Proceedings of the 19th Annual Pittsburgh Coal Conference*, September 23-27, 2002, Pittsburgh, PA.

Guenther, C. and Syamlal, M. 2000. "The Use of Deferred Correction in Fluidized Beds to Stabilize the Discretization of Convective Terms." Paper Presented at the First SIAM Conference on Computational Science and Engineering, September 2000, Washington D.C.

Guenther, C., Syamlal, M., and O'Brien, T.J. 2000. "Simulation of the Fluidized Bed Pyrolysis of Silane." Paper Presented at Chemical Reaction Engineering VII: Computational Fluid Dynamics, August 6-11, 2000, Quebec, Canada.

Guenther, C., Syamlal, M., Shadle, L., and Ludlow, C. 2002. "A Numerical Investigation of an Industrial Scale Gas-Solids CFB." In *Proceedings of the 7th International Conference on Circulating Fluidized Beds*, May 5-8, 2002, Niagra Falls, Ontario, Canada.

Guenther, C., Syamlal, M., Smith, P.V., and Longanbach, J. 2003. "Two-Fluid Model of an Industrial Scale Transport Gasifier." Paper Presented at the AIChE Annual Meeting, November 16-21, 2003, San Francisco, CA.

Loezos, P.N., Syamlal, M., and Sundaresan, S. 2000. "Coarse-Grid Simulation of Riser Flows." Paper Presented at the AIChE Annual Meeting, November 12-17, 2000, Los Angeles, CA.

Loezos, P.N., Syamlal, M., and Sundaresan, S. 2000. "Role of Meso-Scale Structures on Dilute Gas-Particle Flows." Paper Presented at the Engineering Foundation Conference: Chemical Reaction Engineering VII: Computational Fluid Dynamics, August 6-11, 2000, Quebec, Canada.

O'Brien, T. 2000. "DOE National Laboratories Capabilities for CFD in the Steel Industry." Paper Presented at the Workshop in Computational Fluid Dynamics in the Steel Industry, October 19, 2000, Pittsburgh, PA.

O'Brien, T.J., and Syamlal, M. 2003. "CFD Simulations of Reactive, Bubbling Fluidized Beds." Paper Presented at SIAM Conference on Computational Science and Engineering, February 10-13, 2003, San Diego, CA.

O'Brien T. J., and Syamlal, M. 2001. "Simulation of the Hydrodynamic Behavior of a Bubbling Fluidized Bed." Paper Presented at the Fluidization X: Fluidization for Sustainable Development Conference, May 20-25, 2001, Beijing, China.

O' Brien,T., Syamlal,M., and Pannala, S. 2002. "MFIX - 3-D Parallel Multi-Phase CFD Code for Reacting Fluidized Beds." Poster Presented at the GRC Conference on Granular & Granular-Fluid Flow, June 30-July 5, 2002, at the Holderness School, Plymouth, NH.

Pannala, S., D'Azevedo, E., Syamlal, M., and O'Brien, T. 2003. "Hybrid (Mixed SMP/DMP) Parallelization of MFIX: A Multiphase CFD Code for Modeling Fluidized Beds." Paper Presented at the ACM Conference, March 2003, Melbourne, FL.

Shahnam, M., Syamlal, M., and Cicero, D. 2000. "Numerical Modeling of Combustion and Gasification Processes Using the Discrete Particle Method." Paper Presented to the ASME Fuels & Combustion Technologies Division at the 2000 International Joint Power Generation Conference, July 24-26, 2000, Miami, FL.

Sreekanth P., D'Azevedo, E., Syamlal M., and O'Brien, T. 2003. "Hybrid (MPI/OpenMP) Parallelization of MFIX: A Multiphase CFD Code for Modeling Fluidized Beds." In *Proceedings of 2003 ACM Symposium on Applied Computing (SAC 03)*, March 9-12, 2003, Melbourne, FL.

Srivastava, A., Syamlal, M., and Sundaresan, S. 2000. "CFD of Friction-Dominated Gas-Particle Flows." Paper Presented at the Engineering Foundation Conference: Chemical Reaction Engineering VII: Computational Fluid Dynamics, August 6-11, 2000, Quebec, Canada.

Syamlal, M, and Fiveland, W. 2003. "Roadmap for the Development of a Vision 21 Simulator." Paper Presented at the 29th International Technical Conference on Coal Utilization & Fuel Systems, March 10-14, 2003, Clearwater, FL.

Syamlal, M., Madsen, J.I., Rogers, W.A., and Zitney, S.E. 2003. "Application of an Integrated Process Simulation and CFD Environment to Model Fuel Cell Systems." Paper Presented at the AIChE 2003 Spring Meeting, March 30 - April 3, New Orleans, LA .

Syamlal, M., and O'Brien, T. 2000. "Numerical Simulation of a Chemically Reactive Bubbling Fluidized Bed." Paper Presented at the AIChE Annual Meeting, Nov. 12-17, 2000. Los Angeles, CA.

Syamlal M., and O'Brien, T. 2000. "Fluid Dynamic Simulation of O3 Decomposition in a Bubbling Bed." Paper Presented at the AIChE Meeting, November 12-17, 2000, Los Angeles, CA.

Syamlal, M., and O'Brien, T.J. 2000. "Simulation of a Catalytic Reaction in a Bubbling Fluidized Bed." Paper Presented at the Chemical Reaction Engineering VII: Computational Fluid Dynamics, August 6-11, 2000, Quebec, Canada.

Syamlal, M., O'Brien, T., and Guenther, C. 2004. "Simulation of Chemically Reactive Fluidized Beds." Paper Presented at the 11th International Conference on Fluidization: Present and Future for Fluidization Engineering, May 9-13, 2004 Sorrento (Napoli), Italy.

Appendix A

Fluid Dynamic Simulation of O_3 Decomposition in a Bubbling Fluidized Bed

Fluid Dynamic Simulation of O_3 Decomposition in a Bubbling Fluidized Bed

Madhava Syamlal

Fluent, Inc., Morgantown, WV 26505

Thomas J. O'Brien

National Energy Technology Laboratory, P.O. Box 880, Morgantown, WV, 26507

Abstract

Recent advances in dense, multiphase, computational fluid dynamics (CFD) have allowed accurate simulation of the gas and particle motion in bubbling and circulating fluidized beds. Since fluidized-bed reactors are used for many chemical processes, a simulation must also be able to couple chemical reactions to bed hydrodynamics accurately. The catalytic decomposition of ozone (O_3) has often been used to study experimentally the contacting behavior of catalytic reactors. Simulations were conducted of laboratory-scale experiments of premixed O_3 decomposition in a bubbling fluidized bed using the multiphase CFD code MFIX. The grid-independent results are in very good agreement with reported experimental data on total conversion over a range of fluidization velocities and initial bed heights. This confirms the ability of multiphase hydrodynamic models to capture the effect of hydrodynamics on chemical reactions in a bubbling fluidized bed.

Topical Heading: Particle Technology and Fluidization

Key Words: Particles, fluidization; simulation, ozone, reactive, chemical, computational fluid dynamics.

Introduction

Fluidized catalyst beds have better heat transfer and ease of solids handling than fixed beds. However, at a given flow velocity, the conversion in a fluidized bed is lower than in a fixed bed; the less efficient solids contacting is a result of by-passing associated with bubbles. Since the design of a fluidized-bed process is a compromise between these competing effects, the degree of contacting in any particular configuration must be quantified.

In recent years, methods of simulating the detailed behavior of bubbling fluidized beds have been developed, based on concepts of dense, multiphase, computational fluid dynamics (CFD) (Anderson and Jackson 1967; Gidaspow 1994). Using these methods, simulations of a bubbling bed's hydrodynamic behavior have been reported (Syamlal and O'Brien 1985; Kuipers and others 1992; Boemer, Qi, and Renz 1998; van Wachem and others 1998; Guenther and Syamlal 2001). Such calculations provide detailed information on the transient gas-solids flow patterns in these beds. However, in designing fluid-bed chemical reactors, simulations must also accurately describe mixing, chemical reactions, and heat transfer. Thus, previous computational studies need to be extended to include these phenomena. This has been done for circulating fluidized beds (Samuelsberg and Hjertager 1995; Theologos and Markatos 1993; Gidaspow and Therdthianwong 1993). Although these simulations show qualitatively reasonable results, none of these previous studies demonstrate quantitative agreement between experimental data and

grid-independent simulation results. This paper reports on a study that couples chemical reactions to the hydrodynamic behavior of a bubbling fluidized-bed, and provides quantified agreement with experimental results.

The ozone (O_3) decomposition reaction, catalyzed by Fe_2O_3, has become a surrogate reaction for chemical-reactor-design analysis. Although this process has no commercial applications, it has been frequently used to characterize fluidized bed reactors, specifically to quantify gas-solids contacting (Frye, Lake, and Eckstrom 1958; van Swaaij and Zuiderweg 1972; Orcutt, Davidson, and Pigford 1962; Hovmand, Freedman, and Davidson 1971; Fryer and Potter 1976; Ouyang, Lin, and Potter 1993). This reaction requires only low concentrations of the reactant, detection is rapid and accurate (using fairly simple methods), and there is a measurable reaction rate at ambient temperature and pressure (Frye, Lake, and Eckstrom 1958). Moreover, since these studies have been performed with premixed O_3 at very low concentrations, density and temperature changes that occur because of the reaction can be neglected. Low concentrations also guarantee that the reaction is essentially irreversible. Being premixed, there are no issues of gas-phase reactant or product mixing. Thus the effect of gas-solids contacting on the chemical reaction is isolated in these experiments. For these same reasons, simulations of the O_3 decomposition reaction are used here to validate the coupling of chemistry and gas-solids hydrodynamics.

From studies on packed beds of silica sand impregnated with Fe_2O_3, O_3 decomposition has been determined to be first order in O_3 concentration and first order in Fe_2O_3 catalyst surface area (Frye, Lake, and Eckstrom 1958; Orcutt, Davidson, and Pigford 1962; Fryer and Potter 1976).

The reaction rate constant is independent of the flow rate or conversion level. The reported activation energy, about 126 kJ/mol, is consistent with a surface rate-controlled reaction. Based on this work, the reaction scheme in the present simulation is described as a simple, one-step reaction, $2\ O_3 \rightarrow 3\ O_2$, catalyzed by ferric oxide, Fe_2O_3. The gas phase O_3 thermal decomposition reaction is known to occur through a chain reaction scheme involving the atomic O free radical, and a homogeneous gas-phase scheme has been described in detail (Heimerl and Coffee 1980). However, this reaction mechanism cannot be applied directly to catalytic decomposition in fluidized beds since the important effects of the particulate phase, such as radical quenching on the particle surfaces, have not been accounted for. In this study, an empirical global reaction rate expression is used.

There have also been several attempts to analyze the experimental results for O_3 decomposition in fluidized beds using traditional simulation techniques. Van Swaaij and Zuiderweg (1972) interpreted their experiments using the model developed by van Deemter (1961), based on a two-phase model of fluidized beds that allows axial diffusion in the dense phase. The assumptions include: no solids in the bubble phase, plug flow in the bubble phase, negligible dense-phase gas through-flow, and eddy diffusion mixing in the dense phase. The authors concluded that the mass transfer between the bubbles and the dense phase limited conversion. Fryer and Potter (1972) developed a "back-mixing" model to account for the experimentally observed reverse flow of gases, which causes the O_3 concentration to pass through a minimum value within the reactor. Later, Bukur (1978) showed a weakness of the back-mixing model: near the conditions of flow reversal, the model predicts that the cross-sectional area of the bubble and its cloud exceeds the cross-sectional area of the bed. Peters, Fan, and Sweeney (1982) developed a model by dividing

the fluidized bed into a number of axial compartments, each consisting of bubble, cloud, and emulsion phases. In their report, the compartment sizes varied from 0.5 to10 cm, and the number of compartments varied from 5 to 25. The model contains several parameters that characterize fluidization: superficial gas velocity in bubble, cloud and emulsion phases; volume ratio between cloud and bubble phases; bubble diameter; number of bubbles per compartment; volume fraction of each phase; expanded bed height; gas interchange coefficient; and cross flows. The authors used empirical correlations to calculate the parameters and obtained excellent agreement between the experimental data and model predictions.

For the model described in this paper, the only empirical information about the fluidized bed needed is the easily determined minimum fluidization velocity. The formation and behavior of the bubble, cloud, and emulsion phases are predicted by solving the momentum and continuity (hydrodynamic) equations. The effect of these phases on the chemical reactions is described by solving the species mass balance equations, coupled with the hydrodynamic equations. The advantage of this approach, once validated, is its ability to describe fluidized beds of any size or configuration without re-calibrating the model. The disadvantage, however, is the significantly higher computational cost. This paper addresses the validation issue.

Fryer and Potter Experimental Facility

The operating conditions and hydrodynamic and chemical behavior of the experimental facility must be known for a validation study. The experimental report of Fryer and Potter (1976) provide the most detailed information over the broadest range of operating parameters. Their

experimental apparatus was a cylindrical 200 × 22.9 cm diameter stainless steel and glass reactor with a bubble-cap distributor, a plate with 61 caps at 27.8-mm spacing. The bed was fluidized with dry air (since the reaction is extremely sensitive to water vapor concentration at room temperature) to which a small amount of O_3 was added. The bed material was sand impregnated with iron oxide as a catalyst. The reactivity of the catalyst was determined by measurements in a fixed bed. The simulation conditions are listed in Table I; some parameters were specified in the experimental paper and others were deduced as discussed below.

Parameters not specified by Fryer and Potter (labeled Other Assumed Parameters in Table I) were obtained as follows: the sphericity of 0.75 was obtained from Figure 1 in Kunii and Levenspiel (1991) for the void fraction, ε_{mf}. The reported U_{mf} was used to determine parameters c and d in the drag formula. This ensures that the drag formula gives the experimentally observed drag force at the minimum fluidization condition. The coefficient of restitution (Viscous Regime, Table II) was chosen as 0.8, which is a typical value for the sand used in the experiment. Furthermore the simulation results are not sensitive within a typical range of this value because the dominant forces in a bubbling bed are the drag and gravitational forces (for example, van Wachem and others 2001). The angle of internal friction (Plastic Regime, Table II) is important for predicting a freely bubbling state (Syamlal 1998a); the value of 30° is typical for sand. The fluid viscosity used is that for air at ambient conditions. A small value for the O_3 mass fraction at the inlet was chosen: 0.1.

Simulation

The conditions of the Fryer and Potter (1976) experiments were simulated using the MFIX code (Syamlal, Rogers, and O'Brien 1993). The equations solved by this code are based on an interpenetrating fluids formalism of multiphase flow (Anderson and Jackson 1967). The precise form of the equations and the method of solution are described in detail in MFIX documentation manuals (Syamlal, Rogers, and O'Brien 1993; Syamlal 1998b). The equations relevant to this simulation are listed in Table I. These equations represent the conservation of mass and momentum for two interpenetrating phases (gas and catalyst particles) and mass conservation of the gas-phase species (O_2, N_2, and O_3). The stress in the granular phase is described by the kinetic theory of granular material (Lun and others 1984; Gidaspow 1994). The granular temperature was calculated using an algebraic closure (Viscous Regime, Table II).

The drag law, F_{gs}, which depends on the local slip velocity and void fraction, represents the momentum exchange between the phases. The form used in MFIX is based on experimental correlations of the settling velocity. Such general drag correlations typically can predict the drag force only to an accuracy of about 20 percent because of the inability to include information accurately about particle size and shape distributions in such correlations. This amount of error is unacceptable in bubbling fluidized-bed simulations. For example a 5-percent change in the drag force near minimum fluidization conditions can make a big difference in the fluidization characteristics—which can range from a packed bed to a vigorously bubbling bed with even such a small change in the drag force. Here we propose a method to address this problem, which ensures that the drag force calculated under minimum fluidization conditions exactly matches the experimental drag force. This can be done quite easily, because for any given drag correlation, one can derive an algebraic formula for the minimum fluidization velocity. Here we use such a

formula to adjust the parameters c (= 0.765) and d (= 2.93) in the formula for B (Gas-solids drag, Table II) to ensure that the simulated value of U_{mf} corresponded to the reported experimental value of 1.7 cm/s. This ensures that the drag force given by F_{gs} matches the experimental value at the minimum fluidization condition. The correlation is formulated such that the drag force is guaranteed to agree with the single-sphere drag force at the other extreme of very low solids volume. The variation of the drag force with respect to void fraction (albeit modified because B is adjusted) and Reynolds number comes from an experimentally validated Richardson Zaki type correlation (Garside and Al-Dibouni 1977).

The term R_{gn} represents the reaction rate for species n of the gas phase. For this simple kinetics scheme there are three species ($N_g = 3$), only two of which are reactive species; N_2 is included as an inert component. Fryer and Potter (1976) determined that the O_3 decomposition reaction is first order with respect to the O_3 concentration and have reported rate constants for different catalytic activities. The rate constants *k* were measured in a packed bed reactor and reported per volume of solid; multiplying their rate expression by ε_s converts it to the form used in MFIX, per volume of the reactor, so that

$$R_{O_3} = -\frac{3}{2} R_{O_2} = -\frac{k\ \varepsilon_s\ \rho_g\ X_{O_3}}{MW_{O_3}}.$$

This set of coupled partial differential equations was solved by MFIX, using a variety of computer platforms (SGI, IBM SP3, Beowulf cluster).

The simulations were performed for a range of conditions reported by Fryer and Potter (1976) assuming two dimensional (2-D) cylindrical symmetry, initially with a 36 x 56 (radial x axial) mesh resolution, corresponding to a computational mesh with $\delta r = 0.318$ cm and $\delta z = 0.536$ cm. We used the second order accurate Superbee spatial discretization scheme, which is needed to accurately calculate bubble shape (Guenther and Syamlal 2001). The initial conditions for the simulations were a uniform initial condition, a packed bed. These simulations were repeated at twice the mesh resolution (72 x 112; $\delta r = 0.159$ cm, $\delta z = 0.268$ cm). All except one of these simulations were started by using the final results of the corresponding coarse-grid simulation as the initial condition. One fine-grid simulation was started from a uniform initial condition, as in the coarse-grid simulations, producing results consistent with the other runs. We thus verified that the results of the fine-grid simulation were insensitive to whether or not the coarse-grid simulation results were used as the initial conditions. Using the coarse-grid solution as an initial condition reduced the simulation time required to eliminate all the initial transients. Numerical results were compared with the reported experimental information by time-averaging the O_3 mass fraction data for a 10-s period after a statistical steady state was achieved.

Comparison Between Simulation and Experiment

Bed Expansion

As a global measure of the degree to which these simulations capture the correct hydrodynamic behavior of the bed, Figure 1 compares the reported percent-bed-expansion data with the calculated values for the three mesh resolutions (36 x 56, 72 x 112, and 114 x 224). This series of

simulations was for a fixed initial bed height (H_{mf} = 11.5 cm) over a range of superficial velocities (U_{sup} = 2, 4, 6, 8, 10, 12, 14 cm/s). Bed height in the experiment was measured by observing "a probe tip from above." Such measurements seem highly subjective and no error bars were presented. Fryer and Potter (1976) state that the experimental technique "may well underestimate the average bed height " because of the "difficulty of measurement caused by the vigorous motion of the bed." There is no explicit equivalent of this "bed height" in the model results and no unequivocal way to translate the numerical results into a bed height. The void fraction distribution must be post-processed in some manner to determine this quantity. One way is to time-average the data and then scan downward in the freeboard and mark the first location where the void fraction drops below a certain value—with the idea that the probe tip is visible down to that location. However, this method fails at high fluidization velocities because the upper region of the bed becomes too dilute and may cause the unrealistic prediction of bed contraction. A more realistic way is to calculate the height of the bed that contains a certain percentage of the bed weight. We chose that method because it directly correlates with bed pressure drop measurements. The bed heights reported by Fryer and Potter perhaps corresponds to an (unknown) combination of the above two techniques. Therefore, the comparison in Figure 1 is at best semi-quantitative.

After a statistical steady state was achieved, we time-averaged the solids distribution; the height that contained 95 percent of the bed weight was taken as the simulated bed height. The height determined this way was normalized by the value corresponding to 95 percent of the initial bed height (0.95 x 11.5-cm). Although this is an arbitrary criterion, the results are not sensitive to the percent bed-weight value chosen (within a small range), because the experimental values are

reported as percent bed expansion rather than as actual bed height. For example, using 80 percent of the bed weight as the criterion made little difference in the simulation results. However, 100-percent bed weight cannot be used as a criterion because small amounts of bed material are thrown to high levels. Although the solids volume fraction in the freeboard drops off rapidly with height, the entire freeboard height is required to contain 100 percent of the solids. Therefore, the bed height would not change (at the total height of the domain) with gas flow rate, except perhaps at the lowest gas flow rate.

The solid curves in Figure 1 show simulations at two mesh resolutions. Both simulations show the correct qualitative behavior, expanding from a slumped bed at the minimum fluidization velocity, with expansion slowing at higher fluidization velocity. However, the coarser mesh underestimates bed height at the lowest velocity and significantly overestimates the expansion over the rest of the range. The finer mesh quantitatively tracks the experimental curve (to within the reported reproducibility) up to a superficial velocity of 6 cm/s (3.5 x U_{mf}). The one point calculated using the finest mesh (114 x 224) (at 8 cm/s) shows improved agreement with the experimental results. The disagreement at higher velocities is partly because of inadequate mesh resolution and partly because of the previously mentioned uncertainty in comparing simulated data with experimental results. Because of this uncertainty and the cost of fine grid simulation fine grid simulations for a range of velocities was not conducted.

Ozone Conversion

Since the bed initially contained no O_3, the outlet concentration of O_3 rapidly increases during the first few seconds. This initial transient lasts for 6 to 20 s; the startup lasts longer for deeper beds and lower velocities. After this, the outlet concentration fluctuates around a mean with less than 1-percent deviation. The average, used to compare with the experimental data, was taken for a 10-s period under these statistically steady conditions. As an example, Figure 2 shows the average outlet concentration of O_3 as a function of time for the simulation at U = 10.4 cm/s, H_{mf} = 10.8 cm, and k = 0.33 m^3-gas/m^3-cat ·s. (The units are henceforth abbreviated as s^{-1}; e.g. k = 0.33 s^{-1}). The initial transients die down after a period of about 10 s, and a statistical steady state is achieved. The standard deviation from 20 to 30 s is very small (0.8 percent).

Two series of simulations were executed at different mesh resolutions in order to determine the accuracy with which they could duplicate the experimental values reported for total O_3 conversion, C_{out}/C_{in} . This is a global measure of the accuracy of the mathematical description of the chemical process as incorporated into MFIX. The first series was for a fixed initial bed height (H_{mf} = 11.5 cm) over a range of superficial velocities (U = 2, 4, 6, 8, 10, 12, 14 cm/s). The reported effective rate constants for this bed, as measured by experiments in a packed bed, was k = 1.57 s^{-1}.

The results at the lowest mesh resolution (36 x 56; δr = 0.318 cm x δz = 0.536 cm) are shown in Figure 3 in the curve labeled MFIX-36x56. The simulation at this level of resolution shows reasonable agreement with the experiments, predicting the shape of the curve and the general trend. However, the outlet concentration is significantly under-predicted.

The simulations were repeated at twice the mesh resolution (72 x 112; δr = 0.159 cm, δz = 0.268 cm). All except one of these simulations (at U=8 cm/s) were started by using the final results of the corresponding coarse grid simulation as the initial condition. At this mesh resolution, the simulation results for conversion agree quantitatively with those reported experimentally over the full range of superficial velocities studied. (See the curve labeled MFIX-72x112 in Figure 3.) In order to establish firmly the mesh-independence of these simulations for this global experimental measurement, a simulation was repeated at one superficial velocity (U = 8 cm/s) at an even higher resolution (144 x 224; δr = 0.0795 cm, δz = 0.134 cm). Only a slight change in the calculated conversion value occurred for this point, shown as MFIX-144x244 in Figure 3. Thus, based on the results shown in Figures 1 and 3, the solution for 72x112 appears to be grid-independent. These criteria used for judging grid-independence, bed expansion, and total conversion, are global measures of the hydrodynamic and chemical behavior of the bed. This is a necessary first step, from which we can conclude that the full solution is reasonably grid-independent.

The presence of a solids volume fraction in the rate expression couples the hydrodynamics and the chemical reactions. To determine how strong an influence hydrodynamics has on the chemical reactions, we have plotted the results of two simple models that idealize gas-solids hydrodynamics in a fluidized bed: a plug flow reactor, and a well-mixed reactor. Formulas for conversion in plug flow and well-mixed reactors are derived (ignoring the volume change caused by the reaction, about 3 percent) as follows:

plug flow:

$$\frac{[X_{O3}]_{outlet}}{[X_{O3}]_{inlet}} = \exp\left(-k\varepsilon_s H_{mf} \Big/ U\right) \quad \text{and}$$

well-mixed:

$$\frac{[X_{O3}]_{outlet}}{[X_{O3}]_{inlet}} = \frac{1}{1+\left(k\varepsilon_s H_{mf} \Big/ U\right)} \quad ,$$

where H_{mf} is the bed height at minimum fluidization, and U is the fluidization velocity. (We purposely use H_{mf} rather than the actual bed height to avoid having to include any information based on bed hydrodynamics in this model; the actual bed height, defined in some manner, would have to be obtained from experimental data.) We want to demonstrate that such models, which idealize bed hydrodynamics, cannot predict the observed conversion as a function of gas velocity. This in turn implies that hydrodynamics affect the chemical reaction and that the experimental data are useful for validating the model's ability to capture the influence of hydrodynamics on chemical reactions. There are other models that include other hydrodynamic information (bubble size, rise velocity, wake fraction, and so on) that can easily describe the observed reactor behavior (for example, Fryer and Potter 1976). The advantage of the present model is that it requires only one (easily measured) hydrodynamic parameter—minimum fluidization velocity—to calibrate the drag correlation.

Figure 3 shows that at the minimum fluidization velocity, the experimental data and the results of the simulation are similar to the plug-flow reactor, which is to be expected because the solids are not moving. At higher velocities, the outlet concentration (experimental and predicted) steadily becomes greater than that of a plug-flow reactor. Perhaps the gas mixing induced by the bubbles causes this, which suggests the usage of a well-mixed reactor model to describe the fluidized bed. Figure 3 shows that to some extent the well-mixed reactor describes the fluidized-bed

reactor. At low velocities the outlet concentration is lower than that in a well-mixed reactor; as the velocity is increased, the outlet concentration becomes closer to that of a well-mixed reactor. Surprisingly, at velocities larger than 5 cm/s (~3 U_{mf}) the conversion in the fluidized-bed reactor is worse than that in a well-mixed reactor. The higher outlet concentration (or lower conversion) is because of the gas by-passing the catalyst bed through bubbles. MFIX predicts this transition remarkably well.

A second series of simulations was conducted for a fixed-fluidization velocity (U = 10.4 cm/s) over a range of bed heights (H_{mf} = 10.8, 23.1, 39.5, 64.5 cm). The reported effective rate constant for this bed, as measured by experiments in a packed bed, was k = 0.33 s^{-1}. The grid size was held constant at δr = 0.159 cm and δz = 0.268 cm, which corresponds to the resolution (72 x 112) that gave a grid-independent solution in the first series of simulations. Figure 4 shows the outlet O_3 concentration as a function of bed height. The simulation results agree with experimental data very well over the entire range of initial bed heights.

We saw that the calculated outlet O_3 concentration agrees remarkably well with experimental data without any need for adjustable constants. To further validate the hydrodynamic model, we compared detailed profiles of field variables in the model. Such data are often difficult to measure. Fortunately Fryer and Potter gives axial profiles of O_3 concentration. In Figure 5, we compare that data with calculated profiles for H_{mf} = 23.1 cm, U = 10.4 cm/s, and k = 0.331 s^{-1}.

Fryer and Potter measured the O_3 concentrations at four (unstated) radial locations in the bed and reported an average value. To mimic the experimental technique, we sampled the concentration

at four radial locations in the bed, 0.2, 3.8, 7.6, and 11.3 cm from the centerline, and obtained an average from these four values. Experiments showed that "concentrations detected by four probes across any one radius do not differ significantly in comparison with axial variations." The simulation results for the region near the top of the bed agree with this observation. In the bottom part of the bed, however, the simulation results show significant variation in the radial direction.

A remarkable feature of the experimental data is that the concentration reaches a minimum value in the bed. This was consistently observed in the experiments for fluidization velocities above 5.8 cm/s. Fryer and Potter (1976) gives reasons to justify that this is a real phenomena rather than an artifact caused by sampling. The simulation curve shows a minimum, but one that is significantly less pronounced and occurs much deeper in the bed than in the experimental data. (The data point for H = 35 cm shown in Figure 5 was not included in the profile data, but was reported separately as outlet concentration by Fryer and Potter.) Although there is good agreement between the experimental and calculated outlet concentrations, there is considerable deviation in the axial concentration profiles. Without error estimates for the experimental radial profiles, we cannot assess the reasons for this discrepancy.

Comparisons with plug-flow and stirred-tank reactors show that reactor hydrodynamics critically affect overall conversion. To understand how this occurs, we examined the instantaneous behavior of the bed. Figure 6 shows the instantaneous (t = 13.8 s) void fraction and species mass fraction distributions with superimposed gas and solids velocity vectors for H_{mf} = 11.5 cm, U = 8 cm/s, and k=1.57 s^{-1}. The results plotted are for 2-D axisymmetric simulation. In each of the plots, the left edge is the centerline and the right edge is the outside wall.

The left panel of Figure 6 shows the voidage as a color plot. The color scale varies from 0.4 (red) to 1 (blue). Superimposed on this panel are the solids velocity vectors; for clarity, only one in nine of the calculated vectors is plotted. The right hand panel shows the O_3 mass fraction on a color scale 0 (red) to 0.1 (blue). The gas velocity vectors are superimposed on this panel. The bubble rise path determines the flow pattern in the bed.

In general, the simulations show a narrow region near the distributor (which is simulated as a uniform flow boundary condition), with a layer of an expanded bed. Slightly above the distributor, this band rolls up into a bubble, which usually initially forms near the outside lower edge of the bed. Once formed, these bubbles rise and migrate toward the centerline of the bed. On average, this generates a sloping band of reduced voids from the lower outside region of the vessel toward the centerline. This is a band of high gas flow, related to gas by-passing the bed in the "bubble phase." The bubble-induced time-averaged solids motion shows a downward circulation pattern near the centerline, and there is also downward flow of solids near the outside wall near the top of the bed. The bed is not deep enough to establish an upwards solids circulation pattern near the centerline; bubbles do not have enough time to migrate completely to the center of the bed before bursting at the surface. This type of pattern is typical of shallow bubbling beds.

In the void fraction plot (left panel), a bubble close to the top of the bed is visible. The O_3 mass-fraction plot is quite similar to the void-fraction plot: in high-void fraction regions, the O_3 concentration is high and vice versa. This is because the rate of O_3 decomposition is proportional

to the solids volume fraction. However, there is a significant deviation from this trend within a region in the bubble wake. Interestingly, the O_3 mass fraction is high in a region where the void fraction is low. The low conversion in that region appears to be because of the high gas flow rate: a gas jet is flowing from the bottom bubble to the top bubble. So gas by-passing is caused by the gas flowing through the bed as a bubble, and the gas flowing from bubble to bubble in the form of jets.

The vector plots also show that the gas and solids flow patterns are quite alike. This is because of the small particle size and the consequent large drag force. In certain regions of the bed, the gas flow is downwards, especially near the bed centerline. Even bubbles caught in this region move downwards. This reverse flow of gas has been used to explain the minimum observed in the axial concentration profile shown in Figure 5 (Peters, Fan, and Sweeney 1982). At sufficiently high downward solids velocity in the emulsion phase, the gas flow will reverse direction in order to maintain a constant relative velocity to the solids.

Figures 7 and 8 show the time-averaged void fraction and velocity vectors for two initial bed heights. The gas-solids circulation pattern predicted by the simulation is similar to those reported for a shallow bed (Kuni and Levenspiel 1991; Werther and Molerus 1973): up at the wall, down near the centerline. Figure 7a presents the time-averaged solids-velocity vectors, superimposed on contour lines representing the time-averaged void fraction—blue represents a void fraction of 1 (as in the freeboard, for example) and red represents a void fraction of 0.4. A similar representation of the time-averaged gas velocity is shown in Figure 7b. The results plotted are for

2-D axisymmetric simulation. As before, in each of the plots a and b, the left edge is the centerline and the right edge is the outside wall.

The overall solid circulation pattern observed in the simulation was—up at the outside and down on the centerline. However, there was much more detail to the pattern than is generally described in the literature. There is a uniform region of low voidage very close to the distributor, because of the uniform constant boundary condition imposed to simulate the distributor. (No attempt was made to resolve the detailed geometry of the bubble-cap distributor used experimentally.) However, this region was unstable and rolled up in a region near the outside wall to form "bubbles."

It is not clear why the instability is stronger near the wall, but this prediction agrees with the experimentally reported behavior: bubbles preferentially form near the junction of the distributor and the outside wall (Werther and Molerus 1973). These bubbles then rose rapidly through the bed, while migrating toward the centerline. However, since the simulated bed was quite shallow, the migration to the centerline was never complete. This general route of bubble motion, of course, results in a solids motion of the same pattern. This upward motion induced a downward flow of particles near the centerline, which diverted to the outside near the distributor. This particle flow was often strong enough to cause downward flow of the entrained gas in this region. There was also a small reverse circulation pattern of solids in the upper outside region of the bed, caused by the migration of the bubbles towards the centerline. Of course, this pattern was more pronounced for the deeper beds.

In Figure 8, the superficial velocity is the same as that shown in Figure 7, 10.4 cm/s; however, the initial bed height has been increased to 23.1 cm. The down-flow region near the center becomes smaller higher up in the bed, and the reverse circulation pattern in the upper-outside corner has intensified. It is this pattern that would presumably grow to establish the second circulation cell characteristic of deeper beds: up at the centerline; down at the wall.

In this paper we have reported the results of 2-D axisymmetric simulations. Although the time-averaged profiles must be axisymmetric, the validity of this approximation in transient simulations is not established. Also, we are not sure whether this approximation may have prevented the bubbles from moving to the center in the 23.1 cm tall bed (Figure 8). Therefore, we have started an investigation using a three dimensional (3-D) geometry. However, 3-D simulations are very slow and time consuming; results will be reported in a future publication.

Conclusions

A gas-solids flow model was used in this study to model a catalytic reaction—the decomposition of O_3 with an iron oxide catalyst—in a bubbling fluidized bed. By using three grid resolutions (36 x 56, 72 x 112, and 114 x 224), we show that a grid-independent solution can be obtained that agrees very well with the observed O_3 outlet concentration as a function of fluidization velocity and initial bed height. The agreement in the bed expansion was good at low fluidization velocities but not as good at high fluidization velocities. However, Fryer and Potter noted an uncertainty in determining bed height at high fluidization velocities. The axial variation in O_3 concentration (cross-section averaged) shows a minimum within the bed as observed in the

experimental data. However, the location and magnitude of the minimum are considerably different from experimental data.

The instantaneous solids circulation and solids distribution patterns agree qualitatively with general observations in fluidized beds. The calculations show that gas may by-pass the bed by jetting between bubbles. The time-averaged void-fraction plots show bubble formation near the wall and migration toward the center. However, bubbles do not reach the center, perhaps because of (a) the short bed heights considered in these simulations, or (b) a limitation of the 2-D axisymmetric assumption used in these simulations. We plan to conduct 3-D simulations to verify this. In summary, the gas-solids multiphase flow model used here is able to capture the effect of gas-solids hydrodynamics on catalytic reactions in a bubbling fluidized bed remarkably well without using any adjustable constants.

Acknowledgments

This work was supported by funding from U.S DOE - Fossil Energy, National Energy Technology Center, and U.S DOE - Energy Efficiency and Renewable Energy, Office of Industrial Technologies. The authors would like to thank the EERE-OIT program manager, Dr. Brian Valentine, for his support.

Literature Cited

Anderson, T.B., and R. Jackson, "A Fluid Mechanical Description of Fluidized Beds," *Industrial and Engineering Chemistry Fundamentals,* **6**, 527 (1967).

Boemer, A., H. Qi, and U. Renz, "Verification of Eulerian Simulation of Spontaneous Bubble Formation in a Fluidized Bed," *Chemical Engineering Science*, **53**, 1835 (1998).

Bukur, D.B., "Analysis of Gas Flow in Fluidized-Bed Reactors," *Industrial and Engineering Chemistry Fundamentals*, **17**, 120 (1978).

Fryer, C., and O.E. Potter, "Countercurrent Backmixing Model for Fluidized Bed Catalytic Reactors. Applicability of Simplified Solutions," *Industrial and Engineering Chemistry Fundamentals*, **11**, 338 (1972).

Fryer, C., and O.E. Potter, "Experimental Investigation of Models for Fluidized Bed Catalytic Reactors," *AIChE Journal*, **22**, 38 (1976).

Frye, C.G., W.C.Lake, and H.C. Eckstrom, "Gas-Solid Contacting with Ozone Decomposition Reaction," *AIChE Journal*, **4**, 403 (1958).

Garside, J., and M.R. Al-Dibouni, "Velocity-Voidage Relationships for Fluidization and Sedimentation in Solid-Liquid Systems," *Industrial & Engineering Chemistry Process Design and Development*, **16**, N2, 206 (1977).

Gidaspow, D., *Multiphase Flow and Fluidization: Continuum and Kinetic Theory Descriptions*, Academic Press, New York (1994).

Guenther, C., and M. Syamlal, "The Effect of Numerical Diffusion on Simulation of Isolated Bubbles in a Gas-Solid Fluidized Bed," *Powder Technology*, **116,** 142 (2001).

Gidaspow, D., and A. Therdthianwong, "Hydrodynamics & SO_2 Sorption in a CFB Loop," *Proceedings of the 4th International Conference on Circulating Fluidized Beds*, 351 (1993).

Heimerl, J.M., and T.P. Coffee, "The Detailed Modeling of Premixed, Laminar Steady-State Flames I. Ozone," *Combustion and Flame*, **39**, 301 (1980).

Hovmand, S., W. Freedman, and J.F. Davidson, "Chemical Reaction in a Pilot-Scale Fluidized Bed," *Transactions of the Institution of Chemical Engineers*, **49**, 149 (1971).

Kuipers, J.A.M., K.J. Van Duin, F.P.H. Van Beckum, and W.P.M. Van Swaaij, "A Numerical Model of Gas Fluidized Beds," *Chemical Engineering Science*, **47**, 8, 1913 (1992).

Kunii, D., and O. Levenspiel, *Fluidization Engineering 2nd ed*., Butterworth-Heinemann, Boston (1991).

Lun, C., S. Savage, D. Jeffrey, and N. Chepurniy, "Kinetic Theories for Granular Flow: Inelastic Particles in Couette Flow and Slightly Elastic Particles in a General Flowfield*," Journal of Fluid Mechanics*, **140**, 223 (1984).

Orcutt, J.C., J.F. Davidson, and R.L. Pigford, "Reaction Time Distribution in Fluidized Catalytic Reactors," *Chemical Engineering Progress Symposium Series, No. 38*, **58**, 1 (1962).

Ouyang, S.J., J. Lin, and O.E. Potter, "Ozone Decomposition in a 0.254 m Diameter Circulating Fluidized Bed Reactor," *Powder Technology*, **74**, 73 (1993).

Peters, M.H., L.-S. Fan, and T.L. Sweeney, "Reactant Dynamics in Catalytic Fluidized Bed Reactors with Flow Reversal of Gas in the Emulsion Phase," *Chemical Engineering Science*, **37**, 553 (1982).

Samuelsberg, A., and B.H. Hjertager, "Simulation of Two-Phase Gas/Particle Flow and Ozone Decompositions in a 0.25m I.D. Riser," *Advances in Multiphase Flow,* A. Serizawa, T. Fukano, and J. Batalille, eds., 679 (1995).

Syamlal, M., "Higher Order Discretization Methods for the Numerical Simulation of Fluidized Beds," *Fluidization Fluid Particle Systems: Recent Research and Development*, 138 (1998a).

Syamlal, M., *MFIX Documentation: Numerical Technique*, EG&G technical report, DE-AC21-95MC31346 (1998b).

Syamlal, M., and T.J. O'Brien, "Computer Simulations of Bubbles in a Fluidized Bed," *AIChE Symposium. Series: Fluidization, Fluid Particle System Fundamentals Applied*, **85**, 22 (1985).

Syamlal, M., W. Rogers, and T. O'Brien, 1993, *MFIX Documentation: Theory Guide*, Technical Note, Morgantown Energy Technology Center, DOE/METC-94/1004 (DE94000087) (1993). Also, see www.mfix.org.

Theologos, K.N., and N.C. Markatos, "Advanced Modeling of Fluid Catalytic Cracking Riser-Type Reactors," *AIChE Journal*, **39**, 1007 (1993).

van Deemter, J.J., "Mixing and Contacting in Gas-Solid Fluidized Beds" *Chemical Engineering Science*, **13**, 143 (1961).

van Swaij, W.P.M. van, and F.J. Zuiderweg, "Investigation of Ozone Decomposition in Fluidized Beds on the Basis of a Two-phase Model*," Proceedings of the 5th European Symposium on Chemical Reaction Engineering*, B 9-25-36 (1972).

van Wachem, B.G.M., J.C. Schouten, R. Krishna, and C.M. van den Bleek, "Eulerian Simulations of Bubbling Behavior in Gas-Solid Fluidized Beds," *Computers Chemical Engineering*, **22** Supplement, S299 (1998).

van Wachem, B.G.M., J.C. Schouten, C.M. van den Bleek, R. Krishna, and J.L. Sinclair, "Comparative Analysis of CFD Models of Dense Gas-Solid Systems," *AIChE Journal*, **47**, 1035 (2001).

Werther, J., and O. Molerus, 1973, "The Local Structure of Gas Fluidized Beds - II. The Spatial Distribution of Bubbles," *International Journal of Multiphase Flow*, **1**, 123 (1973).

List of Figure Captions

Figure 1. Comparison of Calculated Bed Expansion With Data

Figure 2. Achieving a Statistical Steady State in Outlet Ozone Concentration

Figure 3. Outlet Mass Fraction of Ozone as a Function of Gas Velocity (H_{mf} = 11.5 cm, k = 1.57 s^{-1})

Figure 4. Conversion as a Function of Initial Bed Height at U=10 cm/s and k=0.33 s^{-1}

Figure 5. Average Axial Concentration of Ozone at H_{mf} = 23.1 cm, U = 10.4 cm/s and k = 0.331 s^{-1}

Figure 6. Void Fraction and Mass Fraction Distributions and Velocity Vectors

Figure 7. Time-Averaged Velocity Vectors and Contours of Void Fraction (U = 10 cm/s; H_{mf} = 11.5 cm)

Figure 8: Time-Averaged Velocity Vectors and Contours of Void Fraction (U = 10.4 cm/s; H_{mf} = 23.1 cm)

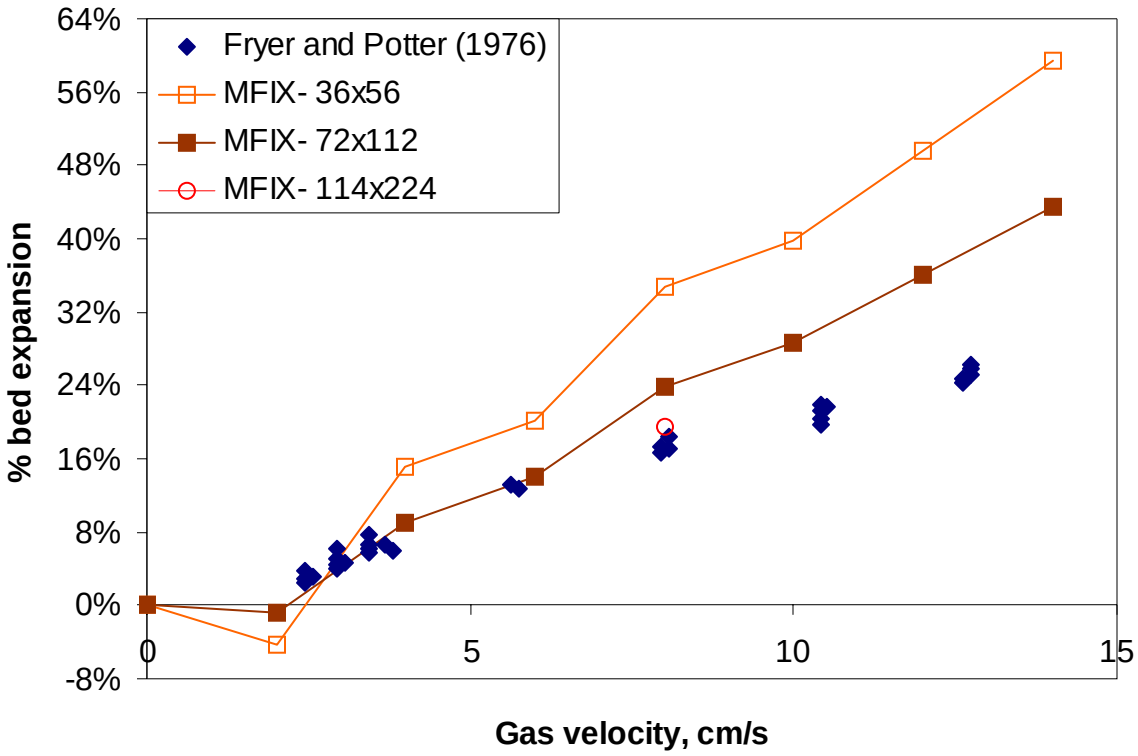

Figure 1. Comparison of Calculated Bed Expansion With Data

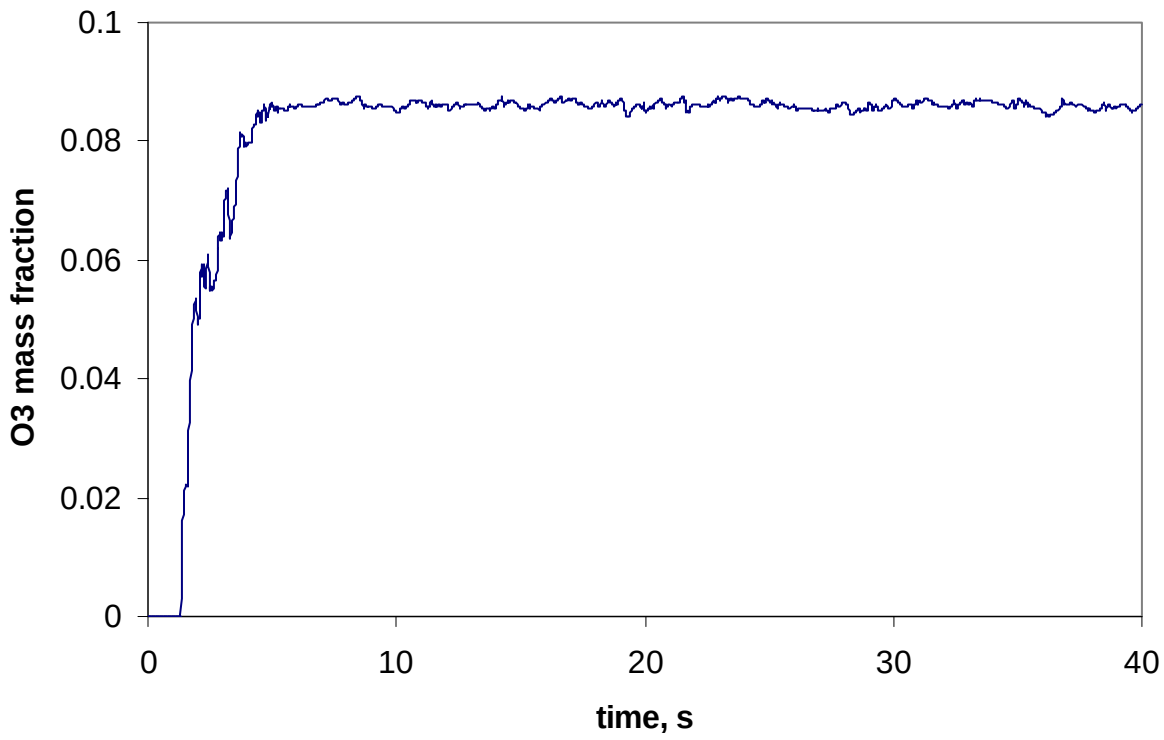

Figure 2. Achieving a Statistical Steady State in Outlet Ozone Concentration

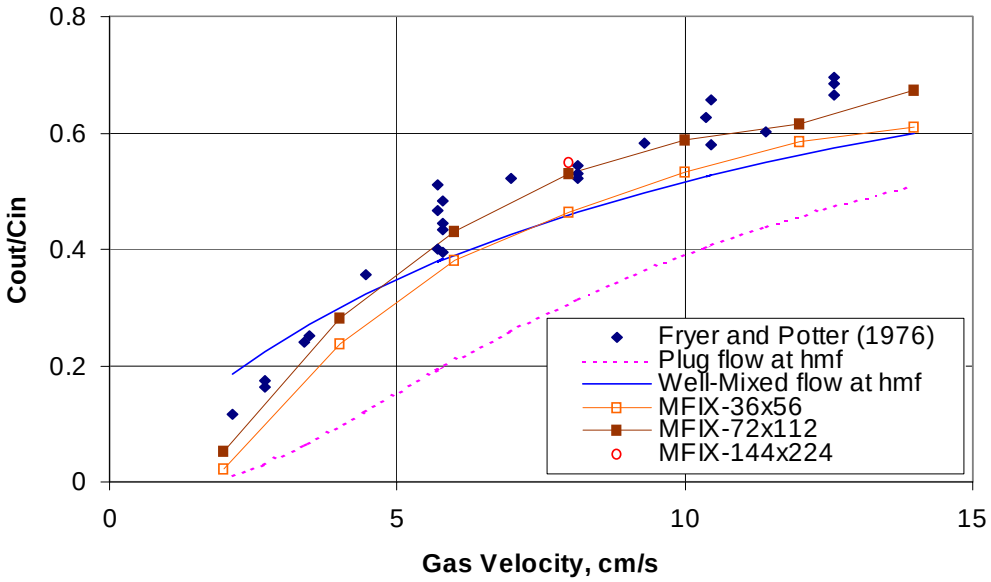

Figure 3. Outlet Mass Fraction of Ozone as a Function of Gas Velocity
(H_{mf} = 11.5 cm, k = 1.57 s^{-1})

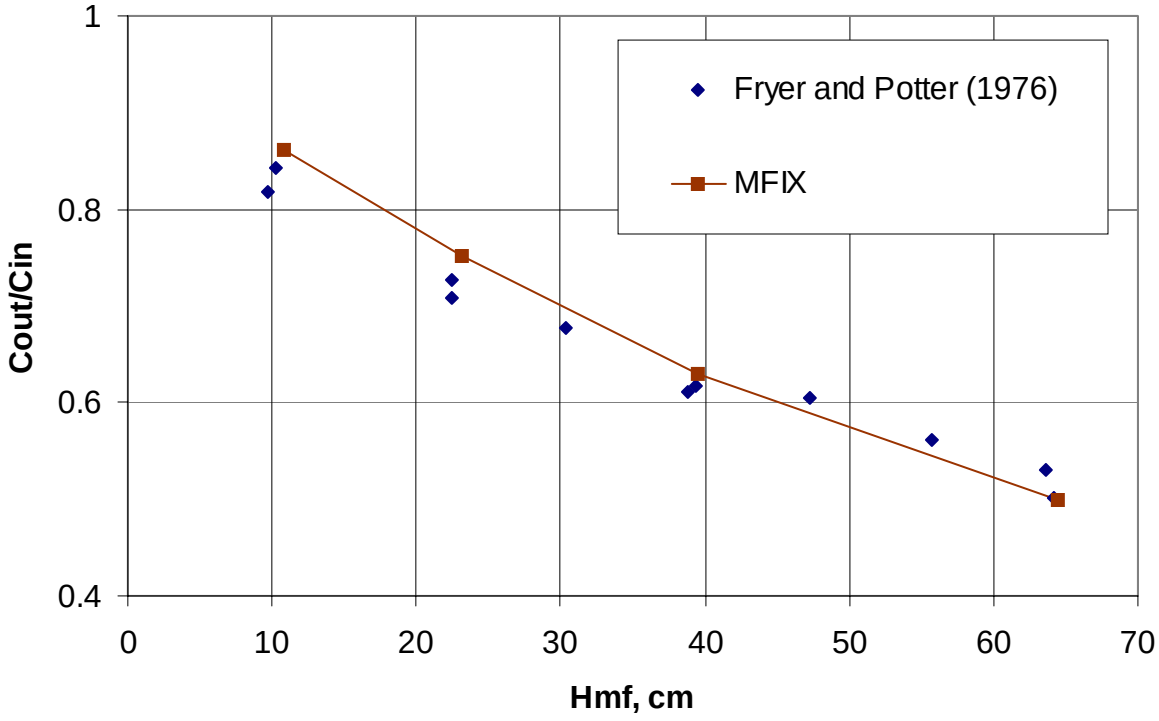

Figure 4. Conversion as a Function of Initial Bed Height at U=10 cm/s and k=0.33 s^{-1}

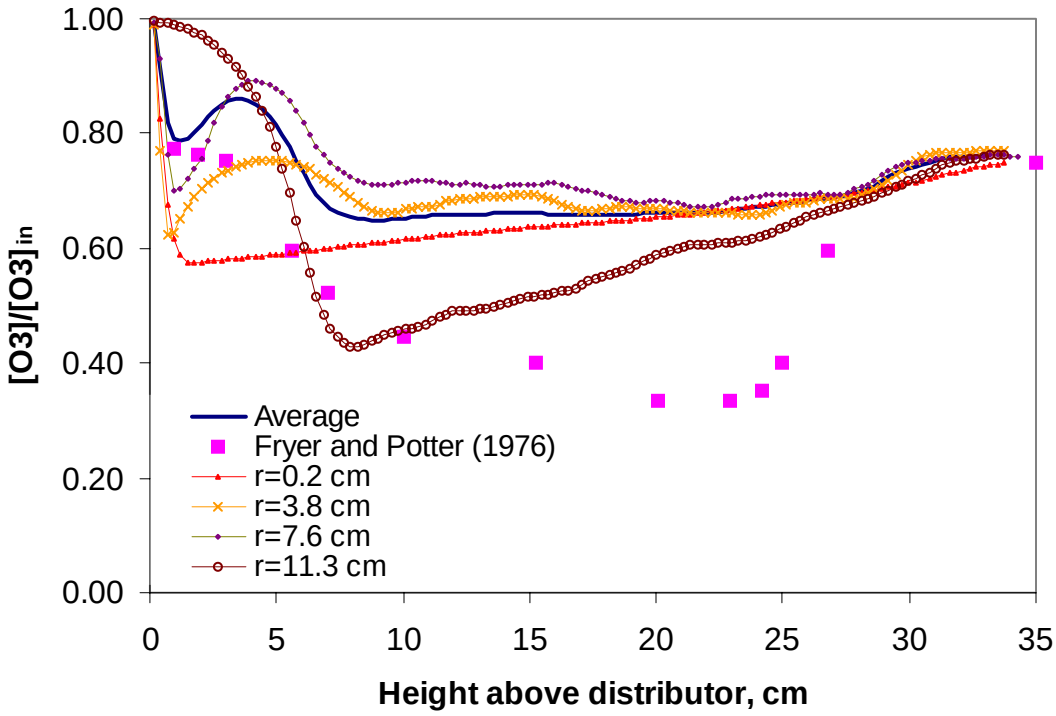

Figure 5. Average Axial Concentration of Ozone at H_{mf} = 23.1 cm, U = 10.4 cm/s and k = 0.331 s^{-1}

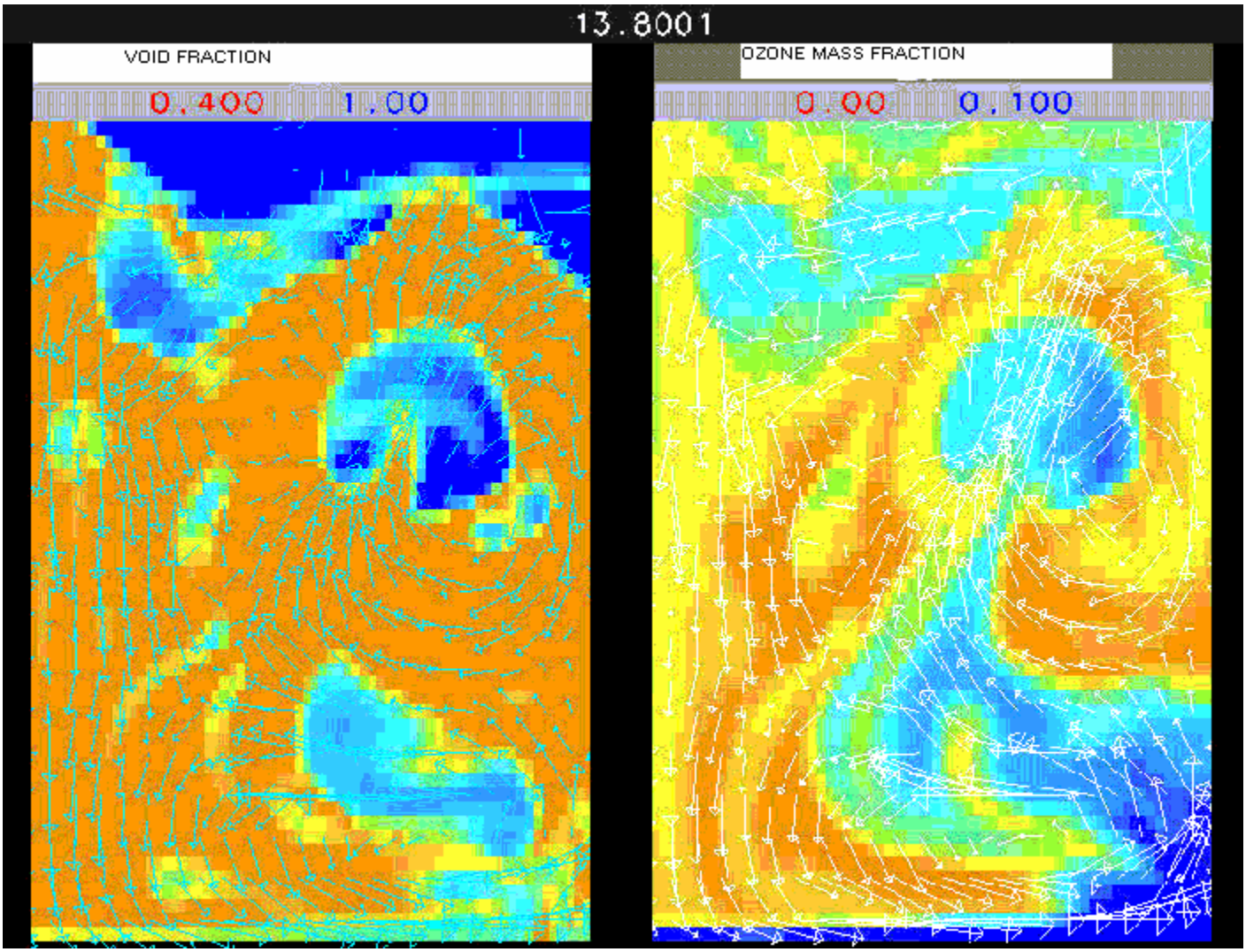

Figure 6. Void Fraction and Mass Fraction Distributions and Velocity Vectors

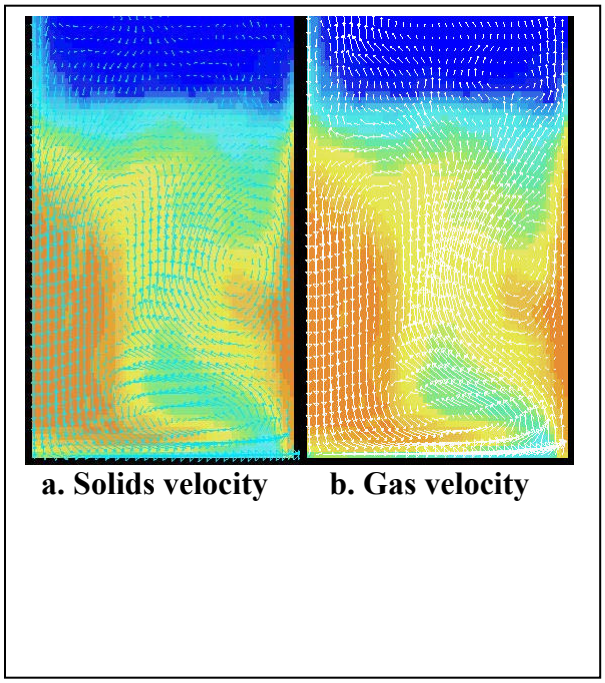

Figure 7. Time-Averaged Velocity Vectors and Contours of Void Fraction (U = 10 cm/s; H_{mf} = 11.5 cm)

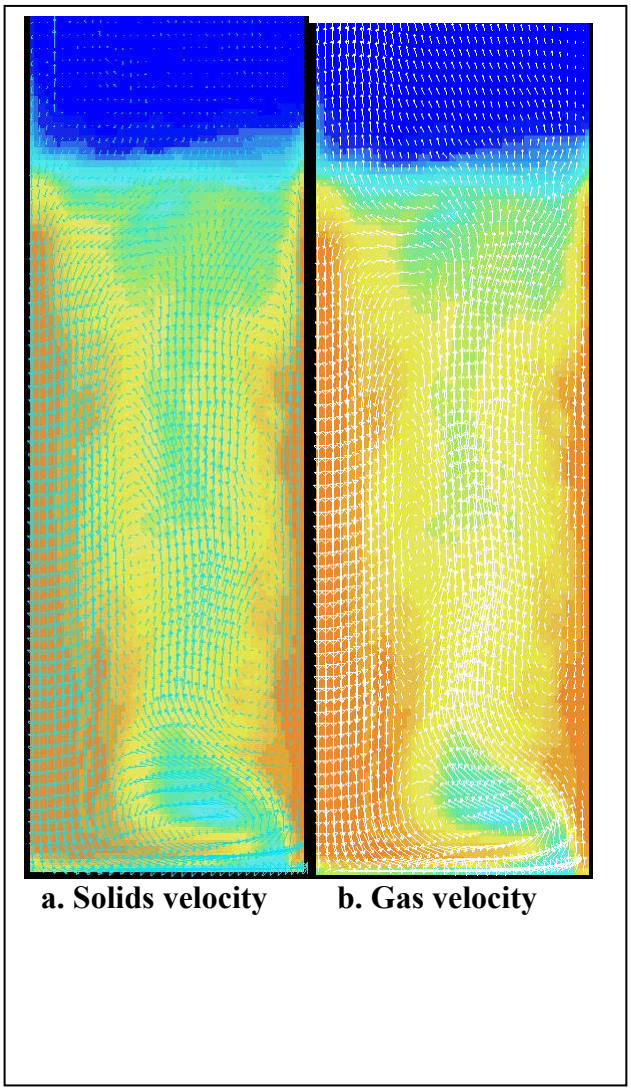

Figure 8: Time-Averaged Velocity Vectors and Contours of Void Fraction
(U = 10.4 cm/s; H_{mf} = 23.1 cm)

Table I. Simulation Conditions

Reported by Fryer and Potter (1976)		
Particle diameter, d_p	117	μm
Particle density, ρ_s	2650	kg/m^3
Minimum fluidization velocity, U_{mf}	1.70	cm/s
Void fraction at U_{mf}, ε_{mf}	0.48	
Bed height at U_{mf}, H_{mf}	10.8-64.5	cm
Fluidization velocity	2-14	cm/s
Reaction kinetic constant	1.57, 0.33	s^{-1}
Other Assumed Parameters		
Sphericity	0.75	
Parameter c in drag formula	0.765	
Parameter d in drag formula	2.928	
Coefficient of restitution	0.8	
Angle of internal friction	30	degree
Fluid viscosity	1.8×10^{-5}	Pa·s
O_3 mass fraction in inlet (O_3-Air) mixture	0.1	

Table II. Summary of MFIX Equations

Gas Continuity: $\frac{\partial}{\partial t}(\varepsilon_g \rho_g) + \nabla \cdot (\varepsilon_g \rho_g \vec{v}_g) = \sum_{n=1}^{N_g} R_{gn}$
Solids Continuity: $\frac{\partial}{\partial t}(\varepsilon_s \rho_s) + \nabla \cdot (\varepsilon_s \rho_s \vec{v}_s) = \sum_{n=1}^{N_s} R_{sn}$
Species Mass Balance: $\frac{\partial}{\partial t}(\varepsilon_g \rho_g X_{gn}) + \nabla \cdot (\varepsilon_g \rho_g X_{gn} \vec{v}_g) = R_{gn}$
Gas Momentum: $\frac{\partial}{\partial t}(\varepsilon_g \rho_g \vec{v}_g) + \nabla \cdot (\varepsilon_g \rho_g \vec{v}_g \vec{v}_g) = \nabla \cdot \bar{\bar{S}}_g + \varepsilon_g \rho_g \vec{g} - \vec{I}_{gs}$
Solids Momentum: $\frac{\partial}{\partial t}(\varepsilon_s \rho_s \vec{v}_s) + \nabla \cdot (\varepsilon_s \rho_s \vec{v}_s \vec{v}_s) = \nabla \cdot \bar{\bar{S}}_s + \varepsilon_s \rho_s \vec{g} + \vec{I}_{gs}$
$\vec{I}_{gs} = -\varepsilon_s \nabla P_g - F_{gs}(\vec{v}_s - \vec{v}_g)$
Gas-Solids Drag: $F_{gs} = \frac{3 \varepsilon_s \varepsilon_g \rho_g}{4 V_{rs}^2 d_p} C_{Ds}\left(\frac{Re_s}{V_{rs}}\right)\lvert\vec{v}_s - \vec{v}_g\rvert$, $V_{rs} = 0.5\left(A - 0.06\, Re_s + \sqrt{(0.06\, Re_s)^2 + 0.12\, Re_s (2B - A) + A^2}\right)$ $A = \varepsilon_g^{4.14}$, $B = \begin{cases} c\, \varepsilon_g^{1.28} & \text{if } \varepsilon_g \le 0.85 \\ \varepsilon_g^{d} & \text{if } \varepsilon_g > 0.85 \end{cases}$
Gas-Phase Stress: $\bar{\bar{S}}_g = -P_g \bar{\bar{I}} + \bar{\bar{\tau}}_g = -P_g \bar{\bar{I}} + 2 \varepsilon_g \mu_g \bar{\bar{D}}_g + \varepsilon_g \lambda_g \mathrm{tr}(\bar{\bar{D}}_g) \bar{\bar{I}}$,
Solids-Phase Stress: $\bar{\bar{S}}_s = \begin{cases} -P_s^p \bar{\bar{I}} + \bar{\bar{\tau}}_s^p & \text{if } \varepsilon_g \le \varepsilon_g^* \\ -P_s^v \bar{\bar{I}} + \bar{\bar{\tau}}_s^v & \text{if } \varepsilon_g > \varepsilon_g^* \end{cases}$,
Viscous Regime (kinetic theory) $P_s^v = K_1 \varepsilon_s^2 \Theta_s$, $K_1 = 2(1+e)\rho_s g_0$, $\bar{\bar{\tau}}_s^v = 2 \mu_s^v \bar{\bar{D}}_s + \lambda_s^v \mathrm{tr}(\bar{\bar{D}}_s)\bar{\bar{I}}$, $\mu_s^v = K_3 \varepsilon_s \sqrt{\Theta_s}$. $\lambda_s^v = K_2 \varepsilon_s \sqrt{\Theta_s}$. $K_3 = \frac{d_p \rho_s}{2}\left\{ \frac{\sqrt{\pi}}{3(3-e)}\left[1 + 0.4(1+e)(3e-1)\varepsilon_s g_0\right] + \frac{8 \varepsilon_s g_0 (1+e)}{5\sqrt{\pi}} \right\}$. $\Theta = \left\{ \frac{-K_1 \varepsilon_s tr(\bar{\bar{D}}_s) + \sqrt{K_1^2 \varepsilon_s^2 tr^2(\bar{\bar{D}}_s) + 4 K_4 \varepsilon_s \left[K_2 tr^2(\bar{\bar{D}}_s) + 2 K_3 tr(\bar{\bar{D}}_s^2) \right]}}{2 K_4 \varepsilon_s} \right\}^2$.

Plastic Regime:

$$\mathrm{P}_{\mathrm{s}}^{p}=10^{25}\quad(\varepsilon_s-\varepsilon_s^{cp})^{10}\ ,\ \overset{=p}{\tau}_{\mathrm{s}}=2\quad\mu_{\mathrm{s}}^{p}\quad\overline{\overline{\mathrm{D}}}_{\mathrm{s}}\quad,\ \mu_{\mathrm{s}}^{p}=P_s^{p}\ \sin\phi\big/2\sqrt{I_{2D}}\ .$$

$$I_{2D}=\left(\left(D_{s11}-D_{s22}\right)^2+\left(D_{s22}-D_{s33}\right)^2+\left(D_{s33}-D_{s11}\right)^2\right)/\,6+D_{s12}^2+D_{s23}^2+D_{s31}^2$$

Appendix B

Hydrodynamics of Particle Segregation in Fluidized Beds

HYDRODYNAMICS OF PARTICLE SEGREGATION IN FLUIDIZED BEDS

Dinesh Gera* and **Madhava Syamlal**

Fluent Incorporated
3647 Collins Ferry Road, Suite A
Morgantown, WV 26505
Ph. (304) 598-7934; Fax (304) 598-7185; E-mail: dfg@fluent.com

Thomas J. O'Brien

US Department of Energy
3610 Collins Ferry Road, MS-N04,
Morgantown, WV 26505
Ph. (304) 285-4571, E-mail: tobrie@netl.doe.gov

ABSTRACT

A two-fluid model is extended to a multi-fluid model to describe fluid-particle flow. In this model, each granular phase represents particles of identical diameter and density. A particle-to-particle drag term was developed to account for the "hindrance effect" that prevents the relative motion of the two granular phases. With this term, the simulations predict no segregation at low fluidization velocities, segregation at intermediate velocities, and vigorous mixing at large fluidizing velocities. This study also allows the maximum packing voidage to vary with the mixture composition. The predicted segregation rate for a three-phase fluidized bed matches very well with the measured values. The model is also applied to describe dilute flow in a circulating fluidized bed loop. A fair agreement is seen between the measured and calculated average particle diameter in the core region of the riser.

Keywords: Fluidized Beds, Particle Segregator, Multi-Phase Flow, Circulating Fluidized Bed

1.0 INTRODUCTION

Research in multiple particulate phase hydrodynamics is important in many industrial applications that involve segregation or mixing processes, specifically in mineral classification, elutriation, sedimentation, crystallization and fluid bed leaching, just to name a few (Reh, 1999). There have been several investigations dealing with

segregation and mixing of particles of different sizes and densities in fluidized bed reactors or classifiers (Jean and Fan, 1986; Hu, 2002; Chen et al., 2002). The studies show that particles will segregate into layers if a bed, consisting of two different size particles with the same density, is fluidized with a velocity that is in between the individual minimum fluidization (u_{mf}) velocities for each particle type. The binary system will not segregate if the fluidizing velocity is higher than the u_{mf} of the larger particles; rather the particles mix vigorously. The models reported in the literature are able to predict the segregation of the particles at an intermediate fluidization velocity (Goldschmidt et al. 2001). However, they predict particle segregation even at a low fluidization velocity, when segregation is not observed. In this study we modified the particle-particle drag term so that the model predicts no segregation at low velocities, segregation at intermediate velocities, and mixing at high velocities. Furthermore we show that the predicted rate of segregation at intermediate velocities agrees quantitatively with experimental data. Additionally, segregation of particles is also demonstrated in a dilute circulating fluidized bed case.

In the last decade, considerable efforts have been made in developing detailed hydrodynamic tools for the simulation of fluidized bed dynamics, including Eulerian/Lagrangian, and the hybrid Eulerian/Lagrangian mapping methods. Eulerian/Eulerian methods consider the primary and secondary (dispersed) phases to be interpenetrating continua, and the equations employed are generalizations of the Navier-Stokes equations (e.g., Gidaspow 1994). Eulerian/Lagrangian models describe the primary phase flow using the continuum equations, and the particulate phase flow is described by tracking the motion of individual particles (e.g., Tsuji 1993; Gera et al., 1998). Lagrangian models include the effects of particle collisions and the forces acting on the particles by the gas.

The hybrid Eulerian/Lagrangian approach is based on the multi-phase particle-in-cell (MP-PIC) technique. This technique solves the governing equations of the fluid phase using a continuum model and maps the particle properties from the Lagrangian tracking of the particulate phase to an Eulerian grid (Snider et al., 1998; Andrews and

O'Rourke, 1996). In the hybrid Eulerian/Lagrangian scheme, collisions between the particles are modeled by computing an isotropic inter-particle stress from the Eulerian grid and mapping it back to particle positions in the Lagrangian scheme. The difference between this technique and the traditional Lagrangian/discrete schemes is that the particle-particle interactions are not computed at an individual particle level, instead these interactions are computed on the grid level.

With the advent of fast and economical computers, researchers have extended the Eulerian/Eulerian two fluid models to multi-fluid models to account for multiple particle sizes and densities (Syamlal 1985, Gidaspow et al. 1986, Hoffman and Kevelam,1999; Mathiesen et al., (2000); Goldschmidt et al., 2001; Clelland and Hrenya, 2002). As a starting point, the current theory of fluidization developed for mono-disperse particles is extended to poly-disperse particle systems by including particle-particle drag terms. Recently, we have extended the multi-fluid model to describe a six-particle system in a liquid bed classifier (Gera et al, 2003).

The focus of this paper is on Eulerian/Eulerian methods for the computation of gas-solids flows. Eulerian/Eulerian methods are potentially faster than Eulerian/Lagrangian methods, but require the formulation of constitutive equations. We extended a two-fluid model (gas and one granular phase) to a multi-fluid model (gas and several granular phases) by adding constitutive equations for the particle-particle drag and the maximum particle packing. The new constitutive equations are added in the MFIX code, an open-source multiphase flow model (Syamlal, *et al.* 1993; www.mfix.org). The model is used to describe solids segregation in a dense fluidized bed and circulating fluidized bed.

2.0 HYDRODYNAMIC MODEL

The mathematical model is based on an assumption that all the phases can be mathematically described as interpenetrating continua; the point variables are averaged over a region that is large compared with the particle spacing but much smaller than the flow domain (e.g., Anderson and Jackson 1967). The equations solved by the

MFIX code used in this study are given in Syamlal et al. (1993). The continuity equation for each phase is written as:

$$\frac{\partial}{\partial t}\left(\varepsilon_m \rho_m\right)+\nabla\cdot\left(\varepsilon_m \rho_m \vec{v}_m\right)=0 \tag{1}$$

where, ρ_m and $\vec{v}_m$ are the density and velocity of the m^{th} phase (m=0 represents the gas phase), respectively, ε_m is the volume fraction of the m^{th} phase with the condition $\sum_m \varepsilon_m = 1$.

The momentum equation for the gas phase is expressed as:

$$\frac{\partial}{\partial t}\left(\varepsilon_0 \rho_0 \vec{v}_0\right)+\nabla\cdot\left(\varepsilon_0 \rho_0 \vec{v}_0 \vec{v}_0\right)=\nabla\cdot\bar{\bar{S}}_0+\varepsilon_0 \rho_0 \vec{g}-\sum_{m=1}^{M}\vec{I}_{0m} \tag{2}$$

where the stress tensor for the gas phase is defined as:

$$\bar{\bar{S}}_0 = -P_0\bar{\bar{I}}+\varepsilon_0 \mu_0 \left[\nabla \vec{v}_0+\left(\nabla \vec{v}_0\right)^T\right]+\varepsilon_0\left(\lambda_0-\frac{2}{3}\mu_0\right)\nabla\cdot\vec{v}_0\ \bar{\bar{I}} \tag{3}$$

Here μ_0 and λ_0 are the shear and bulk viscosity of the gas phase, $\bar{\bar{I}}$ is a unit tensor, $\vec{I}_{0m}$ is an interaction (or drag) force representing the momentum transfer between the gas phase and the m^{th} solid phase. The interaction force $\vec{I}_{0m}$ is written as:

$$\vec{I}_{0m}=\varepsilon_l \nabla P_g - F_{0m}\left(\vec{v}_m - \vec{v}_0\right) \tag{4}$$

where the interaction-exchange coefficient (F_{0m} between the gas phase and the m^{th} solid phase is written as (Gidaspow 1994):

$$F_{0m}=\begin{cases} 150\dfrac{\varepsilon_m(1-\varepsilon_0)}{\varepsilon_0 d_{pm}^2}\mu_0+1.75\varepsilon_m\dfrac{\rho_0}{d_p}\left|v_s - v_g\right| & for\ \varepsilon \le 0.8 \\ \dfrac{0.75\ \varepsilon_m\ \varepsilon_0\ \rho_0}{d_{pm}}\ C_{Ds}\ \left|\vec{v}_m - \vec{v}_0\right|\ \varepsilon_0^{-2.65} & for\ \varepsilon > 0.8 \end{cases} \tag{5}$$

and $$C_D = \begin{cases} 24(1+0.15\,Re^{0.687})/Re, & Re < 1000 \\ 0.43, & Re \geq 1000 \end{cases} \qquad (6)$$

The Reynolds number for the m[th] solids phase is given by

$$\mathrm{Re_m} = \mathrm{d_{pm}} \left| \vec{\mathrm{v}}_{\mathrm{sm}} - \vec{\mathrm{v}}_{\mathrm{g}} \right| \rho_{\mathrm{g}} / \mu_m$$

The momentum equation for each of the 'm' solid phases is expressed as:

$$\frac{\partial}{\partial \mathrm{t}} \left(\varepsilon_m \ \rho_m \ \vec{\mathrm{v}}_m \right) + \nabla \cdot \left(\varepsilon_m \rho_m \ \vec{\mathrm{v}}_m \ \vec{\mathrm{v}}_m \right) = \nabla \cdot \bar{\bar{\mathrm{S}}}_m + \varepsilon_m \rho_m \ \vec{\mathrm{g}} + \vec{I}_{0m} - \sum_{\substack{l=1 \\ l \neq m}}^{\mathrm{M}} \vec{I}_{\mathrm{m}l} \qquad (7)$$

where the stress tensor for the m[th] solid phase is defined by combining the theories of viscous and plastic flow regimes as (Syamlal et al. 1993):

$$\bar{\bar{\mathrm{S}}}_{\mathrm{m}} = \begin{cases} -\mathrm{P}_{\mathrm{m}}^{\mathrm{p}} \bar{\bar{\mathrm{I}}} + \bar{\bar{\tau}}_{\mathrm{m}}^{\mathrm{p}} & \text{if } \varepsilon_0 \leq \varepsilon_0^* \\ \\ -\mathrm{P}_{\mathrm{m}}^{\mathrm{v}} \bar{\bar{\mathrm{I}}} + \bar{\bar{\tau}}_{\mathrm{m}}^{\mathrm{v}} & \text{if } \varepsilon_0 > \varepsilon_0^* \end{cases}, \qquad (8)$$

Here $\mathrm{P_m}$ is the pressure and $\bar{\bar{\tau}}_{\mathrm{m}}$ is the viscous stress in the m[th] solids phase. The superscript p stands for plastic regime and v for viscous regime. In fluidized-bed simulations, ε_0^* is set to the void fraction at the minimum fluidization. The plastic stresses are calculated using Schaeffer's (1987) formulation :

$$\bar{\bar{\tau}}_m^{\ p} = 2 \ \mu_m^p \ \bar{\bar{D}}_m \ , \qquad (9)$$

where

$$\mu_m^p = \frac{\mathrm{P}^* \sin \phi}{2 \sqrt{\mathrm{I}_{2\mathrm{D}}}} \ . \qquad (10)$$

Here $\mathrm{I_{2D}}$ is the second invariant of the deviator of the strain rate tensor (see Syamlal et al.,1993). Similar to the functions typically used in plastic flow theories (Jenike 1987), an arbitrary function that allows a certain amount of compressibility in the solids phase represents the solids pressure term for plastic flow regime (Pritchett et al., 1978):

$$P_m^p = \varepsilon_m \; P^* \quad , \tag{11}$$

where P^* is represented by an empirical power law

$$P^* = 10^{25} \; (\varepsilon_0^* - \varepsilon_0)^{10} . \tag{12}$$

The particle-particle interaction force $\vec{I}_{lm}$ is written as:

$$\vec{I}_{lm} = F_{lm} \; (\vec{v}_m - \vec{v}_l) \tag{13}$$

For the drag coefficient F_{ml} is an extended form of an expression derived by Syamlal (1987):

$$F_{ml} = \frac{3 (1 + e_{lm}) (\pi / 2 + C_{flm} \pi^2 / 8) \varepsilon_l \rho_l \; \varepsilon_m \rho_m (d_{pl} + d_{pm})^2 g_{0_{lm}} |\vec{v}_l - \vec{v}_m|}{2\pi (\rho_l d_{pl}^3 + \rho_m d_{pm}^3)} + C_1 P^* \tag{14}$$

where e_{lm} and C_{flm} are the coefficient of restitution and coefficient of friction, respectively, between the l^{th} and m^{th} granular-phase particles. The radial distribution function at contact, $g_{0_{lm}}$, is that derived by Lebowitz (1964) for a mixture of hard spheres:

$$g_{0_{lm}} = \frac{1}{\varepsilon_0} + \frac{3 d_{pl} d_{pm}}{\varepsilon_0^2 (d_{pl} + d_{pm})} \sum_{\lambda=1}^{M} \frac{\varepsilon_\lambda}{d_{p\lambda}} \tag{15}$$

Additional details about the formulation are given by Syamlal et al, (1993), and the solution algorithm is described by Syamlal (1998).

The first term on the right side of Eq. (14) accounts for the momentum transferred between the phases because of collisions and sliding. The newly-added, second term on the right side of Eq. 14 accounts for a "phase change" in particulate flow. Without this term in the present formulation, a granular medium consisting of two types of particles

would be treated as two distinct phases. When the particles are closely packed and the diameter ratio is such that the fines cannot percolate through the interstices of the packed bed, the description as two separate particulate phases is inadequate. For example, the model would predict that the two types of particles of different densities would segregate even in a packed bed whereas, in reality, they do not. The particles do not experience any buoyant force from solids pressure gradient and behave as a single phase. In a multiphase description of the granular media, one way to model the packed bed is to treat it as a single phase as though a "phase change" (multiphase to single phase) has occurred. Another way, the one adopted in this work, is to make the particle-particle drag so large that the two-phases will move together and, in effect, behave as a single phase. We expect the rate of increase in the particle-particle drag to be analogous to the stresses in the frictional regime (Eqns. 9 and 10), and, hence, proportional to the granular pressure P* (Eq. 12) – the greater the granular pressure the greater the tendency for the two phases to move together as a single phase. The proportionality coefficient C_1=0.3 is determined to provide the correct initial slope in Figure (2).

2.1 Effect of Maximum Packing Voidage

Mixing particles with different sizes leads to an increase in the maximum packing voidage of the bed. For example, if large spherical beads are mixed with smaller spherical beads, the maximum particle volume fraction of the mixture will be greater than the maximum particle volume fraction of either particle type. Fedors and Landel (1979) proposed the following correlations for the maximum packing voidage for a binary mixture of two particle diameters (d_1>d_2) as a function of mixture composition X_1 = $\varepsilon_1/(\varepsilon_1+\varepsilon_2)$:

if $$X_1 \le \frac{\varepsilon_1^{\max}}{\left(\varepsilon_1^{\max} + (1-\varepsilon_1^{\max})\varepsilon_2^{\max}\right)}$$

$$\varepsilon_0^* = 1.0 - \left(\varepsilon_1^{\max} - \varepsilon_2^{\max} + \left[1 - \sqrt{\frac{d_2}{d_1}} \right] (1-\varepsilon_1^{\max})\varepsilon_2^{\max} \right) \left(\varepsilon_1^{\max} + (1-\varepsilon_2^{\max})\varepsilon_1^{\max} \right) \frac{X_1}{\varepsilon_1^{\max}} + \varepsilon_2^{\max}$$

otherwise

$$\varepsilon_0^* = 1.0 - \left[1 - \sqrt{\frac{d_2}{d_1}} \right] \left(\varepsilon_1^{\max} + (1-\varepsilon_1^{\max})\varepsilon_2^{\max} \right) (1-X_1) + \varepsilon_1^{\max} \qquad (16)$$

These correlations are used for the maximum packing voidage as a function of mixture composition in the granular pressure and particle-particle drag terms in Eqs.(8, 12 and 14).

3.0 BINARY PARTICLE SIMULATIONS IN DENSE REGIME

The hydrodynamic model equations are solved for a dense bed of binary-dispersed spherical glass beads of 1.5 mm and 2.5 mm diameter with density of 2524 kg/m^3, as shown in Figure 1. A solids volume fraction of 30% for each of the two granular phases is the initial condition in the bed. The properties of the glass beads (see Table 1) are taken from Goldschmidt et al. (2001). The minimum fluidization velocity (u_{mf}) of the small particles is 0.78 $\pm$ 0.02 m/s; that of the large particles is 1.25 $\pm$ 0.01 m/s. Two fluidization velocities are used in the simulations: 1.1 m/s, a condition for which segregation should occur; and 1.25 m/s, a condition for which vigorous mixing should occur. These velocities are chosen to demonstrate (a) the segregation of particles when the fluidizing velocity is in between the u_{mf} of two particle types, and (b) vigorous mixing when the fluidizing velocity is equal to or greater than the u_{mf} of the larger particles. The computational grid in the present simulations consists of 15 x 50 rectangular cells. The discretized equations on the above grid are solved using second order superbee flux limiter (Leonard and Mokhtari, 1990, Syamlal and Guenther 2001).

Table 1: Properties of glass beads used in the simulations

	Small Particles	Large Particles
Diameter (d_{p1}, d_{p2})	1.5 mm	2.5 mm
Density (ρ_1, ρ_2)	2524 kg/m^3	2524 kg/m^3
Minimum Fluidization Velocity (u_{mf})	0.78 m/s	1.25 m/s
Coefficient of normal restitution (e)	0.97	0.97
Coefficient of friction (C_{flm})	0.15	0.15

The segregation rate has been quantified by Goldschmidt et al. (2001) using a digital image analysis technique. We used the same procedure as proposed by Goldschmidt et al. (2001) for calculating the average height of the solids phases in the bed:

$$< h_m >= \frac{\sum_{cell} \varepsilon_{m,cell} h_{cell}}{\sum_{cell} \varepsilon_{m,cell}} \tag{17}$$

where $\varepsilon_{m,cell}$ is the volume fraction of solids phase m in the cell and h_{cell} is the height of the cell center above the distributor plate; the sum is over all cells in the computational domain. The average height of the two phases predicted by the current model is compared with the experimental data of Goldschmidt et al. (2001) at 1.10 m/s in Figure 2(a). We adjusted the one constant C_1 to match the initial rate of segregation of the large particles. The model captures the slow segregation during the first eight seconds followed by a rapid segregation during the next 10 seconds. At the end of 18 seconds, the segregation is nearly complete. We continued the simulation up to 60 seconds to determine the steady state heights of the particulate phases. The height of the small particle layer is well captured by the model. The predicted height of the large particle layer is larger than the experimental value. Equation (17), used for calculating the heights, does not impose any constraint on the sum of the heights. Thus, a good match in the height of the small particle layer does not imply a good match in the height of the large particle as well.

To aid the visualization of the binary particle system, the number of particles in a grid cell is calculated from the solid volume fraction and a corresponding number of dots are placed randomly in each cell in Figure 2b. Initially the particles are well mixed. By 20 seconds a distinct large particle layer forms at the bottom of the bed. That layer appears to be free of small particles. However, the upper layer, which predominantly consists of small particles, contains a fair number of large particles. This causes the over prediction of the height of the large particle layer (Figure 2a). We suspect that the inability of the numerics to sharply resolve the interface between the small and large particles is the cause of this discrepancy.

The average height of solids phases predicted by the current model at 1.25 m/s is compared with the experimentally measured values in Figures 3(a) and (b). The corresponding particle number concentration is plotted in Figure 3(c). The current model predicts the mixing phenomenon very well, unlike previously reported models (e.g., Goldschmidt et al., 2001). The value of the constant C_1 was kept unchanged in this simulation. It can be seen that for 1.25 m/s, the bed starts to bubble and hence leads to the mixing of the particles.

4.0 BINARY PARTICLE SIMULATIONS IN A DILUTE REGIME

The current model is further validated with the experimental data of Mathiesen *et al.*, (2000) obtained from a circulating fluidized bed loop as shown in Figure 4. The computational domain is divided into a 34 x 68, non-uniform, rectangular mesh. The properties of the particles are listed in Table 2. The bed is initially filled to 0.04 m with the total solid volume fraction of 0.63. The two granular phases are assumed to be perfectly mixed and to have an identical initial volume fraction. The bed is fluidized at 1.0 m/s and 0.8 m/s. A detailed comparison of the particle volume fraction distribution at several axial locations has been made for the case of 1.0 m/s velocity. At the exit, a porous boundary condition that allowed the gas (but not the particles) to escape is used (Gas outlet in Figure 4). The simulations are conducted for 25 seconds. The simulation results reported are time-averaged values for the last 5 seconds, when a pseudo-steady state is reached.

An average particle diameter of the binary mixture is calculated by accounting for the solid volume fraction of each phase:

$$d_{av} = \frac{\varepsilon_1 d_2^3 d_1 + \varepsilon_2 d_1^3 d_2}{\varepsilon_1 d_2^3 + \varepsilon_2 d_1^3} \tag{18}$$

where ε_1 and ε_2 are the solids volume fractions of phase 1 and phase 2, and d_1 and d_2 are their diameters. The average predicted diameter profile is compared with the measured diameter profile along the axis of the riser for two superficial velocities (0.8 and 1.1 m/s) in Figure 5. Due to the dense zone near the bottom of the riser, Mathiesen et al. (2000)

were unable to collect the data below 0.2 m in the riser. At 0.8 m/s the large particles (185 μm) tend to collect at the bottom of the riser. Therefore, the average diameter is high at the bottom (< 0.2 m height). At the top, it drops to about 120 μm, the diameter of the small particles. When the fluidization velocity is increased to 1 m/s the circulation rate of the large particles increases. The average diameter decreases at the bottom of the riser and increases at the top of the bed. The model captures this feature of the experimental data very well.

Table 2: Properties of glass particles in a dilute circulating fluidized bed

	Small Particles	Large Particles
Diameter (d_{p1}, d_{p2})	120 μm	185 μm
Density (ρ_1, ρ_2)	2400 kg/m^3	2400 kg/m^3
Coefficient of normal restitution (e)	0.99	0.99

The predicted radial-averaged diameter profile is compared with the experimental data at three axial locations above the distributor plate of the riser in Figure 6. A fair agreement is observed in the core region. The experimental data suggests that the large particles migrate toward the wall. The model does not predict this trend. We are not sure whether this is due to a limitation of the physical model or it is because of inadequate grid resolution.

The model does predict the core annular flow in the riser as evidenced by the velocity distribution of the two phases shown in Figure 7. The downward flow of particles near the wall (near x/D=0 and x/D=1.0) can be seen very well. The velocity of the particles is maximum in the center of the core and minimum in the center of the annulur region. The simulations are in fair agreement with the experiments. Perhaps, the predictions could be improved by simulating the bed in 3-D instead of 2-D. 3-D simulations are much more expensive than 2-D simulations and will be attempted in the future.

4.0 CONCLUSIONS

A two fluid model is extended to a 3-phase, multi-fluid model. In this model, a primary air phase and two additional particulate phases (each representing a separate class of particle diameters) were tracked in dense and dilute regimes. A particle-particle drag term was developed to account for a "hindrance" effect that prevents the relative motion of the two granular phases. With this term, the simulations predict no segregation at low fluidization velocities, segregation at intermediate velocities, and vigorous mixing at large fluidizing velocities. The maximum packing voidage considered a function of mixture composition. The predicted segregation rate for a three-phase fluidized bed matches very well with the measured values. The model is also applied to describe dilute flow in a circulating fluidized bed loop. A fair agreement is seen between the measured and calculated average particle diameter in the core region of the riser.

ACKNOWLEDGEMENTS

The authors would like to thank Dr. M.J.V Goldschmidt of Akzo Nobel Chemicals Research in The Netherlands for providing the experimental data in electronic format for the dense bed segregator, and Dr. Vidar Mathiesen of Telemark University College, Norway, for providing the experimental data for the circulating fluidized bed. Their help is gratefully acknowledged.

REFERENCES

Anderson, T.B., and Jackson, R., (1967), "A Fluid Mechanical Description of Fluidized Beds," *I&EC Fundam.*, **6**, 527-534.

Andrews, M.J., and O'Rourke, P.J., (1996), "The Multiphase Particle-in-Cell (MP-PIC) Method for Dense Particulate Flows, " Int. Journal of Multiphase Flow, Vol. 22(2), pp. 379-402

Chen, A., Grace, J.R., Epstein, N., and Lim, C.J., (2002), "Steady State Dispersion of Mono-Size, Binary and Multi-Size Particles in a Liquid Fluidized Bed Classifier," Chemical Engineering Science, Vol. 57, pp. 991-1002.

R. Clelland and C. M. Hrenya, (2002), "Simulations of a Binary-sized Mixture of Inelastic Grains in Rapid Shear Flow," Physical Review E, 65, article. no. 031301

Fedors, R.F., and Landel, R.F., (1979), "An Empirical Method of Estimating the Void Fraction in Mixtures of Uniform Particles of Different Size," Powder Technology, Vol. 23, pp. 225-31

Gera, D., Gautam, M., Tsuji, Y., Kawaguchi, T., and Tanaka, T., (1998), "Computer Simulationof Bubbles in Large-Particle Fluidized Beds," Powder Technology, Vol. 98, pp. 38-47

Gera, D., Syamlal, M., and O'Brien, T.J., (2003), " Hydrodynamics of Multiple Size Particles in a Liquid Fluidized Bed Classifier," ASME Fluids Engineering Division Meeting, Honolulu, HI, July 6-10, 2003

Gidaspow, D., M. Syamlal, Y.C. Seo, "Hydrodynamics of Fluidization of Single and Binary Size Particles: Supercomputer modeling," in Fluidization V: Proceedings of the 5th Engineering Foundation Conference in Fluidization, Engineering Foundation, New York, 1-8, (1986).

Gidaspow, D., Multiphase Flow and Fluidization, Continuum and Kinetic Theory Description, Academic Press, 1994.

Goldschmidt, M.J.V., Kuipers, J.A.M., and van Swaiij, W.P.M., (2001), "Hydrodynamic Modeling of Dense Gas-Fluidized Beds Using the Kinetic Theory of Granular Flow: Effect of Coefficient of Restitution on Bed Dynamics," Chemical Engineering Science, Vol. 56, pp. 571-78

Goldschmidt, M.J.V., Kuipers, J.A.M., and van Swaiij, W.P.M., (2001), "Segregation in Dense Gas-Fluidised Beds: Validation of Multi-Fluid Continuum Model with Non-intrusive Digital Image Analysis Measurements," 10th Engineering Foundation Conference on Fluidization, Beijing, China, May 20-25, pp.795-802

Hoffman, A.C., and Kevelam, J., (1999), "Model for the Interparticle Surface Separation in Concentrated Mono- and Polydisperse Suspensions," AIChE Journal, Vol. 45(2), pp. 285-90

Hu, X., (2002), "Prediction of the Inversion Velocity in the Binary-Solid Liquid Fluidized Beds," Chemical Engineering Science, Vol. 57, pp. 3149-53

Jean, R.-H., Fan, L.S., (1986), "On the Criteria of Solid Layer Inversion in a Liquid-Solid Fluidized Bed Containing a Binary Mixture of Particles, "Chemical Engineering Science, Vol. 41(11), pp. 2811-21

Jenike, A.W., (1987), "A Theory of Flow of Particulate Solids in Converging and Diverging Channels Based on a Conical Yield Function," *Powder Tech.*, **50**, 229-236

Johnson, P.C., and Jackson, R., 1987, "Frictional-Collisional Constitutive Relations for Granular Materials with Application to Plane Shearing," *J. Fluid Mech.*, **176**, 67-93.

Lebowitz, J.L., (1964), "Exact Solution of Generalized Percus-Yevick Equation for a Mixture of Hard Spheres," *Phys. Rev.*, **A133**, 895-899.

Leonard, B.P., S. Mokhtari, (1990), "Beyond first-order upwinding: the ultra sharp alternative for non-oscillatory steady-state simulation of convection," *Int. J. Numer. Methods Eng*., **30**, 729 (1990).

Mathiesen, V., Solberg, T., and Hjertager, B.H., (2000), "An Experimental and Computational Study of Multiphase Flow Behavior in a Circulating Fluidized Bed," Int. Journal of Multiphase Flow, Vol. 26, pp. 387-419

Pritchett, J.W., Blake, T.R., and Garg, S.K., 1978, "A Numerical Model of Gas Fluidized Beds," *AIChE Symp. Series No. 176*, **74**, 134-148.

Reh, L., (1999), "Challenges of Circulating Fluid-Bed Reactors in Energy and Raw Materials Industries," Chemical Engineering Science, Vol. 54, pp. 5359-68

Schaeffer, D.G., (1987), "Instability in the Evolution Equations Describing Incompressible Granular Flow," J. Diff. Eq., **66**, 19-50.

Snider, D.M., O'Rourke, P.J., and Andrews, M.J., (1998), "Sediment Flow in Vessels Calculated using a Multiphase Particle-in-Cell Model for Dense Particle Flows," International Journal of Multiphase Flow, Vol. 24, pp. 1359-82

Syamlal, M.,"Multiphase Hydrodynamics of Gas-Solids Flow," Ph.D. Dissertation, Illinois Institute of Technology, Chicago, 1985.Syamlal, M., (1987), "The Particle-Particle Drag Term in a Multiparticle Model of Fluidization," Topical Report, DOE/MC/21353-2373, NTIS/DE87006500, National Technical Information Service, Springfield, VA.

Syamlal, M., and T.J. O'Brien, "Simulation of Granular Layer Inversion in Liquid Fluidized Beds," *International J. of Multiphase Flow*, **14**, 473-481 (1988).

Syamlal, M., Rogers, W.A., and O'Brien, T.J., (1993), MFIX Documentation and Theory Guide, DOE/METC-94/1004, NTIS DE94000087. Electronically available from: http://www.mfix.org/docs/Theory.pdf

Syamlal, M. December 1998. MFIX Documentation: Numerical Techniques. DOE/MC-31346-5824. NTIS/DE98002029.

Syamlal, M., and Guenther, C., (2001), "The Effect of Numerical-Diffusion on Simulation of Isolated Bubbles in a Gas-Solid Fluidized Beds," Powder Technology, Vol. 116, pp. 142-54

Tsuji, Y., Kawaguchi, T., and Tanaka, T., (1993), "Discrete Particle Simulation of Two-Dimensional Fluidized Bed," Powder Technology, Vol. 77, pp. 79-87

Appendix C

Simulation of Chemically Reactive Fluidized Beds

Simulation of Chemically Reactive Fluidized Beds

M. Syamlal[1], T. O'Brien*[2], and Chris Guenther[1]

[1]Fluent, Inc., 3647 Collins Ferry Road,
Morgantown, WV 26507, USA
[2]National Energy Technology Laboratory, 3610 Collins Ferry Road,
Morgantown, WV, 26507-0880, USA
T: 304 285-4571; F: 304 285-4403; E: thomas.obrien@netl.doe.gov

ABSTRACT

Considerable progress has been made in the use of multiphase computational fluid dynamics (CFD) in the simulation of isothermal, nonreactive fluidized beds. The utility of this computational approach is now being demonstrated for chemically reactive flows with heat transfer. Results for several case studies (ozone decomposition, silane pyrolysis, silicon hydrochlorination, methane combustion, and coal gasification) are presented which demonstrate the current capabilities.

INTRODUCTION

During the development of the fluidization industry in the 20th century, most of the design effort was based on the use of algebraic correlations derived from the analysis of experimental information. A very sophisticated mathematical description of the fluidization process was developed, however, which is known by various names: two-phase (or two-fluids) theory or the theory of interpenetrating continua (1). This formulation involves a system of coupled Navier-Stokes-like partial differential equations (PDEs), which must be closed using empirical information, and then solved … a formidable challenge. In recent years, due in large part to significant advances in the computational resources, it has become possible to accurately solve the full set of PDEs (2-9). However, this is still a formidable challenge since grid-independent results require high resolution, which is not always possible for large-scale units. Nonetheless, considerable progress has been made in the use of multiphase computational fluid dynamics (CFD) in the simulation of isothermal, nonreactive fluidized beds.

However, for the most part, CFD has been used to describe only the hydrodynamic behavior of beds. Of course, in order to be useful in the chemical, petroleum or power production industry, this computation approach must also be validated for chemically reactive flows with heat transfer. This will require an extensive study of the many different types of chemical

processes. Catalytic reactions require contacting between the gas and solid phases. In such a process the reactive gas is well mixed with the fluidization media, and the major issue is the extent that the bed is by-passed due to bubble formation (or cluster formation in a circulating fluidized bed). Ozone decomposition has been used as a surrogate reaction for such a process. For chemical processes in which reactive species are injected into the bed, the mixing process must also be understood; this is obviously strongly dependent on the hydrodynamics of the bed. Tracer gas studies (using helium, for example) have been performed to explore this mixing phenomenon (see, e.g., 10). A further complication can occur when there is significant gas formation (or removal) due to the chemical reactions. In such a case, the local hydrodynamics of the bed will be affected by the upstream reactions. Finally, the reaction rates and properties of the gas are strongly affected by the temperature, so that simulations must also be able to describe exo- or endothermic reactions.

At NETL our main aim is to develop a detailed model of coal gasification, a difficult reactive gas-solids flow problem. To validate this simulation capability we have taken the approach of applying the general model to different chemically reactive systems, of increasing complexity, in which different physical phenomena are isolated and for which experimental data are available. These studies, as well as current simulations of a coal gasifier, are summarized here. The purpose of this paper is to present the breadth of the validation work.

FORMALISM

The two-fluid formalism for modeling dense gas-solid flows leads to the coupled set of transient PDEs, which describe the conservation of mass, momentum, energy, and species transport for either the gas (m = g) or solid (m = s) (see (11)):

$$\frac{\partial}{\partial \mathrm{t}}(\varepsilon_m \rho_m) + \nabla \cdot (\varepsilon_m \rho_m \vec{\mathrm{v}}_m) = \sum_{l=1}^{N_m} R_{ml}$$

$$\frac{\partial}{\partial \mathrm{t}}\left(\varepsilon_m \rho_m \vec{\mathrm{v}}_m\right) + \nabla \cdot \left(\varepsilon_m \rho_m \vec{\mathrm{v}}_m \vec{\mathrm{v}}_m\right) = \nabla \cdot \overline{\overline{S}}_m + \varepsilon_m \rho_m \vec{\mathrm{g}} \mp \vec{I}_{mn}$$

$$\varepsilon_m \rho_m C_{pm}\left(\frac{\partial T_m}{\partial t} + \vec{\mathrm{v}}_m \cdot \nabla T_m\right) = -\nabla \cdot \vec{q}_m \pm \gamma_{gs}\left(T_s - T_g\right) - \Delta H_{rm} + H_{wall}\left(T_{wall} - T_m\right)$$

$$\frac{\partial}{\partial t}\left(\varepsilon_m \rho_m X_{ml}\right) + \nabla \cdot \left(\varepsilon_m \rho_m X_{ml} \vec{\mathrm{v}}_m\right) = R_{ml}$$

These equations must be closed by equations for the momentum and energy exchange, and the phasic stresses, heat capacities, and heat fluxes, as well as the chemical rates and heats of reaction. Of particular interest in this study are the terms related to chemical reaction rates, which must be specified in order to describe the particular chemical scheme thought to occur.

CHEMICALLY REACTIVE SYSTEMS

Ozone Decomposition. This process has been used extensively to study the contacting behavior of both bubbling and circulating fluidized beds. Ozone is well-mixed in the plenum, so these studies isolate the importance of contacting between the fluid and the granular material in the bed. Alternatively, the ozone could be introduced at a specific location in the fluidized bed to study bed mixing, although this is usually done using He as a tracer (10). An extensive study (12) was based on the simulations of experiments conducted by Fryer and Potter (13). Ozone decomposition was represented using first order global kinetics of the form $R_{\mathrm{O}_3} = -3R_{\mathrm{O}_2}/2 = -k\,\varepsilon_{\mathrm{s}}\,\rho_{\mathrm{g}}\,\mathrm{X}_{\mathrm{O}_3}/MW_{O_3}$. The catalytic rate constant k was determined

by experimental measurements in a fixed bed. As seen in Figure 1, these simulations very accurately reproduced the over-all decomposition of ozone over a range of fluidization velocities and reasonably represent the bed expansion, which was more difficult to measure at higher velocities. As the fluidization velocity was increased, bubble formation increased; this resulted in decreased decomposition since more of the ozone by-passed the bed. The study showed that it was important to numerically resolve the bubble formation in order to correctly simulate this feature. At low numerical resolution, the bubbles still contained considerable amounts of the granular phase so that contacting occurred even in these by-pass regions. Higher resolution was required to calculate "clear" bubbles that allowed the ozone to avoid contact with the catalyst. In this study, since the ozone was only present in trace amounts, there were no thermal effects and no effect of the chemical reactions on the bed dynamics. Quite recently, this same experimental data has been quite successfully simulated using an agent-based model, which is based on simple rules for bubble interactions. This approach was computationally very efficient (14).

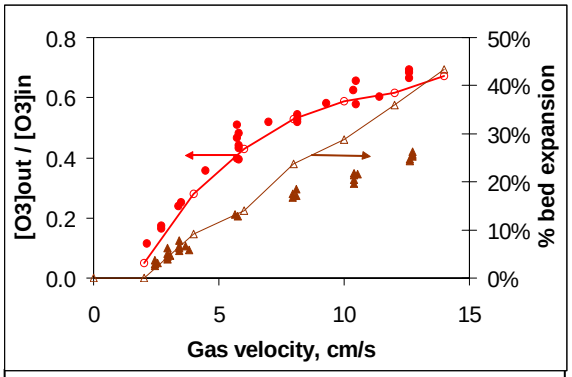

Figure 1. Ozone conversion, $[O_3]_{oulet}/[O_3]_{inlet}$ (left) and % bed expansion (right) as a function of superficial velocity; comparison between simulations with MFIX (connected open symbols) and experimental values (filled symbols).

Silane Pyrolysis. One process for the formation of ultrapure silicon from metallurgical grade (m.g.) silicon involves extensive gas phase separations to form ultrapure SiH_4 or $SiCl_4$. This is then thermally decomposed in a Seimens reactor to recover purified Si . An alternative process has been studied in which the thermal decomposition occurs in a fluidized bed (15,16). The heterogeneous decomposition, $SiH_4(g) : Si(s) + 2H_2(g)$ was represented by a global reaction (17)

$$\left(\frac{d[SiH_4]}{dt}\right)_f\left(\frac{\text{mol}}{\text{cm}^3\cdot s}\right)=\frac{6(1-\varepsilon_g)2.1510^{10}\,e^{-23016/T}\,[SiH_4]}{d_p\left(1+0.034\,P_{H2}+0.0076e^{(3954/T)}\,P_{SiH4}\right)}.$$

A slightly more complicated pseudo-mechanistic scheme (18) yielded similar results. In these simulations the inlet gas was well-mixed. Also, since the bed was maintained at a fixed temperature, thermal effects were not included in the simulation. A slight effect of the chemical reaction on the bed dynamics could be seen, due to the change in composition. The simulations were able to reproduce the exit gas composition reported (16). However, in order to resolve the chemistry an order of magnitude smaller time step was required than was required to simulate the bed hydrodynamics only.

Silicon Chlorination: Trichlorosilane is the most common precursor for the commercial production of high purity, polycrystalline metallic silicon for the electronics industry (20). A two step global reaction scheme for the chlorination of m.g. silicon is used in the simulation. The initial step is a slow homogeneous gas-phase reaction, $SiCl_4 + H_2$ 6 $SiHCl_3 + HCl$, represented as

$$R_{\text{TCS-homo}}\left(mol/\left(cm^3\cdot\sec\right)\right)=0.267/T_g^{1/2}\;e^{-27{,}680/T_g}\left[P_{STC}\,P_{H_2}^{1/2}-P_{TCS}\,P_{HCl}/\left(K_{EQ}\,P_{H_2}^{1/2}\right)\right]$$

In this expression, the partial pressures are expressed in g/(cm·s^2) and the temperature is in Kelvin. The dimensionless thermodynamic equilibrium constant is expressed as $K_{EQ} = \exp\left(4.2873 - 8790.7 / T_g\right)$. This reaction is complemented by a fast heterogeneous reaction, Si(s) + 3 HCl 6 $SiHCl_3$ + H_2, represented by

$$R_{\mathrm{TCS-hetero}}\left(mol/\left(cm^3 \cdot \sec\right)\right) = 1.698 \times 10^{-3}\left(6\left(1-\varepsilon_g\right)/d_p\right) e^{-11{,}575/T_g}\left[P_{HCl}\right]^{1/2}.$$

Figure 2 shows the transient response of the principal components of the outlet stream when the reactor feed is changed from pure hydrogen to a mixture of hydrogen and $SiCl_4$. The first ten seconds represent a fast start up transient caused by the change in the feed composition. The change in the outlet composition because of chemical reactions is a slower process and the simulation needs to be conducted for a longer period of time to determine the steady state exit gas composition.

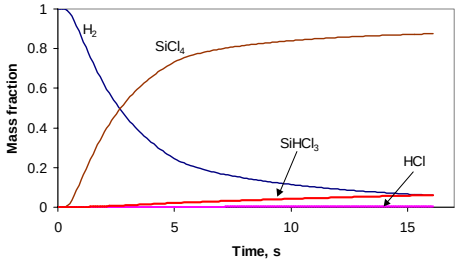

Figure 2. Gas phase species, as a function of time, in the exit stream simulating the chlorination of a bed of metallurgical grade silicon by reaction with H_2 and $SiCl_4$.

Methane combustion: For methane combustion, although the chemical reactions are all in the gas phase, the solids phase exerts significant influence by quenching the free radicals and moderating temperature changes. It is difficult to quantify the extent of these effects. A global kinetics scheme was used in the simulation, based on a simple two step reaction combustion scheme (CH_4 + 3/2 O_2 6 CO + 2 H_2O; CO + ½O_2 6 CO_2), including six gas phase species: CH_4, CO_2, CO, H_2O, O_2, and N_2. The reaction rates used were those of Dryer and Glassman (21)

$$Rate(\text{mole/cm}^3 \cdot \text{s}) = d\left[CH_4\right]/dt = -\varepsilon_g 10^{13.2}\left[CH_4\right]^{0.7}\left[O_2\right]^{0.8} e^{-48{,}400/RT}$$

$$Rate(\text{mole/(cm}^3 \cdot \text{s}) = d\left[CO_2\right]/dt = \varepsilon_g 10^{14.75}\ e^{-43{,}000/RT}\left[C\ O\right]^{1.0}\left[H_2O\right]^{0.5}\left[O_2\right]^{0.25}$$

Note that an ε_g has been included in the Dryer and Glassman (21) rate expression, which converts the basis of the rate expression from gas-volume to reactor volume. The above rate expression had to be changed in another significant manner, however. The experimental data (22) show that methane is consumed rather gradually over a height of about 13 cm above the distributor (Figure 3). In stark contrast, the simulation results (not shown in Figure 3) showed that methane is consumed almost immediately (in less than 1 cm) above the distributor. This is because the above rate expression, developed for gas-phase combustion, does not account for a combustion inhibition (caused by free-radical quenching on particle surfaces) observed in packed beds (23-25). Since we are not aware of any rate expression that accounts for the inhibition we chose the ad hoc method of turning off the reactions where the solids volume fraction exceeds a certain threshold. Figure 3 shows the time-averaged simulation results when the combustion reactions are suppressed when the solids volume fraction exceeds 0.1. We note that the methane concentration profile is in better agreement with the adjusted rate expression. Although the calculation demonstrated that such a simulation is feasible, the agreement with the experimental results is incomplete since there is great uncertainty in these reaction rates. The curves are not smooth near the grid due to inadequate mesh resolution.

Coal Gasification: For coal gasification, in addition to the effect of heat release, there are also many heterogeneous reactions which requires accounting for the effect on fluidization of gas released by the chemical conversion. The chemical kinetics scheme used to describe coal gasification, although global, is still quite complicated, tracking 8 gas phase species and 4 solid phase species (26):

Drying: Moisture (coal) 6 H_2O(g)

$$Rate\,(g/cm^3 \cdot s) = 1.1 \times 10^5 \exp(-21200/RT_s)\,\varepsilon_s\,\rho_s\,X_{sH20}$$

Devolatilization:

Volatile Matter 6 β_d^{Tar} Tar + β_d^{CO} CO + β_d^{CO2} CO_2 + β_d^{CH4} CH_4 + β_d^{H2} H_2 + β_d^{H2O} H_2O;

$$Rate(g/cm^3 \cdot s) = \begin{cases} 1.1 \times 10^5 \exp(-21200/RT_s)\varepsilon_s\ \rho_s(X_{sVM} - X^*) & X_{sVM} \geq X^* \\ 0 & X_{sVM} < X^* \end{cases}$$

$$X^* = (X^0_{sVM}/100)(867.2/(T_s - 273))^{3.914} \text{ for } T_s < 1223;\ = 0, \text{ otherwise.}$$

Tar-cracking:

Tar 6 α_c Fixed Carbon + β_c^{CO} CO + β_c^{CO2} CO_2 + β_c^{CH4} CH_4 + β_c^{H2} H_2 + β_c^{H2O} H_2O

$$Rate(g/cm^3 \cdot s) = 2.5 \times 10^7 \exp(-29000/RT_g)\,\varepsilon_g\,\rho_g\,X_{gTar}$$

Steam gasification: C + H_2O 6 CO + H_2;

$$Rate(mol/cm^3 \cdot s) = 930 \exp(-45000/RT_g)(\varepsilon_s\,\rho_s\,X_{sC}/12)(p_{H2O} - p^*_{H2O})$$

$$p^*_{H2O} = (p_{H2}\ p_{CO})/(\exp(17.29\text{-}16326/T_g))$$

CO_2 gasification: C + CO_2 : 2CO

$$Rate(mol/cm^3 \cdot s) = 930 \exp(-45000/RT_g)(\varepsilon_s\,\rho_s\,X_{sC}/12)(p_{CO2} - p^*_{CO2})$$

Methanation: C + $2H_2$: CH_4

$$Rate(mol/cm^3 \cdot s) = \exp(-7.087 - 8078/T_g)(\varepsilon_s\,\rho_s\,X_{sC}/12)(p_{H2} - p^*_{H2})$$

$$p^*_{H2} = \sqrt{p_{CH4}/(\exp(-13.43+10999/T_g))}$$

Carbon combustion: 2C + O_2 6 2CO

$$Rate(mol/cm^3 \cdot s) = -6\ \varepsilon_s\ p_{O_2}/[d_p\,(k_f^{-1} + k_a^{-1} + k_r^{-1})]$$

CO combustion: CO + ½O_2 6 CO_2

$$Rate = 3.98x10^{14} \exp(-40000/RT_g)\varepsilon_g \left(\rho_g X_{gO2}/MW_{O2}\right)^{0.25} \left(\rho_g X_{gCO}/MW_{CO}\right) \left(\rho_g X_{gH2O}/MW_{H2O}\right)^{0.5}$$

CH_4 combustion: $CH_4 + 2O_2$ 6 $CO_2 + 2H_2O$

$$Rate(mol/cm^3 \cdot s) = 6.7\ x\ 10^{12}\ \exp(-48400/RT_g)\varepsilon_g \left(\rho_g X_{gO2}/MW_{O2}\right)^{1.3} \left(\rho_g X_{gCH4}/MW_{CH4}\right)^{0.2}$$

H_2 combustion: $H_2 + \frac{1}{2}O_2$ 6 H_2O

$$Rate(mol/cm^3 \cdot s) = 1.08\ x\ 10^6\ \exp(-30000/RT_g)\varepsilon_g \left(\rho_g X_{gO2}/MW_{O2}\right) \left(\rho_g X_{gH2}/MW_{H2}\right)$$

Tar combustion: Tar + $f_{O2}\ O_2$ 6 $f_{CO2}\ CO_2 + f_{H2O}\ H_2O$

$$Rate(mol/cm^3 \cdot s) = 3.8\ x\ 10^{11} \exp(-30000/RT_g)\varepsilon_g \left(\rho_g X_{gO2}/MW_{O2}\right)^{1.5} \left(\rho_g X_{gTar}/MW_{Tar}\right)^{0.25}$$

Water gas - shift reaction: $CO + H_2O$: $CO_2 + H_2$

$$Rate(mol/cm^3 \cdot s) = 2.877\ x\ 10^5\ w_{g3} f_3 P^{(0.5-P/250)} \exp(-27760/RT_g) \left(X_{gCO} X_{gH2O} - X_{gCO2} X_{gH2}/K_3\right)$$

$$f_3 = \varepsilon_g(1-\varepsilon_g) X^0_{Ash}\ \rho_s\ \exp(-8.91 + 5553/T_g),\ K_3 = \exp(-3.63061 + 3.95571/T_g)$$

Using this kinetic scheme, simulations have been performed at the large transport gasifier at Power System Development Facility, operated by Southern Company in Wilsonville, Alabama, USA (27). Since this is an industrial scale facility, only limited detailed data are available for validation. Figure 4 shows good agreement between the simulation and the experiments of the distribution of the major species in the product gas. However, there is great uncertainty in the carbon content of the recycle solid stream in this facility, and the simulations are quite sensitive to this number. Such a calculation demonstrates that it is possible to provide detailed information about the flow and chemical processes within a large industrial unit.

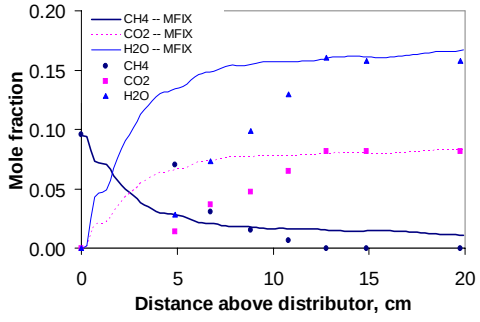

Figure 3. Experimental (filled symbols) and simulated (lines) gas composition in a fluidized bed methane combustor.

CONCLUSIONS

Through a series of case studies it has been demonstrated that fluidized bed processes can be simulated using the techniques of computational fluid dynamics, accounting for the coupled effects of bed hydrodynamics, chemical reactions and heat transfer. These calculations require extensive computational resources

ACKNOWLEDGEMENT

This work was supported by funding from U.S DOE - Fossil Energy, National Energy Technology Center, and U.S DOE - Energy Efficiency and Renewable Energy, Office of Industrial Technologies. The authors would like to thank the EERE-OIT program manager, Dr. Brian Valentine, for his support.

NOTATION

ΔH_{rm}	heat of reaction of in the mth phase
$\vec{I}_{mn}$	momentum exchange between phases
C_{pm}	heat capacity at constant pressure of the mth phase
MW_l	molecular weight of the lth species
$\vec{q}_m$	heat flux of the mth phase
R_{ml}	chemical reaction rate of the lth species of the mth phase
$\overline{\overline{S}}_m$	stress of the mth phase
T_m, T_{wall}	temperature of the mth phase, wall
$\vec{v}_m$	local velocity of the mth phase
X_{ml}	mole fraction of the lth species in the mth phase
γ_{gs}	coefficient of energy exchange between phases
H_{wall}	heat transfer coefficient
ε_m	volume fraction of the mth phase
ρ_m	density of the mth phase

REFERENCES

1. Anderson, T.B., and R. Jackson, "A fluid mechanical description of fluidized beds," *Industrial and Engineering Chemistry Fundamentals,* **6**, 527 (1967).
2. De Wilde, J., G.B. Marin, and G.J. Heynderickx, "The effects of abrupt T-outlets in a riser: 3D simulation using the kinetic theory of granular flow" *Chem. Eng. Science*, **58**, 877 (2003).
3. McKeen, T., and T. Pugsley "Simulation and experimental validation of a freely bubbling bed of FCC catalyst," *Powder Tech.*, **129**, 139 (2003).
4. Peirano, E., V. Delloume, F. Johnsson, B. Leckner, and O. Simonin, "Numerical simulation of the fluid dynamics of a freely bubbling fluidized bed: influence of the air supply system," *Powder Tech.*, **122**, 69 (2002).
5. Peirano, E., V. Delloume, and B. Leckner, "Two- or three-dimensional simulations of turbulent gas-solid flows applied to fluidization," *Chem. Eng.*

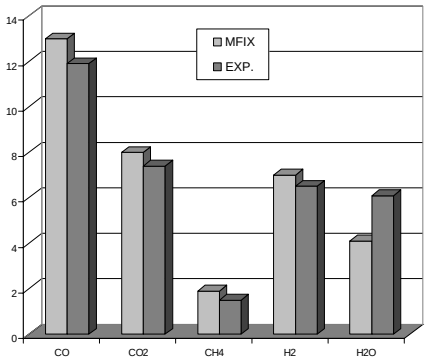

Figure 4. Comparison between the measured and simulated product gas distribution from a particular run of the transport gasifier at the Power System Development Facility.

Science, **56**, 4787 (2001).
6. Halvorsen, B., and V. Mathiesen, "CFD modeling of a lab-scale fluidized bed," in *42nd Conference on Simulation and Modelling*, Porsgrunn, Norway, 2001.
7. Neri, A., and D. Gidaspow, "Riser hydrodynamics: simulation using kinetic theory," *AIChE J.*, **46**, 52 (2000).
8. Boemer, A., H. Qi, and U. Renz, "Verification of Eulerian simulation of spontaneous bubble formation in a fluidized bed," *Chem. Eng. Science*, **53**, 1835 (1998).
9. Theologos, K.N., and N.C. Markatos, "Advanced modelling of fluid catalytic cracking riser-type reactors," *AIChE J.*, **39**, 1007 (1993).
10. Sternéus, J., F. Johnsson, and B, Leckner, "Gas mixing in circulating fluidised-bed risers", *Chemical Engineering Science*, **55**, 129 (2000).
11. Syamlal, M., W. Rogers, and T. O'Brien, "MFIX documentation: theory guide," DOE/METC-94/1004, NTIS/DE94000087, National Technical Information Service, Springfield, VA (1993).
12. Syamlal, M., and T.J. O'Brien, "Fluid dynamic simulation of O_3 decomposition in a bubbling fluidized bed" accepted for publication, *AIChE J.*, (2003).
13. Fryer, C., and O.E. Potter, "Experimental investigation of models for fluidized bed catalytic reactors," *AIChE J.*, 22, 38 (1976).
14. Pannala, S., S. Daw, and J. Halow, "Agent-based model for bubbling fluidized beds," SIAM Conf. on Computational Science and Engineering, San Diego, CA, 2/10-13/2003.
15. JPL Contract No. 954334 Final Report, "Feasibility of the silane process for producing semiconductor grade silicon," Union Carbide Corp., June 1979.
16. Caussat, B., Hsmati, M., & Couderc, J.P "Silicon deposition from silane or disilane in a fluidized bed – Part I: experimental study," *Chem. Eng. Science*, **50**, 3615 (1995).
17. Furusawa, T., T. Kojima, H. Hiroha, "Chemical vapor deposition and homogeneous nucleation in monosilane pyrolysis within interparticle spaces, application of fines formation analysis to fluidized bed CVD," *Chem. Eng. Science.*, **43**, 2037 (1988).
18. Caussat, B., Hsmati, M, and Couderc, J. "Silicon deposition from silane or disilane in a fluidized bed – part II: theoretical analysis and modeling," *Chem. Eng. Science*, **50**, 3625, 1995.
19. Guenther, C., T. O'Brien, and M. Syamlal, "A numerical model of silane pyrolysis in a gas-solids fluidized bed," Proc. Inter. Conf. Multiphase Flow, New Orleans, LA, 5/27-6/1, 2001.
20. JPL Contract No. 955533 Quarterly Reports, "Development of a polysilicon process based on chemical vapor deposition," Hemlock Semiconductor Corporation, 1979-1982.
21. Dryer and Glassman "High temperature oxidation of CO and CH4," 14th Symposium (International) on Combustion, The Combustion Institute, Pittsburgh, 987-1003, 1973.
22. Van der vaart, D.R., "Mathematical modeling of methane combustion in a fluidized bed," *Ind. Eng. Chem. Res.*, **31**, 999 (1992).
23. Hayhurst, A.N., and R.F. Tucker, "The combustion of carbon monoxide in a two-zone fluidized bed," *Combustion and Flame*, **79**, 175 (1990).
24. Hesketh, R.P., and J.F. Davidson, "Combustion of Methane and propane in an incipiently fluidized bed," *Combustion and Flame*, **85**, 449 (1991).
25. Srinivasan, R.A., S. Sriramulu, S. Kulasekaran, and P.K. Agarwal, "Mathematical modeling of fluidized bed combustion - 2: combustion of gases," *Fuel*, **77**, 1033 (1998).
26. Syamlal, M., and L. Bisset, "METC gasifier advanced simulation (MGAS) model," Technical Note, DOE/METC-92/4108, NTIS/DE92001111, National Technical Information Service, Springfield, VA (1992).
27. Leonard, R., T. Pinkston, L. Rogers, R. Rush, and J. Wheeldon"The PSDF—commercial readiness of coal power--revisited" 19th Ann. Pitt. Coal Conf., September 23-27, 2002.

Appendix D

Two-Fluid Model of an Industrial Scale Transport Gasifier

Two-Fluid Model of an Industrial Scale Transport Gasifier

Chris Guenther * Madhava Syamlal * James Longanbach †

Peter V. Smith ‡

Session 10D05 Novel Computer Applications in Chemical Engineering
AIChE 2003 Annual Meeting
November 16-21, 2003, San Francisco, California, USA
(KBR Paper No. 1788)

Abstract

In this investigation a two-fluid model is used to conduct transient three-dimensional simulations with chemistry and heat transfer of an industrial scale Kellogg, Brown & Root(KBR) Transport Gasifier in operation at the Power Systems Development Facility (PSDF) in Wilsonville, Alabama. The Department of Energy-National Energy Technology Laboratory (NETL) has jointly developed PSDF with Southern Co., KBR and others and the primary purpose is to facilitate development of cost-competitive, environmentally acceptable coal-based power generation. The two-fluid model used in this investigation is MFIX (Multiphase Flow with Interphase eXchanges, www.mfix.org) developed at NETL. MFIX provides time dependent information of pressure, temperature, composition, void fraction, and velocity distribution inside the gasifier. The chemistry model in MFIX uses global reaction rates to account for devolitization, tar cracking, water-gas shift reaction, gasification and combustion. The gas phase consists of eight species O_2, CO, CO_2, CH_4, H_2, H_2O, N_2, and tar and the solids phase consists of

*Fluent Incorporated, 3647 Collins Ferry Rd., Morgantown, WV, 26505, (304)285-4483, cpg@fluent.com.

†National Energy Technology Laboratory, 3610 Collins Ferry Rd., Morgantown, WV, 26507.

‡Kellogg Brown and Root, Inc. (KBR), P.O. Box 1069, Wilsonville, AL 35186.

four species carbon, volatile matter, ash, and moisture. Simulation results of a western sub-bituminous and a western bituminous coal are presented which show excellent agreement with experimental data. Furthermore, results are presented comparing oxygen and air blown gasification conditions.

1 Introduction

This investigation focuses on the CFD modeling of the KBR Transport Reactor at the Power Systems Development Facility located near Wilsonville, Alabama. This facility is on a scale sufficiently large enough to provide data for commercial scale-up and is part of a Department of Energy joint venture with industry to demonstrate advanced coal-fueled power systems. What makes this investigation unique is the fact that simulations were transient and done on an industrial scale, in 3D, with chemistry and heat transfer.

One of the accomplishments of this investigation, shown in an earlier paper ([1]), was the ability of the MFIX model to quantitatively predict correct hydrodynamic features of the lower and upper regions of the Transport Reactor. That is, MFIX showed the correct trend in the solids distribution and pressure drop through the lower and upper portions of the reactor. Furthermore, that work suggested that good agreement with experimental gas exit concentrations could be achieved with proper modifications to gasification rates taken from [2].

This paper continues to explore adjustments to the steam and CO_2 gasification rates as well as the reaction rate for the water-gas-shift reaction taken from [2]. The reaction rates for the initial stage kinetics (drying, devolitization, and tar cracking) were taken from [3] and kept fixed. Similarly, the combustion reaction rates taken from [4] and [5] were kept fixed. This paper summarizes the work presented in [1] and how reaction rates were adjusted for a western sub-bituminous coal over a variety of air blown operating conditions. This paper also presents simulation results under oxygen blown conditions, as well as, results of a bituminous coal under air and oxygen blown conditions. Oxygen blown gasification is of much interest to the energy industry because it can result in nitrogen free syngas which facilitates CO_2 capture and sequesteration.

2 Mathematical Model

Two-fluid hydrodynamic models, also referred to as Eulerian-Eulerian models, treat the fluid and solids as two continuous and fully interpenetrating phases. This approach results in mass, momentum, and energy balance equations for both the gas and solids phases. For isothermal conditions, the continuity, momentum balance, and species balance equations for two phases (gas and solids) with chemical reactions are given below.

Gas-phase continuity

$$\frac{\partial}{\partial t}(\varepsilon_g \rho_g) + \nabla \cdot (\varepsilon_g \rho_g \vec{v}_g) = \sum_{n=1}^{N_g} R_{gn} \tag{1}$$

Solids-phase continuity

$$\frac{\partial}{\partial t}(\varepsilon_s \rho_s) + \nabla \cdot (\varepsilon_s \rho_s \vec{v}_s) = \sum_{n=1}^{N_s} R_{sn} \tag{2}$$

Gas-phase momentum

$$\begin{aligned} \frac{\partial}{\partial t}(\varepsilon_g \rho_g \vec{v}_g) + \nabla \cdot (\varepsilon_g \rho_g \vec{v}_g \vec{v}_g) &= -\varepsilon_g \nabla P_g + \nabla \cdot \bar{\bar{\tau}}_g + F_{gs}(\vec{v}_s - \vec{v}_g) \\ &+ \varepsilon_g \rho_g \vec{g} - R_0 \left[\xi_0 \vec{v}_s + \bar{\xi}_0 \vec{v}_g\right] \end{aligned} \tag{3}$$

Solids-phase momentum

$$\begin{aligned} \frac{\partial}{\partial t}(\varepsilon_s \rho_s \vec{v}_s) + \nabla \cdot (\varepsilon_s \rho_s \vec{v}_s \vec{v}_s) &= -\varepsilon_s \nabla P_g + \nabla \cdot \bar{\bar{S}}_s - F_{gs}(\vec{v}_s - \vec{v}_g) \\ &+ \varepsilon_s \rho_s \vec{g} - R_0 \left[\xi_0 \vec{v}_g + \bar{\xi}_0 \vec{v}_s\right] \end{aligned} \tag{4}$$

Species balance

$$\frac{\partial}{\partial t}(\varepsilon_m \rho_m X_{mn}) + \nabla \cdot (\varepsilon_m \rho_m X_{mn} \vec{v}_m) = R_{mn} \tag{5}$$

where $m = g$ or s for the gas or solids phase and $\bar{\xi}_0 = 1 - \xi_0$ and $\xi_0 = 1$ if $R_0 < 0$; else $\xi_0 = 0$. The eight dependent hydrodynamic variables in 3D: void fraction ε_g (the solids fraction $\varepsilon_s = 1 - \varepsilon_g$), pressure P_g, and six velocity components are

found by using MFIX to numerically solve the coupled non-linear partial differential equations (1)-(4). The number of species mass fractions (X_{mn}) tracked are given in Section 4. Constitutive relations needed to close the system (1)-(4), and the gas and solids energy balance equations can be found in [6] and [7]. A discussion of the solution procedure and further references can be found in [1], [7], and [8].

3 Description of Experiments

The sections to be modeled at the Power Systems Development Facility (PSDF) KBR Transport Reactor in Wilsonville, AL consisted of a riser section 62-ft in height attached to an expanded mixing zone 20-ft in height. Powder River Basin (PRB), a subbituminous coal or Hiawatha, a western bituminous coal was fed into the upper region of the mixing zone and hot standpipe solids were fed into the lower region of the mixing zone. The primary burner air was located below the recirculating standpipe solids feed and additional air was fed into the mixing zone from various locations between the coal and standpipe solids inlet ports. Further details of the reactor can be found in [9]. For oxygen blown conditions and all subsequent air blown conditions PSDF added a section (lower mixing zone) below the original mixing zone. This geometry change was incorporated into the CFD simulations for the comparison between air and oxygen blown operating conditions.

4 Chemical Model

In this investigation the gas phase consists of eight species (O_2, CO, CO_2, CH_4, H_2, H_2O, N_2, and Tar). The solids phase (coal) contains the four pseudo-species (fixed carbon, volatile matter, moisture, and ash). The MFIX model considered a single particle size for the hydrodynamics based on the mean size (175 μ) of the standpipe solids. However, the chemistry model consider a significantly smaller particle size (20μ) in the reaction mechanisms. Ash does not take part in any reactions, moisture is released in an initial stage reaction, and volatile matter produces several gas-phase species through devolitization ([3]). Light hydrocarbons were lumped into CH_4 and the species H_2S and NH_3 were ignored. The gas phase reactions are tar decomposition, water gas shift reaction and combustion. Combustion reactions for H_2, CH_4, CO, and C were considered using the following overall

reactions

$$2H_2+O_2 \rightarrow 2H_2O$$

$$CH_4+2O_2 \rightarrow CO_2+2H_2O$$

$$2CO+O_2 \rightarrow 2CO_2$$

$$2C+O_2 \rightarrow 2CO$$

Reaction mechanisms for the kinetics can be found in [4] and [5].

The overall reactions used to describe the gasification process are

$$C+H_2O \leftrightarrow CO+H_2$$

$$C+CO_2 \leftrightarrow 2CO$$

$$C+2H_2 \leftrightarrow CH_4$$

Reaction mechanisms for these kinetics were taken from [2] and [3]. The kinetics for the water-gas shift reaction

$$CO+H_2O \leftrightarrow CO_2+H_2$$

were also taken from [2] where it was assumed that char catalyzes the reaction and that the heat of reaction is added to the char. The remaining initial stage kinetics are given by the following overall reactions

$$\text{Coal Moisture} \rightarrow H_2O$$

$$\text{Volatile Matter} \rightarrow \text{Tar and Gases}$$

and rates for these reactions can be found in [3].

5 Numerical and Experimental Results

The simulations conducted in this investigation were transient and the computational mesh was generated in 3-dimensional cylindrical coordinates. The total number of computational cells was approximately 260K and the results were time-averaged after steady state operating conditions were reached. Steady state operating conditions were determined from the riser inventory and a full discussion of this can be found in [10]. The results reported in this investigation were time-averaged over several seconds of data, as well as, spatially averaged in both the radial and azimuthal directions. To address concerns of simulation CPU time, MFIX was ported to the terascale machine at the Pittsburgh Supercomputer Center (PSC) and run on 16 processors. As a result, the speed-up over the results presented in [1] were quite good. For example, a typical simulation generating 10 seconds of data typically requires about a week of CPU time as opposed to a month of computing time to produce the same basic results before.

Two very important contributions from [1] were the change in gas species molar fractions by adjusting gasification rates and the change in these values as a result of varying the carbon amount in the solids recycle material. The exact amount of carbon in the solids recycle material is very hard to measure experimentally and the error could be as much as $\pm$ 50%. Because of this, the boundary condition for the solids recycle material was varied to account for the maximum error in the measured value of the carbon content. For a given operating condition three different simulations were performed, a base case using the measured value of the carbon, increasing that value by fifty percent and decreasing the value by fifty percent. These values were then kept fixed at the boundary for the length of the simulation.

The steam and CO_2 gasification rates were increased by a factor of 100 in the pre-exponential factor and used in each simulation. The basic results of this approach done over a variety of operating conditions produced molar fractions of CO and CO_2 which varied dramatically from experimental results depending on the carbon content while molar fractions of CH_4, H_2, and H_2O remained relatively insensitive to these changes and all the gas species showed poor agreement with experimental results. However, there was a clear trend in the CO and CO_2 molar fractions which showed that low CO levels resulted in high CO_2 levels and vice versa.

Based on these results the water gas shift reaction was parametrically varied in the pre-exponential factor to hopefully drive species molar fractions towards experimental results. An increase by a factor of 3, in the pre-exponential factor,

dramatically improved the CO and CO_2 molar fractions when compared with experimental results, but had very little effect on the remaining species with H_2 and H_2O consistently being under and over predicted.

A further increase to the steam gasification rate to a factor of 1000 keeping the CO_2 rate increase at 100 and the water gas shift increase at 3. This had the desired effect by driving the remaining species H_2 and H_2O towards experimental values. Experimental and predicted gas molar percentage at the exit, CO/CO_2 molar ratio, exit gas temperature, and carbon conversion are summarized in Table 1 for the PRB coal. Carbon conversion is defined by the ratio of carbon leaving the reactor in the gas stream with the amount of carbon entering the reactor with the fresh coal. The large error in the molar fraction of H_2O in Table 1 is most likely due to a steam leak during this operating period causing a high experimental value.

	Carbon Content			
	-50%	Base	+50%	Experiment
CO	8.1	19.7	26.0	11.0
CO_2	10.8	2.6	.8	7.4
CH_4	1.6	1.8	1.6	1.0
H_2	8.1	6.6	6.5	6.2
H_2O	3.8	3.2	2.6	8.3
$\frac{CO}{CO_2}$	.75	7.5	33.0	1.5
T_g	1755	1730	1717	1758
Carbon Conversion	80	100	100	95-97

Table 1. (PRB) Air Blown Experimental and Predicted Results

Table 2 reports the same information for a different set of operating conditions. The main difference in the operating conditions for the results given in Table 2 are lower operating temperatures, and lower solids recirculation rate. Pressures and mass flow rates were similar between the two operating conditions.

	Carbon Content			
	-50%	Base	+50%	Experiment
CO	7.6	13.0	22	11.9
CO_2	12.2	8.0	3.0	7.4
CH_4	1.4	1.9	1.1	1.5
H_2	8.7	7.0	5.5	6.5
H_2O	6.2	4.1	2.7	6.1
$\frac{CO}{CO_2}$	.62	1.6	7.3	1.6
T_g	1731	1707	1691	1725
Carbon Conversion	83	87	100	95-97

Table 2. (PRB) Air Blown Experimental and Predicted Results

As the carbon content is varied, both Table 1 and Table 2 show a clear trend in all the predicted measurements except CH_4. Since the primary source of CH_4 is from devolitization and tar cracking and these reaction rates are kept fixed it is not surprising a clear trend in this quantity as a function of carbon content in the solids recycle material is not visible.

The same simulation approach described above was used to compare air and oxygen blown operating conditions. Recall that a lower mixing zone was added and the results presented here include this modification. Table 3 and Table 4 summarizes air and oxygen blown cases. Despite the generally good agreement for the air blown cases molar fraction trends in both the air and oxygen blown cases did not move through the experimental values as before. Furthermore, the gas species in these cases are not as sensitive to changes in the carbon content as the results presented in Tables 1 and 2. This indicates that the geometry change might be having a significant impact on the chemistry most likely due to different mixing patterns, residence times, and/or species concentrations in the mixing zone.

To try and improve the predicted results presented in Tables 3 and 4 further simulations were conducted parametrically varying the gasification and water-gas shift reaction rates. This resulted in better quantitative agreement for both cases when lower gasification rates were used and these results were independent of the water gas shift reaction rate. Table 4 also shows lower carbon conversion rates both predicted and experimentally. Lower conversion for oxygen blown conditions is obviously a concern for process design and hopefully more work in this modeling effort will help explain why conversion drops under oxygen blown conditions.

	Carbon Content			
	-50%	Base	+50%	Experiment
CO	6.0	8.0	8.2	9.1
CO_2	11.0	11.0	10.9	8.8
CH_4	.8	1.1	1.4	1.2
H_2	7.4	7.6	9.0	7.3
H_2O	8.0	6.4	5.4	8.9
$\frac{CO}{CO_2}$	.54	.75	.75	1.03
T_g	1740	1732	1736	1713
Carbon Conversion	100	100	100	96

Table 3. (PRB) Air Blown Experimental and Predicted Results

	Carbon Content			
	-50%	Base	+50%	Experiment
CO	18.2	19.7	24.0	11.7
CO_2	9.0	8.9	8.7	14.1
CH_4	1.8	1.3	1.1	2.8
H_2	22.0	23.7	26.0	14.7
H_2O	18.0	16.1	13.1	22.9
$\frac{CO}{CO_2}$	2.0	2.2	2.7	.8
T_g	1644	1647	1655	1674
Carbon Conversion	62	62	67	92

Table 4. (PRB) Oxygen Blown Experimental and Predicted Results

The results for the Hiawatha bituminous coal under air and oxygen blown conditions are summarized in Tables 5 and 6. Again, these results are with the addition of the lower mixing zone. In general these results showed similar trends as before. That is, molar fraction trends with the steam gasification rate increased by a factor of 1000, the CO_2 rate increased by 100, and the water gas shift reaction rate increased by 3 did not move through the experimental values. Also, conversion dropped as temperatures increased and in general results were not as sensitive to changes in the carbon content as the results presented in Tables 1 and 2.

	Carbon Content			
	-50%	Base	+50%	Experiment
CO	5.0	8.1	11.0	3.5
CO_2	11.0	10.4	9.5	9.3
CH_4	2.3	2.3	2.0	1.3
H_2	6.3	8.8	11.0	4.8
H_2O	14.0	10.9	8.0	22.9
$\frac{CO}{CO_2}$	.46	.8	1.2	.4
T_g	1750	1744	1731	1779
Carbon Conversion	67	80	83	89

Table 5. (Hiawatha) Air Blown Experimental and Predicted Results

	Carbon Content			
	-50%	Base	+50%	Experiment
CO	13.0	17.5	22.0	6.4
CO_2	14.1	13.1	12.0	12.6
CH_4	3.4	3.0	3.0	2.3
H_2	16.3	20.4	24.0	9.4
H_2O	30.5	24.0	19.1	33.8
$\frac{CO}{CO_2}$	.9	1.3	1.8	.5
T_g	1776	1770	1757	1714
Carbon Conversion	80	97	100	85

Table 6. (Hiawatha) Oxygen Blown Experimental and Predicted Results

Because of the improvement to the results in Tables 3 and 4 by further adjusting gasification rates further simulations were conducted with the Hiawatha coal. It was found that decreasing the steam gasification rate to an increase in the pre-exponential factor of 200, using the CO_2 rate given in [2] and keeping the increase in the water gas shift reaction rate of 3 resulted in very good agreement with experimental molar fractions. These simulations are summarized in Tables 7 and 8. For the air blown and oxygen blown cases the computer simulations only considered the base case for the carbon content.

	Carbon Content	
	Base	Experiment
CO	4.1	3.5
CO_2	11.0	9.3
CH_4	2.9	1.3
H_2	5.0	4.8
H_2O	17.4	22.9
$\frac{CO}{CO_2}$	.4	.4
T_g	1756	1779
Carbon Conversion	65	89

Table 7. (Hiawatha) Air Blown Experimental and Predicted Results

	Carbon Content	
	Base	Experiment
CO	9.8	6.4
CO_2	14.0	12.6
CH_4	3.6	2.3
H_2	12.8	9.4
H_2O	36.3	33.8
$\frac{CO}{CO_2}$	.7	.5
T_g	1804	1714
Carbon Conversion	73	85

Table 8. (Hiawatha) Oxygen Blown Experimental and Predicted Results

Despite the excellent agreement between the predicted and experimental molar fractions in Table 7 and 8 these results again show a drop in the carbon conversion as temperatures increase. The fact that carbon conversion drops as temperatures increase suggest oxygen might be breaking into the upper regions of the mixing zone and combusting with volatiles. Further post processing of results indicated that indeed some of the cases did show high levels of oxygen in the upper regions of the mixing zone, but in other cases levels were quite low.

6 Conclusions

This investigation has shown that the operating conditions used in the Transport Gasifier at PSDF required changes to the gasification and water-gas shift reactions rates taken from the literature to achieve good agreement in gas species

molar fractions. This is not surprising since the reaction rates taken from the literature were derived under much different hydrodynamic conditions. However, with the addition of the lower mixing zone to the Transport Reactor, especially under oxygen blown conditions, the gasification rates needed further adjustments to the pre-exponential factor to produce good agreement with experimental results. Obviously, having reaction rates dependent on a geometry modification is undesirable and current work is continuing to try and determine an appropriate set of reaction rates independent of geometry modifications and valid for both air and oxygen blown conditions. Furthermore, devolitization, tar cracking, and combustion reaction rates are being investigated to try and understand the role these rates have and if some adjustment to these rates is necessary.

Nomenclature

F_{gs}	coefficient for the interphase force (kg/m^3s)
$\vec{g}$	force due to gravity (cm/s^2)
P_g	pressure in the gas phase (Pa)
R	rate of production of the nth gas/solids species (kg/m^3s)
S_{DC}	source term contribution from deferred correction
S_P	discretized scalar source term
T_g	gas temperature (Fahrenheit)
$\bar{\bar{S}}_s$	solids phase stress tensor (Pa)
$\vec{v}_m$	gas/solids velocity (cm/s)
X_{mn}	n^{th} gas/solids species mass fraction

Greek Symbols

ε_m	gas/solids void fraction
ρ_m	gas/solids density
$\bar{\bar{\tau}}_g$	gas phase stress tensor Pa
ϕ_P	general hydrodynamic property
ϕ^{LO}	low order cell face approximation
ϕ^{HO}	high order cell face approximation

References

[1] C. Guenther, M. Shahnam, M. Syamlal, J. Longanbach, D. Cicero, and P. Smith 'CFD Modeling of a Transport Gasifier', 'Nineteenth Annual International Pittsburgh Coal Conference', September 23-27, 2002.

[2] C. Wen, H. Chen, and M. Onozaki. 1982 'User's Manual for Computer Simulation and Design of the Moving Bed Coal Gasifier', DOE/MC/16474-1390 (DE83009533).

[3] M. Syamlal and L. Bissett, 1992. 'METC Gasifier Advanced Simulation (MGAS) Model', DOE/METC-92/4108 (DE92001111).

[4] N. Peters, 1979. 'Premixed Burning in Diffusion Flames, The Flame Zone model of Libby and Economos', Int. J. Heat Mass Transfer, 22, 691-703.

[5] C. Westbrook and F. Dryer, 1981. 'Simplified Mechanisms for the Oxidation of Hydrocarbon Fuels in Flames', Combustion Science and Technology, 27, 31-43.

[6] M. Syamlal, W. Rogers, and T. O'Brien, 1993. 'MFIX documentation: theory guide', Technical Note, DOE/METC-95/1013.

[7] M. Syamlal, 1998. 'MFIX documentation, numerical technique', EG&G technical report, DE-AC21-95MC31346.

[8] C. Guenther and M. Syamlal, 2001. 'The effect of numerical diffusion on isolated bubbles in a gas-solid fluidized bed', Powder Technol., 116, 142-154.

[9] B. Davis, P. Vimalchand, G. Liu, P. Smith, and J. Longanbach, 'Operation of the PSDF Transport Gasifier', 'Nineteenth Annual International Pittsburgh Coal Conference', September 23-27, 2002.

[10] C. Guenther, M. Syamlal, L. Shadle, and C. Ludlow, 2002. 'A Numerical Investigation of an Industrial Scale Gas-Solids CFB', in 'Circulating Fluidized Bed Technology VII', J. Grace, J. Zhu, and H. de Lasa (Eds), CSCHE, Otawa, pp 483-488.

Appendix E

The Effect of Model Parameters on the Predictions of Core Annular Flow Behavior in a Fast-Fluidized Gas/Solids Bed

The effect of model parameters on the predictions of core-annular flow behavior in a fast-fluidized gas/solids bed

Sofiane Benyahia and Madhava Syamlal
Fluent Incorporated
3647 Collins Ferry Road, Suite A
Morgantown, WV 26505
Ph. (304) 598-5863; Fax (304) 598-7185; E-mail: sof@fluent.com

Thomas J. O'Brien
US Department of Energy
MS-N04, 3610, Collins Ferry Road
Morgantown, WV 26505
Ph. (304) 285-4571, E-mail: tobrie@netl.doe.gov

Abstract

The main purpose of this study is to investigate the ability of three gas-solids flow models – standard granular kinetic theory (see Gidaspow, 1994), and two gas-solids turbulence models (Balzer et al. 1996, and Cao and Ahmadi 1995) – to predict core-annular flow behavior commonly observed in dense gas/solids flows (>3% solids volume fraction). For dense gas/solids flows, these models use similar closures for the solids stresses derived from kinetic theory of granular materials and differ mainly in their treatment of the gas/solids turbulence interchange. The effect of three types of boundary conditions, Jenkins (1997), Johnson and Jackson (1987), and the free slip condition, was also investigated. Care was taken to ensure that the comparisons are based on grid-independent solutions. This study has demonstrated that the granular kinetic theory, Balzer et al. 1996, and Cao and Ahmadi 1995 models give similar predictions for a dense fully developed flow in a vertical channel, and that the gas turbulence may not have a dominant effect in relatively dense gas/solids flows. Finally, the core-annular flow behavior with maximum solids concentration at the walls was not observed if the boundary condition causes production of granular energy at the wall. Boundary conditions that dissipate granular energy near the wall are needed to predict a core-annular flow structure.

Introduction

Experimental investigations of dilute gas/solids flow with high gas/solids velocities, showing a migration of solids toward the core of the flow system, have been widely reported in the literature (Tsuji et al., 1991; Jones and Sinclair, 2003). This phenomenon has been predicted by the use of different gas/solids turbulence models (Balzer et al., 1996; Cao and Ahmadi, 1995; Jones and Sinclair, 2003), which are dominated by the turbulence properties of the carrier gas.

For denser flows, solids migrate towards the walls, establishing a core-annular flow regime. Tsuo and Gidaspow (1990) were probably the first to compute clusters and streamers in the riser section of a circulating fluidized bed. More recently, Agrawal et al. (2001) have conducted a detailed analysis of the formation of clusters and their impact on the gas/solids flow behavior. They computed a large slip velocity between gas and solids that can be several times that of terminal velocity for a single particle. The granular temperature was also computed to be much higher than that of a uniform state due to the large gradients in solids velocity associated with the formation of clusters.

The formulation of the solids pressure, which causes solids migration, is generally agreed upon (Lun et al.,1984; Sinclair and Jackson, 1989; Cao and Ahmadi, 1995; Balzer et al., 1996). However, the models differ in their representation of gas/solids turbulence interaction terms, closure equations for solids viscosity and conductivity, and the drag term. Boundary conditions for the solids granular temperature and slip velocity (Johnson and Jackson, 1987; Jenkins and Louge, 1997; free slip) are another source of variation. We investigate the effects of these differences, using the same numerical code (MFIX) under the same simplified flow conditions. The differences in the predicted granular temperature profiles had a direct impact on the establishment of the core-annular flow.

Description of the models used for gas/solids flow predictions

The model equations for gas/solids flows used in the present study are summarized in Table 1. All the models used in this study, including Simonin model, use solids stresses that are derived from the kinetic theory of granular flows (KTGF) (e.g., Gidaspow 1994). It is reasonable to use KTGF since the simulated gas/solids flows in this study were all conducted at relatively high solids concentrations (3% average solids volume fraction). More details of Ahmadi and Simonin models can be found elsewhere (Cao and Ahmadi, 1995; Balzer et al., 1996; Benyahia et al., 2004). The major differences in these models reside in their treatment of the turbulence exchange terms as shown in Table 1. In this study, we used an algebraic formulation of the gas-particle instantaneous velocity cross-correlation k_{12}, which was found to yield similar results compared with the PDE formulation (Balzer et al. 1996) and yet accelerate significantly the numerical simulations. This algebraic expression was obtained by assuming the dissipation term to be equal to the exchange term in the k_{12} equation (see equation 17 in Benyahia et al., 2004), which is a reasonable assumption since heavy particles (glass beads) are used in this study. Also, unlike Ahmadi and Simonin, who have often used low Reynolds k-epsilon model to describe the gas phase turbulence, we use wall functions and avoid the mesh refinement near a wall boundary necessary to resolve the laminar boundary layer.

We use the boundary conditions for the solids phase developed by Jenkins (1997) and Johnson and Jackson (1987) and a free slip boundary condition to asses the sensitivity of the numerical results to the wall boundary condition.

Continuity equation index m=1 (gas) or 2 (solids).

$$\frac{\partial}{\partial t}\left(\alpha_m \rho_m\right) + \frac{\partial}{\partial x_i}\left(\alpha_m \rho_m U_{mi}\right) = 0$$

Momentum equation

$$\alpha_m \rho_m \left[\frac{\partial U_{mi}}{\partial t} + U_{mj}\frac{U_{mi}}{\partial x_j}\right] = -\alpha_m \frac{\partial P_1}{\partial x_i} + \frac{\partial \tau_{mij}}{\partial x_j} + I_{lmi} + \alpha_m \rho_m g_i$$

Turbulence modeling in the continuous phase

$$\alpha_1 \rho_1 \left[\frac{\partial k_1}{\partial t} + U_{1j}\frac{\partial k_1}{\partial x_j}\right] = \frac{\partial}{\partial x_i}\left(\alpha_1 \frac{\mu_1^t}{\sigma_k}\frac{\partial k_1}{\partial x_i}\right) + \alpha_1 \tau_{1ij}\frac{\partial U_i}{\partial x_j} + \Pi_{k1} - \alpha_1 \rho_1 \varepsilon_1$$

$$\alpha_1 \rho_1 \left[\frac{\partial \varepsilon_1}{\partial t} + U_{1j}\frac{\partial \varepsilon_1}{\partial x_j}\right] = \frac{\partial}{\partial x_i}\left(\alpha_1 \frac{\mu_1^t}{\sigma_\varepsilon}\frac{\partial \varepsilon_1}{\partial x_i}\right) + \alpha_1 \frac{\varepsilon_1}{k_1}\left(C_{1\varepsilon}\,\tau_{1ij}\frac{\partial U_i}{\partial x_j} - \rho_1 C_{2\varepsilon}\,\varepsilon_1\right) + \Pi_{\varepsilon 1}$$

Turbulence modeling of the dispersed phase $\Theta_s = \frac{2}{3}k_2$

$$\alpha_2 \rho_2 \left[\frac{\partial k_2}{\partial t} + U_{2j}\frac{\partial k_2}{\partial x_j}\right] = \frac{\partial}{\partial x_i}\left(\alpha_2 \rho_2 K_2^t \frac{\partial k_2}{\partial x_i}\right) + \alpha_2 \rho_2 \tau_{2ij}\frac{\partial U_{2i}}{\partial x_j} + \Pi_{k2} - \alpha_2 \rho_2 \varepsilon_2$$

Stress tensor

$$\tau_{mij} = 2\,\nu_m^t\, S_{mij} - \frac{2}{3}\delta_{ij}\left(k_m + \nu_m^t \frac{\partial U_{mk}}{\partial x_k}\right)$$

Gas/solids momentum interchange term

$$I_{lmi} = \beta\left(u_{li} - u_{mi}\right),\ \beta = \frac{3}{4}C_D \frac{\rho_g \alpha_1 \alpha_2 \left|u_l - u_m\right|}{d_p}\alpha_1^{-2.65},\ C_D = \begin{cases} 24/\mathrm{Re}\left(1 + 0.15\,\mathrm{Re}^{0.687}\right), & \mathrm{Re} < 1000 \\ 0.44, & \mathrm{Re} \ge 1000 \end{cases}$$

Solids pressure

$$P_2 = \frac{2}{3}\alpha_2 \rho_2 k_2\left[1 + 2\alpha_2 g_0\left(1+e\right)\right],\ g_0 = \left[1 - \left(\frac{\alpha_2}{\alpha_2^{\max}}\right)^{1/3}\right]^{-1}$$

Solids shear and bulk viscosity

$$\nu_2^t = \nu_2^{kin} + \nu_2^{col},\ \lambda_2 = 5/3\,\nu_2^{col},\ \nu_2^{kin} = 2/3\left(k_2\left(1+\zeta_c \alpha_2 g_0\right)\right)\tau_c,\ \nu_2^{col} = 4/5\,\alpha_2 g_0\left(1+e\right)\left(\nu_2^{kin} + d_p\sqrt{\frac{2k_2}{3\pi}}\right)$$

Solids granular conductivity

$$K_2^t = K_2^{kin} + K_2^{col},\ K_2^{kin} = 2/3\left(k_2\left(1+\varpi_c \alpha_2 g_0\right)\right)\tau_2^c,\ K_2^{col} = 6/5\,\alpha_2 g_0\left(1+e\right)\left(K_2^{kin} + 5/9\,d_p\sqrt{\frac{2k_2}{3\pi}}\right),\ \varpi_c = \frac{\left(1+e\right)^2\left(2e-1\right)}{100}$$

Granular model

$\nu_g^t = \nu_g^{laminar}$

$\Pi_{k2} = 0$

Ahmadi model

$$\nu_g^t = \frac{0.09k_1^2/\varepsilon_1}{1 + \frac{\tau_{12}^x}{\tau_1}\left(\frac{\alpha_2}{\alpha_2^{\max}}\right)^3}$$

$\Pi_{k1} = 2\beta\left(k_2 - k_1\right)$

$\Pi_{\varepsilon 1} = 0$

$$\Pi_{k2} = 2\beta\left(\frac{k_1}{1 + \tau_{12}^x/\tau_1} - k_2\right)$$

Simonin model

$$\nu_g^t = \frac{0.09k_1^2/\varepsilon_1}{1 + 0.314X_{12}\frac{\tau_{12}^x}{\tau_1}/\left(1 - k_{12}/2k_1\right)}$$

$\Pi_{k1} = X_{12}\beta\left(k_{12} - 2k_1\right)$

$\Pi_{\varepsilon 1} = 1.2\left(\varepsilon_1/k_1\right)\Pi_{k1}$

$\Pi_{k2} = \beta\left(k_{12} - 2k_2\right)$

$$k_{12} = \frac{2\,\tau_{12}^t/\tau_{12}^x}{1 + \left(1 + X_{12}\right)\tau_{12}^t/\tau_{12}^x}\left(k_1 + X_{12}k_2\right)$$

$$X_{12} = \frac{\alpha_2 \rho_2}{\alpha_1 \rho_1}$$

Table 1 Model equations for multiphase flows

Gas-phase wall boundary conditions for turbulent flows

$$\left.\frac{\partial U_1}{\partial x}\right|_w = \frac{\rho_1 \kappa U_1 C_{1\mu}^{1/4} k_1^{1/2}}{\left(\mu_1 + \mu_1^t\right)\ln\left(E\,x^*\right)},\ x^* = \frac{\rho_1 C_{1\mu}^{1/4} k_1^{1/2} \Delta x/2}{\mu_1}$$

$$\left.\frac{\partial k_1}{\partial x}\right|_w = 0\ ,\ \left.\frac{\partial \varepsilon_1}{\partial x}\right|_w = 0$$

$$k_1\ production\big|_{at\ fluid\ cells\ next\ to\ wall} = \alpha_1\ \tau_{1ij}\frac{\partial U_i}{\partial x_j} + \beta_{12}\ k_{12} = \alpha_1 \rho_1 \sqrt{C_{1\mu}}\, k_1 \frac{U_1}{\Delta x/2 \ln\left(E\,x^*\right)}$$

$$k_1\ dissipation\big|_{at\ fluid\ cells\ next\ to\ wall} = \alpha_1 \rho_1 \varepsilon_1$$

$$\varepsilon_1\big|_{at\ fluid\ cells\ next\ to\ walls} = \frac{C_{1\mu}^{3/4} k_1^{3/2}}{\kappa \Delta y/2}$$

Johnson and Jackson boundary condition for the solids phase

$$\nu_2^t \left.\frac{\partial V_s}{\partial x}\right|_w + \frac{\phi\pi\, V_s g_0 \sqrt{2/3\, k_2}}{2\sqrt{3}\ \alpha_2^{\max}} = 0$$

$$K_2^t \left.\frac{\partial k_2}{\partial x}\right|_w - \frac{\phi\pi\, V_s^2 g_0 \sqrt{2/3\, k_2}}{2\sqrt{3}\ \alpha_2^{\max}} + \frac{\sqrt{3}\pi\ g_0\left(1-e_w^2\right)\left(2/3\, k_2\right)^{3/2}}{4\,\alpha_2^{\max}} = 0$$

Jenkins and Louge small frictional limit

$$S^{sf}/N^{sf} = \mu\ ,\ \frac{Q^{sf}}{N^{sf}\left(3\Theta_s\right)} = \frac{3}{8}\left[\frac{7}{2}\left(1+e_w\right)\mu^2 - \left(1-e_w\right)\right]$$

Free slip boundary condition

$$\left.\frac{\partial V_s}{\partial x}\right|_w = 0\,,\ \left.\frac{\partial \Theta_s}{\partial x}\right|_w = 0\,,\ \left.\frac{\partial V_g}{\partial x}\right|_w = 0$$

Table 2 Model boundary conditions for multiphase flows

Description of physical and numerical parameters

We report the simulation results for the isothermal flow of air and glass beads in a vertical channel of 10 cm width. A superficial gas velocity of 5 m/s and an average solids volume fraction of 3% are used in all these simulations unless otherwise specified. A constant gas mass flux was prescribed in these simulations. The gas pressure drop was allowed to fluctuate in order to guaranty a constant gas flow rate. The glass beads used in these simulations had a diameter of 120 microns and density of 2.4 g/cm^3. Particle-particle restitution coefficient of 0.95 and particle-wall coefficient of 0.7 were used. In most of the simulations, the Jenkins low frictional limit was used as the solids phase boundary condition with a particle-wall friction coefficient value of 0.2. Uniformly distributed computational grids have been used in this study with a standard grid of 40 cells along the channel width. Second order discretization scheme of Van Leer was used for the convective terms. The numerical time step was allowed to vary but rarely exceeded a millisecond.

Verification study of model predictions and grid convergence

A recent paper by John Grace (2004) has focused on the shortcomings of current models used for the predictions of gas/solids flows. More specifically, the paper points out the lack of verification studies. Although verification is invariably a part of numerical model development, it seldom gets reported. For example, the research code MFIX used in this study is verified with a suite of 35 test cases every time a stable version of the code is created. Commercial CFD codes are rigorously tested using a large number of test cases. We start this paper by reporting on a test case we used specifically for this study to test the implementation of the granular theory model.

In a recent study Gidaspow (2003) derived a closed form solution for the granular temperature radial profile, in the case where solids velocity has a parabolic profile (Poiseuille flow):

$$V_s = 3/2 \; V_s^{avg} \left[1 - \left((X - H)/H\right)^2\right]$$

In this case, the granular temperature has a fourth power dependency on the dimensionless channel width as shown by the following equation:

$$\Theta_s = 2 \, V_s^{avg} \, \frac{\mu_s}{\lambda_s} \left[1 - \left((X - H)/H\right)^4\right].$$

In order to verify the numerical code in MFIX, a simulation was conducted after prescribing the granular temperature to be the fourth power profile (Figure 1-b). The results of the simulation are shown in Figure 1. Figure 1-c shows an exact match between the analytical and numerical solutions for solids velocity. Figure 1-a shows the predicted solids volume fraction profile and a function proportional to the inverse of granular temperature. An exact inverse relationship between the granular temperature and the solids volume fraction can be deduced from the radial momentum balance. These exact matches partially verifies the kinetic theory expressions coded in MFIX. (Although not relevant to this verification test, for reference Figure 1-b also shows the granular temperature profile predicted using kinetic theory, which does not compare well with the prescribed granular temperature profile.) Figure 1-a also shows that in the case where the full solids pressure is used (kinetic and dense parts) the solids volume fraction was lower near the walls of the channel. The core-annular flow behavior with higher solids concentration near the walls of the channel is always observed when the highest granular temperature occurs at the center of the channel.

The difference between the predicted gas and solids axial velocity (Figure 1-c) matches exactly the terminal velocity of a single glass bead particle estimated at about 80 cm/s. We will demonstrate later that the slip velocity between gas and solids can be several times that of a single particle terminal velocity due to cluster formation. In this case, clusters did not form because the imposed granular temperature profile forced the code to produce steady (time invariant) results.

A grid sensitivity analysis was conducted in the periodic 1-D channel to determine the minimum computational grid size needed to achieve a grid independent solution. Several grid densities were considered in this study varying from a relatively coarse mesh of 10 grids distributed along the channel width to a finer mesh of 160 grids. Figure 2 shows that a grid density of 40 along the channel width was necessary to achieve grid independent time-averaged results. Although the coarse grid of 10 cells was able to predict the core-annular flow, the numerical predictions of other variables are not accurate as demonstrated by Figure 2.

One-dimensional versus two-dimensional clusters and their effect on flow predictions
Two-dimensional simulations have been carried out in a channel of 10 cm width and 40 cm height with a uniform computational grid of 40x160. The choice of a length to width ratio of four has been found to produce optimal results (Agrawal et al., 2001). Figure 3-a shows the solids volume fraction distribution along the width of the channel at an elevation half that of the total height. The 2-D simulation predicted a core-annular flow similar to the 1-D simulation. However, the solids concentration at the walls of the channel was less in the case of a 2-D simulation. The clusters and streamers (sheets of high solids concentration) formed in the 2-D channel and followed a complex path in their fall due to gravity. Although most clusters and streamers remained near the walls of the channel, some clusters moved to the center of the channel. This was demonstrated by the relatively smaller concentration of solids near the walls and higher concentration of solids in the center of the riser in the 2-D simulations compared to the 1-D results.

The computed granular temperature in a 2-D system was lower than that in the 1-D case as seen in Figure 3-b. The relatively smaller clusters computed near the channel walls in the 2-D case lead to a smaller downward velocity, which in turn yielded smaller solids velocity gradients that are the main mechanism for granular temperature production.

Figure 3-c shows a comparison of the computed gas axial velocity profiles between 1-D and 2-D results. The average gas velocity was fixed in both cases to 5 m/s, thus the profiles for 1-D and 2-D systems were similar except near the walls where the 1-D simulation predicted a larger downward velocity due to entrainment by the larger computed clusters.
The 2-D results showed higher solids velocity magnitude relative to 1-D simulation as seen in Figure 3-d. The 2-D shape of clusters makes them more susceptible to entrainment by the upward flowing gas. A better exchange of momentum is achieved in a 2-D cluster relatively to a 1-D cluster that extends infinitely in the axial direction. For these reasons, the 2-D solids velocity profiles were higher in magnitude relative to the 1-D results. However, the trends and magnitude of all the computed results were similar in both 1-D and 2-D simulations. These results suggest that using a 1-D system to study the effect of model parameters and boundary conditions is acceptable. One should point out that the 1-D results may not compare well with experiments; however, the purpose of this study is to compare the different turbulence models and boundary conditions.

Effect of gas/solids turbulence models on the flow predictions
Three different models were used to predict the gas/solids flow in a one-dimensional channel: a standard kinetic theory model (KTGF) with no dissipation or production of

granular temperature due to drag terms (see Gidaspow, 1994); Simonin model (Balzer et al., 1996); and Ahmadi (Cao and Ahmadi, 1995) model. For the heavy particles at high solids loading used in these simulations, the three models had differences only in the gas/solids turbulence interaction terms. Simonin and Ahmadi models predicted similar granular stresses as the standard KTGF model.

Figure 4-a shows that all three models predicted similar solids volume fraction distributions. The core-annular behavior was predicted due to the transient fluctuations in the solids volume fraction. Animations of the solids volume fraction showed that all models predicted an oscillatory behavior with a period of 6-7 sec. This oscillatory behavior created clusters that moved from one wall of the channel to the other. When averaged over time, the solids volume fraction distribution showed a core-annular behavior with solids concentration higher at the walls of the channel. The dissipation in the granular temperature equation due to inelastic collisions or interactions with the gas turbulence in the cases of Simonin or Ahmadi models did not affect the core-annular behavior predicted by all these models. A previous study by Sinclair and Jackson (1989) using a steady-state model has shown an undue sensitivity of their model to the particle-particle restitution coefficient. Another study by Hrenya and Sinclair (1997) demonstrated the limitations of a steady state model and re-derived a Reynolds-averaged model with proposed closures to the generated correlations. Their model explained the nature of core-annular behavior that is due to the formation of clusters, which is a transient phenomenon that can be captured by the standard model based on the kinetic theory of granular flow with a sufficiently fine computational grid.

Figure 4-b shows the gas and solids time-averaged turbulent kinetic energy distribution along the channel width ($k_2 = 3/2\,\Theta_s$). The predicted granular temperature was the highest in the case of a granular model due to the absence of gas/solids turbulence exchange term in the granular temperature equation. Simonin model predicted a higher granular temperature due to the low predictions of the gas turbulent energy. Ahmadi model predicted similar magnitude and profiles of gas and solids turbulent energy. The high magnitude of the gas turbulent energy predicted by Ahmadi model was due to the high production turbulence exchange term in the k_1 equation. There was a slight increase in the gas turbulent energy near the walls in both Ahmadi and Simonin models due to the use of standard wall functions.

Figure 4-c shows the time-averaged gas axial velocity profile along the channel width. Simonin and Ahmadi models along with the laminar model predicted the same gas velocity profile even when the gas turbulent kinetic energy was significantly different in both profile and magnitude. This is a clear indication that the gas turbulence model does not play a significant role in dense (3% averaged solids volume fraction) flows. It also indicates that a model based only on the kinetic theory for granular flows is sufficient to model gas/solids flows in relatively dense systems. The transient dense flow of gas and solids indicates that the gas flow through regions of minimum solids concentration. The presence of highly concentrated regions (or clusters) prohibits the high velocity flow of gas. Thus, the gas velocity profile is affected mainly by the solids volume fraction profile and not by the gas turbulent energy distribution, as in single-phase flows.

Figure 4-d shows the time-averaged solids axial velocity profiles along the10-cm channel width. Solids flow downward near the walls of the channel because of the high solids concentration in these regions. At the center of the channel, where solids concentrations are low, the highest solids velocity is observed. This is typical of a core-annular flow behavior commonly observed in experiments. The difference between gas and solids axial velocity was computed to be several times that of a single particle terminal velocity, which is approximately equal to 80 cm/s. This was due to the formation of clusters that can accelerate downward at a speed higher than that of a single particle, which is in agreement with the observations of Agrawal et al. (2001).

Effect of different boundary conditions for the solids stresses on flow predictions

Three different boundary conditions were used in this study: Jenkins and Louge (1997) small frictional limit, Johnson and Jackson (1987) boundary condition commonly used for gas/solids flows, and the free slip boundary condition. Apart from the parameters described in the physical and numerical section in this study, the Jenkins boundary condition used a friction coefficient (μ) equal to 0.2, and a specularity coefficient (ϕ) of 0.01 was used with the Johnson and Jackson boundary condition.

Figure 5 shows the predictions of the granular model using different wall boundary conditions for the solids stresses as summarized in Table 2. Both the free slip and Jenkins boundary conditions (BC) predict maximum solids concentration at the walls of the channel. However, Johnson and Jackson BC predicts a thicker annulus and the maximum solids concentration occurred at a small distance from the walls. This was caused by the fact that the minimum granular temperature occurred at a location close to the walls. In fact, Figure 5-b shows that the Johnson and Jackson BC predicted a small production of granular temperature at the walls. By further increasing the specularity coefficient to 0.1, we did not observe the presence of the core-annular flow behavior and the code predicted a steady flow with maximum solids volume fraction away from the wall region. The same behavior was observed by using a higher friction coefficient (μ) in the Jenkins BC. In fact, by using a friction coefficient of 0.25, we did not observe a core-annular behavior, which was similar to the results observed using Johnson and Jackson BC with a high specularity coefficient. To explain the reason for this change in behavior, let's examine the Jenkins BC for granular temperature: $\frac{Q^{sf}}{N^{sf}(3\Theta_s)} = \frac{3}{8}\left[\frac{7}{2}(1+e_w)\mu^2 - (1-e_w)\right]$. This boundary condition will yield a production of the granular temperature at the walls only if $7/2(1+e_w)\mu^2 > (1-e_w)$. When the particle-wall restitution coefficient is 0.7, this analysis shows that for a value of the friction coefficient higher than about 0.22, a production of granular temperature occurs at the walls. This indicates that a core-annular flow behavior will form if the walls dissipate granular temperature, thus demonstrating the significance of boundary conditions and their effect on the model predictions.

Figure 5-d shows the solids axial velocity predictions using different wall boundary conditions. The larger the wall-particle friction, the lower the solids slip velocity computed at the walls. In this case, the Johnson and Jackson BC had the largest friction as seen in Figure 5-d. The gas is usually entrained with the solids even near a wall boundary as seen

in Figure 5-c. Therefore, different wall boundary conditions for the gas phase may not be important in dictating the overall gas/solids flow patterns due to the lower inertia of the gas in dense systems. Figure 5-d shows also that most solids downward flow occurs with the free slip condition due to the lack of wall friction that tends to slow the downward flow of large clusters.

Conclusions

The verification of the granular model in MFIX was conducted by using a closed form solution of the granular temperature derived by Gidaspow (2003); it was verified that by fixing the granular temperature profile, the numerical and analytical solutions for the solids velocity matched exactly. A series of simulations were conducted with increasing grid refinement to select a grid size that gives grid-independent, time-averaged solutions.

The comparison of different turbulence models and boundary conditions was done by conducting several transient 1-D simulations, which are useful for comparing models because they are considerably faster than 2-D or 3-D simulations. A few 2-D simulations were also conducted to test the validity of comparisons based on 1-D simulations. A major difficulty with 1-D simulation is that the size of the clusters in the flow directions is infinite, and, therefore, their downward velocity near the wall is larger than that predicted by a 2-D simulation. Nevertheless, the solids velocity profiles predicted by 1-D and 2-D simulations agreed qualitatively. There was good quantitative agreement in predicted solids volume fraction and gas velocity profiles.

Three gas/solids models have been examined to study a relatively dense (3% solids by volume) gas/solids fully-developed and transient flow. For dense gas/solids flows, these models use similar closures for the solids stresses derived from kinetic theory of granular materials and differ mainly in their treatment of the gas/solids turbulence interchange. This study has demonstrated that the granular kinetic theory, Balzer et al. 1996, and Cao and Ahmadi 1995 models give similar predictions for a dense fully developed flow in a vertical channel, and that the gas turbulence may not have a dominant effect in relatively dense gas/solids flows.

Finally, the core-annular flow behavior with the maximum solids concentration at the walls was not observed if the boundary condition causes production of granular energy at the wall. Boundary conditions that dissipate granular energy near the wall are needed to predict a core-annular flow structure.

References

Agrawal, K., Loezos, P.N., Syamlal, M and Sundaresan, S., 2001. The Role of Meso-Scale Structures in Rapid Gas-Solid Flows, J. Fluid. Mech., 445, 151-185.

Benyahia, S., Syamlal, M. and O'Brien, T.J., 2004. Evaluation of Boundary Conditions used to Model Dilute, Turbulent Gas/Solids Flows in a Pipe. Submitted for publication in *Powder Technology*.

Balzer, G., Simonin, O., Boelle, A. and Lavieville, J., 1996. A unifying modelling approach for the numerical prediction of dilute and dense gas-solid two phase flow, CFB5, *5th Int. Conf. on Circulating Fluidized Beds*, Beijing, China.

Cao, J. and Ahmadi, G., 1995. Gas-particle two-phase turbulent flow in a vertical duct. *Int. J. Multiphase Flow*, Vol. 21 No. 6, pp. 1203-1228.

Gidaspow, D. (2003), Hydrodynamics of fluidization using kinetic theory: An emerging paradigm?, in Recent Res. Devel. Chemical Eng., Transworld Research Network, Trivandrum, India, Vol 5, 53-81.

Gidaspow, D., 1994. Multiphase Flow and Fluidization: Continuum and Kinetic Theory Description. Academic Press.

Grace, J.R. and Taghipour, F., 2004. Verification and validation of CFD models and dynamic similarity for fluidized beds. Powder Technology, vol. 139, pp. 99-110.

Hrenya, C.M., and Sinclair, J.L, 1997, Effects of particulate-phase turbulence in gas-solids flows, AIChE J., 42, 853-869.

Jenkins, J.T. and Louge, M.Y., 1997. On the Flux of Fluctuating Energy in a Collisional Grain Flow at a Flat Frictional Wall, *Phys. Fluids* 9 (10), pp. 2835-2840.

Johnson, P.C. and Jackson, R., 1987. Frictional-Collisional Constitutive Relations for Granular materials, with Application to Plane Shearing. *J. Fluid Mech.*, 176, 67-93.

Jones, N.E. and Sinclair, J.L., 2003. Effect of Solids Loading in Dilute and Dense Gas-Solid Flow, to be published in *AIChE J*.

Lun, C.K.K., Savage, S.B., Jeffrey, D.J. and Chepurniy, N., 1984. Kinetic theories of granular flows: inelastic particles in Couette flow and slightly inelastic particles in a general flow field. J. Fluid Mech., Vol. 140, pp. 223-256.

Simonin, O., 1996. "Continuum modeling of dispersed two-phase flows, in Combustion and Turbulence in Two-Phase Flows, Von Karman Institute of Fluid Dynamics Lecture Series 1996-2.

Sinclair, J.L. and Jackson, R., 1989. Gas-Particle Flow in a Vertical Pipe with Particle-Particle Interactions, *AICHE J.*, **35(9)**, 1473-1486.

Tanaka, T. and Tsuji, Y., 1991. Numerical Simulation of Gas-Solid Two-Phase in a Vertical Pipe: on the Effect of Inter-Particle Collision, in *4th Symposium on Gas-Solid Flows*, ASME FED, Vol. 121, 123-128.

Tsuo, Y.P. and Gidaspow, D., 1990. Computation of flow patterns in circulating fluidized beds. *AICHE J.*, Vol. 36, pp. 964-970.

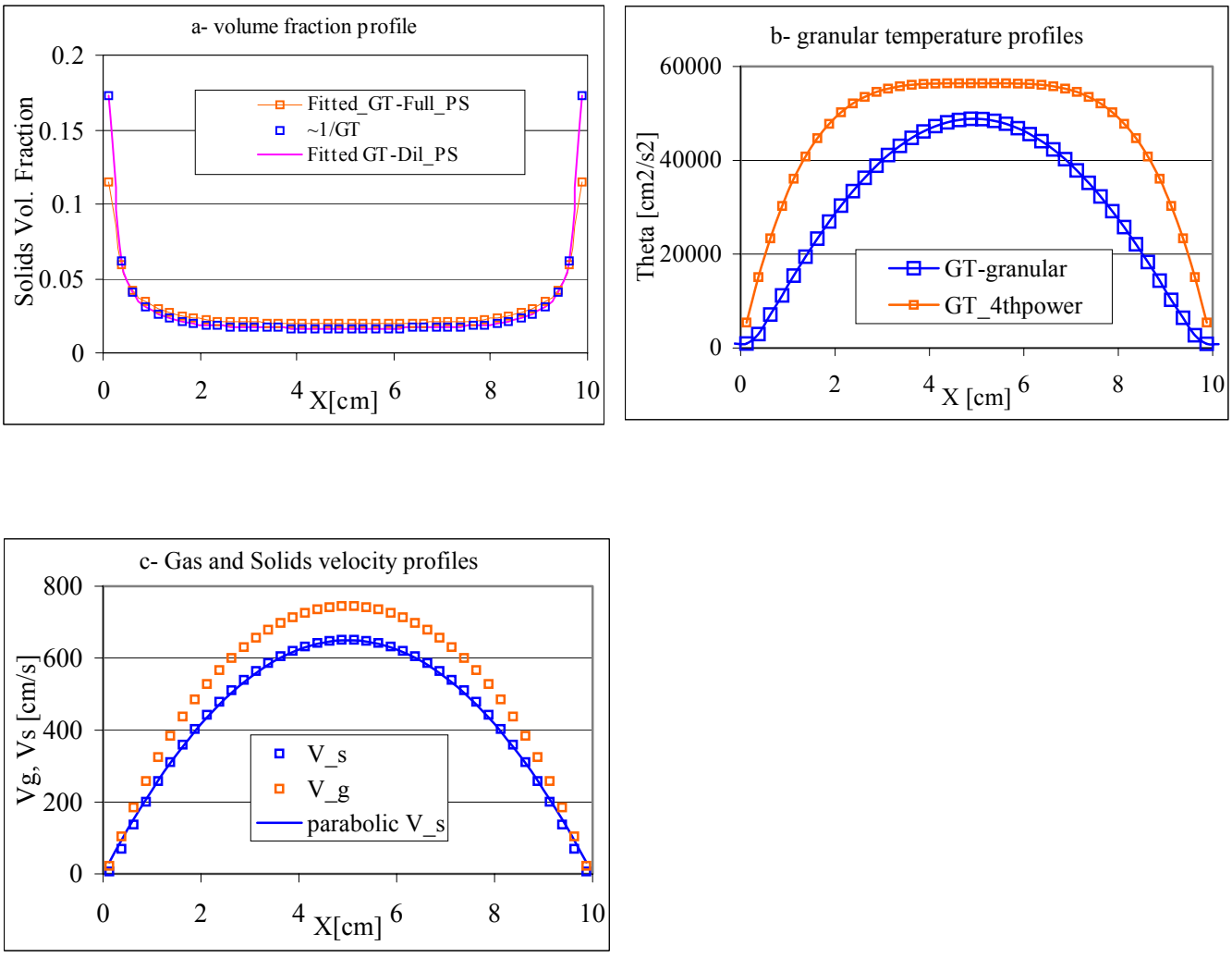

FIGURE 1. Verification of the numerical implementation of the granular model in MFIX by imposing a theoretically derived granular temperature profile.

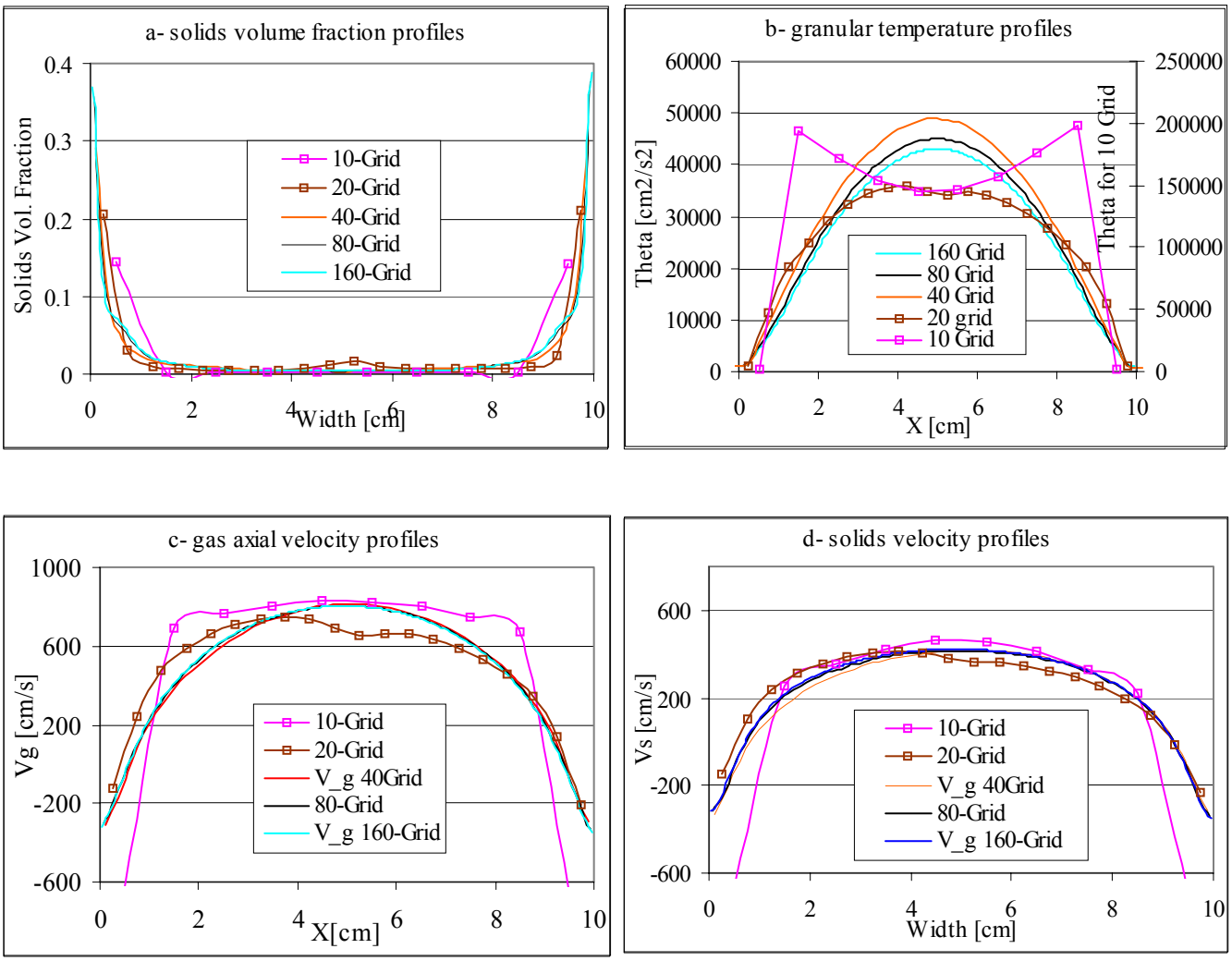

FIGURE 2. Grid sensitivity analysis of the time-averaged flow variables conducted in a one-dimensional fully developed channel.

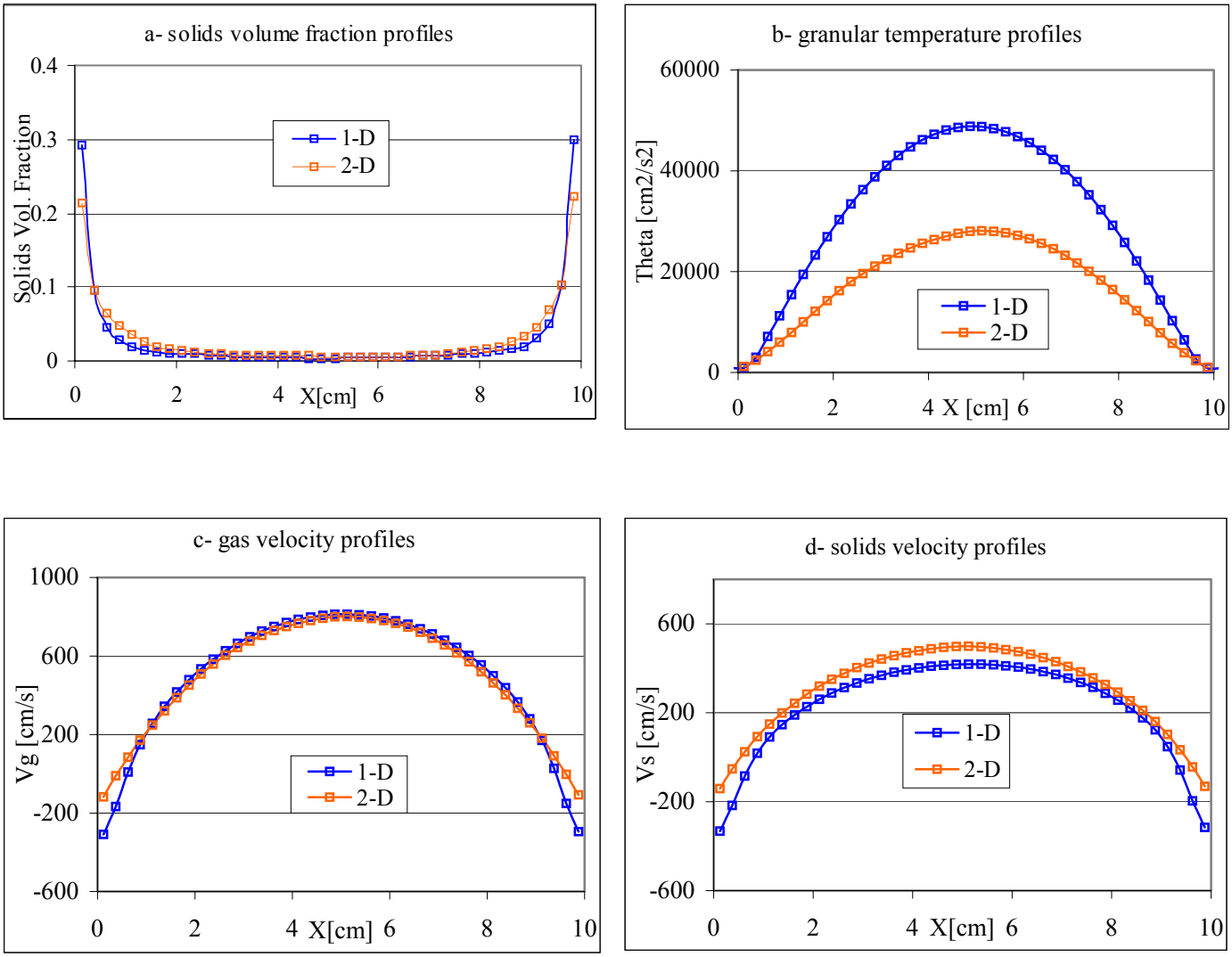

FIGURE 3. Comparison of the one-dimensional versus two-dimensional flow predictions in a fully developed channel.

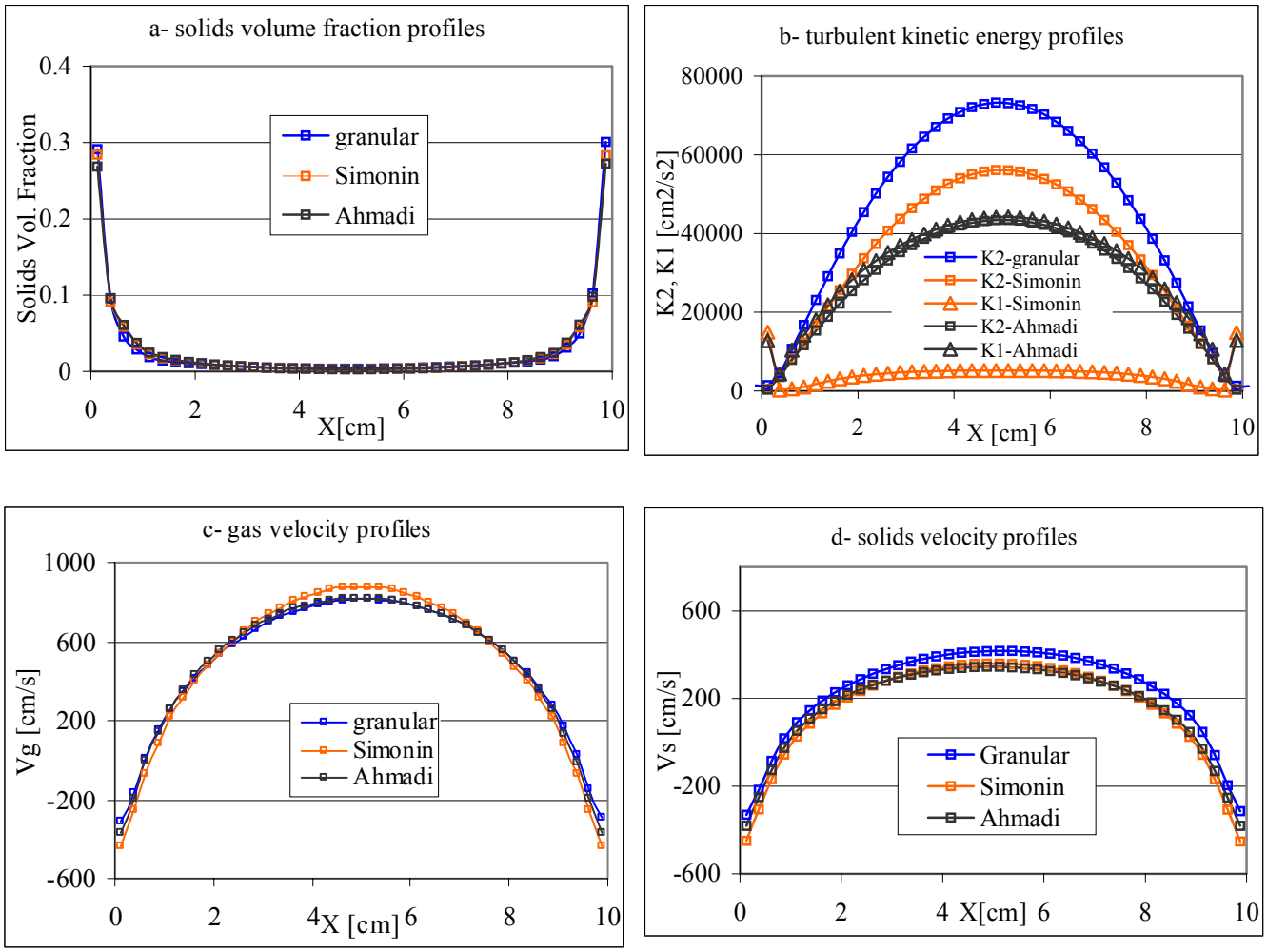

FIGURE 4. Effect of using different gas/solids turbulence models on the flow predictions in a one-dimensional fully developed channel.

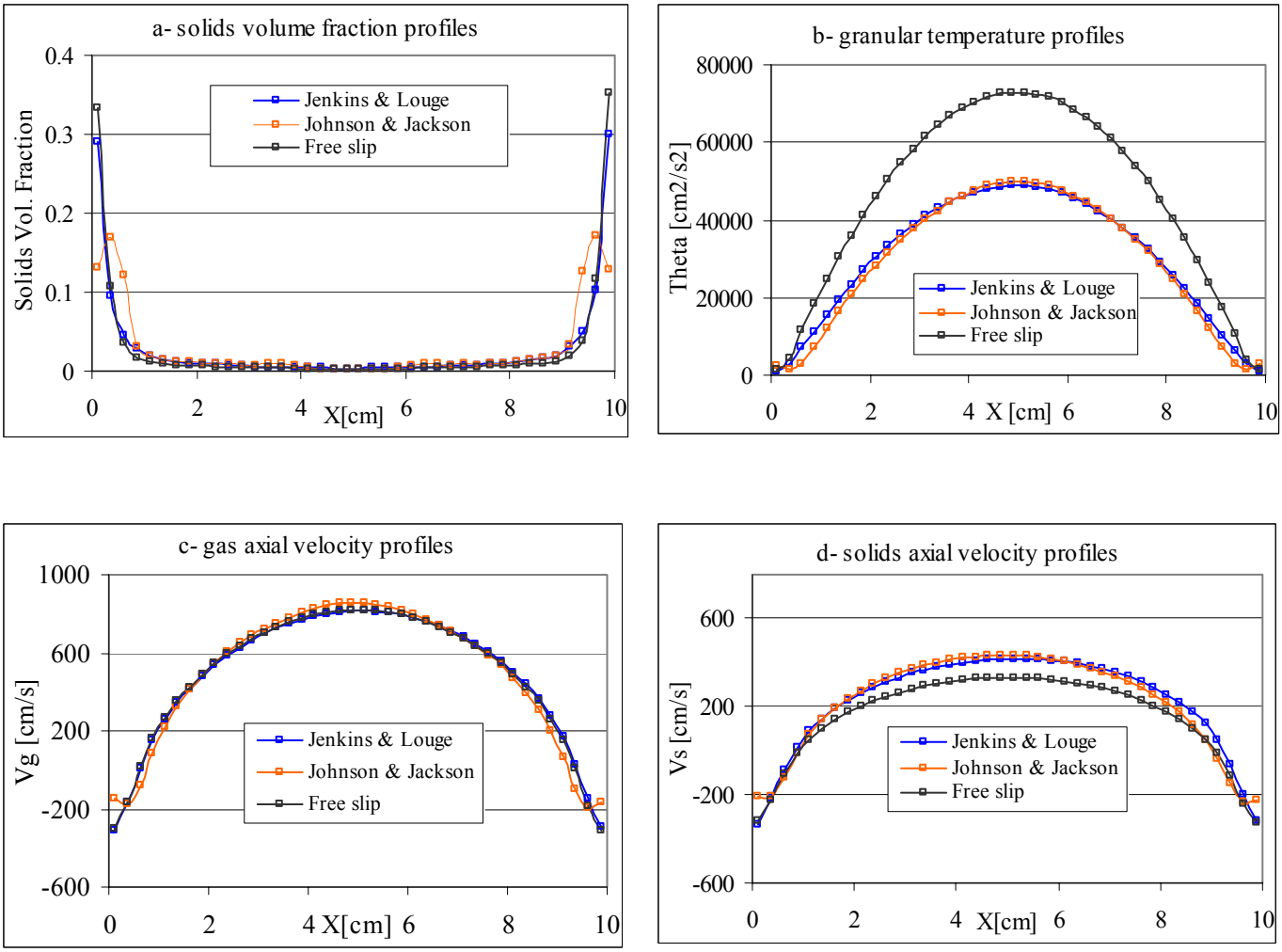

FIGURE 5. Effect of using different wall boundary conditions for the solids stresses on the time-averaged flow variables.

Appendix F

Presentation of the Comparison of MFIX and Fluent Results in a 2-D Riser

Schematic Drawing of the Developing Region of a Small 2-D Riser

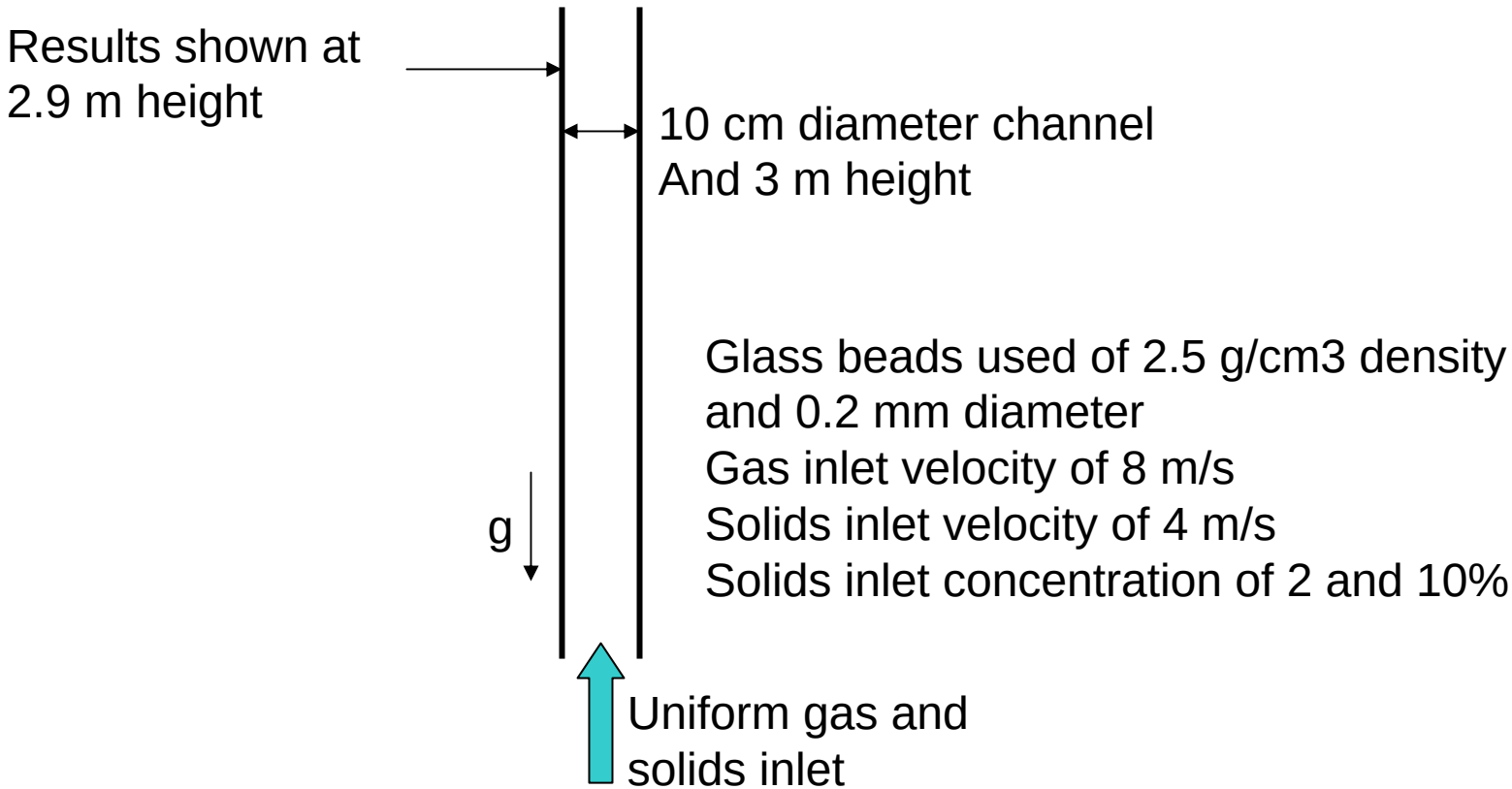

Comparison of Fluent 6.2 and MFIX results using the KTGF with Johnson and Jackson BC for the case of a dilute flow

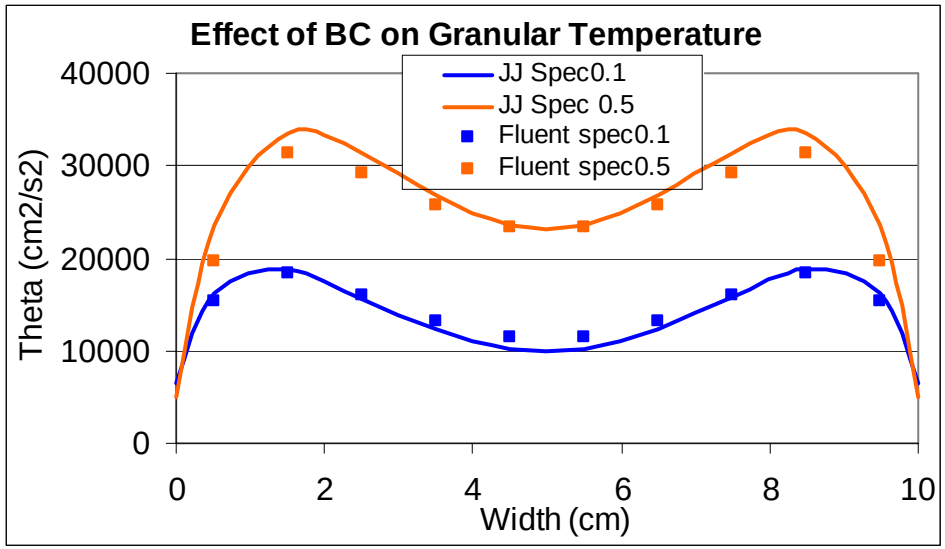

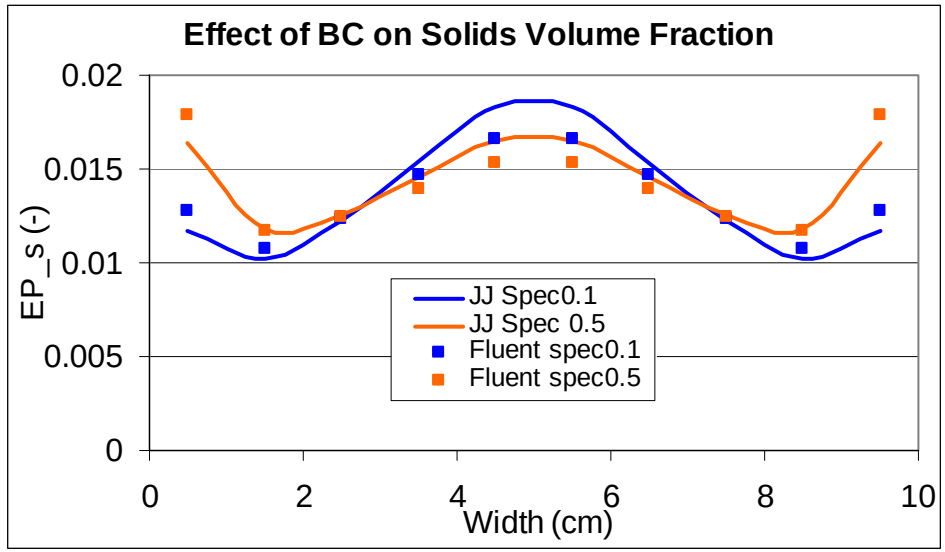

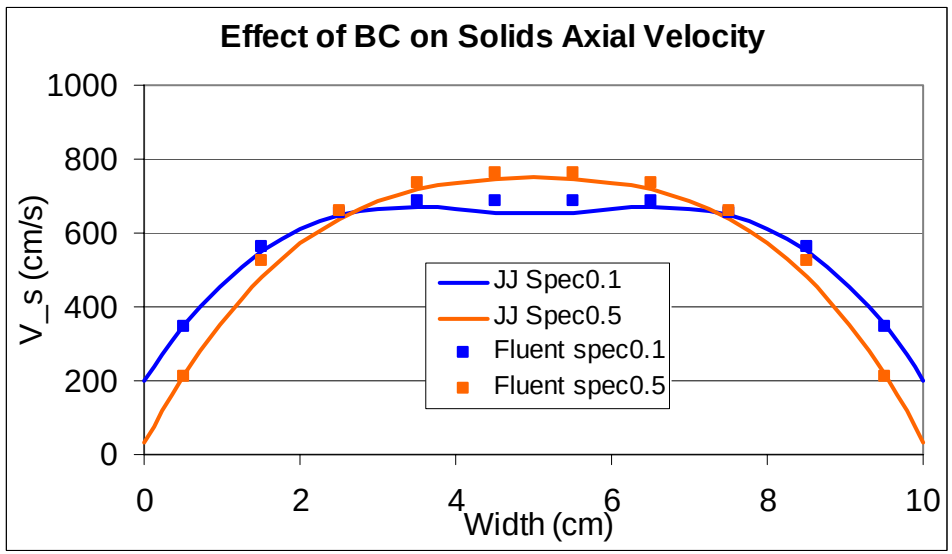

Comparison of Fluent 6.2 and MFIX results using the KTGF with Johnson and Jackson BC for the case of a dense flow

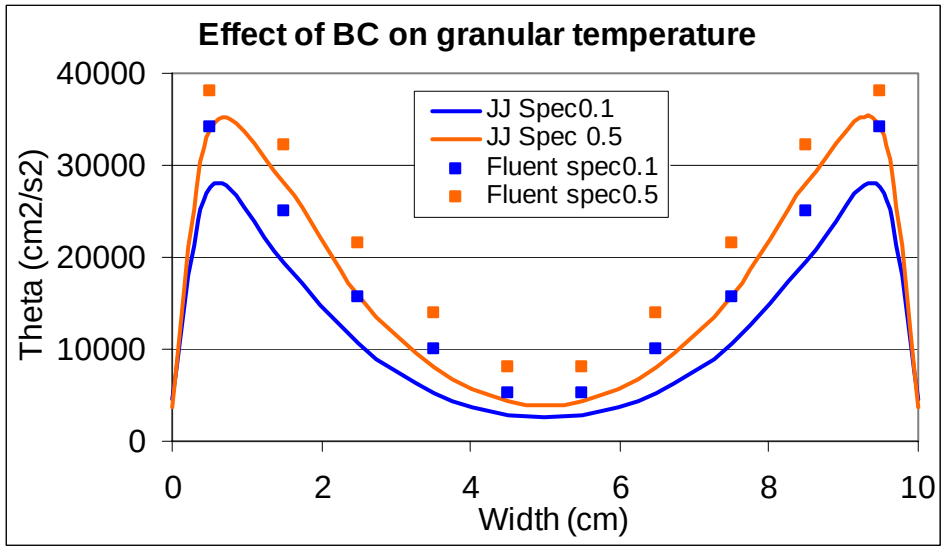

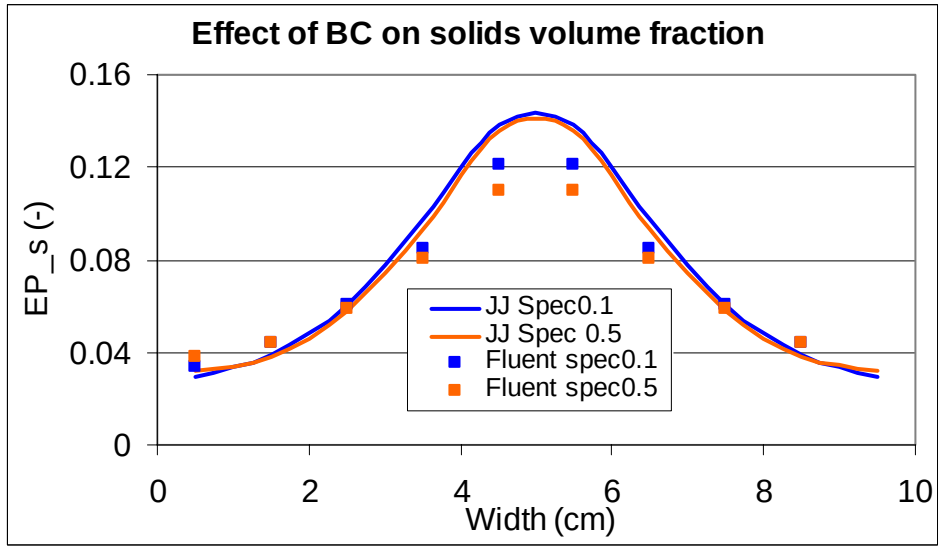

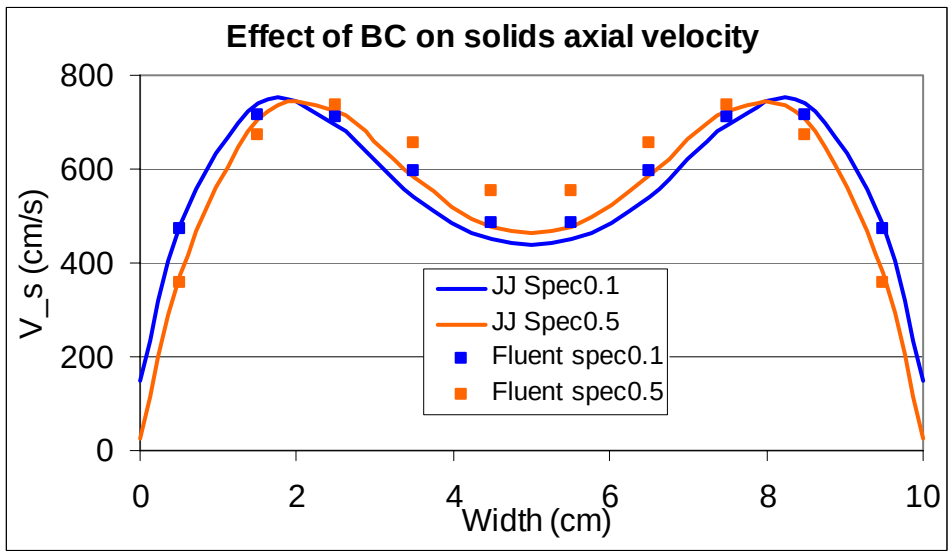

Appendix G

Evaluation of Boundary Conditions Used to Model Dilute, Turbulent Gas/Solids Flows in a Pipe

Evaluation of Boundary Conditions used to Model Dilute, Turbulent Gas/Solids Flows in a Pipe

Sofiane Benyahia and Madhava Syamlal
Fluent Incorporated
3647 Collins Ferry Road, Suite A
Morgantown, WV 26505
Ph. (304) 598-5863; Fax (304) 598-7185; E-mail: sof@fluent.com

Thomas J. O'Brien
US Department of Energy
MS-N04, 3610, Collins Ferry Road
Morgantown, WV 26505
Ph. (304) 285-4571, E-mail: tobrie@netl.doe.gov

ABSTRACT

A turbulent gas/solids model, based on the work of Simonin [1], has been recently implemented in the MFIX computational fluid dynamic (CFD) code. This theory includes the effects of turbulence in the gas phase as well as inter-particle collisions. The extension of this theory [2] to dense gas/solids systems was made possible by including the kinetic theory of granular material to describe the solids stresses.

The turbulence model and boundary conditions were evaluated by simulating the gas/solids flow experiments of Jones and Sinclair [3]. Their experimental results included velocity and turbulence measurements for fully developed flows for a range of particle loading from very dilute to relatively dense. Our numerical calculations were conducted by imposing periodic boundary conditions as well as in a long pipe with different length-to-diameter ratios to achieve a fully developed condition.

We propose modifications to the single-phase wall functions, to include the effect of the particulate phase. However, these modifications had only a minor effect on the predictions of gas turbulent kinetic energy due to the dilute nature of the flow considered in this study.

The turbulent gas/solids flow model based on the work of Simonin [1] is able to predict reasonably well dilute gas/solids flows with appropriate boundary conditions (BC). Four different types of boundary conditions were investigated to assess their sensitivity. The experimental data fall between the large-friction/no-sliding and small-friction/all-sliding limits of Jenkins and Louge [4] BC. However, the physical behavior of the particle-wall interactions is close to the small-friction/all-sliding limit of Jenkins and Louge BC or the Johnson and Jackson [5] BC with a small specularity coefficient or simply the free-slip BC.

Keywords: Multiphase turbulence, CFD, Simonin model, Gas/Solids dilute flow, kinetic theory, boundary condition, fluidization.

1. Introduction

Multiphase flows are important to most chemical, petroleum and pharmaceutical industries. Rare are the chemical processes that do not involve solids handling. Turbulent gas/particle flows are encountered commonly in processes such as pneumatic conveying, coal combustion, and fluid catalytic cracking. There is a worldwide effort in using computational fluid dynamics (CFD) to model such gas/solids flows; e.g., see Gidaspow [6]. It has been demonstrated that CFD models capture qualitative features of gas/ solids multiphase flows such as bubbles, streamers, clusters, pressure fluctuations, etc. very well. However, to improve the quantitative accuracy of CFD models, further validation of constitutive relations, turbulence models, and boundary conditions used in CFD is essential. This study addresses turbulence modeling and boundary conditions in gas/solids flows.

Dasgupta, Jackson and Sundaresan [7] demonstrated that particles are driven to regions having a low intensity of particle-phase velocity fluctuations and employed a speculative $k-\varepsilon$ model to illustrate the occurrence of segregation. Bolio and Sinclair [8], Hrenya and Sinclair [9], Kashiwa et al. [10], Balzer et al. [2], Simonin [1], and He and Simonin [11] have reported the use of turbulence models for gas/solids flows. As a starting point we use the turbulence model developed by Simonin's group in France, which is well documented [1,2,11,12] and has been used to describe gas/solids flows ranging from very dilute systems to bubbling fluidized beds [13,14,15]. We investigated the use of different gas and solids boundary conditions in conjunction with the above turbulence model. The model was implemented in MFIX, the platform used by National Energy Technology Laboratory (NETL) to develop and evaluate gas-solids flow models [16]. The model predictions are compared with the recently published data of Jones and Sinclair [3].

The turbulence model consists of a modified $k-\varepsilon$ model for the gas phase turbulence and a two-equation model (k_2-k_{12}) for the granular phase. The $k-\varepsilon$ model used in this study is similar to single-phase turbulence models with the exception of exchange terms due to the interfacial drag force. The k_2 equation for granular phase velocity fluctuations combines the turbulent eddy viscosity concept with the kinetic theory for granular material. In addition, a k_{12} equation for the gas-particle velocity correlation is also solved.

The equations used in this study make no distinction between kinetic theory and turbulence. Kinetic theory is used for deriving expressions for momentum transfer that occurs at a length scale of particle size because of particle collisions and translations [17]. The stresses resulting from kinetic theory can be viewed as laminar stresses and analogous to single phase flow the Reynolds stresses in the granular fluid may be viewed as resulting from turbulence [for example 9]. Recently Tartan et al. [18] measured the two types of stresses in risers and bubbling fluidized beds and concluded that the kinetic theory stresses are larger than Reynolds stresses at the core of a riser and vice versa near the wall. Neither Balzer et al. [2] nor Kashiwa [10] distinguish between the kinetic theory and turbulence stresses. They take the pragmatic approach that the turbulence theory must go to the correct limits; i.e. to kinetic theory limit in a dense bed and to single phase turbulence limit as the void fraction approaches one.

The extension of this turbulence model to dense flows has been developed by Simonin [2] and was successfully applied to a bubbling fluidized bed [13]. This extension included modifications to the collisional part of the solids stresses [e.g., see 17]. The main feature of this new approach is the formulation of the dissipative time scale (τ_2) as a harmonic mean of the particle relaxation time (τ_{12}^x) and the particle collisional time (τ_2^c): $1/\tau_2 \approx 1/\tau_{12}^x + 1/\tau_2^c$. For $\alpha_s \le 0.001$, particle-particle collisions are rare and the main dissipative time scale is due to the gas-particle interaction through drag, and the dilute turbulence theory of Simonin [1] is recovered. For $\alpha_s > 0.01$, the collisional time scale becomes very small, and the standard kinetic theory of granular flows [17] is recovered. In intermediate regimes ($0.001 \le \alpha_s \le 0.01$), both particle-particle collisions and gas-particle interactions due to drag contribute to granular stresses.

The boundary conditions for the particulate turbulent energy (or granular temperature) and axial velocity are complex; a particle colliding with the wall may slide or bounce back tangentially depending on the value of the collisional angle, as described by Jenkins [20]. When tracking individual particles, this angle may be computed directly, but in the two-fluid model the collisional angle is not accounted for explicitly by the boundary conditions. Nevertheless, there are two limits in a collisional exchange of momentum and kinetic energy between particles and a wall: a small-friction/all-sliding limit and a large-friction/no-sliding (or sticking) limit. Lately, Jenkins and Louge [4] have improved those boundary conditions and suggested that the appropriate boundary conditions could be found by interpolating between the two limits. In this study we found no obvious way to interpolate between the two limits in our model. Furthermore, this boundary condition requires material properties that may not be readily available for all the types of particles and walls. Another type of boundary condition commonly used in fluidization was derived by Johnson and Jackson [5]. This boundary condition uses a specularity coefficient, which may vary under different flow conditions, to characterize the extent of sliding and bouncing back. This approach allows more flexibility in adjusting this parameter to fit a certain flow behavior. We report simulation results obtained by applying these boundary conditions.

2. Description of the gas/solids turbulent flow model

The governing equations are written in terms of the mean velocities averaged with respect to phase m, $\mathbf{U}_m = \langle \mathbf{u}_m \rangle_m$, where index m=1 (gas) or 2 (solids).

Continuity equation

$$\frac{\partial}{\partial t}\left(\alpha_m \rho_m\right) + \frac{\partial}{\partial x_i}\left(\alpha_m \rho_m U_{mi}\right) = 0 \tag{1}$$

Momentum equation

$$\alpha_m \rho_m \left[\frac{\partial U_{mi}}{\partial t} + U_{ml}\frac{U_{mi}}{\partial x_j}\right] = -\alpha_m \frac{\partial P_1}{\partial x_i} + \frac{\partial \Sigma_{mij}}{\partial x_j} + I_{mi} + \alpha_m \rho_m g_i \tag{2}$$

The effective stress tensor has two contributions,

$$\Sigma_{mij} = \sigma_{mij} + \alpha_m \rho_m \left\langle u'_{mi}\, u'_{mj} \right\rangle_m \tag{3}$$

Here the averaging operator $\langle\ \rangle_m$ represents a density weighted (or Favre) averaging with respect to phase m. Also, $\left\langle u'_{mi}\, u'_{mj} \right\rangle_m$ is the second order velocity moment where $u'_{mi} = u_{mi} - U_{mi}$ is the fluctuation about the mean, for the velocity of the m[th] phase. For the continuous phase, σ_{1ij} is the viscous stress tensor; for the dispersed phase, σ_{2ij} is the collisional stress tensor.

Inter-phase momentum transfer:
For gas-particle flow, the interphase momentum exchange is modeled as:

$$I_{2i} = -I_{1i} = -\beta_{21} U_{ri} \tag{4}$$

where β_{21} is the drag coefficient modeled following Syamlal and O'Brien [16]. Note that the mean relative velocity is modified with a drift velocity to take into account the velocity fluctuations [1],

$$U_{ri} = U_{2i} - U_{1i} - U_{di} \tag{5}$$

By definition, the drift velocity, $U_{di} = \left\langle u'_{1i} \right\rangle_2$, is the fluctuation in the fluid velocity as seen by the granular phase. It is modeled as:

$$\alpha_1 \alpha_2 U_{di} = -\frac{D_{12}^t}{\sigma_{12}} \frac{\partial \alpha_2}{\partial x_i} \tag{6}$$

The binary dispersion coefficient is modeled as:

$$D_{12}^t = \frac{1}{3} k_{12} \tau_{12}^t \tag{7}$$

The crossing trajectory effect is accounted for by τ_{12}^t, the fluid Lagrangian integral time-scale, computed along the particle trajectory (the eddy-particle interaction time) [1]. It is related to the fluid phase turbulent time-scale using

$$\tau_{12}^t = \frac{\tau_1^t}{\sqrt{1 + C_\beta \xi_r^2}} \tag{8}$$

Where: $\xi_r^2 = \dfrac{3\left|U_{iir}\right|^2}{2k_1}$.

Here: $|U_{iir}| = \sqrt{(U_{gi} - U_{si})(U_{gi} - U_{si}) + 2(k_1 + k_2 - k_{12})}$, which is the definition of the relative velocity magnitude, proposed Simonin [1] and Enwald and Almstedt [21], was used in the formulation of the drag term. The details of a non-linear formulation for the dependence of the drag term on the instantaneous relative velocity can be found in Sakiz and Simonin [22].

The quantity C_β depends on the type of flow and also its direction (span-wise or stream-wise):
$C_\beta = 1.8 - 1.35\cos^2(\theta)$.
Here θ is the angle between the mean particle velocity and the mean relative velocity.

Turbulence modeling in the continuous phase

Turbulence predictions for the carrier phase are obtained from a modified $k-\varepsilon$ model:

$$\alpha_1\rho_1\left[\frac{\partial k_1}{\partial t} + U_{1j}\frac{\partial k_1}{\partial x_j}\right] = \frac{\partial}{\partial x_i}\left(\alpha_1\,\frac{\mu_1^t}{\sigma_k}\,\frac{\partial k_1}{\partial x_i}\right) + \alpha_1\,\tau_{1ij}\,\frac{\partial U_i}{\partial x_j} + \prod_{k1} - \alpha_1\rho_1\varepsilon_1 \tag{9}$$

$$\alpha_1\rho_1\left[\frac{\partial \varepsilon_1}{\partial t} + U_{1j}\frac{\partial \varepsilon_1}{\partial x_j}\right] = \frac{\partial}{\partial x_i}\left(\alpha_1\,\frac{\mu_1^t}{\sigma_\varepsilon}\,\frac{\partial \varepsilon_1}{\partial x_i}\right) + \alpha_1\,\frac{\varepsilon_1}{k_1}\left(C_{1\varepsilon}\,\tau_{1ij}\,\frac{\partial U_i}{\partial x_j} - \rho_1\,C_{2\varepsilon}\,\varepsilon_1\right) + \prod_{\varepsilon 1} \tag{10}$$

The above equations are identical to single phase $k-\varepsilon$ model, except for the exchange terms $\prod_{k1}$ and $\prod_{\varepsilon 1}$.

Closure relations for gas turbulence modeling:

The Reynolds-Stress tensor, τ_{1ij}, is defined as:

$$\tau_{1ij} = 2\,\mu_1^t\,S_{1ij} - \frac{2}{3}\delta_{ij}\left(\rho_1\,k_1 + \mu_1^t\frac{\partial U_{1k}}{\partial x_k}\right) \tag{11}$$

Here, S_{1ij} is the mean strain-rate tensor, which is written as:

$$S_{1ij} = \frac{1}{2}\left(\frac{\partial U_{1i}}{\partial x_j} + \frac{\partial U_{1j}}{\partial x_i}\right) \tag{12}$$

The eddy viscosity μ_1^t is defined as:

$$\mu_1^t = \rho_1\,C_{1\mu}\,\frac{k_1^2}{\varepsilon_1} \tag{13}$$

The terms $\prod_{k1}$ and $\prod_{\varepsilon 1}$ represent the influence of the solids phase on the gas turbulence and are defined by the following equations:

$$\prod_{k1} = \beta_{12}\,\left[k_{12} - 2\,k_1 + (U_{2i} - U_{1i})\cdot U_{di}\right] \tag{14}$$

$$\prod_{\varepsilon 1} = C_{3\varepsilon}\,\frac{\varepsilon_1}{k_1}\prod_{k1} \tag{15}$$

The constants in the $k-\varepsilon$ modeling approach are the same as the ones used in single-phase modeling (i.e. Wilcox [23]). The multiphase turbulence model contains a new constant: $C_{3\varepsilon}$, for which Simonin [1] determined a value of 1.2 by fitting the model predictions to experimental data in turbulent particle-laden jets.

Turbulence modeling of the dispersed phase

Turbulence predictions in the dispersed phase are obtained following the work of Simonin [1], where $k_2 = \frac{1}{2}\langle u'_{2i}u'_{2i}\rangle_2$, and $k_{12} = \langle u'_{1i}u'_{2i}\rangle_2$; the granular temperature $\Theta_s = \frac{2}{3}k_2$. The $k_2 - k_{12}$ model is described by the following equations:

$$\alpha_2\rho_2\left[\frac{\partial k_2}{\partial t} + U_{2j}\frac{\partial k_2}{\partial x_j}\right] = \frac{\partial}{\partial x_i}\left(\alpha_2\rho_2 K_2^t \frac{\partial k_2}{\partial x_i}\right) + \alpha_2\rho_2\tau_{2ij}\frac{\partial U_{2i}}{\partial x_j} + \prod_{k2} - \alpha_2\rho_2\varepsilon_2 \tag{16}$$

$$\alpha_2\rho_2\left[\frac{\partial k_{12}}{\partial t} + U_{2j}\frac{\partial k_{12}}{\partial x_j}\right] = \frac{\partial}{\partial x_i}\left(\alpha_2\rho_2\frac{\nu_{12}^t}{\sigma_k}\frac{\partial k_{12}}{\partial x_i}\right) + \alpha_2\rho_2\tau_{12ij}\left(\frac{\partial U_{2i}}{\partial x_j} + \frac{\partial U_{1j}}{\partial x_i}\right) + \prod_{k12} - \alpha_2\rho_2\varepsilon_{12} \tag{17}$$

Closure relations for solids turbulence modeling:

The interaction terms in the $k_2 - k_{12}$ equations are written as:

$$\prod_{k2} = -\alpha_2\rho_2\frac{1}{\tau_{12}^x}(2k_2 - k_{12}) \tag{18}$$

$$\prod_{k12} = -\alpha_2\rho_2\frac{1}{\tau_{12}^x}\left[(1+X_{21})k_{12} - 2k_1 - 2X_{21}k_2\right] \tag{19}$$

With $X_{21} = \frac{\alpha_2\rho_2}{\alpha_1\rho_1}$

The dissipation rate due to inelastic collisions is written as:

$$\varepsilon_2 = \frac{1}{2}\frac{(1-e^2)}{\tau_2^c}\frac{2}{3}k_2 \tag{20}$$

The dissipation term in the k_{12} equation accounts for the destruction rate due to viscous action in the continuous phase and the loss of correlation by crossing-trajectory effects,

$$\varepsilon_{12} = k_{12}/\tau_{12}^t \tag{21}$$

The solids phase stresses are defined as:

$$\tau_{2ij} = \nu_2^t \left(S_{2ij} - \frac{2}{3}\delta_{ij} \frac{\partial U_{2k}}{\partial x_k} \right) - \left(P_2 - \lambda_2 \frac{\partial U_{2k}}{\partial x_k} \right) \delta_{ij} \tag{22}$$

The solids pressure is defined as:

$$P_2 = \alpha_2 \rho_2 2/3 k_2 \left[1 + 2\alpha_2 g_0 (1+e) \right] \tag{23}$$

With the radial distribution function at contact $g_{0,}$ which becomes large as the solids volume fraction approaches maximum packing ($\alpha_2^{\max} = 0.62$), defined as:

$$g_0 = \left[1 - \left(\frac{\alpha_2}{\alpha_2^{\max}} \right)^{1/3} \right]^{-1} \tag{24}$$

In fully developed flows the radial momentum equation for the solids phase reduces to $\frac{\partial(\alpha_2 k_2)}{\partial x_j} = 0$, which implies that α_2 and k_2 are inversely proportional. Therefore, it is expected that higher concentration of particles exist in regions where the solids phase turbulence is low. This has been demonstrated and recognized in several papers in the literature [7, 11, 24]. The Princeton group [7, 24] has argued that a high solids turbulent energy (or granular temperature) in the center of a riser (operating at relatively high solids fluxes) causes the migration of particles toward the walls of the riser. A similar argument can be used to explain the experimental findings of Tanaka and Tsuji [25] who found that particles tend to concentrate along the pipe axis in very dilute flows ($\alpha_2 \approx 10^{-04}$). In these types of flows, however, the higher solids turbulent energy occurs near the walls of the riser, which causes the particles to migrate toward the center [11].

The shear and bulk viscosities are defined as: $\nu_2^t = \nu_2^{kin} + \nu_2^{col}$, and $\lambda_2 = 5/3\, \nu_2^{col}$.

$$\nu_2^{kin} = 2/3 \left(k_{12}\, \eta_{21} + k_2 (1 + \zeta_c \alpha_2 g_0) \right) \tau_2 \tag{25}$$

$$\nu_2^{col} = 4/5\, \alpha_2 g_0 (1+e) \left(\nu_2^{kin} + d_p \sqrt{\frac{2k_2}{3\pi}} \right) \tag{26}$$

Where, $\zeta_c = 2/5\,(1+e)(3e-1)$ and

$$\frac{1}{\tau_2} = \frac{2}{\tau_{12}^x} + \frac{\sigma_c}{\tau_2^c} \tag{27}$$

Balzer et al. [2] defined τ_2 in this manner to combine the dilute turbulence model [1] with kinetic theory applicable to dense flows [17].

The ratio between the Lagrangian integral time scale and the particle relaxation time is defined as: $\eta_{21} = \frac{\tau_{12}^t}{\tau_{12}^x}$.

The particle relaxation time, τ_{12}^x, is the characteristic time scale of fluid-particle interaction. It is defined by:

$$\tau_{12}^x = \alpha_2 \, \rho_1 \, \beta_{21}^{-1} \left(\frac{\rho_2}{\rho_1} \right) \tag{28}$$

Similarly, the effective diffusivity is expressed in terms of its kinetic and collisional contributions: $K_2^t = K_2^{kin} + K_2^{col}$

$$K_2^{kin} = 2/3 \left(9/10 \, k_{12} \, \eta_{21} + k_2 \left(1 + \varpi_c \alpha_2 g_0 \right) \right) \left(\frac{9/5}{\tau_{12}^x} + \frac{\xi_c}{\tau_2^c} \right)^{-1} \tag{29}$$

$$K_2^{col} = 6/5 \, \alpha_2 g_0 \left(1 + e \right) \left(K_2^{kin} + 5/9 d_p \sqrt{\frac{2k_2}{3\pi}} \right) \tag{30}$$

With the constant $\varpi_c = \left(1 + e \right)^2 \left(2e - 1 \right) / 100$.

The resulting solids viscosity and turbulent conductivity are consistent with the two limits: for very dilute flows, these parameters are controlled by fluid turbulence as expressed in the previous sections, and in the dense cases they reduce to the kinetic theory expressions for granular flow [17]. In the intermediate regimes, these two mechanisms contribute according to the characteristic dissipation time scale τ_2.

Combining the two approaches in the above manner also eliminates a difficulty with the kinetic theory, as pointed out by He and Simonin [11]. In the classical kinetic theory for granular flow, the kinetic solids viscosity at very dilute flows is a constant independent of the particles volume fraction, implying that the particle mean free path can be several times higher than the bed diameter, which needs to be corrected in some manner [24, 26]. In this generalized theory, however, dilute flow conditions are not controlled by the collisional time scale, but rather by the particle relaxation time, which controls the dissipation mechanism of turbulence. Thus the difficulty caused by the large mean free path is eliminated without the need for any ad hoc corrections.

Gas-phase wall boundary conditions

We evaluated two types of boundary conditions for gas phase: a standard and modified wall function based boundary condition.

The use of wall functions allows the computation of turbulent flows without the need to resolve the turbulent boundary layer, which would require a prohibitively large number of mesh points near the wall. In most single-phase turbulent flows, the logarithmic law for the mean fluid

velocity near the wall can be used to get a realistic prediction for the flow with a relatively coarse computational grid. The boundary condition for the gas velocity is defined as:

$$\left.\frac{\partial U_1}{\partial x}\right|_w = \frac{\rho_1 \kappa U_1 C_{1\mu}^{1/4} k_1^{1/2}}{\left(\mu_1 + \mu_1^t\right)\ln\left(E\,x^*\right)} \tag{31}$$

Where: $x^* = \dfrac{\rho_1 C_{1\mu}^{1/4} k_1^{1/2} \Delta x/2}{\mu_1}$.

Wall functions that include the effect of particles do not exist in the literature as pointed out by De Wilde et al. [27]. We modified the standard wall functions for k_1 to include the effect of particles as shown below:

$$production = \alpha_1\, \tau_{1ij} \frac{\partial U_i}{\partial x_j} + \beta_{12}\, k_{12} = \alpha_1 \rho_1 \sqrt{C_{1\mu}} k_1 \frac{U_1}{\Delta x/2 \ln\left(E\,x^*\right)} + \beta_{12}\, k_{12} \tag{32}$$

$$dissipation = \alpha_1 \rho_1 \varepsilon_1 + 2\,\beta_{12}\, k_1 \tag{33}$$

The above modifications make the wall functions consistent with the multiphase turbulence models (the effect of drag being included), and the modified equations reduce to single-phase wall function for the case of zero drag. The exchange term is the only term that appears in the multiphase $k-\varepsilon$ model that does not exist in single-phase $k-\varepsilon$ model. It was, thus, natural to include the interaction terms in the multiphase wall functions to reflect the additional effect due to turbulence interaction between phases.

In the computational cells next to the wall the above expressions are used as the production and dissipation terms in the k_1 equation and the normal derivative dk_1/dn is set to zero at the wall boundary. Just as in the case of single-phase flow the wall function for the ε_1 equation is a specified constant value in the cells next to the wall defined as:

$$\varepsilon_1 = \frac{C_{1\mu}^{3/4} k_1^{3/2}}{\kappa \Delta y/2} \tag{34}$$

Solids-phase wall boundary conditions

Three sets of boundary conditions (BC) were implemented in MFIX to check the sensitivity of the turbulence model to different BCs: Johnson and Jackson [5], and two limits of a boundary condition proposed by Jenkins and Louge [4].

Johnson and Jackson [5] have developed a set of boundary conditions for the tangential solids velocity and fluctuating energy at a solid wall for a granular flow. These BCs are expressed below in a form that has been incorporated into MFIX:

$$\nu_2^t \left.\frac{\partial V_s}{\partial x}\right|_w + \frac{\phi\pi\, V_s g_0 \sqrt{2/3\, k_2}}{2\sqrt{3}\, \alpha_2^{\max}} = 0 \tag{35}$$

$$K_2^t \frac{\partial k_2}{\partial x}\bigg|_w - \frac{\phi\pi\, V_s^2 g_0 \sqrt{2/3\, k_2}}{2\sqrt{3}\, \alpha_2^{\max}} + \frac{\sqrt{3}\pi\, g_0 \left(1-e_w^2\right)\left(2/3\, k_2\right)^{3/2}}{4\, \alpha_2^{\max}} = 0 \tag{36}$$

Here the parameter ϕ, the specularity coefficient, varies from zero (smooth walls) to one (rough walls), as explained by Jones and Sinclair [3]. For a specularity coefficient tending towards zero, a free slip boundary condition for the solids tangential velocity is imposed at a smooth wall boundary.

The dissipation of solids turbulent kinetic energy by collisions with the wall is specified by the particle-wall restitution coefficient, e_w. High value of specularity coefficient implies high production at the wall and a value of e_w close to unity implies low dissipation of granular energy at the wall. It is expected that these two parameters (specularity coefficient and particle-wall restitution coefficient) need to be calibrated for a given gas/particle flow system because the specularity coefficient cannot be measured and e_w can only be measured with some difficulty.

Another formulation of the boundary condition was first developed by Jenkins [20]. He derived expressions for the solids shear stress and granular energy flux at the wall for two limiting cases: small-friction/all-sliding and large-friction/no-sliding. A revised form of these expressions was given by Jenkins and Louge [4]. Following [4], the ratio of the shear stress (S^{sf}) to the normal stress (N^{sf}) is expressed by the coefficient of friction (The superscript *sf* here indicates the small-friction/all-sliding limit):

$$S^{sf} / N^{sf} = \mu \tag{37}$$

The ratio of the flux of the fluctuation energy (Q^{sf}) to N^{sf} is:

$$\frac{Q^{sf}}{N^{sf}\left(2\Theta_s\right)} = \frac{2}{\left(1+e_w\right)}\left(\frac{2}{3\pi}\right)^{1/2}\left[\frac{1}{7}\mu_0^2 - \frac{1}{2}\left(1-e_w^2\right) - \mu_0\mu e_w\left(\frac{1+e_w}{e_w+2/e}\right)\right] \tag{38}$$

Where: $\mu_0 = (7/2)(1+e_w)\mu$.

In the large-friction/no-sliding limit (superscript *lf*), the ratio of the shear stress (S^{lf}) to the normal stress (N^{lf}) is:

$$\frac{S^{lf}}{N^{lf}} = \frac{3}{7}\frac{\left(1+\beta_0\right)}{\left(1+e_w\right)} r \tag{39}$$

Where $r = \left|U_s - U_w\right| / \left(2\Theta_s\right)^{1/2}$ and U_w is the wall velocity. The ratio of the flux of the fluctuation energy (Q^{lf}) to N^{lf} is:

$$\frac{Q^{lf}}{N^{lf}\left(2\Theta_s\right)} = \frac{3}{28\left(1+e_w\right)}\left[2\left(1+\beta_0\right)^2 r^2 - \left(1-\beta_0^2\right)\right] \tag{40}$$

The above equation (40), a simplified version of the equation for the energy flux at the wall [Eq. 6 in 4], is given here to give the reader an idea about the parameters involved. In this study, however, we used the complete (lengthy) form of Jenkins and Louge equation [Eq. 24 in 4].

Values for the coefficient of friction (μ), the particle-wall restitution coefficient (e_w), and the tangential particle-wall restitution coefficient (β_0), although measurable, are rarely available in the literature. Some example of these coefficients may be found in Foerster et al. [28].

3. Simulation of a dilute gas/solids flow in a pipe

The simulation results were compared with experimental measurements reported by Jones and Sinclair [3]. All measurements were made at the exit of a small pipe of about 14.2 mm diameter. The authors report that the flow was fully developed since the experimental L/D was 100. The solids were glass beads (ρ_s = 2500 kg/m^3, d_p=70 μm), and the solids loading ($m = \alpha_s \rho_s V_s / \alpha_g \rho_g V_g$) ranged from m = 1 to a maximum loading of 30. The average gas superficial velocity of 14.85 m/s was maintained constant for all solids loadings (Re = 13,800). The calculation of a fully developed flow can be achieved by using periodic boundary conditions in the streamwise direction of the flow[1]. We performed several computations in the fully developed regime using periodic boundaries in the streamwise direction. However, it was difficult to specify desired values of both the gas superficial velocity and the solids loading; MFIX allows only the setting of the pressure drop and the solids concentration (and not mass flow rates) for a fully developed flow. Thus, we decided to solve the flow in a long tube with inlet and outlet conditions. We fixed the inlet superficial gas velocity and solids flux at the desired values.

An axisymmetric cylindrical coordinate system was used with a grid size of 15x300. The transient simulations were run for about a second because a stationary state was reached after only 0.2 sec of physical time. This stationary state can be explained by the absence of clustering in the solids phase due to the dilute nature of the flow (for solids loadings m = 1 and 4 reported in this study). Jones and Sinclair [3] observed cluster formation only in denser flow regimes (m > 9). Such clusters can be computed by a model based on kinetic theory formulation of the solids stresses as pointed out by Agrawal et al. [19]. Even with an achieved steady-state mode, we still used the transient algorithm in MFIX with a maximum time step of about 50 μs . The results presented here are values obtained after about 1 sec of physical time.

First we present results for a mass loading of m=1. In this simulation the Johnson and Jackson boundary condition was used with physical parameters used by Jones and Sinclair [3]: e = 0.94,

[1] The fully developed flow simulations may be used to ascertain the significance of the inlet and outlet effects. A fully developed flow can be computed and checked against computational (or experimental) data of the whole riser geometry including the actual inlet and outlet design and conditions. The difference between these two results may be used to quantify the inlet and outlet effects.

e_w = 0.15. They [3] used a specularity coefficient ϕ=0.008. However, we needed to use a higher specularity coefficient (ϕ = 0.02) in order to correctly compute k_2 for the case of m = 1. Figure 1 shows the mean gas and solids velocity profiles along the radial direction. The experimental measurements were made throughout the pipe diameter. However, since our simulations were conducted assuming an axisymmetric geometry, only the profile over half the diameter is plotted. The gas velocity profile is similar to a single-phase turbulent profile because of the very dilute flow conditions. The profile of the gas turbulent kinetic energy in Figure 2 is also similar to that in the case of single-phase turbulent flow. However, the low value of k_1 at the center of the pipe is a clear indication of the high concentration of particles in that region. The predicted and measured values of k_2 are in good agreement (Figure 3). In fact we have used a relatively high specularity coefficient, which is one of the main parameters in Johnson and Jackson [5] boundary condition, so that there is a good match at m=1. However, we find that this leads to a poor match in the case of the average solids velocity (Figure 1), which strongly depends upon the value of k_2. It appears that one cannot get good agreement in both solids velocity and k_2 in very dilute flows because of the strong anisotropy that exists in the axial and radial solids fluctuating velocity. The mechanism of particle turbulence production is shear in the axial direction and interaction with the gas turbulence in the radial direction. Moreover, in very dilute flows, where particle-particle collisions are almost non-existent, the solids radial fluctuating velocity may be several times smaller than the axial velocity fluctuations. So perhaps the use of a scalar k_2 is inadequate for very dilute flows [29]. Fortunately in the case of a relatively dense flow, which is our main interest, this limitation of the model becomes less pronounced.

Figure 4 shows the radial variation of the solids volume fraction profile. As explained earlier $\alpha_s\ k_2$ is a constant for fully developed flows. Therefore, the solids volume fraction profile is an inverse function (high near the center) of the solids turbulent kinetic energy k_2 profile (low near the center). This is in agreement with the experimental observations [3].

To verify the assumption of a fully developed flow, the solids radial velocity (U_s) was plotted for the different solids mass loadings in Figure 5 for L/D=40. In general, a small solids radial velocity magnitude must be verified for any simulation to claim that a fully developed flow has been achieved. It is seen that the magnitude of the solids radial velocity is small except for the highest solids loading of m = 30. For this loading, the high values of U_s indicate that the particles were still redistributing and a greater length of the pipe would be needed to achieve a fully developed flow. Figure 6 shows that with an increase in the length of the pipe from L/D = 40 to L/D = 100, the solids radial velocity was further reduced to almost zero. Figures 7 to 10 show that no significant changes in the flow behavior occurred when the pipe length was increased from L/D = 40 to 100. Therefore, for a solids loading of m = 4, a pipe length of L/D = 40 was sufficient to achieve a fully developed flow. Furthermore, the difference between computational and experimental data for the solids fluctuating velocity was larger in the case of m = 4 (as seen in Figure 9) than in the case of m = 1 (see Figure 3). This was due to setting the specularity coefficient (ϕ=0.02) in order to correctly compute k_2 for the case of m = 1. The experimental data of solids fluctuating velocity varied significantly between the solids loading of m = 1 and m = 4, which was not captured with the current model. As explained before, strong anisotropy in solids turbulent energy is the main cause of these differences. Therefore, boundary parameters such as the specularity coefficient in the Johnson and Jackson boundary conditions may be set in relatively denser flow conditions where particle collisions are dominant. Furthermore, the current

model may not be appropriate for extremely dilute conditions such as for solids loading of m = 1 because of the strong anisotropy of turbulent fluctuations [29].

In the rest of the paper we report our investigations of the wall boundary conditions. Figure 11 compares the calculated radial profile of the gas turbulent kinetic energy (k_1) with experimental data. The calculations were done with the standard wall function as well as the modified wall function proposed here. The agreement with experimental data is good in both cases. The modified wall function gives a decrease in k_1 near the wall because the interaction with solids tends to decrease the turbulence. However, the effect is relatively small and confined near the wall because of the low solids volume fraction in that region.

Figure12 shows the effect of the boundary condition on the solids axial velocity profiles for m = 4. Four different BCs have been used in these simulations: Johnson and Jackson [5], no friction at the wall (free-slip BC for the solids axial velocity and zero flux for the granular temperature), and two limiting cases of Jenkins and Louge [4] boundary condition. For the Jenkins and Louge boundary condition we used the same particle-wall properties as the ones determined experimentally by Foerster et al. [28]; *i.e.*, particle-wall restitution coefficient $e_w = 0.83$, particle-wall friction coefficient $\mu = 0.125$, and a tangential coefficient of restitution $\beta_0 = 0.31$. As mentioned, the BC developed by Jenkins and Louge [4] has two limits: small-friction/all-sliding and large-friction/no-sliding. These authors suggested that these two limits represent the two extremes, and flows that involve some sliding may be captured by interpolating between these two limits. Figure 12 does show that the experimental data fall between the two limits. However, there is no obvious way to interpolate between the two limits. In the small friction as well as no friction limits, the solids velocity was slightly over-predicted. On the other hand, the solids velocity was greatly under-predicted in the large-friction limit. This indicates that the physical behavior of the particle-wall interactions is close to the small-friction/all-sliding limit. Furthermore, Figures 12 and 14 show that the higher the friction at the wall, the higher the turbulence level and the lower the predicted solids axial velocity will be. Thus, it is clear that with a smaller specularity coefficient (less friction), it would be possible to obtain a higher solids velocity magnitude and a better comparison with experimental data will be achieved. In fact, using a free slip boundary condition, which is the same as using a specularity coefficient equal to zero, compared better with experimental data. Using frictionless boundary conditions (free slip), He and Simonin [11] have also reported that in dilute gas/solids flow a good agreement with the experimental data of Tanaka and Tsuji [25] was achieved.

Figure 13 shows that the gas turbulent kinetic energy was under-predicted for most cases, except for that of large-friction. Although the large-friction BC is applied to solids phase, the BC affects the gas turbulence through the turbulence exchange terms. For example, k_1 was over-estimated at the center of the pipe because of the large values for k_2 computed at the center.

Figure 14 shows the radial distribution of the solids fluctuating velocity. The highest turbulence intensity was produced using the large-friction/no-sliding limit of Jenkins and Louge [4] BC. Similar to Figure 12, the experimental data in this case lie between the limits of small and large friction.

Figure 15 shows the radial profile of the solids volume fraction. Again we see considerable difference in the profiles between the small and large friction limits. Also as expected the shape of the radial profile of the solids volume fraction is inversely proportional to that of the solids turbulent energy [7, 24].

Our simulations have shown that the boundary condition can significantly affect the model predictions. One advantage of the Jenkins and Louge [4] BC is that the parameters appearing in it are all measurable, admittedly with some difficulty. For example, Foerster et al. [28] have measured and reported such properties for two types of particles and walls. Our simulation results confirm that experimental data for solids velocity, gas turbulent kinetic energy, and solids turbulent kinetic energy fall between the small-friction/all-sliding and large-friction/no-sliding limits. Unfortunately, there is no obvious way to interpolate between the two limits and to get a good match with experimental data.

The BC developed by Johnson and Jackson [5], with its adjustable specularity coefficient, can be viewed as an alternative way of expressing the BC of Jenkins and Louge [4]. In fact, a high specularity coefficient is comparable to the large-friction/no-sliding limit, and a low specularity coefficient is similar to the small-friction/all-sliding limit. It is therefore easier to use the Johnson and Jackson [5] BC and adjust the specularity coefficient to fit the experimental data.

In this study we found that experimental data are close to the small or no friction limit. At the high gas and solids velocities used in this study (about 15 m/s), the solids near the wall boundary must follow the gas streamlines parallel to the wall. This means that the collisional angle between solid particles and the wall is small. Jenkins [20] has determined that a small-friction/all-sliding limit is obtained at particle-wall collisional angles less that a threshold defined by particle-wall friction coefficient and particle tangential restitution coefficient.

4. Conclusions

A turbulent gas/solids flow model based on the work of Simonin [2] is able to predict reasonably well dilute gas/solids flows with appropriate boundary conditions.

The fully developed flow assumption was checked in this study by examining the solids radial velocity. Small magnitude of the solids radial velocity indicated that using an L/D of about 40 was sufficient for studying the dilute case of m = 4.

We propose modifications to the single-phase wall functions, to include the effect of the particulate phase. However, these modifications had only a minor impact on the predictions of gas turbulent kinetic energy due to the dilute nature of the flow considered in this study.

The experimental data fall between the large-friction/no-sliding and small-friction/all-sliding limits of Jenkins and Louge [4] BC. However, the physical behavior of the particle-wall interactions is close to the small-friction/all-sliding limit of Jenkins and Louge BC or the Johnson and Jackson [5] BC with a small specularity coefficient or simply the free-slip BC.

5. Nomenclature

$C_{1\mu}$, $C_{1\varepsilon}$, $C_{2\varepsilon}$, $C_{3\varepsilon}$: constants in the gas turbulence model of values: 0.09, 1.44, 1.92, and 1.2, respectively.

d_p: particle mean diameter.

D_{12}^t: binary dispersion coefficient.

e: particle-particle restitution coefficient.

e_w: particle-wall restitution coefficient.

E: constant in wall function formulation equal to 9.81.

g_0: radial distribution function at contact.

I_{im}: momentum exchange

k_m: turbulent kinetic energy of phase m.

k_{12}: cross-correlation of gas and solids fluctuating velocities.

K_2: conductivity of solids turbulent energy.

N: normal force (solids pressure) of the solids phase at a wall boundary.

P_m: pressure of phase m.

Q: flux of granular temperature at a wall boundary

S_{mij}: mean strain-rate tensor.

S: shear force of the solids phase at a wall boundary.

U_m, V_m: averaged velocity of phase m.

Greek letters:

α_m: volume fraction of phase m.

β_{21}: drag coefficient.

β_0: tangential coefficient of restitution.

Δx: width of computational cell next to the wall.

ε_1: turbulent energy dissipation in the gas phase.

ε_{12}: dissipation term in the k_{12} equation.

ε_2: dissipation of solids fluctuating energy due to inter-particle collisions.

ζ_c and ϖ_c: constants depending on particle restitution coefficient.

η_{21}: ratio between Lagrangian and particle relaxation time scales.

θ: angle between mean particle velocity and mean relative velocity.

θ_s: granular temperature equal to $2k_2/3$

κ: Von Karmen constant of value: 0.42.

λ_2: bulk viscosity in the solids phase.

μ: coefficient of friction.

μ_0: constant in Jenkins and Louge boundary condition.

μ_m^t: turbulent eddy viscosity for phase m.

ν_m^t : turbulent kinematic viscosity for phase m.

Π : turbulence exchange terms.

ρ_m : density of phase m.

σ_{mij} : viscous stress tensor of phase m.

σ_k , σ_ε : constants in the gas turbulence model of values: 1.0, 1.3, respectively.

$\sum_{mij}$: effective stress tensor.

τ_{12}^x : particle relaxation time scale.

τ_{12}^t : eddy-particle interaction time scale.

τ_1^t : energetic turbulent eddies time scale.

τ_{mij} : Reynolds stresses for phase m.

ϕ : specularity coefficient.

ω_c : constant depending on particle restitution coefficient.

Indices:
col: collisional
d: drift
i, j, k: indices used to represent spatial direction and in Einstein summation convention
m: phase m, takes values 1 and 2 for gas and solids phases.
max: maximum packing
kin: kinetic
lf: large frictional limit
r: relative
s, p: solids or particulate phase.
sf: small frictional limit
w: wall

6. Acknowledgement

The authors gratefully acknowledge the comments and guidance of Prof. Olivier Simonin during the implementation of his model in MFIX.

7. References

[1] Simonin, O., 1996. "Continuum modeling of dispersed two-phase flows, in **Combustion and Turbulence in Two-Phase Flows**, Von Karman Institute of Fluid Dynamics Lecture Series 1996-2.

[2] Balzer, G., Simonin, O., Boelle, A. and Lavieville, J., 1996. A unifying modelling approach for the numerical prediction of dilute and dense gas-solid two phase flow, CFB5, *5th Int. Conf. on Circulating Fluidized Beds*, Beijing, China.

[3] Jones, N.E. and Sinclair, J.L., 2003. Effect of Solids Loading in Dilute and Dense Gas-Solid Flow, to be published in *AIChE J.*

[4] Jenkins, J.T. and Louge, M.Y., 1997. On the Flux of Fluctuating Energy in a Collisional Grain Flow at a Flat Frictional Wall, *Phys. Fluids* **9** (10), pp. 2835-2840.

[5] Johnson, P.C. and Jackson, R., 1987. Frictional-Collisional Constitutive Relations for Granular materials, with Application to Plane Shearing. *J. Fluid Mech.*, **176**, 67-93.

[6] Gidaspow, D. (2003), Hydrodynamics of fluidization using kinetic theory: An emerging paradigm?, in Recent Res. Devel. Chemical Eng., Transworld Research Network, Trivandrum, India, Vol 5, 53-81.

[7] Dasgupta, S., Jackson, R. and Sundaresan, S., 1994. Turbulent Gas-Particle Flow in Vertical Risers, *AICHE J.*, **40(2)**, 215-228.

[8] Bolio, E.J. and Sinclair, J.L., 1995. Gas Turbulence Modulation in the Pneumatic Conveying of Massive Particles in Vertical Tubes, Int. J. Multiphase Flow, **21**, 985-1001.

[9] Hrenya, C.M., and Sinclair, J.L, 1997, Effects of particulate-phase turbulence in gas-solids flows, AIChE J., **42**, 853-869.

[10] Kashiwa, B.A. and VanderHeyden W.B., 2000. Toward a general theory for multiphase flow part I: Development and gauging of model equations, LA-13773-MS, Los Alamos National Laboratory.

[11] He, J. and Simonin, O., 1993. Non-Equilibrium Prediction of Particle-Phase Stress Tensor in Vertical Pneumatic Conveying, in ***Gas-Solid Flows***, ASME FED Vol. 166, 253-263.

[12] Simonin, O., Personal communications, 2003.

[13] Peirano, E., V. Delloume, and B. Leckner, "Two- or three-dimensional simulations of turbulent gas-solid flows applied to fluidization," *Chemical Engineering Science*, **56**, (2001) 4787.

[14] Ferschneider, G. and Mege, P., 2002. Dilute Gas-Solid Flow in a Riser, Chemical Engineering Journal, **87**, 41-48.

[15] Zhang, Y. and Reese, J.M., 2001. Particle-Gas Turbulence Interactions in a Kinetic Theory Approach to Granular Flows, International J. of Multiphase Flow, **27**, 1945-1964.

[16] Syamlal, M., Rogers, W.A., and O'Brien, T.J., (1993), MFIX Documentation and Theory Guide, DOE/METC-94/1004, NTIS DE94000087. Electronically available from: http://www.mfix.org/documentation/Theory.pdf

[17] Gidaspow, D., 1994. Multiphase Flow and Fluidization: Continuum and Kinetic Theory Description. Academic Press.

[18] Tartan, M., Gidaspow, D., and Jung, J., Measurement and computation of turbulence in risers using kinetic theory, Proceedings of FEDSM'03: 4th ASME/JSME Joint Fluids Engineering Conference, Honolulu, Hawaii, July 6-11, 2003.

[19] Agrawal, K., Loezos, P.N., Syamlal, M and Sundaresan, S., 2001. The Role of Meso-Scale Structures in Rapid Gas-Solid Flows, J. Fluid. Mech., **445**, 151-185.

[20] Jenkins, J.T., 1992. Boundary Conditions for Rapid Granular Flow: Flat, Frictional Walls, *Transactions of the ASME* **59**, 120-127.

[21] Enwald, H. and Almstedt, A.E., 1999. Fluid Dynamics of a Pressurized Fluidized Bed: Comparison Between Solutions from Two-Fluid Models and Experimental Results, *Chem. Eng. Science*, **54**, 329-342

[22] Sakiz, M. and Simonin, O., 1998. Continuum Modeling and Lagrangian Simulation of the Turbulent Transport of Kinetic Particle Stresses in a Vertical Gas-Solid Channel Flow, Third International Conf. on Multiphase Flow, ICMF'98, 1-9.

[23] Wilcox, D.C., "Turbulence Modeling for CFD", DCW Industries, California, 1994.

[24] Sinclair, J.L. and Jackson, R., 1989. Gas-Particle Flow in a Vertical Pipe with Particle-Particle Interactions, *AICHE J.*, **35(9)**, 1473-1486.

[25] Tanaka, T. and Tsuji, Y., 1991. Numerical Simulation of Gas-Solid Two-Phase in a Vertical Pipe: on the Effect of Inter-Particle Collision, in ***4th Symposium on Gas-Solid Flows***, ASME FED, Vol. 121, 123-128.

[26] Louge, M., Mastorakos, E., and Jenkins, J.T., 1991. The role of particle collisions in pneumatic transport, J. fluid Mech., **231**, 345-359.

[27] De Wilde, J., Marin, G.B., Heynderickx, G., 2003. The Effects of Abrupt T-Outlet in a Riser: 3D Simulation Using the Kinetic Theory of Granular Flow, *Chemical Engineering Science*, **58**, 877-885.

[28] Foerster, S.F., Louge, M.Y., Chang, H. and Allia, K. 1994. Measurements of the Collision Properties of Small Spheres. *Phys. Fluids*, **6** (3), 1108-115.

[29] Simonin, O., 2000. Statistical and continuum modeling of turbulent reactive particulate flow, Part I : Theoretical Derivation of Dispersed Phase Eulerian Modelling from Probability Density Function Kinetic Equation. Von Karman Institute of Fluid Dynamics Lecture Series.

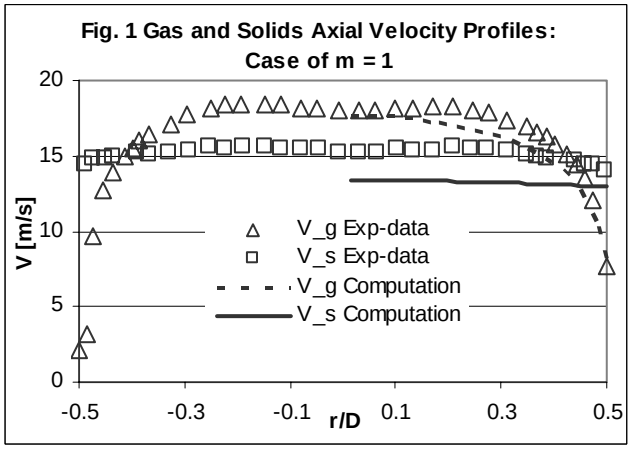
Fig. 1 Gas and Solids Axial Velocity Profiles: Case of m = 1
V [m/s]
r/D
V_g Exp-data
V_s Exp-data
V_g Computation
V_s Computation

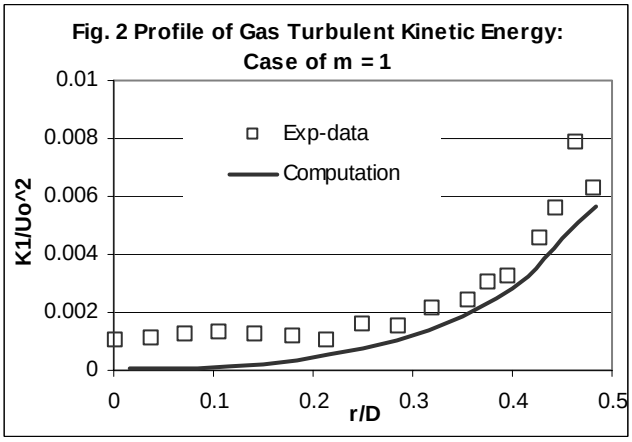
Fig. 2 Profile of Gas Turbulent Kinetic Energy: Case of m = 1
K1/Uo^2
r/D
Exp-data
Computation

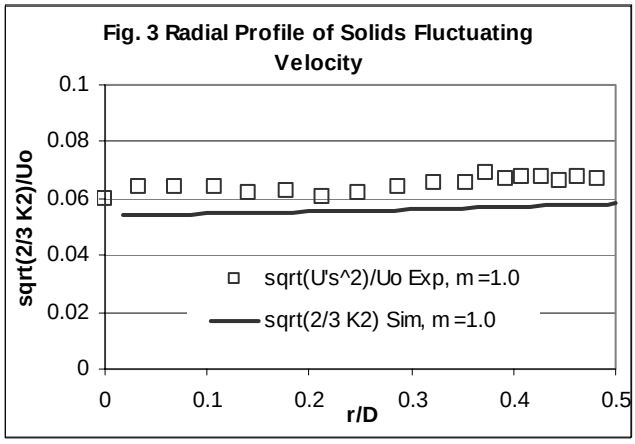
Fig. 3 Radial Profile of Solids Fluctuating Velocity
sqrt(2/3 K2)/Uo
r/D
sqrt(U's^2)/Uo Exp, m =1.0
sqrt(2/3 K2) Sim, m =1.0

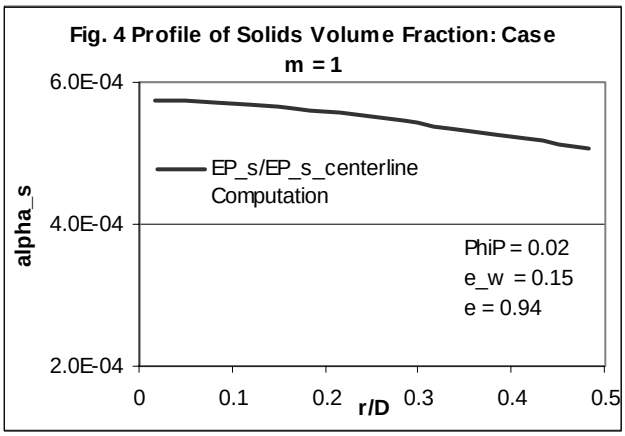
Fig. 4 Profile of Solids Volume Fraction: Case m = 1
alpha_s
r/D
EP_s/EP_s_centerline Computation
PhiP = 0.02
e_w = 0.15
e = 0.94

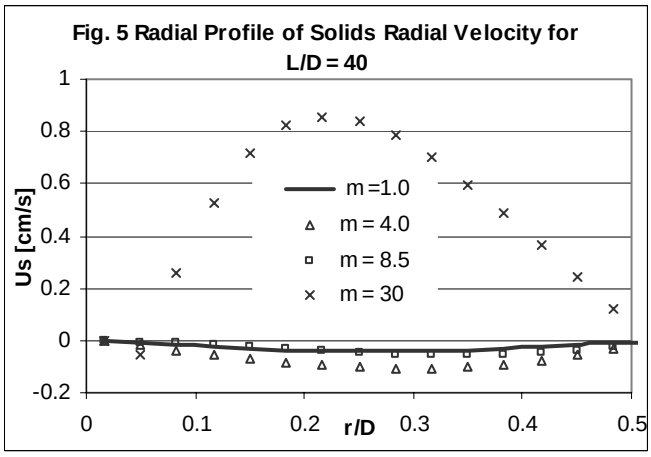
Fig. 5 Radial Profile of Solids Radial Velocity for L/D = 40
Us [cm/s]
r/D
m =1.0
m = 4.0
m = 8.5
m = 30

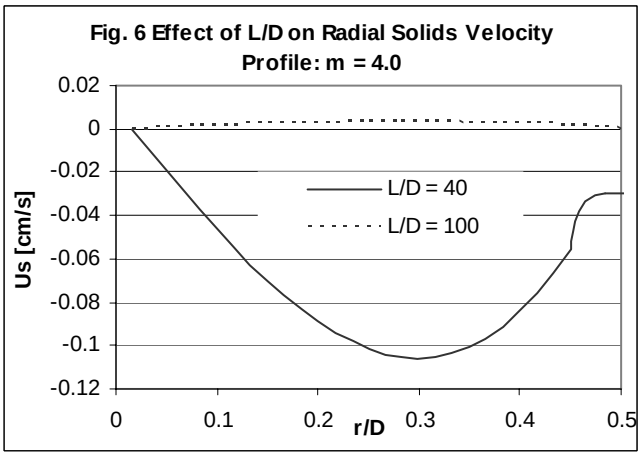
Fig. 6 Effect of L/D on Radial Solids Velocity Profile: m = 4.0
Us [cm/s]
r/D
L/D = 40
L/D = 100

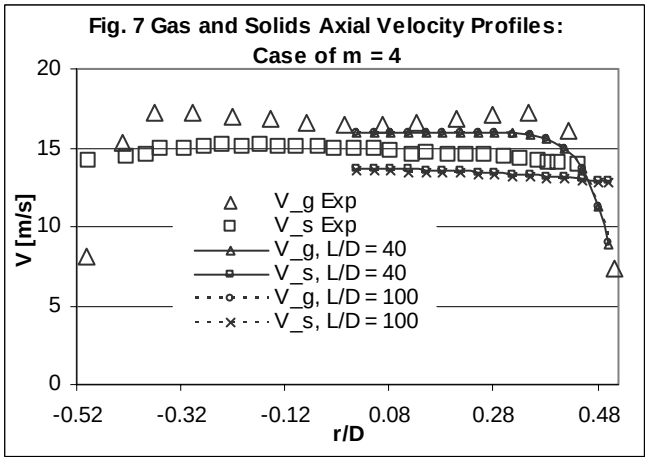
Fig. 7 Gas and Solids Axial Velocity Profiles: Case of m = 4
V [m/s]
r/D
V_g Exp
V_s Exp
V_g, L/D = 40
V_s, L/D = 40
V_g, L/D = 100
V_s, L/D = 100

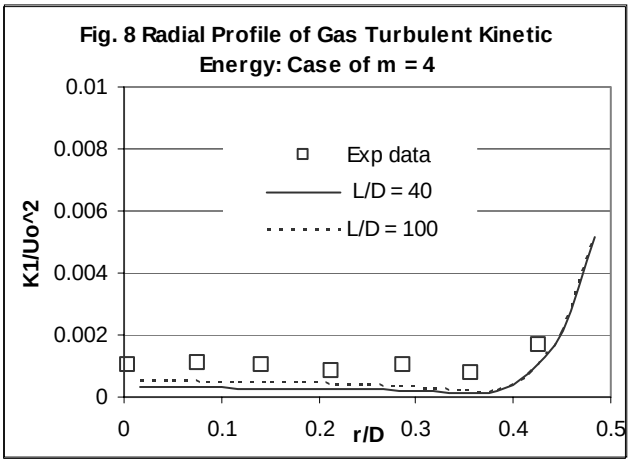
Fig. 8 Radial Profile of Gas Turbulent Kinetic Energy: Case of m = 4
K1/Uo^2
r/D
Exp data
L/D = 40
L/D = 100

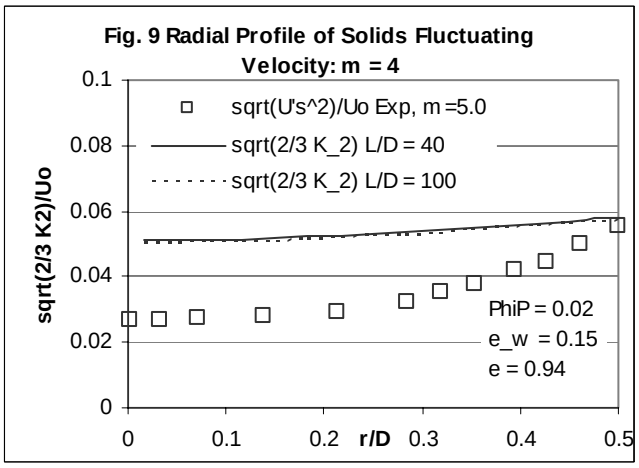
Fig. 9 Radial Profile of Solids Fluctuating Velocity: m = 4
sqrt(2/3 K2)/Uo
r/D
sqrt(U's^2)/Uo Exp, m =5.0
sqrt(2/3 K_2) L/D = 40
sqrt(2/3 K_2) L/D = 100
PhiP = 0.02
e_w = 0.15
e = 0.94

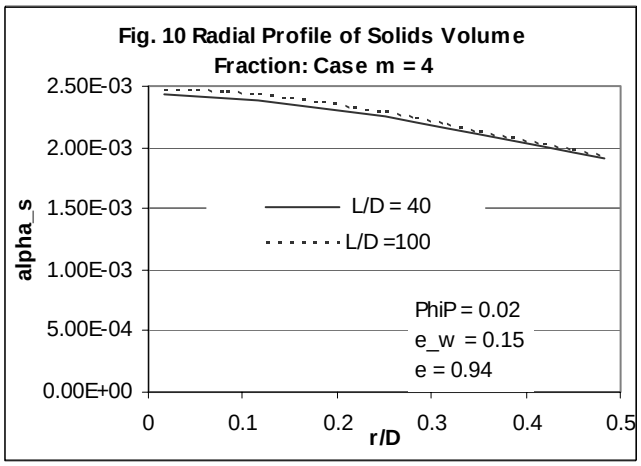
Fig. 10 Radial Profile of Solids Volume Fraction: Case m = 4
alpha_s
r/D
L/D = 40
L/D =100
PhiP = 0.02
e_w = 0.15
e = 0.94

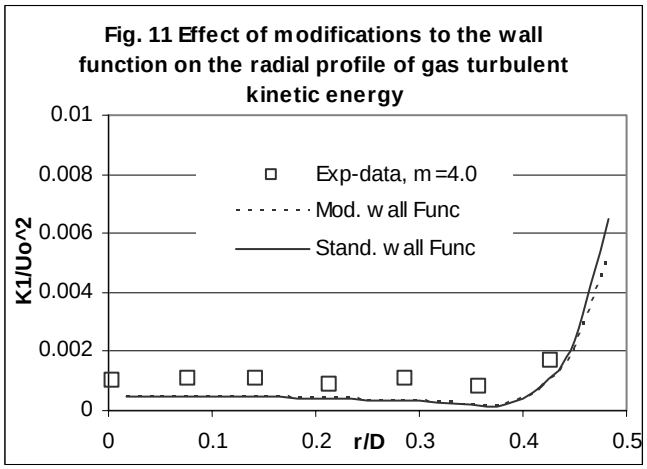
Fig. 11 Effect of modifications to the wall function on the radial profile of gas turbulent kinetic energy
K1/Uo^2
r/D
Exp-data, m =4.0
Mod. wall Func
Stand. wall Func

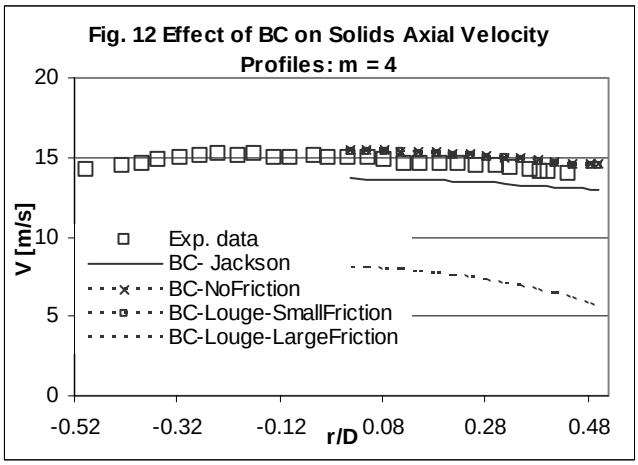
Fig. 12 Effect of BC on Solids Axial Velocity Profiles: m = 4
V [m/s]
r/D
Exp. data
BC- Jackson
BC-NoFriction
BC-Louge-SmallFriction
BC-Louge-LargeFriction

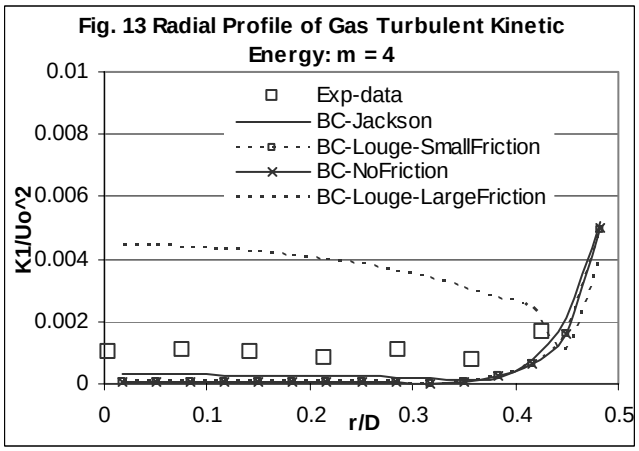
Fig. 13 Radial Profile of Gas Turbulent Kinetic Energy: m = 4
K1/Uo^2
r/D
Exp-data
BC-Jackson
BC-Louge-SmallFriction
BC-NoFriction
BC-Louge-LargeFriction

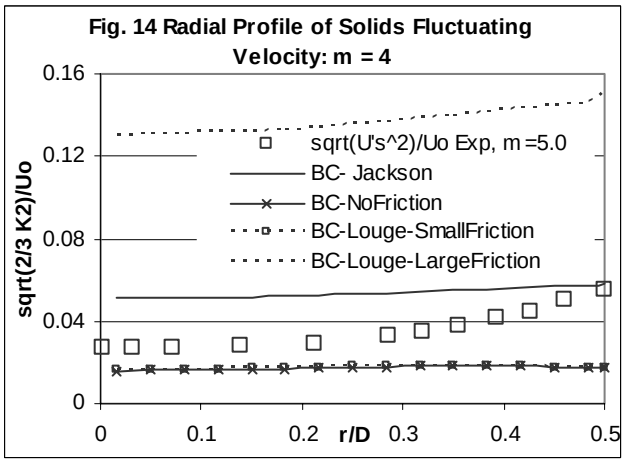
Fig. 14 Radial Profile of Solids Fluctuating Velocity: m = 4
sqrt(2/3 K2)/Uo
r/D
sqrt(U's^2)/Uo Exp, m =5.0
BC- Jackson
BC-NoFriction
BC-Louge-SmallFriction
BC-Louge-LargeFriction

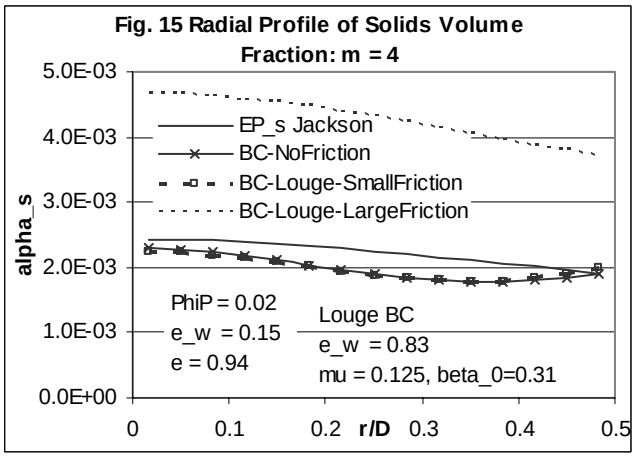
Fig. 15 Radial Profile of Solids Volume Fraction: m = 4
alpha_s
r/D
EP_s Jackson
BC-NoFriction
BC-Louge-SmallFriction
BC-Louge-LargeFriction
PhiP = 0.02
e_w = 0.15
e = 0.94
Louge BC
e_w = 0.83
mu = 0.125, beta_0=0.31

Appendix H

Transport Gasifier Simulation: Testing Fluent's Eulerian-Eulerian Model

Transport Gasifier Simulation

Test Fluent's Eulerian-Eulerian Model

FLUENT

NETL

2D Test Case

Inlet B.C.

Air Inlet: 1 m/s

Cork Inlet: **1** m/s, particle size: 0.0006902 m,
volume fraction: 0.05, density: 190 kg/m^3

Operating Condition:

P: 106200 Pa

T: 298 K

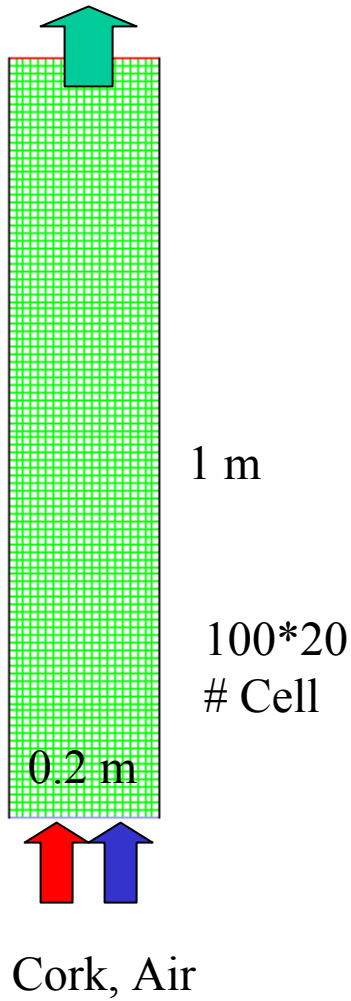

FLUENT

NETL

Simulation Setups

- First order implicit unsteady solver
- First order upwind discretization
- Algebraic granular temperature model
- Syamlal-Obrien drag model
- No virtual mass, no lift, no mass transfer
- Laminar flow
- Time step: 1e-04
- Under-relaxation for volume fraction: (a) 0.2 with residual criteria of 1e-3, (b) 0.7 with residual criteria of 1e-5.

Solid Phase Volume Fraction at Different Time

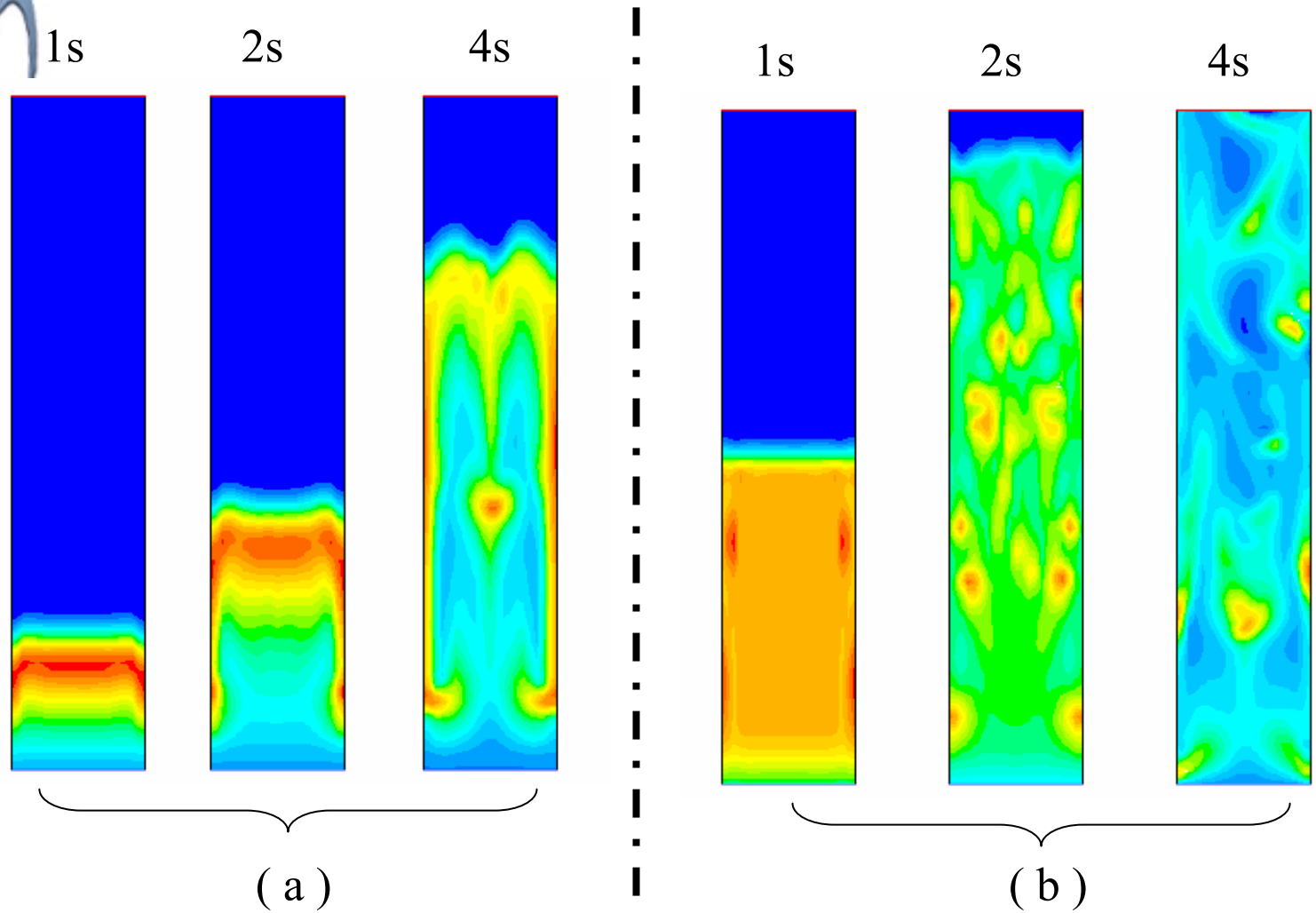

FLUENT

NETL

Comparisons Between Fluent and MFIX (Instantaneous Voidage)

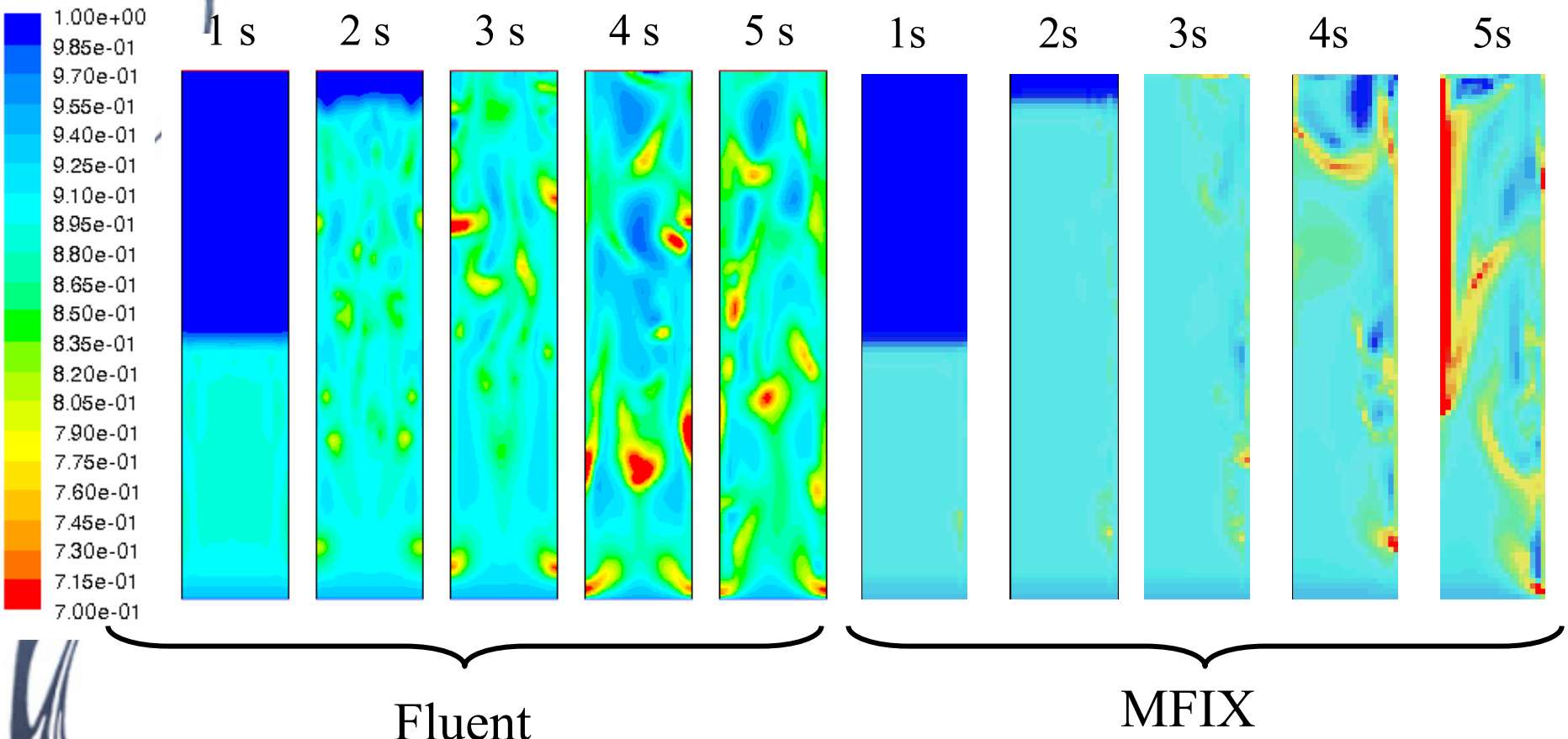

Comparisons Between Fluent and MFIX (Average Y-Velocity (10 seconds))

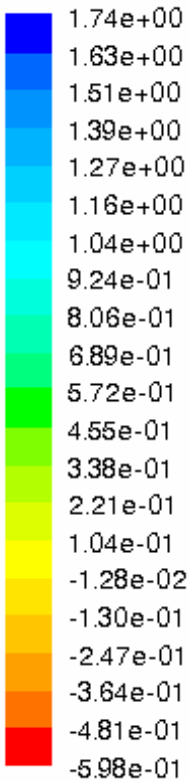

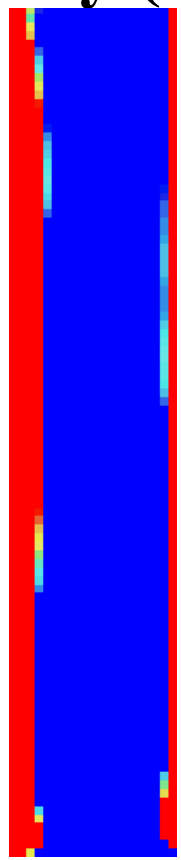

Fluent

MFIX

FLUENT

NETL

Comparisons Between Fluent and MFIX (Average Voidage (10 seconds))

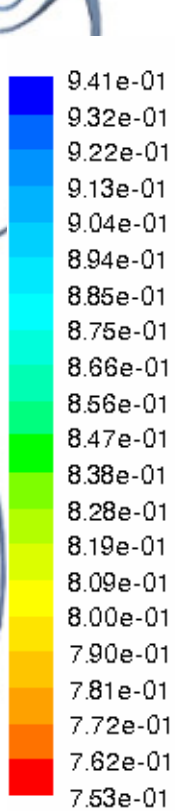

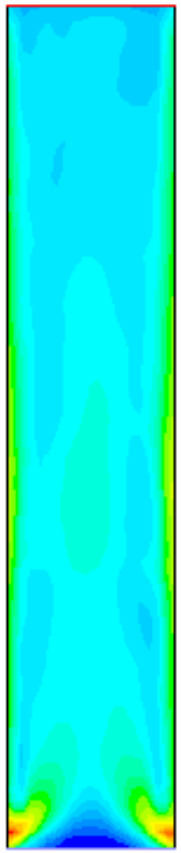

Fluent

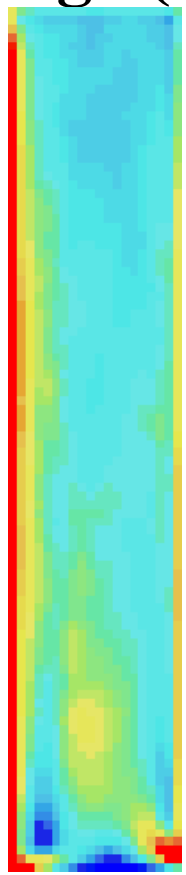

MFIX

Inventory Mass (kg)	4.65 Fluent
	5.32 MFIX

FLUENT

NETL

Geometry of A Riser (3D)

D = 0.305 m

L = 16.92 m

Inlet B.C.

Air Inlet: 5.1 m/s

Cork Inlet: **Cork:** 0.061 m/s, particle size: 0.0006902 m, volume fraction: 0.6, density: 190 kg/m^3

Air: 0.147 m/s.

Operating Condition:

P: 106200 Pa

T: 298 K

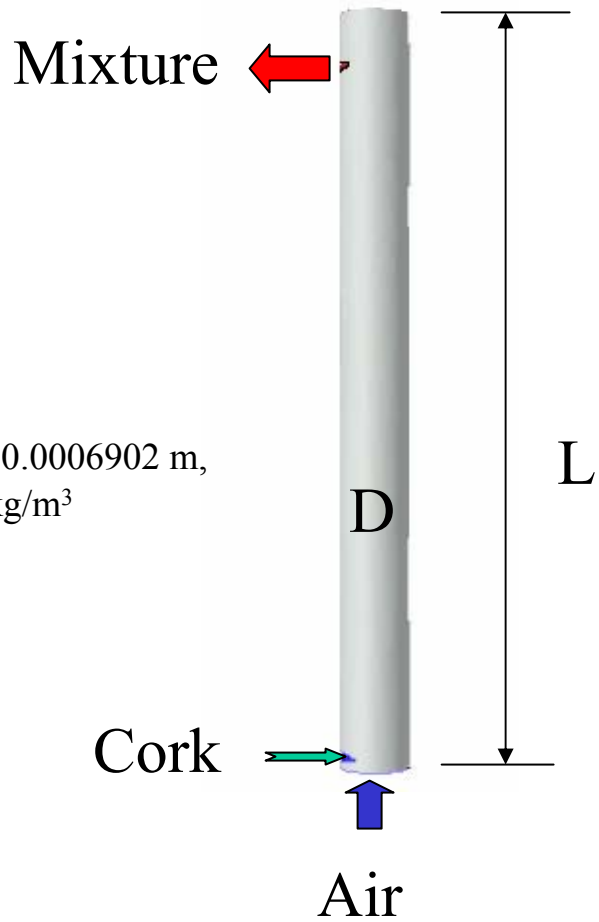

FLUENT

NETL

Simulation Setups

- First order implicit unsteady solver
- First order upwind discretization
- Algebraic granular temperature model
- Syamlal-Obrien drag model
- No virtual mass, no lift, no mass transfer
- Laminar flow
- Time step: 1e-04

Task1 results (Comparisons of the elapsed time and CPU time between Fluent and MFIX)

For 5 s flow time with dt = 1e-4 and residuals criteria of 1e-3:

T = 5s	Elapsed Time (days)	CPU time (days)	note
Fluent	4.986	3.095	1-2 iter./time-step
MFIX		7.46	8-12 iter./time-step

For 10 s flow time with dt = 0.1 and residuals criteria of 1e-3:

T = 10 s	Elapsed Time (hours)	CPU time (hours)	note
Fluent	6	5.7	30-50 iter./time-step
MFIX			

FLUENT

NETL

Task1 results (instantaneous voidage)

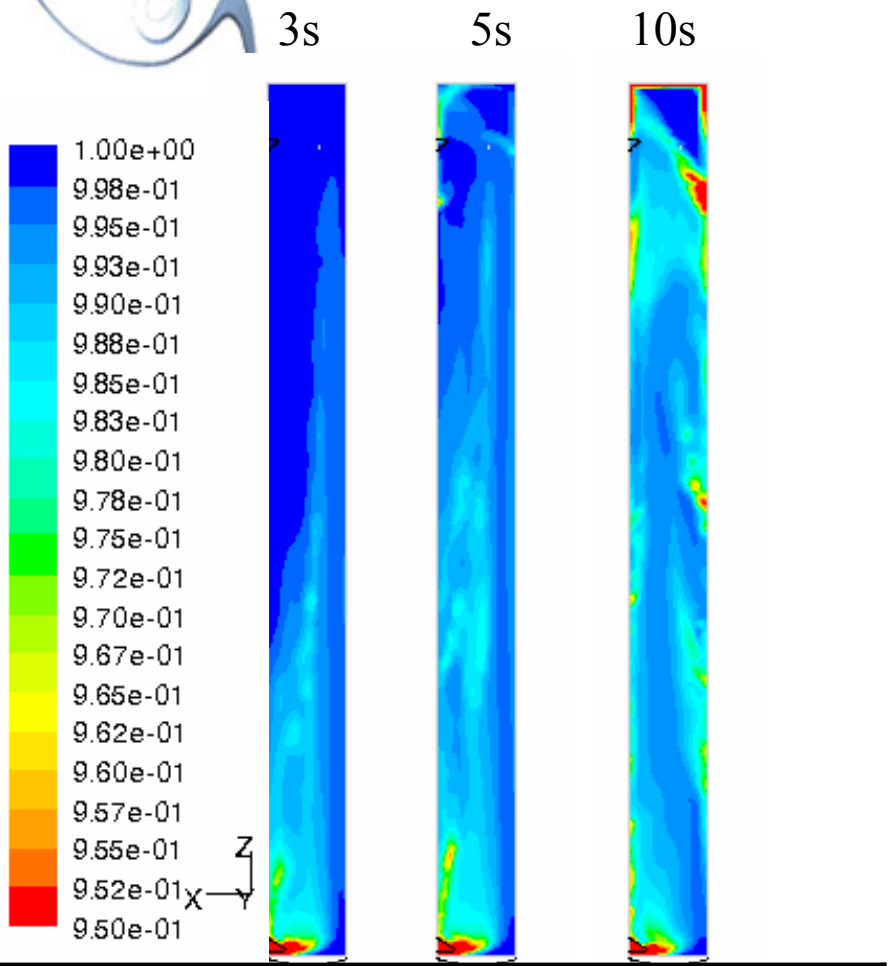

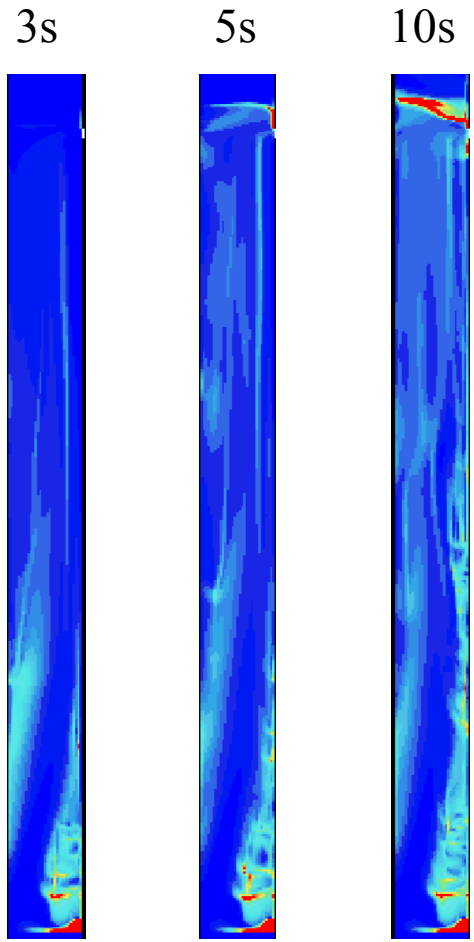

Inventory Mass (kg)	Fluent	1.18	1.81	3.04
	MFIX	1.07	1.41	1.82

MFIX

FLUENT

NETL

Task 2 results (instantaneous voidage)

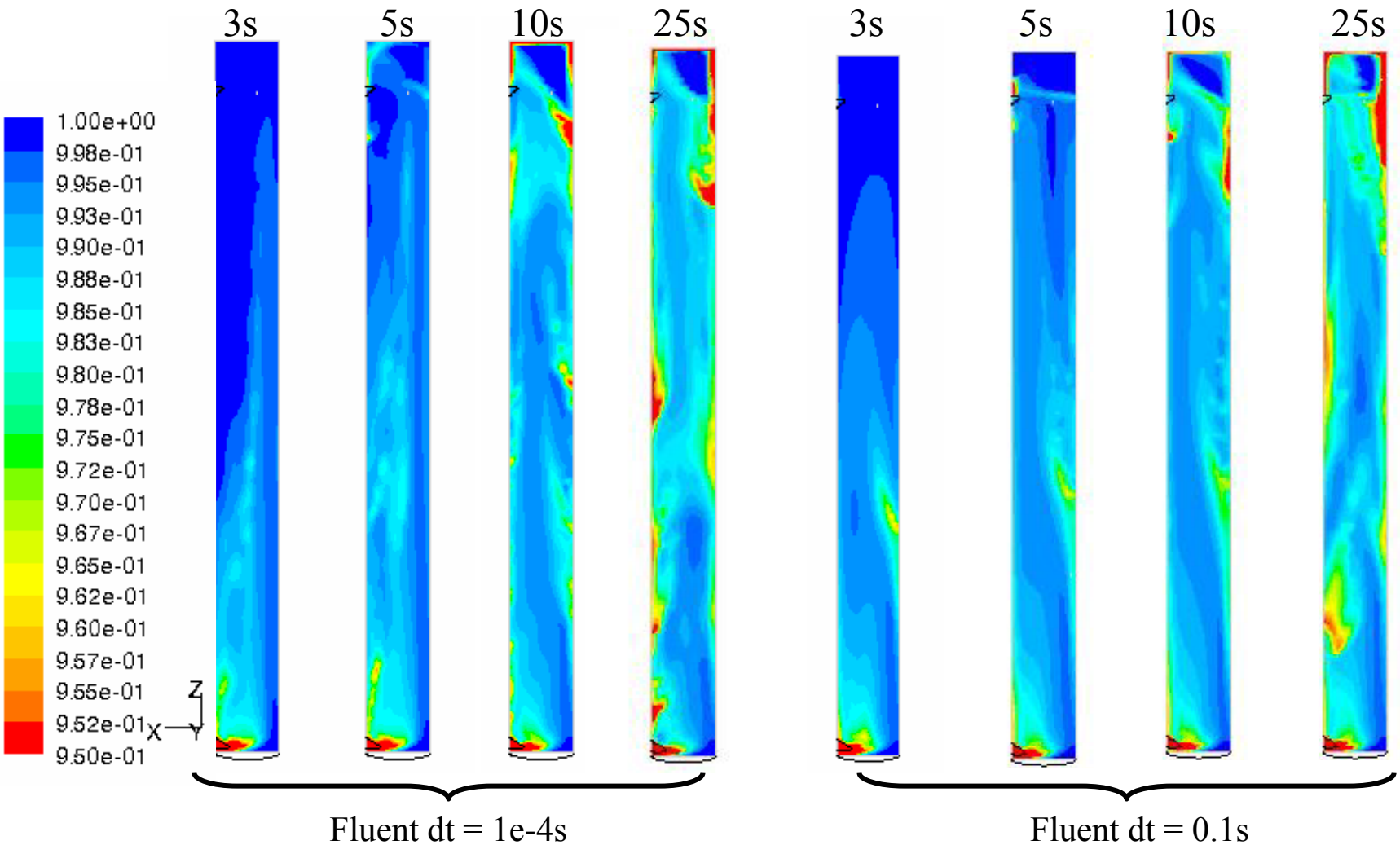

Inventory Mass (kg)	**1.18**	**1.81**	**3.04**	**4.74**

1.18	**1.75**	**2.61**	**4.73**

Task 3 results (Average voidage of 15 s)
Comparisons between Fluent and MFIX

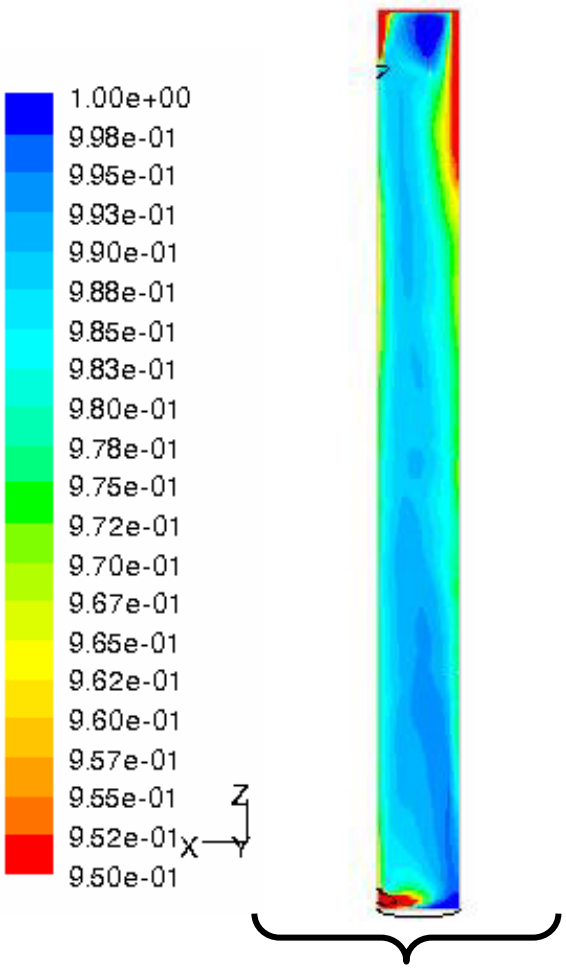

Fluent

MFIX

Task 3 results (Average solid phase z-velocity of 15 s) Comparisons between Fluent and MFIX

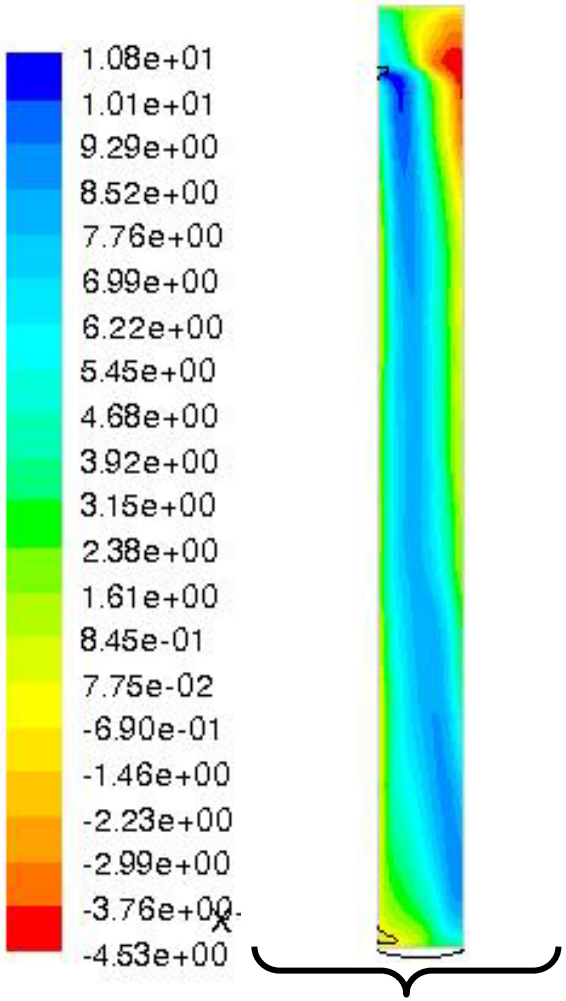

Fluent

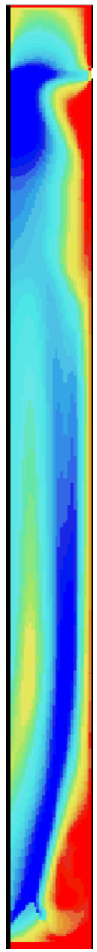

MFIX

Task 3 results (Instantaneous voidage at 25 s)
Comparisons between Fluent and MFIX

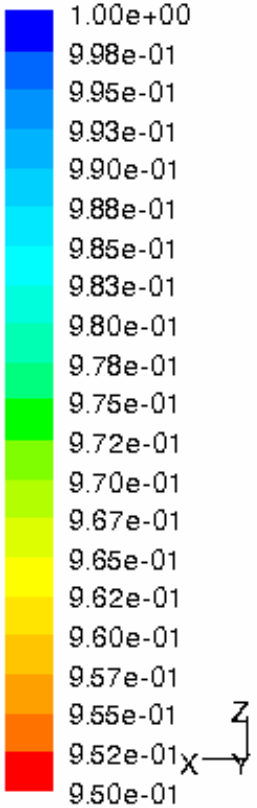

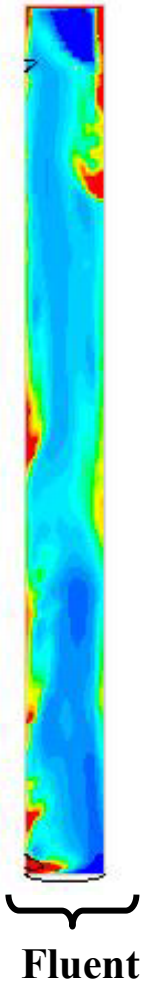

Fluent

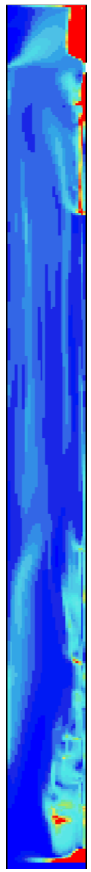

MFIX

Inventory Mass (kg)	**Fluent**	**4.74**
	MFIX	**3.10**

Task 3 results (Average voidage and vertical velocityat a center line) Comparisons between Fluent and MFIX

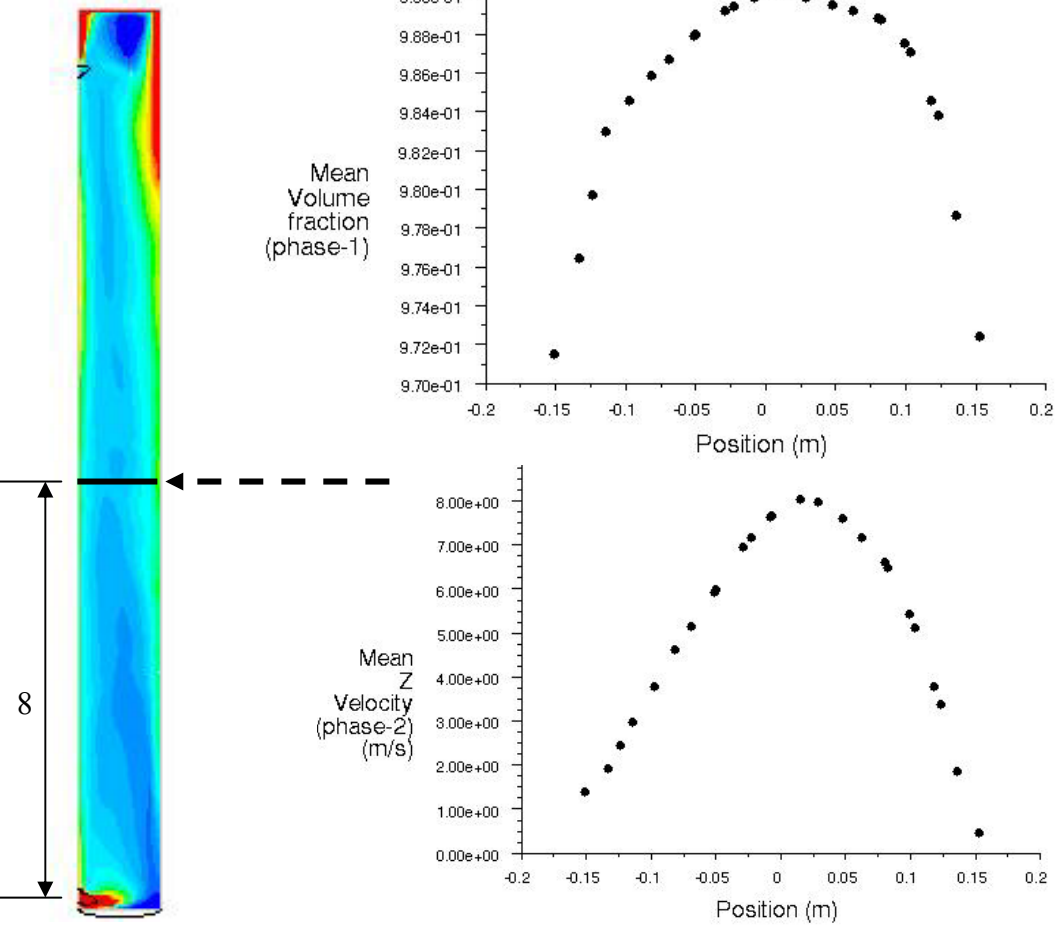

Fluent

MFIX

Task 3 results (Average voidage at a vertival line) Comparisons between Fluent and MFIX

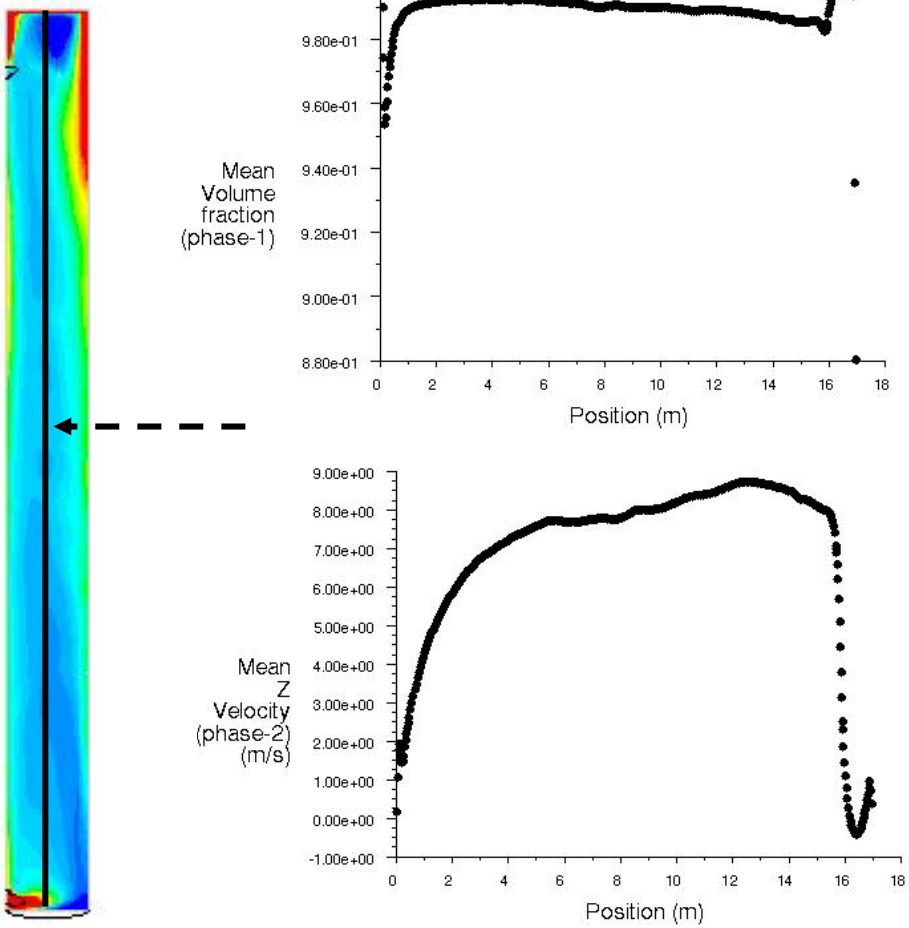

Fluent

MFIX

Task 4 results (Parallel performace) Comparisons between Fluent and MFIX

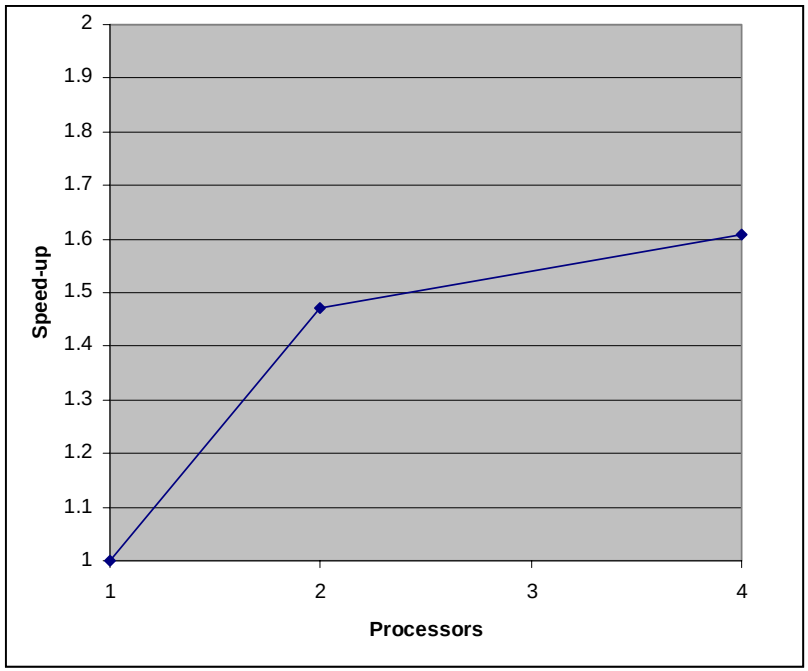

Fluent

MFIX

Appendix I

Transport Gasifier Simulation: Testing Fluent's Eulerian-Eulerian Model

Transport Gasifier Simulation

Test Fluent's Eulerian-Eulerian Model

Shaoping Shi

Jan. 04, 2005

FLUENT

NETL

Geometry of A Riser (B22)

D = 0.305 m

L = 16.92 m

Inlet B.C.

Air Inlet: Air

Cork Inlet: Air+cork. Particle size: 0.0006902 m, volume fraction: 0.4, density: 190 kg/m^3

Mesh #: 550 K

Operating Condition:

P: 106200 Pa

T: 298 K

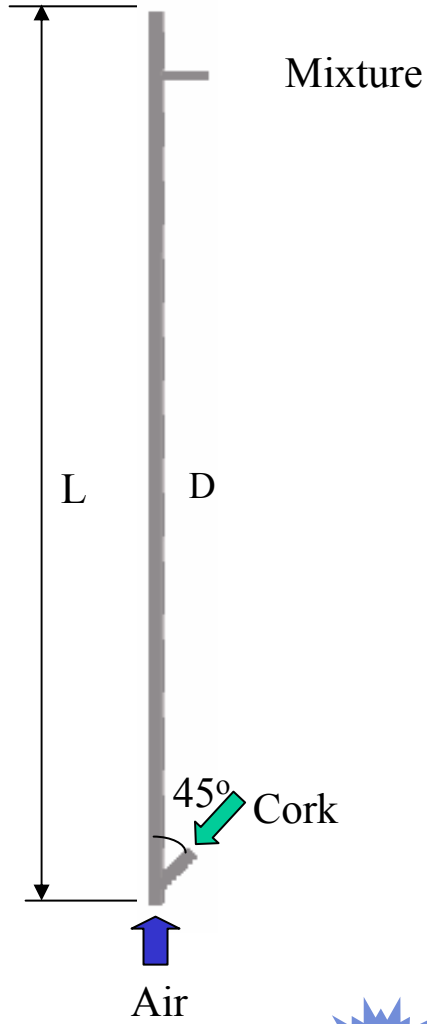

FLUENT

NETL

Simulation Cases

	Vg at Air inlet (m/s)	Vel. of Cork (m/s) vf = 0.4	Vg at the Cork inlet (m/s)
RP07	3.82524	0.284869327	0.725044214
RP11	4.6482	0.196687683	0.487078326
RP16	5.1054	0.103982222	0.458563895
RP13	4.559808	0.064284091	0.442232903

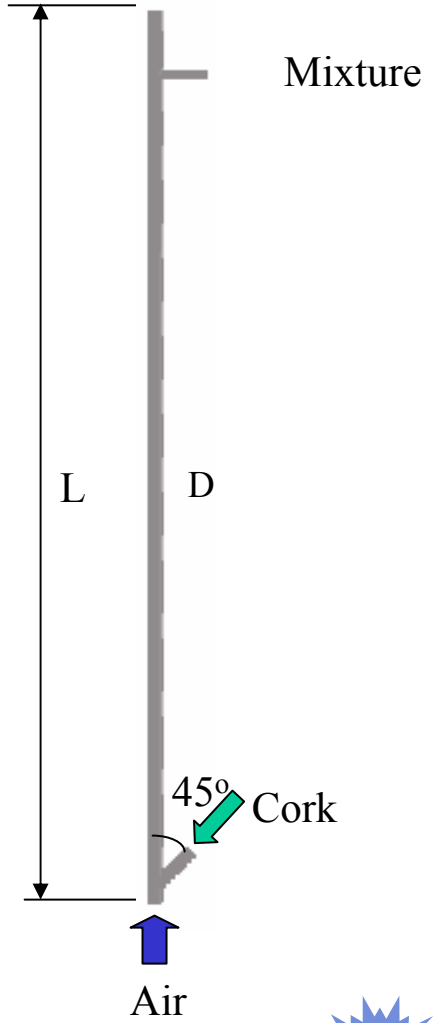

FLUENT

NETL

Simulation Setups

- First order implicit unsteady solver
- First order upwind discretization → QUICK
- PDE granular temperature model
- Syamlal-O'Brien drag model → Gidaspow
- Johnson & Jackson wall boundary condition for granular temperature.
- No virtual mass, no lift, no mass transfer
- Laminar flow
- Time step: depends on how dense the solid phase is

Simulation Setups

- Johnson & Jackson wall boundary condition for granular temperature.

$$\nu_s^{\,t}\left.\frac{\partial V_s}{\partial x}\right|_w + \frac{\phi\pi V_s g_0\sqrt{2/3\Theta}}{2\sqrt{3}\alpha_2^{\max}} = 0$$

Specularity coefficient

$$K_s^t\left.\frac{\partial \Theta}{\partial x}\right|_w - \frac{\phi\pi V_s^{\,2} g_0\sqrt{2/3\Theta}}{2\sqrt{3}\alpha_2^{\max}} + \frac{\sqrt{3}\pi g_0(1-e_w^2)(2/3\Theta)^{3/2}}{4\alpha_2^{\max}} = 0$$

Restitution coefficient

•Specularity coef. 0.01 to 0, free slip wall and no production for particle kinetic energy (granular temperature)

•Restitution coef. 0.7 to 0.15, high dissipation of the particle kinetic energy at the wall.

Simulation Setups

- Granular Temperature

Energy exchange between different phase

$$\frac{3}{2}\left[\frac{\partial}{\partial t}(\rho_s \alpha_s \Theta_s) + \nabla.(\rho_s \alpha_s \vec{v}_s \Theta_s)\right] = (-p_s \bar{\bar{I}} + \bar{\bar{\tau}}_s) : \nabla \vec{v}_s + \nabla.(k_{\Theta s} \nabla \Theta) - \gamma_{\Theta s} + \phi_{ls}$$

Convection — Production — diffusion — Collision dissipation

1. If restitution coefficient is unity, there will be no collision dissipation.

$$\gamma_{\Theta s} = \frac{12(1-e_{ss}^2) g_{0,ss}}{d_s \sqrt{\pi}} \rho_s \alpha_s^2 \Theta_s^{3/2}$$

2. Using text fluent command, we can force the energy exchange be zero. Thus granular temperature will be higher away the wall and the particles will be pushed to the wall

$$\phi_{ls} = -3 k_{sl} \Theta_s$$

FLUENT

NETL

RP11 Validation

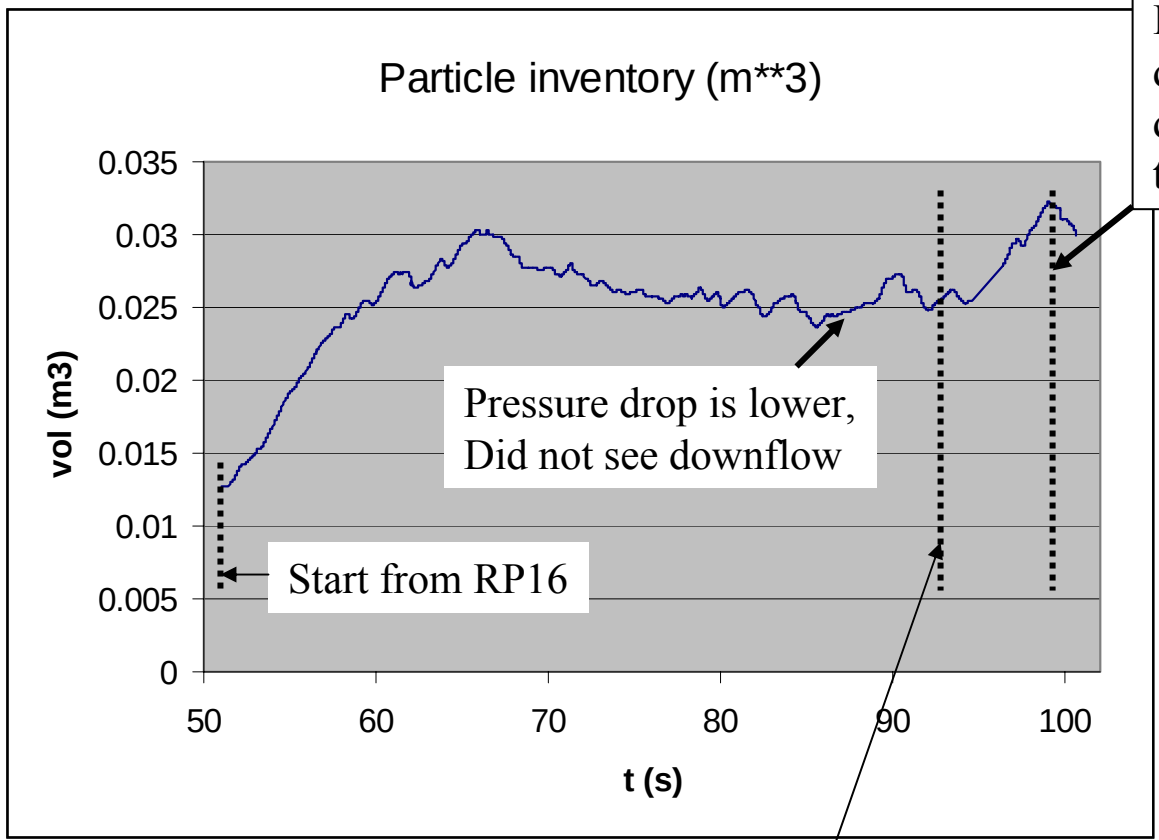

FLUENT

NETL

Solid Volume Fraction

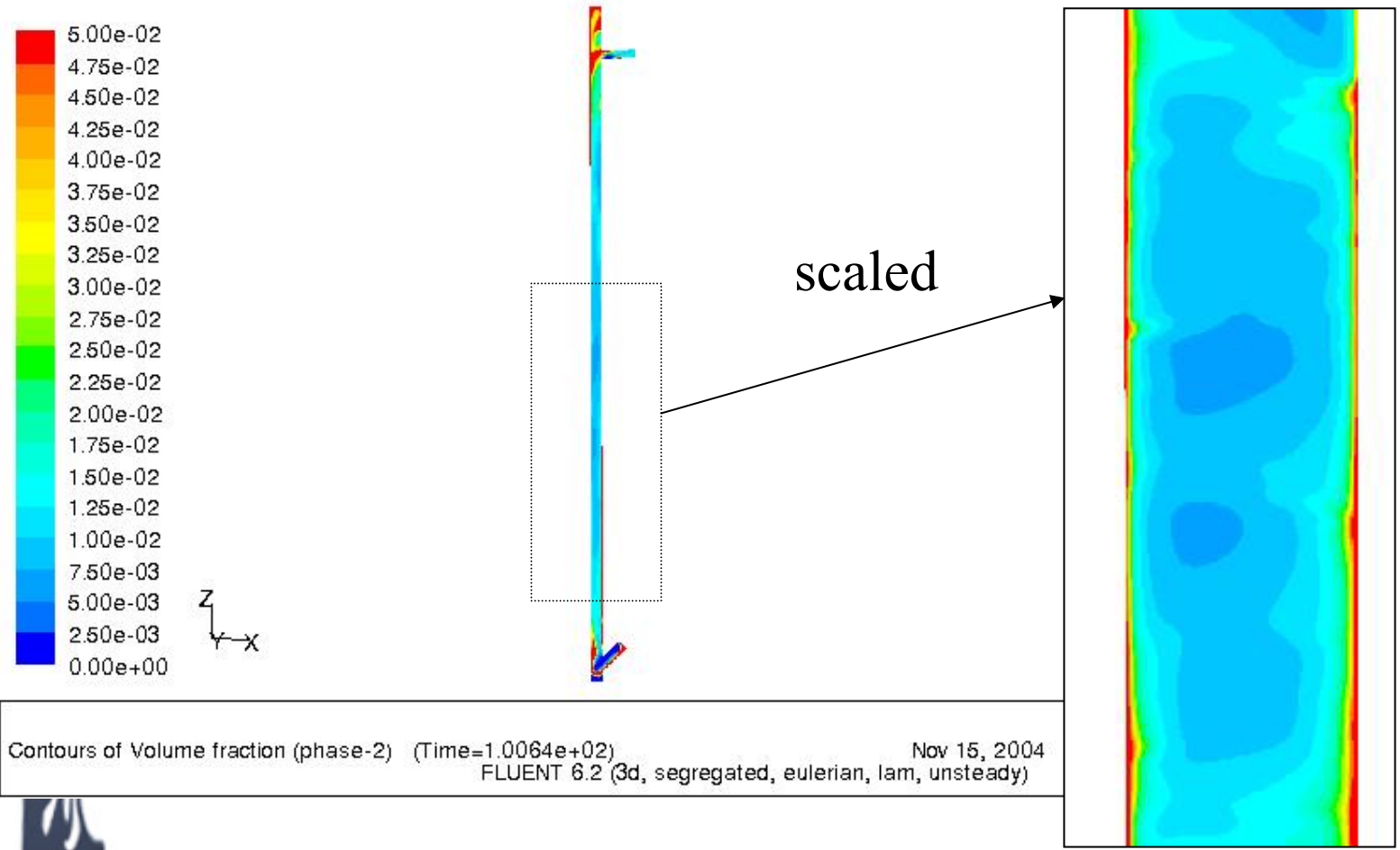

RP11 w PDE

FLUENT

NETL

Pressure Drop

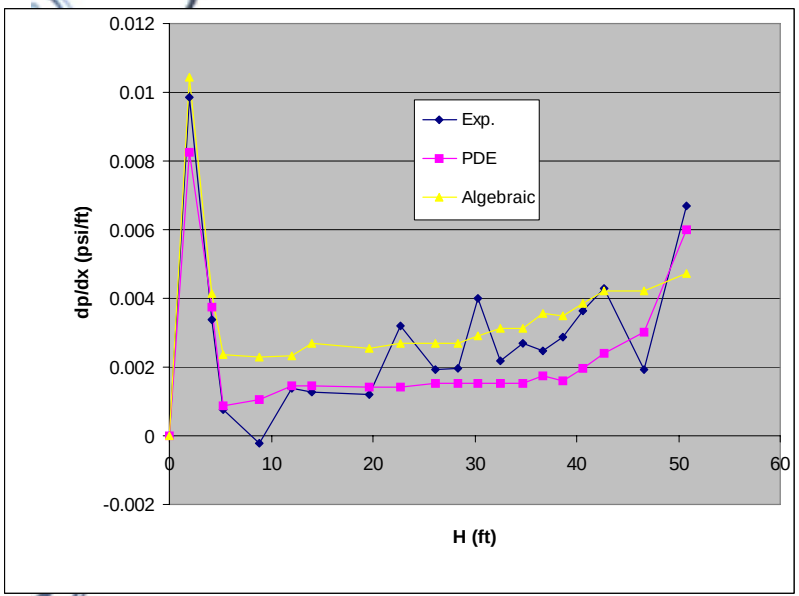

RP11

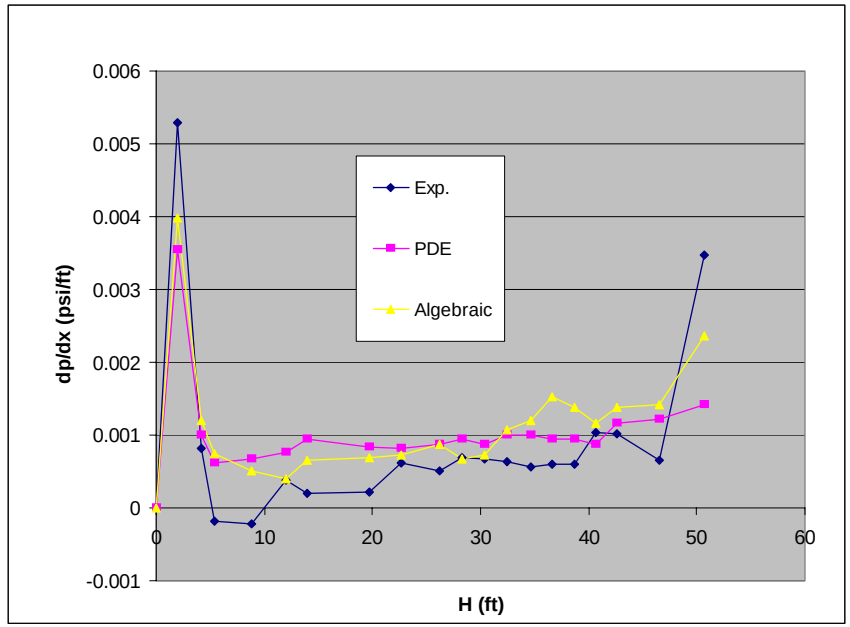

RP13

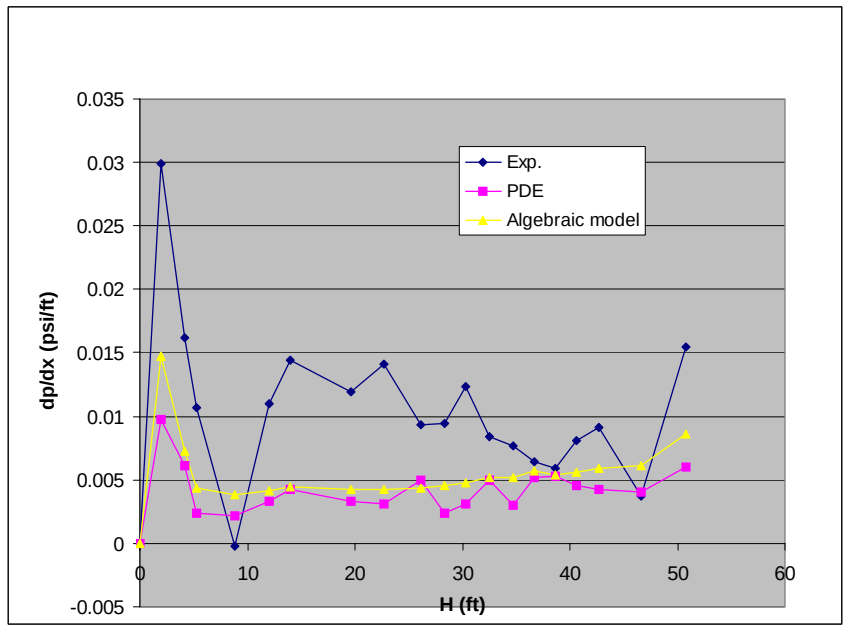

RP07

FLUENT

NETL

Solid Mass Flux with Algebraic model

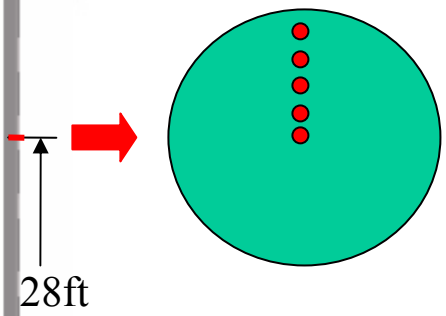

RP11

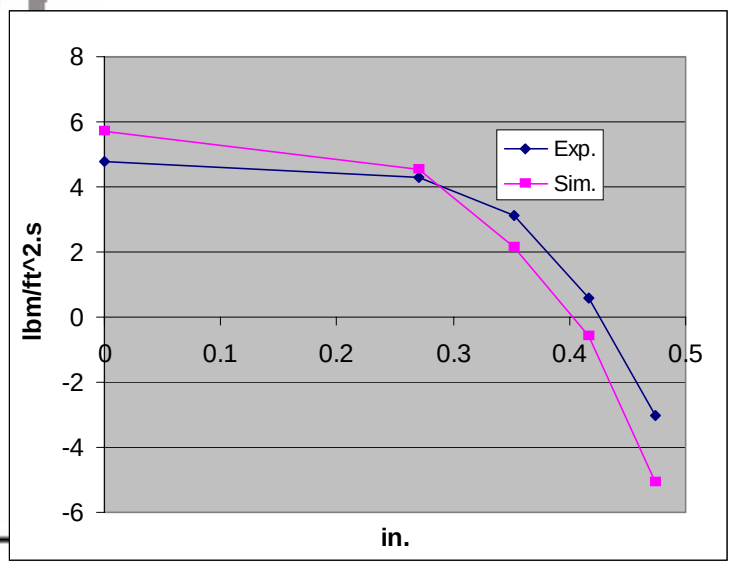

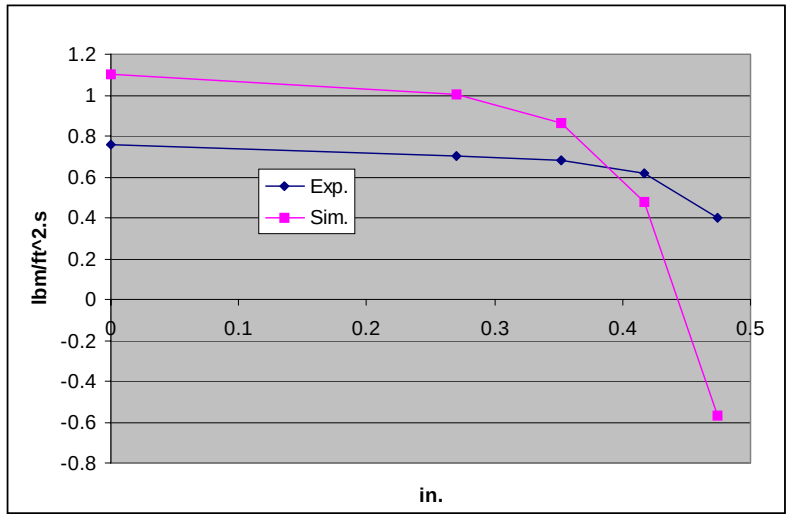

RP13

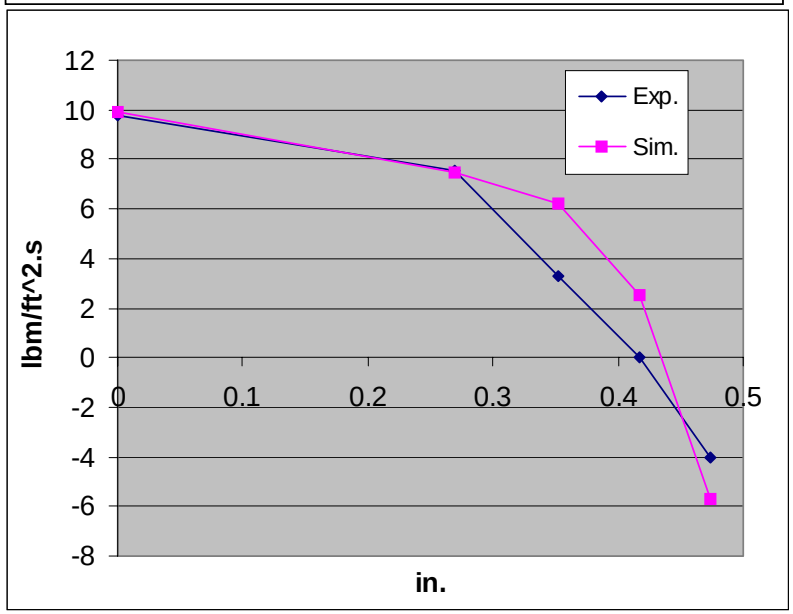

RP07

Solid Mass Flux with Algebraic model

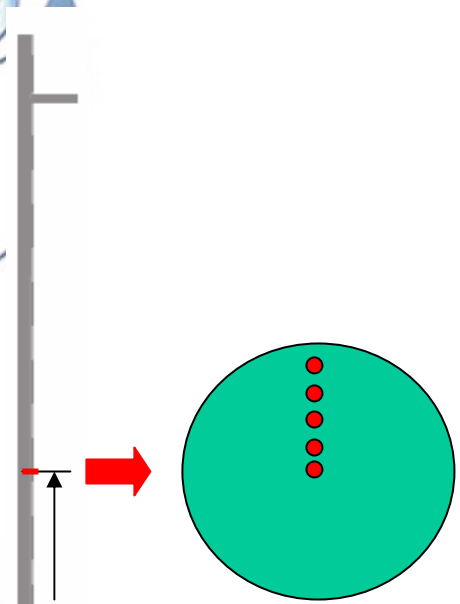

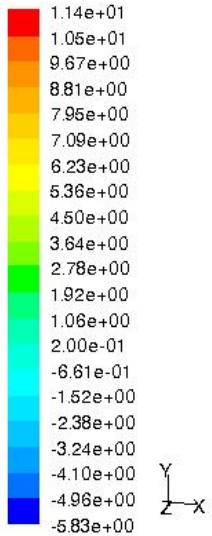

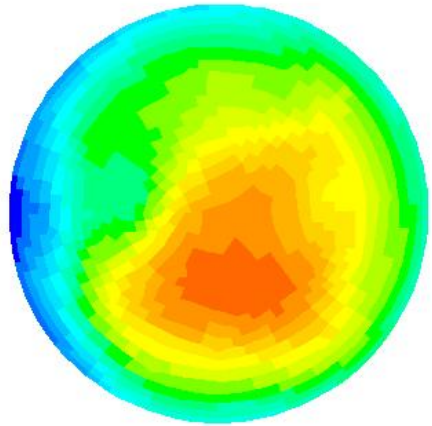

RP11

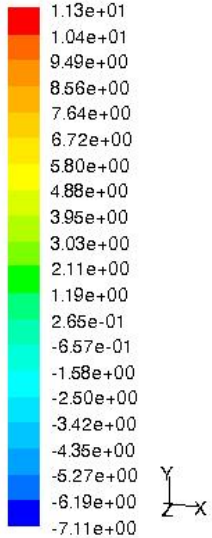

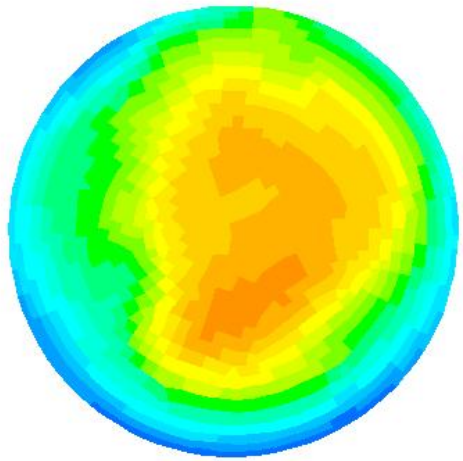

RP07

Contours of Mean Z Velocity (phase-2) (m/s) (Time=9.8762e+01) Dec 19, 2004
FLUENT 6.2 (3d, segregated, eulerian, lam, unsteady)

FLUENT

NETL

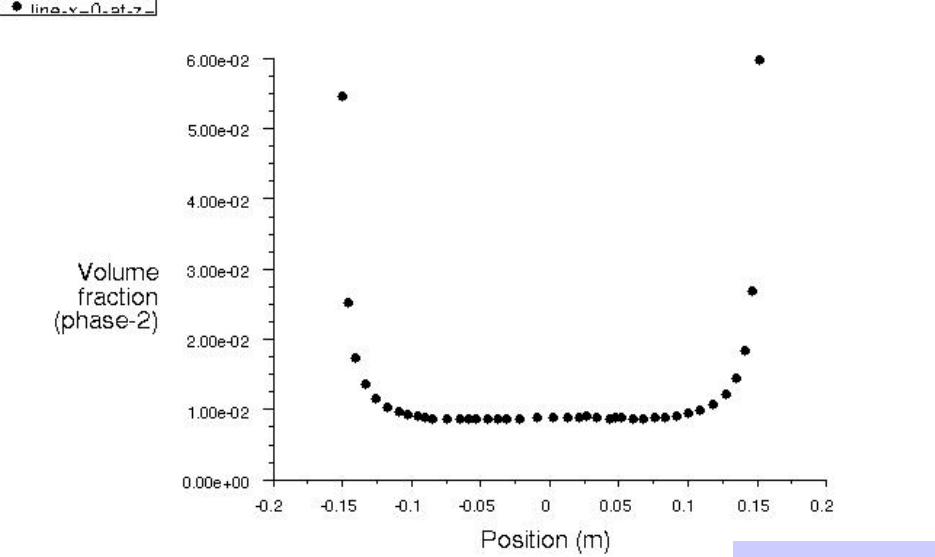

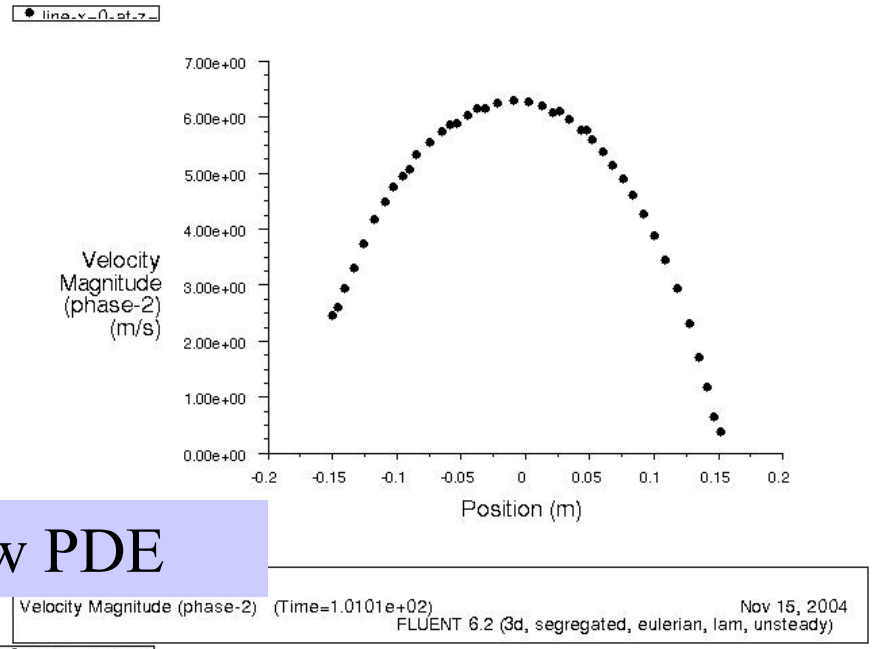

RP11 w PDE

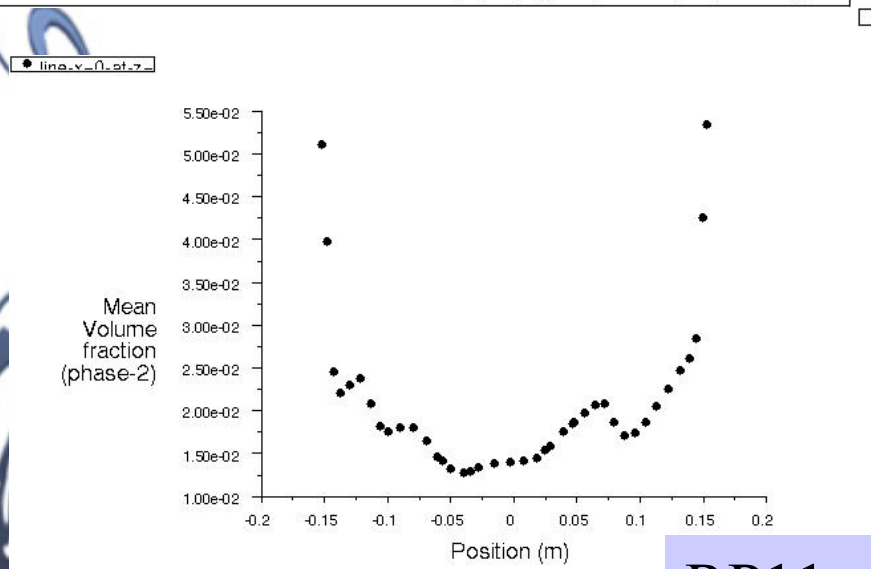

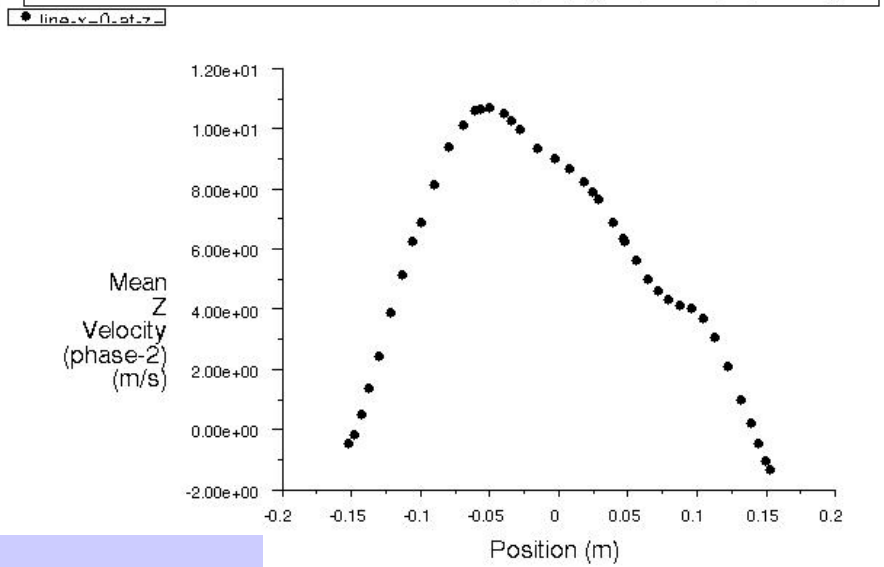

RP11 w Algebraic

RP11

Algebraic

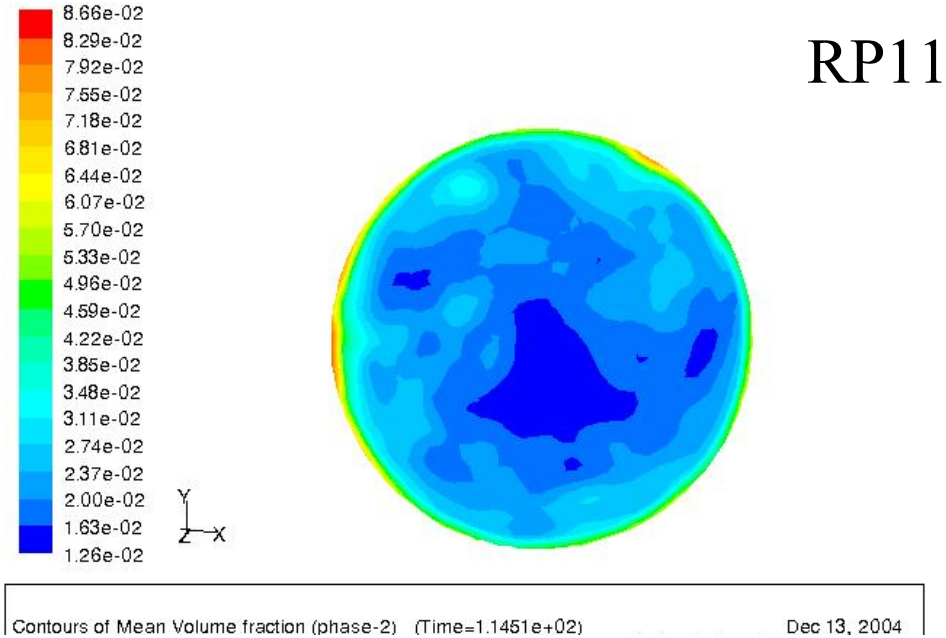

28ft

PDE

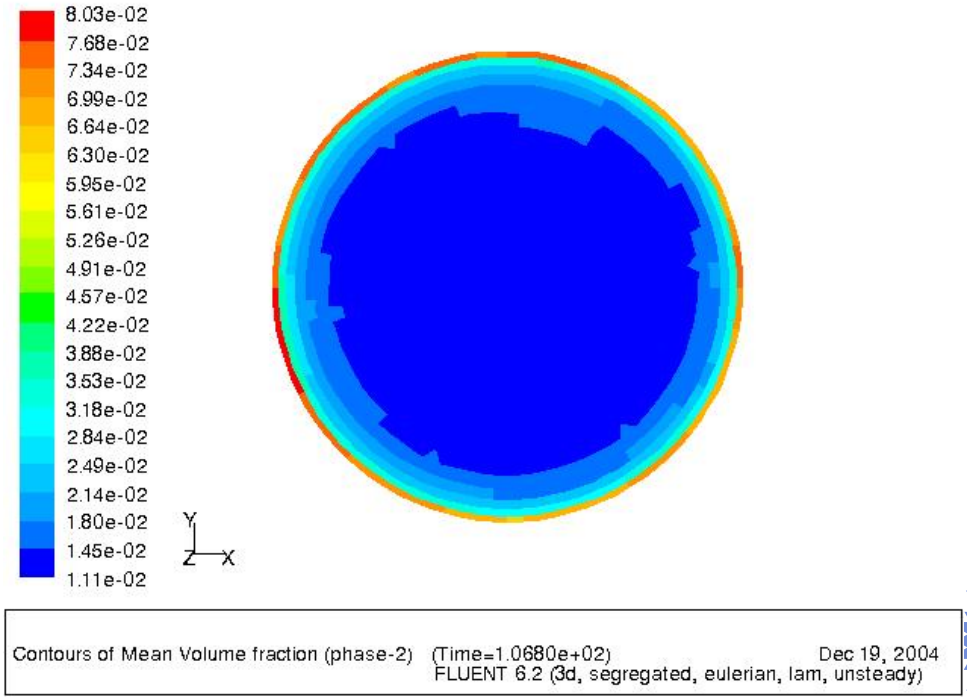

FLUENT

NETL

Appendix J

Extension of Koch and Hill Drag Correlation Over All Ranges of Reynolds Number and Solids Volume Fraction

Extension of Koch and Hill drag correlation over all ranges of Reynolds number and solids volume fraction

Sofiane Benyahia
Fluent Incorporated
3647 Collins Ferry Road, Suite A
Morgantown, WV 26505
Ph. (304) 285-1373; Fax (304) 598-7185; E-mail: sof@fluent.com

Madhava Syamlal and Thomas J. O'Brien
US Department of Energy
MS-N04, 3610, Collins Ferry Road
Morgantown, WV 26505
Ph. (304) 285-4571, E-mail: tobrie@netl.doe.gov

Abstract

Koch and Hill proposed a set of drag correlations, based on data from Lattice-Boltzmann simulations. These correlations, while very accurate within the range of void fractions and Reynolds numbers used in the Lattice-Boltzmann simulations, do not cover the full range of void fractions and Reynolds numbers encountered in fluidized bed simulations. In this paper a drag correlation applicable to the full range of void fractions and Reynolds numbers is developed by blending the Koch and Hill drag correlation with known limiting forms of the gas-solids drag function such that the blended function is continuous with respect to Reynolds number and void fraction. This study also corrects a misinterpretation of the Koch and Hill drag correlation that was published in the literature, which makes the drag function discontinuous with respect to the Reynolds number.
Two examples of gas/solids flows in a bubbling fluidized bed and a one-dimensional channel flow are used to illustrate differences between the proposed extension of Koch and Hill drag correlation and another form published in the literature.

Introduction

Due to the recent advances in computational resources and software development, it has become possible to perform detailed calculations of heavily loaded, gas-particle flows based on two-fluids or DEM-fluid methods [1, 2]. Both of these approaches are based on fundamental physical laws, which imply that they can be used as predictive methods. However, they require the knowledge of several constitutive closure laws the most important of which describes the momentum exchange between the fluid and the particles. Such a correlation is dependent on many parameters of the system, the foremost of which are the Reynolds number of the flow, the fluid/particle density ratio, and the solids loading. Other features, such as particle shape, roughness, and the packing

"fabric" may also be important but are seldom considered. Until recently, this closure law could only be determined by the analysis of experimental data, which leads to empirical correlations with limited theoretical underpinnings [3 and references therein]. Because of the empirical nature of this principal closure law, the two-fluids or DEM-fluid methods can not truly be called *ab initio* methods. Ironically, closure formulations for secondary constitutive law, the granular stress, are much more firmly based in theory, thanks to the kinetic theory of granular materials [4 and references therein].

However, recent articles [5-9] have used the lattice-Boltzmann method (LBM) to calculate the drag exerted by a fluid flow on a collection of randomly dispersed, fixed particles. Such calculations, repeated for different values of the Reynolds number and the volume fraction of the particles, can be used to derive a drag law. Thus, this essential constitutive law of two-fluids and discrete element models of multiphase flow can now be determined from first principles. The most extensive numerical-experimental (a terminology justified by the fact that LBM uses first principles calculations) data reported to date are those of Koch and Hill [5, 6]. They performed calculations over a range of Reynolds numbers and solids volume fraction, ϕ, and reported a functional representation which was precisely fit to this data. By doing so Koch and Hill gives different formulas applicable to different ranges of Re numbers and solids volume fractions; it was not their objective to develop a composite formula applicable to the entire range of Re and ϕ or one which goes to known limiting forms of drag that lay outside the range of conditions used in their study . In contrast, this study offers a drag law that spans a full range of the (Re, ϕ)-space. It is constructed from Koch and Hill formulas, with reasonable continuations in regions of (Re, ϕ)-space for which data are not available. Also care is taken to make formula go to known limiting value of single sphere drag.

The Koch and Hill formulas were used as constitutive relations for gas-solids drag in detailed multiphase flow models of fluidization [10, 11]. Since multiphase flow models need constitutive relations that smoothly, and without gaps, cover a wide range of Re and phi the formulas were blended. While blending two Koch and Hill formulas, problems were noticed in the functional behavior of the drag outside the range of its applicability [10]. There are other issues as well, which will be discussed later in this paper. The purpose of this study is to analyze the results reported by Koch and Hill [5, 6] and extend them to the full range of Reynolds numbers and solids volume fraction.

Drag Coefficient

The friction coefficient, β, is defined [7, eq. 7+1] as:

$$\beta = 18\mu_g (1-\phi)^2 \phi \frac{F}{d^2} \tag{1}$$

Here μ_g is the gas viscosity, ϕ is the solids volume fraction, d is the particle diameter and F is the dimensionless drag force. This equation contains an explicit factor

of $(1-\phi)^2$, consistent with Koch and Hill [5, 6], instead of the factor $(1-\phi)$ adopted by van der Hoef, Beestra, and Kuipers [7]. Another way of expressing the friction coefficient β is in terms of the drag coefficient, C_D as: $\beta = \frac{3}{4}\frac{C_D(1-\phi)\rho_g\phi|u_g - u_s|}{d}$, thus C_D can be expressed as:

$$C_D = 12\frac{(1-\phi)^2}{\mathrm{Re}}F \tag{2}$$

where: $\mathrm{Re} = \frac{\rho_g(1-\phi)|u_g - u_s|d}{2\mu_g}$. Note that following Koch and Hill [5, 6] Re is based on particle radius, rather than particle diameter and, hence, the coefficient in equation (2) is 12 rather than the typical 24.

Low Reynolds number limit

At low Re numbers, the general form for the dimensionless drag force, F, is the following:

$$F = F_0 + F_1 R_e^2 \tag{3}$$

The Stokes contribution to the drag force is best fitted with the following expression:

$$F_0 = \begin{cases} (1-w)\left[\frac{1+3\sqrt{\phi/2}+(135/64)\phi\ln(\phi)+17.14\phi}{1+0.681\phi-8.48\phi^2+8.16\phi^3}\right] + w\left[10\frac{\phi}{(1-\phi)^3}\right] & 0.01 < \phi < 0.4 \\ 10\frac{\phi}{(1-\phi)^3} & \phi \geq 0.4 \end{cases} \tag{4}$$

where: $w = e^{(-10(0.4-\phi)/\phi)}$

This formula has been synthesized from two sources. The Koch and Hill data [5, Table 1] are best represented by the correlation of Koch and Sangani [12, equation 26] at low solids volume fractions, ϕ, and the Carmen relation at high values of ϕ. The Koch and Sangani [12] formulation is used here because an expression proposed by Koch and Hill [5, equation 10] does not represent their data well at intermediate volume fractions ($0.1 \leq \phi < 0.4$). At high solids volume fraction, in equation (4), the Carmen relation, which is also used by Koch and Sangani [12], is used for F_0. Koch and Sangani [12] proposed to add a 0.7 to the Carmen expression to make the high and low solids volume fraction expressions fit at ϕ = 0.4. However, we prefer to use a weighting factor w to blend the formulas [e.g., 13, equation 12] so that the well established Carmen relation need not be modified. Note that only minor differences occur between our approach and that of Koch and Sangani [12].

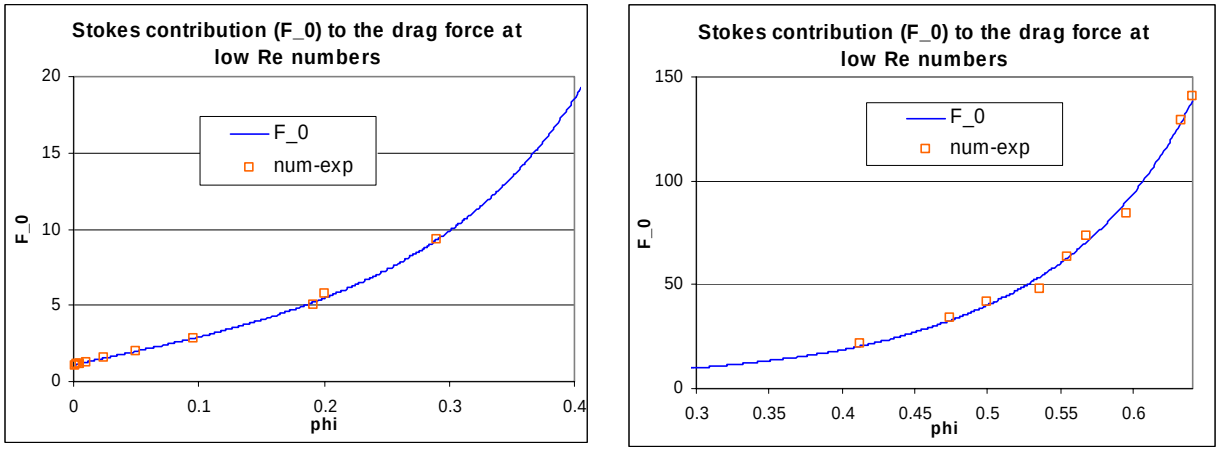

Figure 1 *Stokes contribution to the drag force at low and high solids volume fractions (ϕ). Note the smooth transition at $\phi = 0.4$.*

Figure 1 shows that equation 4 reasonably fits the data of Koch and Hill [5, Table 1] (shown in the figure as numerical-experiments symbols). The smooth transition at ϕ = 0.4 is barely noticeable. All the data of Koch and Hill [5] extend until a maximum solids volume fraction ϕ = 0.641. The Carmen relation can extend beyond this packing value if the maximum packing of some powders exceeds the value ϕ = 0.641.

Surprisingly the inertial contribution to the drag coefficient has a Re^2 dependence, which is justified theoretically [5, 14] for regular and random arrays of particles. However, as Koch and Hill [5] noticed, an experimental validation of expression (3) has not been observed mainly due to the small contribution of the inertial term at low Re numbers.

The low Re number inertial coefficient in the drag formula can be expressed as:

$$F_1 = \begin{cases} \sqrt{\dfrac{2}{\phi}} / 40 & 0.01 < \phi \le 0.1 \\ 0.11 + 0.00051\exp(11.6\phi) & \phi > 0.1 \end{cases} \qquad (5)$$

For low solids volume fraction, the inertial contribution to the drag is represented by Kaneda's theory [5, Figure 14]. Although Koch and Hill [5, equation 47] suggested a better fit to their computation data, we found that it is better to use Kaneda's theory because it intersects naturally with the curve at higher solids volume fraction (second part of equation 5) and fits Koch and Hill data quite well.

At very low solids volume fraction, equation (3) cannot be used to represent drag because it does not reduce to the single-particle drag law as ϕ tends to zero. Therefore, at very low solids volume fraction we propose another form of Kaneda's theory, which has the desired single particle Stokes drag law limit:

$$F = 1 + 3/8\,\mathrm{Re} \qquad \phi \le 0.01 \tag{6}$$

Note that this formula contains only the first two terms in the Kaneda's expression [14, equation 4.2]. The last term in Kaneda's theory was removed because it has a strong hyperbolic dependence on the Re number, and also it didn't fit the drag coefficient at high Re numbers as we will discuss in the following sections. This expression was cited by Koch and Hill [5, equation 2] but was not used by the authors.

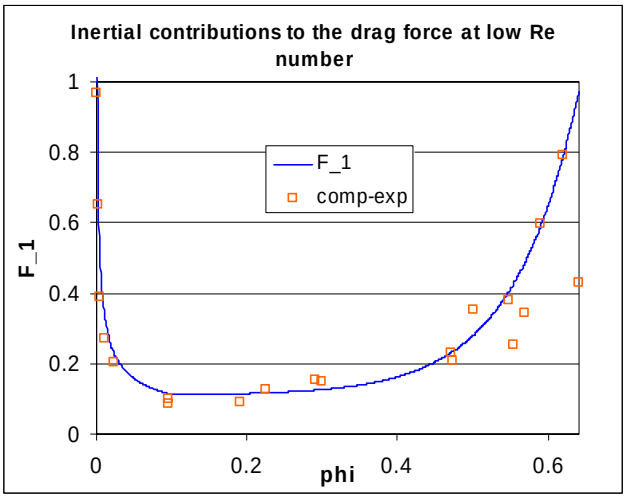

Figure 2 *Inertial contribution to the drag force at low Re number as represented by eq. 4.*

Figure 2 shows the inertial contribution to the dimensionless drag coefficient as function of the solids volume fraction. The comparison with Koch and Hill [5] data shows a very good agreement at low ϕ. At high solids volume fraction, the data of Koch and Hill are more scattered and F_1 fits these data only approximately. However, the accuracy of the dimensional drag force in equation (3) is very good because the inertial contributions ($F_1\,\mathrm{Re}^2$) to F are not significant. Note that equation (6) was not represented in Figure 2 because it falls at very low solids volume fraction were no computational data are available. It will, however, be discussed in the next sections.

High Reynolds number limit

At relatively high Re number, a linear variation of the dimensionless drag force with the Re number is used:

$$F = F_2 + F_3\,\mathrm{Re} \tag{7}$$

This form is familiar to chemical engineers because it resembles the Ergun drag law. In fact, the Ergun equation can be expressed in the form of equation (7) by using the following formula derived by van Der Hoef et al. [7, equation 15]:

$$F = \frac{150}{18}\frac{\phi}{(1-\phi)^3} + \frac{1.75}{18}\frac{\mathrm{Re}}{(1-\phi)^3} \tag{8}$$

The function F_2 in equation (7) was fitted to computational data obtained by Koch and Hill [6] and is expressed as:

$$F_2 = \begin{cases} (1-w)\left[\dfrac{1+3\sqrt{\phi/2}+(135/64)\phi\ln(\phi)+17.89\phi}{1+0.681\phi-11.03\phi^2+15.41\phi^3}\right] + w\left[10\dfrac{\phi}{(1-\phi)^3}\right] & \phi < 0.4 \\ 10\dfrac{\phi}{(1-\phi)^3} & \phi \geq 0.4 \end{cases} \tag{9}$$

This equation is similar to equation (4) and most authors [10, 11 and 15] that represented Koch and Hill [5, 6] correlations assumed F_0 and F_2 to be equal. However, Reghan Hill [private communications, 2004] has mentioned that a better fit for F_2 may be necessary since at low solids volume fraction, their data [6] shows some differences between F_0 and F_2. Thus, we have optimized some coefficients in the function F_2 to better represent Koch and Hill [6] data.

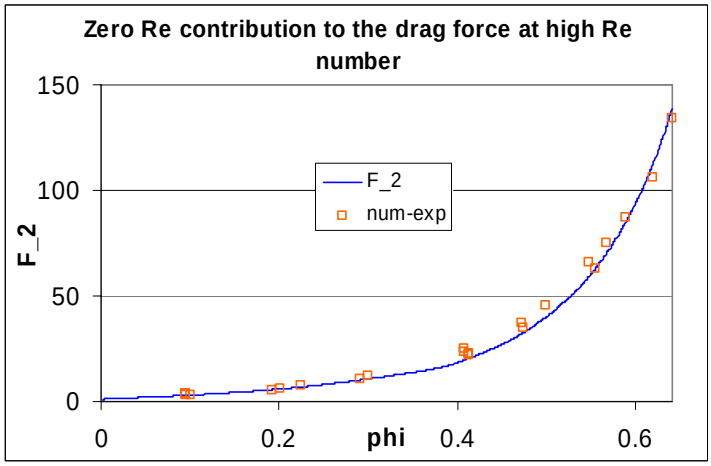

Figure 3 *Zero Re contribution to the drag force at high Re number as represented by eq. 8.*

Figure 3 shows that the numerical-experimental data of Koch and Hill [6, table 1] are well represented by the formula (9). Note the lack of computational data below a solids volume fraction of about 10% (9.53% to be precise), due to the high computational time required by the LBM simulations at low concentration and high Re number.

The function F_3 was fitted to the computational data of Koch and Hill [6, equation 7] for solids volume fraction higher than 0.0953 and was extended to yield the right single

particle drag (Newton's regime) at low ϕ. The value of ϕ = 0.0953 was chosen because LBM data from Koch and Hill [6] were not available below this value. The following expression was obtained:

$$F_3 = \begin{cases} 0.9351\phi + 0.03667 & \phi < 0.0953 \\ 0.0673 + 0.212\phi + 0.0232/(1-\phi)^5 & \phi \geq 0.0953 \end{cases} \quad (10)$$

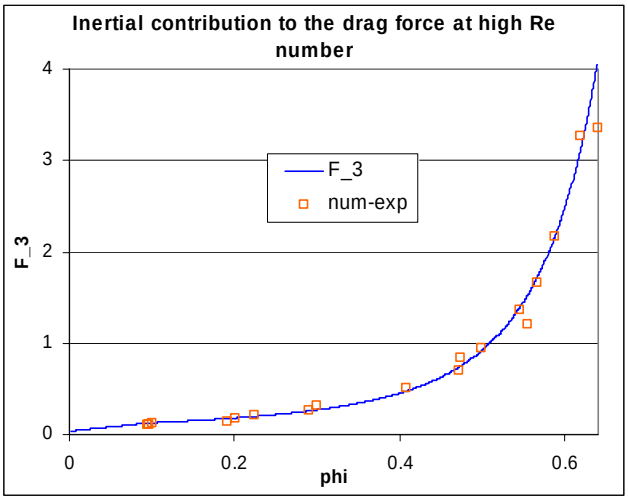

Figure 4 *Inertial contribution to the drag force at high Re number as represented by eq. 9.*

Figure 4 shows that at high solids volume fraction, the data are well represented by equation (10). At ϕ < 0.0953, there is a noticeable decrease in the function F_3 to fit the standard drag coefficient for a single particle (Newton's regime). In fact, when $\phi \to 0$, $F_2 \to 1$ and $F_3 \to 0.03667$, thus $F \to 1 + 0.03667\ \mathrm{Re}$. In this case, the single particle drag coefficient (see equation 2) $C_D \to \frac{12}{\mathrm{Re}}(1 + 0.03667\ \mathrm{Re})$, and when $\mathrm{Re} \to \infty$, $C_D \to 0.44$.

It is very important to note that although the region of the linear fit appears to be small in Figure 4, the range of solids volume fraction covered by that formula is of much practical importance in many chemical engineering applications (gas/solids flow in riser section of a CFB). A smooth transition from the formula validated by Koch and Hill [5, 6] data and the ability to satisfy the limiting value of C_D makes the linear fit a good first approximation. One way to check this linear fit assumption is to compare it with available experimental drag laws, such as the Gibilaro correlation [16, Equation 5]: $\beta = \left(\frac{11.53}{\mathrm{Re}} + 0.366\right)(1-\phi)^{-3.8} \frac{(1-\phi)\rho_g \phi |u_g - u_s|}{d}$. Following equation (1), we can deduce that Gibilaro expression of the dimensionless drag force (F) is:

$$F = \frac{\mathrm{Re}}{12}\left(\frac{11.53}{\mathrm{Re}} + 0.366\right)(1-\phi)^{-5.8} \tag{11}$$

It is clear from Figure 5 that significant differences can occur between our linear fit approximation and the Gibilaro drag law even if both expressions agree at very dilute conditions. Furthermore, Gibilaro correlation predictions are far from the computational results of Koch and Hill at ϕ = 0.0953, which makes connecting this correlation to the available data of Koch and Hill uneasy. Furthermore, Kandhai et al. [9] have tried to match their LBM data with Wen and Yu correlation [9, equation 3], but their data did not extend below ϕ = 0.1. Therefore, we suggest using our linear fit and recommend that more computational data using LBM are necessary for validating this approach.

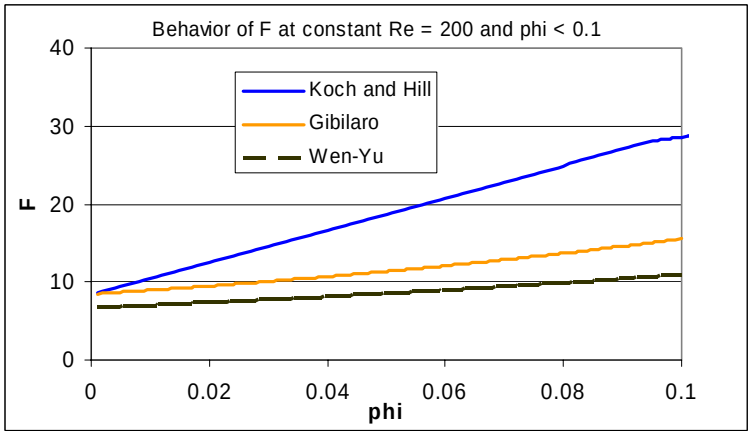

Figure 5 *Comparison of our expression of F and that of Gibilaro and Wen and Yu at low phi and high Re*

Connecting bits and pieces

Now that we laid out the Koch and Hill drag model, we need to make decisions on how to switch between these different equations. More specifically, at what Re number should we switch between the low and high Re number limits? Koch and Hill [15] did not mention a specific Re number where the transition should take place, but rather a range of Re. Previous representation of Koch and Hill drag law have mistakenly assumed an abrupt transition at Re = 20 [10, 11]. The simplest way to answer this question is to find the point where these equations 3 and 7 intersect. To do this, equate equations 3 and 7:

$F = F_0 + F_1\,\mathrm{Re}^2 = F_2 + F_3\,\mathrm{Re}$; this is a quadratic equation with a positive root:

$$\mathrm{Re}^{trans} = \frac{F_3 + \sqrt{F_3^2 - 4F_1(F_0 - F_2)}}{2F_1} \tag{12}$$

At the special case of low Re number and low solids volume fraction where equation (6) applies, there is still a need to connect the low and high Re number regimes. In that case, the transitional Re can be found in a similar way and is expressed as:

$$\mathrm{Re}^{trans} = \frac{(F_2 - 1)}{(3/8 - F_3)} \tag{13}$$

Again here we need to show a smooth transition over all Re numbers as demonstrated in the following figures.

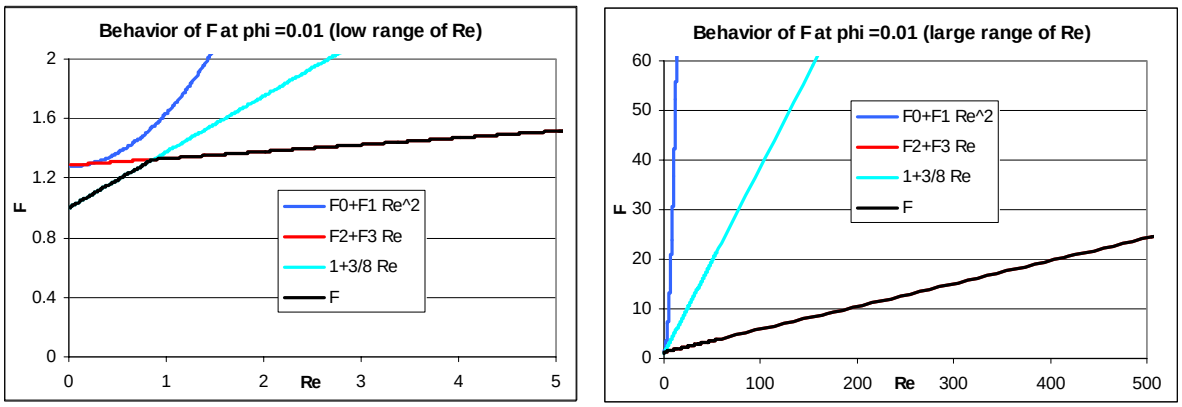

Figure 5 *Behavior of dimensionless drag coefficient at phi = 0.01*

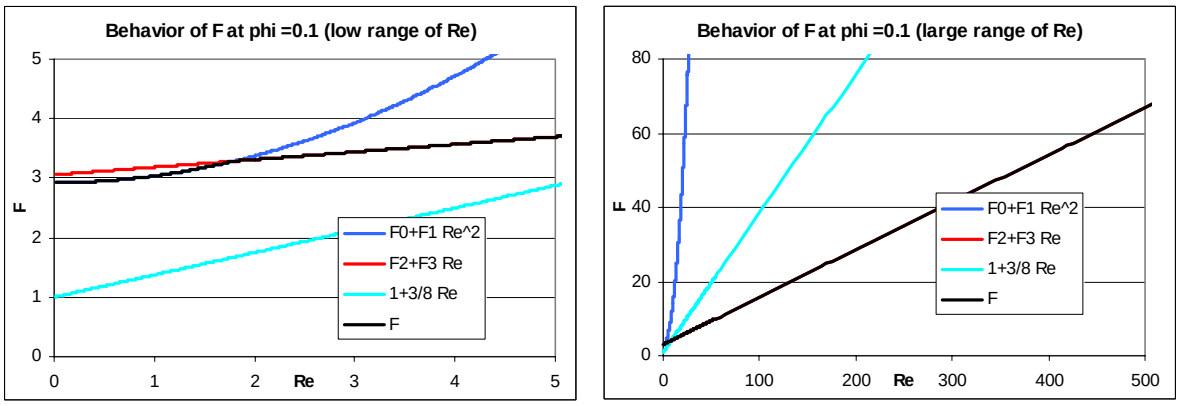

Figure 6 *Behavior of dimensionless drag coefficient at phi = 0.1*

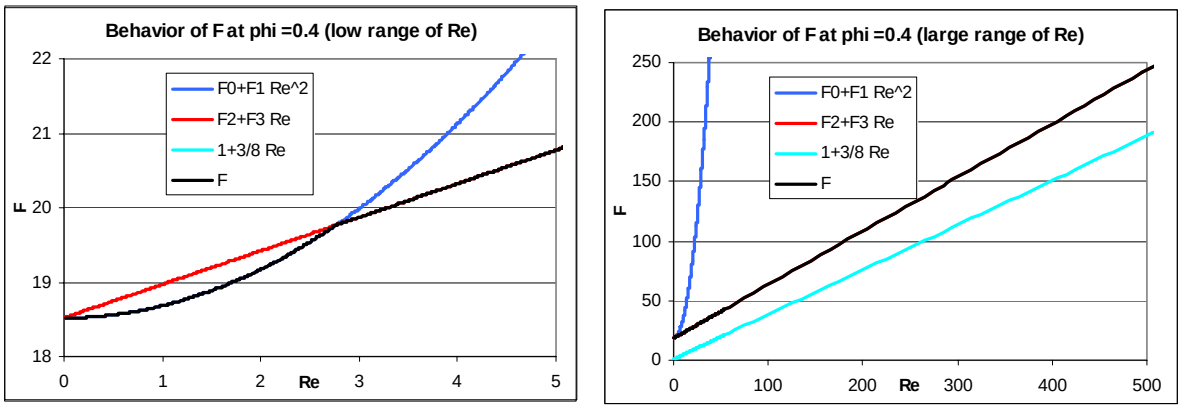

Figure 7 *Behavior of dimensionless drag force at phi = 0.4*

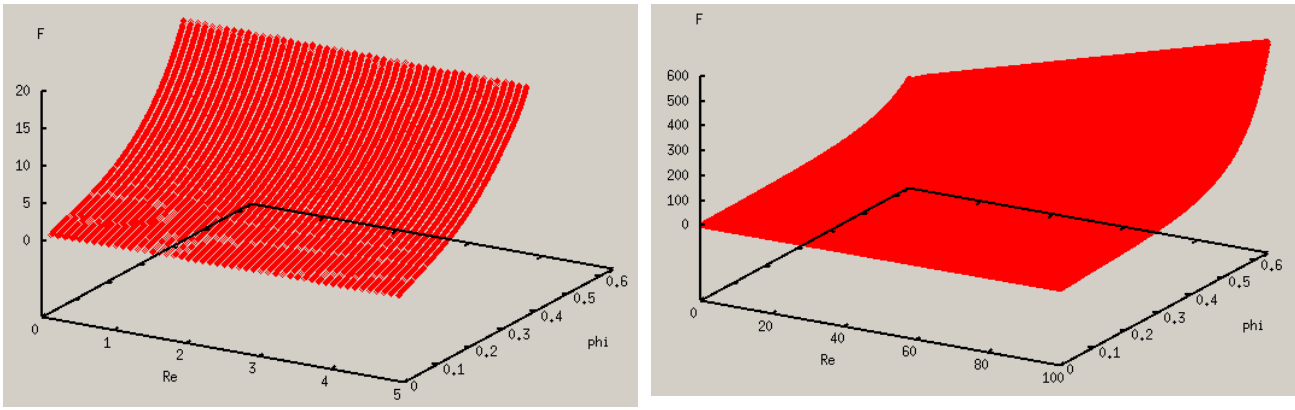

Figure 8 *Global behavior of F at low and overall Reynolds number*

At low Re number, the drag force F follows the curve1+3/8 Re at low solids volume fraction and the F0+F1 Re^2 at high values of ϕ. The transitional Re number depends on the solids concentration and is not set a priori. At high Re number, the dimensionless drag coefficient follows a linear dependence on Re number: F_2+F_3 Re. It is clear from these figures that the linear dependence on Re number is dominant for most ranges of Reynolds number.

In a recent publication, Koch and Hill [15] summarized their drag correlation obtained from LBM simulations. All publications that we found in the literature that use this drag law referred to that summary [15]. In fact, Kuipers group [10] made the assumption that a switch exists in the drag law formulation of Koch and Hill [15] at a Re = 20, and they showed [10, Figure 7] a discontinuity in the drag coefficient (C_D) at that Reynolds number. Figure 9 shows a comparison between the Koch and Hill drag law as expressed by Bokkers et al [10] (mentioned as Kuipers in the graph) and the drag law proposed here. Figure 9 clearly shows that discontinuities at Re = 20 are avoided when using our modified drag coefficient. Also the correct limits of a single sphere drag are predicted for

very dilute flows at both limits of high Re number (C_D = 0.44, Newton's regime) and for low Re number ($C_D = 12/\mathrm{Re}$, Stokes regime).

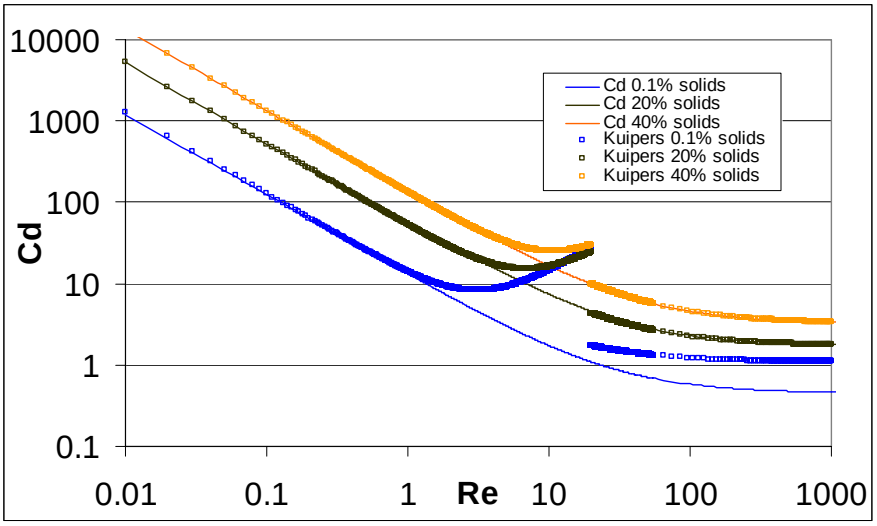

Figure 9 *Drag coefficient variations with Re number*

Summary of our modifications to Koch and Hill drag correlation

Let's summarize all the correlations used in this study in a form that can readily be introduced in a computational fluid dynamic (CFD) code:

$$F = 1 + 3/8\,\mathrm{Re} \qquad \phi \le 0.01 \; and \; \mathrm{Re} \le \frac{(F_2 - 1)}{(3/8 - F_3)}$$

$$F = F_0 + F_1 R_e^2 \qquad \phi > 0.01 \; and \; \mathrm{Re} \le \frac{F_3 + \sqrt{F_3^2 - 4F_1(F_0 - F_2)}}{2F_1}$$

$$F = F_2 + F_3\,\mathrm{Re} \qquad \begin{cases} \phi \le 0.01 \; and \; \mathrm{Re} > \dfrac{(F_2 - 1)}{(3/8 - F_3)} \\ \phi > 0.01 \; and \; \mathrm{Re} > \dfrac{F_3 + \sqrt{F_3^2 - 4F_1(F_0 - F_2)}}{2F_1} \end{cases}$$

And the coefficients are defined as follows:

$$F_0 = \begin{cases} (1-w)\left[\dfrac{1+3\sqrt{\phi/2}+(135/64)\phi\ln(\phi)+17.14\phi}{1+0.681\phi-8.48\phi^2+8.16\phi^3}\right]+w\left[10\dfrac{\phi}{(1-\phi)^3}\right] & 0.01<\phi<0.4 \\ 10\dfrac{\phi}{(1-\phi)^3} & \phi \geq 0.4 \end{cases}$$

$$F_1 = \begin{cases} \sqrt{\dfrac{2}{\phi}}/40 & 0.01<\phi\leq 0.1 \\ 0.11+0.00051\exp(11.6\phi) & \phi>0.1 \end{cases}$$

$$F_2 = \begin{cases} (1-w)\left[\dfrac{1+3\sqrt{\phi/2}+(135/64)\phi\ln(\phi)+17.89\phi}{1+0.681\phi-11.03\phi^2+15.41\phi^3}\right]+w\left[10\dfrac{\phi}{(1-\phi)^3}\right] & \phi<0.4 \\ 10\dfrac{\phi}{(1-\phi)^3} & \phi \geq 0.4 \end{cases}$$

$$\mathrm{F_3} = \begin{cases} 0.9351\phi+0.03667 & \phi<0.0953 \\ 0.0673+0.212\phi+0.0232/(1-\phi)^5 & \phi\geq 0.0953 \end{cases}$$

$$\mathrm{Re} = \frac{\rho_g(1-\phi)|u_g-u_s|d}{2\mu_g}$$

$$w = e^{(-10(0.4-\phi)/\phi)}$$

Figure 10 gives an idea of the range of validity of the different functions that constitute our modified version of the Koch and Hill drag correlation. The major subdivision in this graph is due to the function $\dfrac{F_3+\sqrt{F_3^2-4F_1(F_0-F_2)}}{2F_1}$ shown in blue line. The red line occurring at low Re number and low solids volume fraction is the function: $\dfrac{(F_2-1)}{(3/8-F_3)}$. The vertical black lines are for constant solids volume fractions of (from left to right in the graph): ϕ = 0.01, 0.953, 0.1 and 0.4, which indicate transitions in the functions defining the drag correlation. The only small discontinuities that occur in the global drag correlation F are located at about Re < 0.9 and $\phi \leq 0.01$. In this range a variation of F with respect to ϕ may lead to small discontinuities as shown in Figure 11. Note that one has to vary ϕ and keep Re constant in order to notice this discontinuity. Changing Re and keeping ϕ constant doesn't show any discontinuity in F even at small values of ϕ (see

Figure 5 for an example). The reason being that the different pieces of F were fitted at intersection points with respect to Re number and not in terms of solids volume fractions.

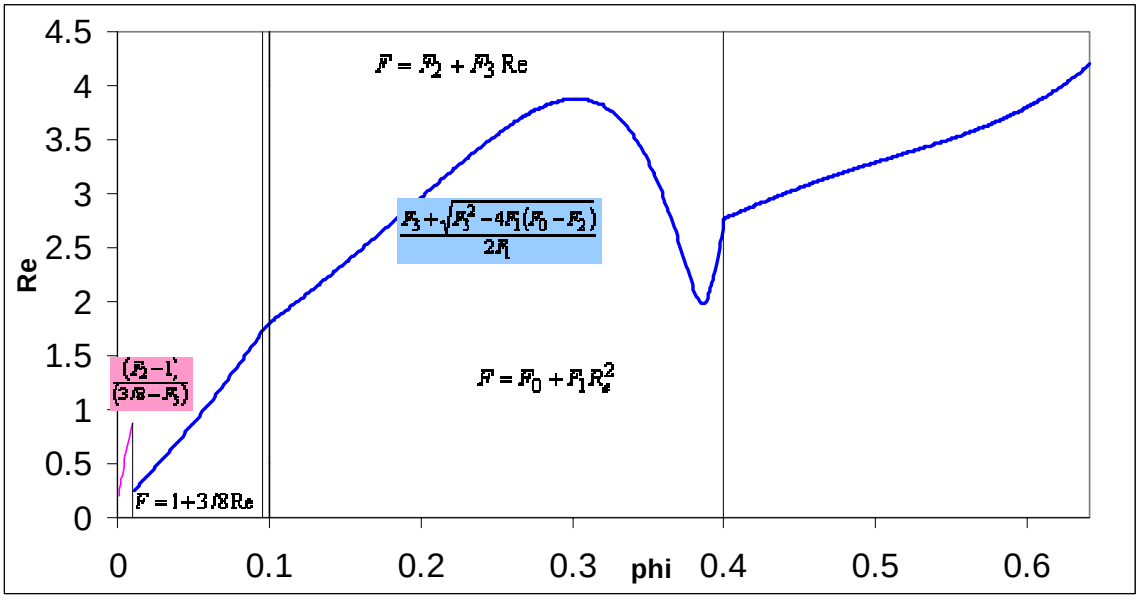

Figure 10 *Range of validity of the different functions used in this drag model*

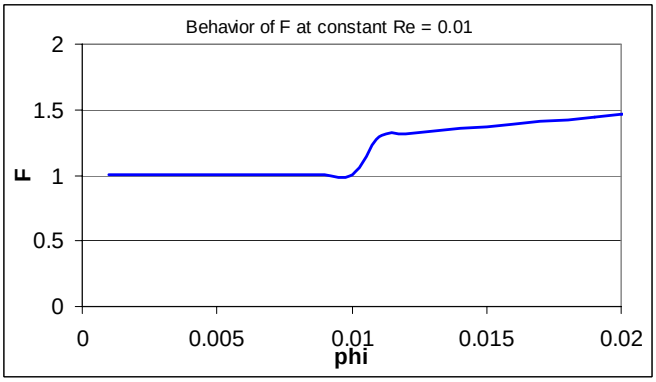

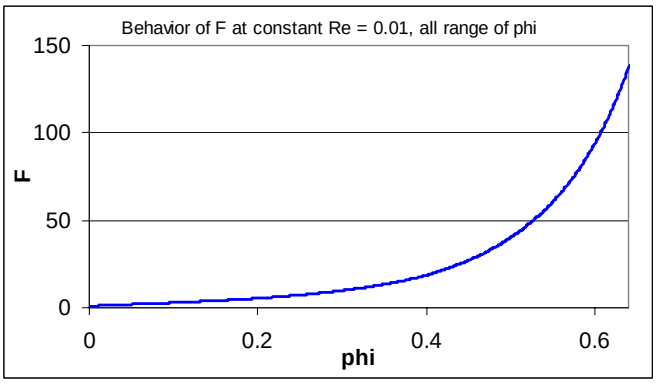

Figure 11 *Small discontinuities in F occurring at low Re number and solids volume fraction*

Application of the modified drag law to gas/solids flows

Two examples were chosen to show major differences in numerical predictions due to different views of the formulation of Koch and Hill drag correlation. We present an example of bubbling fluidized bed and a fully-developed (using periodic boundaries) gas/solids flow in a channel, which cover a wide range of gas/solids flow applications in the chemical industry.

The first example considers a bubbling fluidized bed with a central jet simulated by Gidaspow [4, Figure 7.11] using sand particles of 500 microns and was reproduced using our modified Koch and Hill drag correlation as well as Bokkers et al. [10] representation of this drag law. Detail physical and numerical parameters used in this study can be found

in Guenther and Syamlal [17, section 4.1]. Figure 12 shows contours of gas volume fraction distribution in the fluidized bed after 0.44 sec of fluidization. The computed values of Reynolds number were usually below 40 with high values inside the bubble and low values in the emulsion phase. Since the transitional value of Re = 20 chosen by Bokkers et al. [10] occurred in this simulation, differences in the observed bubble shape seen in Figure 12 can, therefore, be explained by differences in the drag law used in both simulations. We should mention that simulations conducted by Bokkers et al. [10] used large particle diameter values of 2.5 mm along with high gas inlet velocities, and may have only used the high Re branch in the drag law avoiding the observed discontinuity (see Figure 9). However, as demonstrated in this bubbling bed example, Re number of 20 is not uncommon in fluidization, and therefore continuous drag laws, as expressed in this study, are necessary in practical engineering processes.

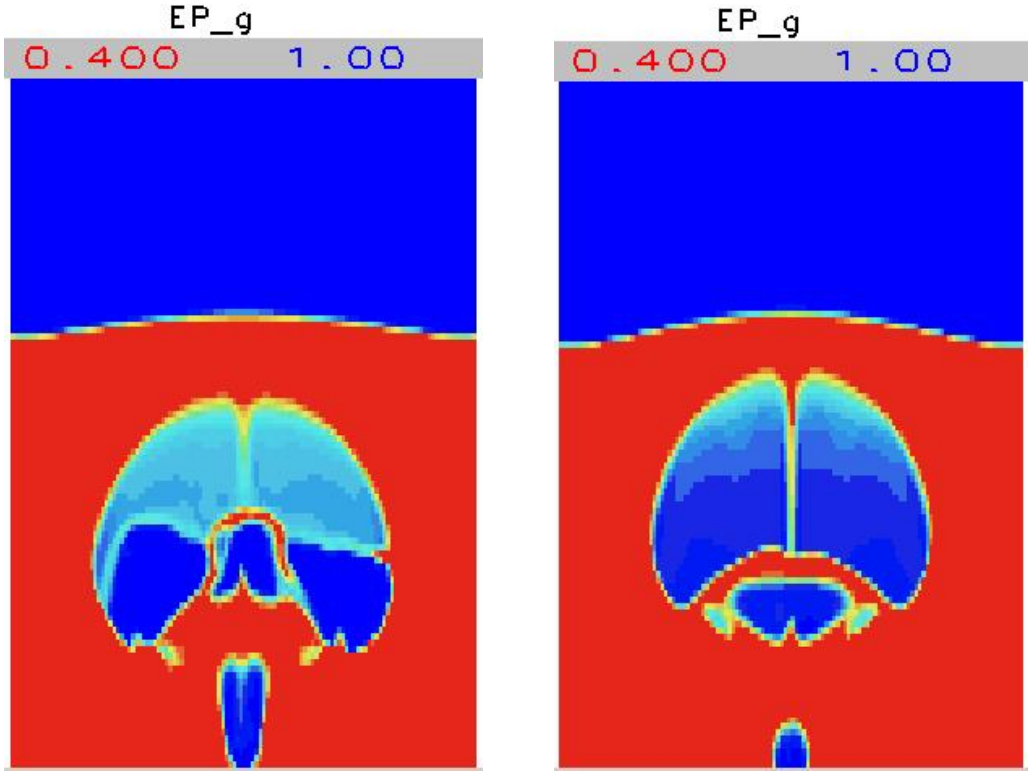

Koch and Hill drag law from Bokkers et al. [10] Our modified Koch and Hill drag law

Figure 12 *Void fraction distribution in a fluidized bed with a central jet after 0.44 sec*

A second example considers a one-dimensional (1-D) gas/solids upward flow in a channel. Glass beads of 120 microns in diameter and an upward mean gas velocity of 5 m/s was considered. Detailed physical and numerical parameters were described elsewhere [18].

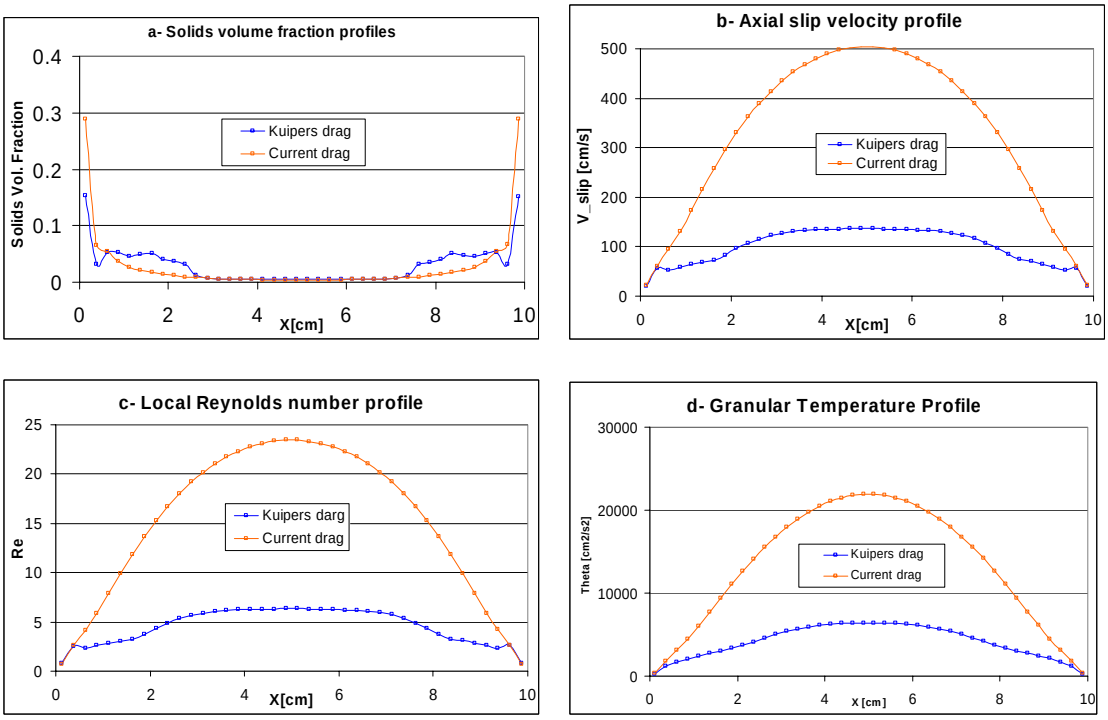

Figure 13 *Time-averaged flow variable profiles across the width of the 1-D channel*

Figure 13 shows quantitative differences of flow variables between our modified Koch and Hill drag correlation and that presented in the literature [10, 11] (noted at Kuipers drag in the graphs). Since the Reynolds number in this case was mostly below 20, large differences were computed for the slip velocity. Our current modified drag law predicted higher slip velocity because the computed drag force was lower. In this flow regime, our modified drag law uses mainly the linear form of the drag force (equation 7), which predicts a lower drag force than the Re^2 formulation (equation 3) used by Kuipers drag (see Figures 5 and 6). The core-annular behavior with high solids concentration near the walls of the channel and more dilute flow in the center was also affected by the drag law due to differences in the computed granular temperature profiles.

Some simplifications to our modified Koch and Hill drag law

Some simplifications to our modified Koch and Hill drag law might be possible because, as Figure 10 suggests, the linear form of this drag law ($F_2 + F_3\,\mathrm{Re}$) is valid over a large domain of the Re-ϕ plane. Following suggestions from Reghan Hill [private communications, 2005], we have tested the two examples shown in the previous section (see Figure 12 and 13) by only using the linear form of this current drag law. The results using the linear form of this drag law showed identical results with those shown in Figure 12 and 13. Therefore, the linear drag formula may be used as a good approximation for many gas/solids flow application.

Another simplification to our drag model can be added by considering $F_2 = F_0$, so that equation (4) is used instead of equation (9). Clay Sutton [private communications, 2005]

indicated that the transitional region in Figure 10 (shown in blue line) is expected to increase with increasing solids volume fraction due to wake interaction with downstream particles. Naturally, this was due to the non-linearity of equation (12), and by assuming that $F_2 = F_0$, the transitional Re number reduces to $\mathrm{Re}^{trans} = \frac{F_3}{F_1}$. Figure 14 shows that the assumption of $F_2 = F_0$ results in a monotonic increase of the transition region.

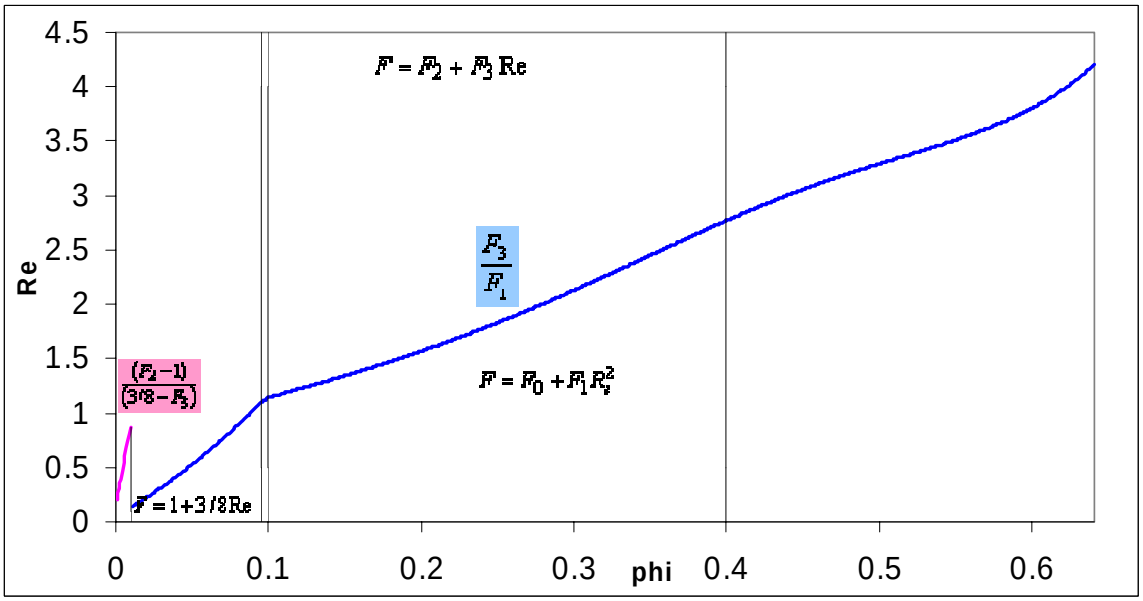

Figure 14 *Re-phi domain showing the monotonic increase in transitional Re by assuming F_2=F_0*

Conclusions

A drag law based on the work of Koch and Hill [5, 6] was extended over the full range of Reynolds number and solids volume fractions. Unlike previous publications [10, 11] that considered an abrupt transition of this drag law at Re = 20, our modified drag law used natural connectivity between the different functions at intersection points, and when the functions didn't intersect, we used a weighting factor to obtain a smooth transition. The previously published discontinuity in the drag coefficient [10] was avoided as presented in this study.

Gas/solids flows in a bubbling bed and in a 1-D channel were used to demonstrate that significant differences in the computed results can occur between our modified Koch and Hill drag law and that previously published in the literature [10, 11].

Nomenclature

d	particle diameter
F	dimensionless drag force

F_0	coefficient in Re expansion of the dimensionless drag force at low Re
F_1	coefficient in Re expansion of the dimensionless drag force at low Re
F_2	coefficient in Re expansion of the dimensionless drag force at high Re
F_3	coefficient in Re expansion of the dimensionless drag force at high Re
Re	Reynolds numbers (Note that Re is based on particle radius rather than diameter)
u_g	interstitial gas velocity
u_s	interstitial solids velocity
β	friction coefficient
C_D	drag coefficient
ϕ	solids volume fraction
μ_g	gas viscosity
ρ_g	gas density

Acknowledgement

The authors gratefully acknowledge the comments and guidance of Prof. Donald Koch at Cornel University, Prof. Reghan Hill at McGill University and Clay Sutton at Lehigh University during the course of this study.

References

[1]- Enwald, H., Peirano, E. and Almstedt, A.E., 1996. Eulerian two-phase flow theory applied to fluidization. *Int. J. Multiphase Flow*, **22**, 21-66.

[2]- Tsuji, Y., Kawaguchi, T. and Tanaka, T., 1993. Discrete particle simulation of two-dimensional fluidized bed. *Powder Technology* **77**, 79–87.

[3]- Yang, J. and Renken, A., 2003. A generalized correlation for equilibrium of forces in liquid-solid fluidized beds. *Chemical engineering J*., **92**, 7-14.

[4]- Gidaspow, D.,1994. Multiphase flow and fluidization: continuum and kinetic theory description. Academic press, Inc., San Diego, Ca.

[5]- Hill, R.J., Koch, D.L. and Ladd, J.C., 2001. The first effects of fluid inertia on flows in ordered and random arrays of spheres. *J. Fluid Mech*., **448**, 213-241.

[6]- Hill, R.J., Koch, D.L. and Ladd, J.C., 2001. Moderate-Reynolds-number flows in ordered and random arrays of spheres. *J. Fluid Mech*., **448**, 243-278.

[7]- van der Hoef, M.A., Beestra, R. and Kuipers J.A.M. Lattice-Boltzmann simulations of low Reynolds number flow past mono- and bidisperse arrays of spheres: results for the permeability and drag force. Accepted for publication in *J. Fluid Mech.*

[8]- Sankaranarayanan K, Shan X, Kevrekidis IG, Sundaresan S, 2002. Analysis of drag and virtual mass forces in bubbly suspensions using an implicit formulation of the lattice Boltzmann method. *J. of Fluid Mech.*, **452**, 61-96.

[9]- Kandhai, D., Derksen, J.J. and Van den Akker H.E.A., 2003. Interphase drag coefficients in gas-solid flows. *AICHE J.*, **49-4**, 1060-1065.

[10]- Bokkers, G.A., van Sint Annaland, M. and Kuipers, J.A.M., 2004. Mixing and segregation in a bidisperse gas-solid fluidized bed: a numerical and experimental study. *Powder Technology*, **140**, 176-186.

[11]- Sutton, C.R. and Chen, J.C., 2004. Dynamic behavior of local solids concentration in fluidized beds: experimental validation of an Eulerian-Eulerian model. Unpublished, presented at the 2004 *AICHE annual meeting*, Austin, TX.

[12]- Koch, D.L. and Sangani, A.S., 1999. Particle pressure and marginal stability limits for a homogenous monodisperse gas-fluidized bed: kinetic theory and numerical simulations. *J. Fluid Mech*., **400**, 229-263.

[13]- Nott, P. and Jackson, R., 1992. Frictional-collisional equations of motion for granular materials and their application to flow in aerated chutes. *J. Fluid Mech*., **241**, 125-144.

[14]- Kaneda, Y., 1986. The drag on a sparse random array of fixed spheres in flow at small but finite Reynolds number. *J. Fluid Mech*., **167**, 455-463.

[15]- Koch, D.L. and Hill, R.J., 2001. Inertial effects in suspension and porous-media flows. *Annu. Rev. Fluid Mech*., **33**, 619-647.

[16]- Makkawi, Y., Wright, P. and Ocone, R., 2004. Comparative analysis of experimental and modelling of gas-solid flow hydrodynamics: Effect of friction and interparticle cohesion forces. Unpublished, presented at the 2004 AICHE annual meeting, Austin, TX.

[17]- Guenther, C. and Syamlal, M., 2001. The effect of numerical diffusion on simulation of isolated bubbles in a gas–solid fluidized bed. *Powder Tech*., **116**,142–154.

[18]- Benyahia, S., Syamlal, M. and O'Brien, T.J., 2004. The effect of model parameters on the predictions of core-annular flow behavior in a fast-fluidized gas/solids bed. Unpublished, presented at the 2004 AICHE annual meeting, Austin, TX.

Appendix K

Comparison of Experimental and CFD Values for Granular Temperature, Turbulent Kinetic Energy and Solids Fraction of Core Particles at the Wall in the Riser of a CFB

Draft paper for submission to Powder Technology 2005

A Comparison of Experimental and CFD values for Granular Temperature, Turbulent Kinetic Energy and Solids Fraction of Cork Particles at the Wall in the Riser of a CFB

by

Ronald W. Breault, Lawrence J. Shadle, and Chris Guenther
National Energy Technology Laboratory
U.S. Department of Energy, 3610 Collins Ferry Road, Morgantown, WV 26507-0880

Abstract

The development of granular theory and the Eulerian- Eulerian representation of flowing two-phase reactive systems provides the methodology to better simulate and design these complex systems. Granular theory is the analogous theory for discrete particles as the kinetic theory of gases is for gas molecules. As each of the thermodynamic and transport properties (pressure, temperature, viscosity, etc.) is defined in the kinetic theory of gases, they are also defined in granular theory. One can also speculate that the transport properties associated with mass transfer in these two-phase systems and the distribution of different solids phases would also be dependent on the granular temperature. In gases the differences in time scales between molecular collisions in which fluctuations in molecular velocities represent temperature and those that represent turbulence spans 5 to 10 orders of magnitude. However, in the granular analogy, the time scales for particle collisions is only 1 or two orders of magnitude smaller than that of turbulent velocity fluctuations. Sometimes, because of the differences in voidage, distributions of velocities and particle sizes, the time scale for velocity fluctuations between collisions is on the same order of magnitude as that of the turbulent fluctuations. In this paper a method is presented to distinguish between particles velocity fluctuations contributing to granular temperature and those contributing to turbulent kinetic energy. Criteria are established to insure adequate resolution necessary to measure granular temperature. Comparisons are made for both granular temperature and turbulent kinetic energy between computational fluid dynamic simulations using NETL's MFIX and experiments using 812 μm cork particles measured near the wall in the core annular flow regime of a circulating fluidized bed riser. These results are discussed with respect to granular temperature measurements and theory in the literature.

In this regard, tests were conducted in a cold flow model of a circulating fluidized bed gasifier to gather model verification data. Similitude analysis was applied to obtain a system operating with air nominally at atmospheric pressure with cork particles approximately 1mm. Particle velocity measurements were obtained with an LDV system

under various operating conditions and at locations near the wall and at penetrations up to 13mm depending on the optical visibility. The overall granular temperatures were found to be 2 to 5 times smaller than the turbulent kinetic energy. Average values for the overall mixture granular temperature in this cork system ranged between 0.02 to 0.1 m^2/s^2, while the Turbulent Kinetic Energy ranged from 0.6 to 0.9 m^2/s^2. Both were dependent upon solids void fractions: decreasing with increasing solids fraction. At the wall, the good visibility led to data with enough character to define clusters and the associated granular temperature and local volumetric solids void fractions within the clusters. The intracluster granular temperature was found to be significantly smaller than that for the overall mixture. The solids fraction within each cluster approached that observed in minimally fluidized bed. The paper also presents the overall granular temperature near the wall as a function of the CFB operating conditions, namely the load ratio.

Introduction

Necessity has once again forged the way for the advancement of scientific theory in the area of developing better predictive and design tools for multiphase chemically reacting systems. The development of granular theory and the Eulerian- Eulerian representation of flowing two-phase reactive systems provides the methodology to better simulate and design these complex systems. Granular theory is the analogous theory for discrete particles as the kinetic theory of gases is for gas molecules. As each of the thermodynamic and transport properties (pressure, temperature, viscosity, etc.) is defined in the kinetic theory of gases, they are also defined in granular theory. One can also speculate that the transport properties associated with mass transfer in these two-phase systems and the distribution of different solids phases would also be dependant on the granular temperature.

Granular Temperature is the analogy property to temperature for the solids in a two phase flowing system. As the thermodynamic temperature is a measure of and proportional to the variance of the molecular velocity distribution, Granular temperature is proportional to the variance of the particles velocity distribution. The similarity is seen in the following two equations:

$$T = \frac{m\left\langle c^2 \right\rangle}{3k} \qquad \textbf{Equation 1}$$

$$\Theta = \frac{\left\langle c^2 \right\rangle}{3} \qquad \textbf{Equation 2}$$

In the first equation, the thermodynamic temperature is shown to be proportional to the variance of the molecular velocity with the proportionality represented by the ratio of the molecular mass (m) to 3 times the Boltzmann constant (k). The ratio m/k converts the

units from velocity squared to absolute degrees. The factor of 3 is a consequence the gas molecule moving randomly in the three dimensional space. In the second equation, this same factor of three appears for the same reason. The units for granular temperature are velocity squared such that *m* and *k* do not appear.

Consideration needs to be given to evaluate and contrast the concepts of temperature and granular temperature to determine the limitation of the analogy. Examining the concept of temperature first, kinetic theory describes a system of individual molecules moving about in a confined space. At ambient conditions, the velocity of the molecules is quite large. Now, looking at the particulate system it is seen that the particles are extremely large when compared to the gas molecule and that the velocity of the particles is relatively small. The questions are, do small particles at high velocity and big particles at low velocity behave in a similar manner and if so under what conditions?

Similar questions need to be asked regarding flowing systems. In a flowing gas system there are several molecular translational displacements that occur. Gas molecules move randomly about at high velocities in all three dimensions similar to the non-flowing system discussed above. Another mode of transport is that for the bulk flow, where the gas moves from one location to another. A third mode of transport is that of turbulent eddies where portions of the gas (eddies) move about similar to the way in which the molecules move, but at lower velocities. These same types of movement occur for the solids. However, there is one issue that needs to be addressed to continue the analogy. In the gas system, the velocity of the molecules and the velocity of the turbulent portions are considerably different. In the solids system, the velocities are not so different, therefore, it is important to be able to separate the two types of motion and develop criteria for this separation.

In the kinetic theory of gases, the time scale for temperature is on the same order as the time scale for molecular collisions. In the analogous granular temperature, the time scale is on the same scale as the particle collision times. This time can be approximated based upon the volume swept out by the particles per unit time. Assuming that all particles are spherical with diameter d_p, if the center of one particle gets within a distance of d_p of the center of another particle, a collision occurs. A particle traveling at velocity *v* sweeps out a volume equal to $\pi d_p^2 v \cdot dt$ over a time interval, dt. If, another particle center falls within this volume a collision will occur. N particles will sweep out N times this volume. For a given particle center, the probability that it falls within the total volume swept out by the other particles is approximately:

$$P_{dt} = \frac{N\pi d_p^2 v dt}{V} \qquad \textbf{Equation 3}$$

where *V* is the total volume, $N >> 1$ and *v* is the average particle speed. The probability of no collisions in time interval, dt, is given by

$$P_{0,dt} = (1 - \frac{N\pi d_p^2 v dt}{V}) \qquad \textbf{Equation 4}$$

The probability of no collisions after m time intervals is

$$P_{0,mdt} = (1 - \frac{N\pi d_p^2 v dt}{V})^m \cong \exp(-\frac{N\pi d_p^2 vt}{V}) \quad \textbf{Equation 5}$$

where t=mdt. The probability of a collision is 1.0 minus the probability of no collision and the expected value for the collision time is

$$\tau_c = E(t) = \frac{V}{N\pi d_p^2 v} \quad \textbf{Equation 6}$$

Multiplying through by 6dp/6dp and recognizing that N times the volume of a particle is the volume of all particles in the total volume, V, the following equation can be obtained.

$$\tau_c = E(t) = \frac{V}{N\pi d_p^2 v} = \frac{d_p}{6(1-\varepsilon)v} \quad \textbf{Equation 7}$$

Granular temperature will be determined for adjacent particles with time interval being less than τ_c. Particles with time interval between adjacent particles, greater than τ_c contribute to the turbulent or the bulk translational kinetic energy.

The time scale for the transition between bulk transport and turbulent kinetic energy can be obtained from an analysis to determine the time constant for particle transport. A time interval between adjacent particle greater than this time constant are bulk transported particles and time interval less than this value but greater than τ_c are undergoing turbulent transport. Assuming no particle collision in the bulk transport and that the particles do not modify the surrounding turbulence the time constant for particle transport, t_p, can be expressed as:

$$\tau_p = \left| \frac{V_p}{\left(\frac{dV_p}{dt} \right)} \right| \quad \textbf{Equation 8}$$

based upon the work of Ainley and neglecting the effect of gravity (Ainley).

Summarizing, granular temperature applies for particles with time interval, dt, less than t_c and turbulent kinetic energy applies for time $\tau_c < dt < \tau_p$.

Experimental Methods

The test unit configuration is shown in Figure 1 and described by Shadle et al (2002). The solids enter the riser from a side port 0.23-m in diameter and 0.27-m above the gas distributor. Solids exit the riser through a 0.20-m port at 90° about 1.2-m below the top of the riser at a point 15.45-m above the solids entry location (centerline to centerline). Riser velocities were corrected for temperature and pressure as measured at the base of the riser. The air's relative humidity was maintained at 20% to minimize effects of static

charge building up on the solids. The riser pressure drop resulting solely from gas flow was found to be negligible over those flow rates studied.

Twenty incremental differential pressures were measured across the length of the riser using transmitters calibrated within 0.1 % of full-scale or about 2 Pa/m. The primary response measurement was the overall riser pressure differential and it was calibrated within 0.45 Pa/m. Mass circulation rate was continuously recorded by measuring the rotational speed of a twisted spiral vane located in the packed region of the standpipe bed (Ludlow et al., 2002). This volumetric flow measurement was converted to a mass flux using the measured packed bed density presented in Table 1. The packed bed void fraction at the point of measurement was found to be essentially constant.

The operator varied operating conditions by adjusting the riser flow or solids circulating rate while maintaining constant system pressure at the base of the riser using feedback control of the back pressure control valve at the exit of the second cyclone. The solids circulation was varied by controlling the aeration at the base of the standpipe and when necessary by adjusting the total system inventory to increase the standpipe bed height. Steady state conditions were defined as holding a constant set of flow conditions and maintaining a constant time averaged response in the pressure differentials and solids circulation rate over a five-minute period.

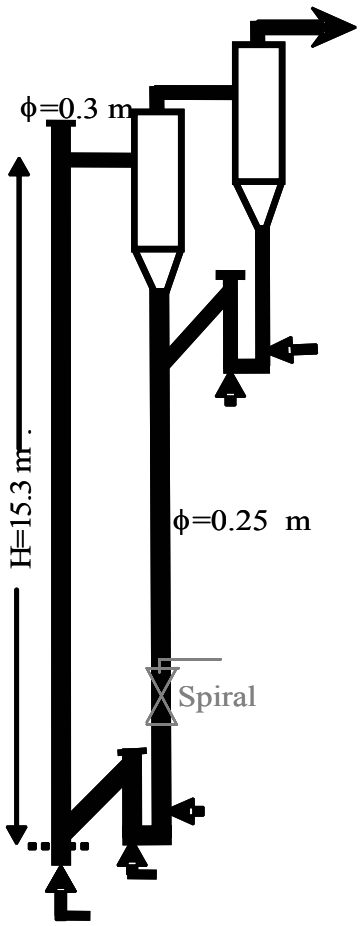

Figure 1. Schematic of CFB cold flow unit indicating gas-solids separation and aeration location

Fluidization bed material properties are presented in Table 1. A relatively light bed material was selected to generate data relevant for advanced high-pressure coal conversion processes. According to a Buckingham-Pi analysis of the riser in a CFB the ratio of gas: solids density is critical factor important in scaling from a model, such as these cold flow tests, to a prototype application, such as a high pressure and high temperature transport reactor (Ghordzoe et al., 2001). Cork offers an excellent bed material which when tested at ambient conditions in air yields a similar density ratio to that of coal processed at 10-20 atmospheres and 1000 C.

ρ_s	kg/m^3	189
ρ_b	kg/m^3	95
d_{sv}	μm	812
U_t	m/s	0.86
U_{mf}	m/s	0.07
ε		0.49
ϕ		0.84

Table 1 Cork Properties.

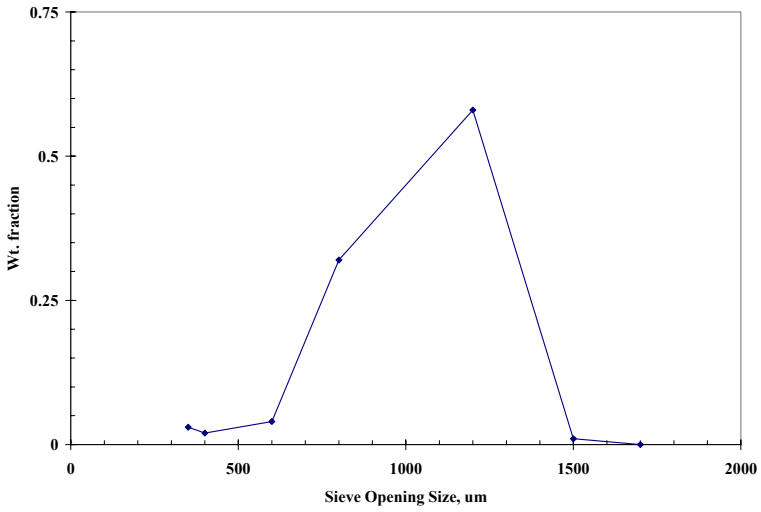

Figure 2 Cork size distribution as measured by sieve analysis.

The particle density was measured using water displacement taking care to wet the surface completely. The cork surface is sufficiently hydrophobic to avoid filling any porosity with water. The particle size was measured using standard sieve analysis. The size distribution is displayed in Figure 2. The minimum fluidization velocity was

measured in the loopseal by closing the slide gate valve in the standpipe and increasing the gas velocity while measuring an incremental pressure drop across the loopseal. In addition, the shape factor for this natural wood material is expected to be comparable to that of coal that was derived from woody tissues and retains much of its morphology. The sphericity was estimated fitting the Ergun equation to the pressure drop - velocity profile taken prior to fluidization. The terminal velocity was calculated from drag laws using the measured solids density and particle size, and sphericity.

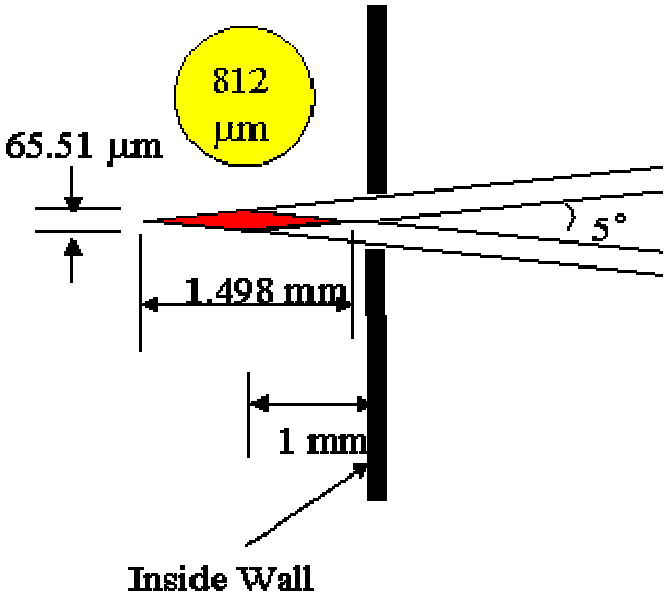

Figure 3 LDV measurement location and relative size

Figure 4 LDV system set-up

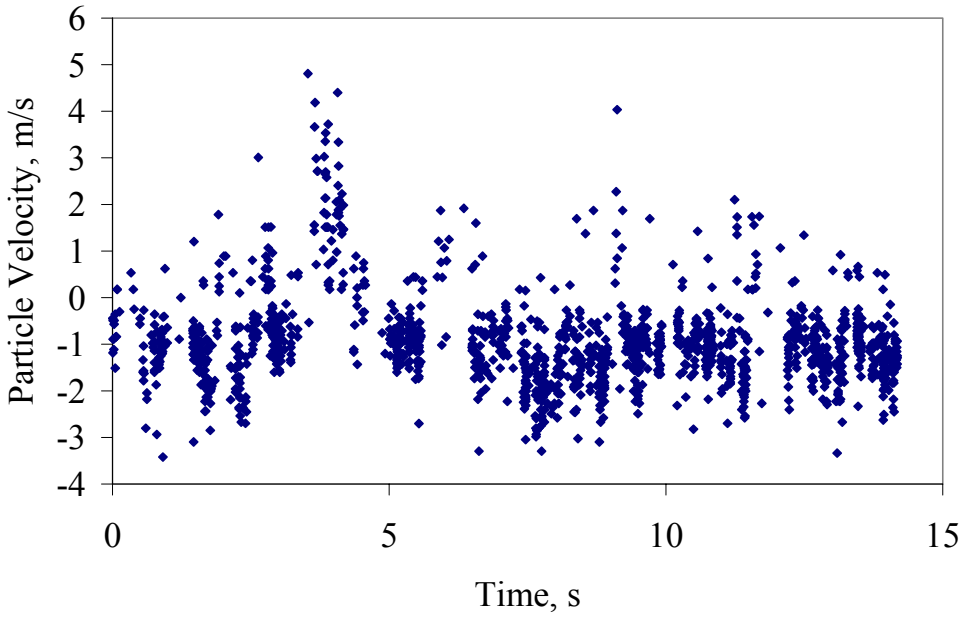

Figure 5 LDV system data for typical run, RP68.

The LDV system used to gather the velocity data is shown in Figure 3. During the tests discussed, it was placed at the 8.5 meter height level of the riser. This instrument is a TSI prototype which incorporates a particle imaging system and a backscatter laser Doppler velocimeter (LDV). The operating principle of the LDV component is well known. A historical review of the LDV principle has been given by Stevenson (1979) and application of various techniques to measure particle velocity in the CFB was reviewed by Pandey et al. (2004). In this TSI unit, a class IV air cooled Argon Ion laser is used for illumination. In the current configuration, it can only measure the two velocity components in the plane normal to the laser beam, i.e. the vertical (z-direction) and horizontal (x-direction) velocity components

The unit was set up as shown in Figure 4 to look at particle velocities at the wall (1mm). Critical to the analysis two instrumental requirements are necessary. Solids fraction or voidage must be measured. To make this measurement with a single instrument, so that the local voidage can be assigned to a given particle, the sample volume must be similar to the particle size and the data collection system fast enough to count every particle passing through it. In other words, the values of voidage necessary to calculate the collision time must not be biased by coincident particles being measured. In addition, the obscuration of particles must be avoided. Thus sample volume must generally be near (within 1 or 2 particle diameters) of the wall especially for dense flowing conditions.

The output from the LDV system can be presented graphically as is done in Figure 5. In this figure, positive velocities are downward and negative velocities are upward. The flow is predominately downward at the wall for these conditions. The close proximity of the data points is suggestive of clustering with the generation of the output signal at that time (e.g. the velocity data between 5 and 6 seconds). Cluster were defined by Pandey et al. (2004) and extended by Breault et al. (2005). According to Breault (2005), the

particles were defined to be in a cluster if the solids in the region of study were adjacent to each other and had similar granular temperatures.

Results and Discussion

Operating conditions were varied by adjusting the riser flow or solids circulating rate Test data in blue: bubble size set equal to solids holdup or ΔP_{riser} while maintaining constant system pressure at the base of the riser. A set of 9 conditions, gas flow rate and solids flow rate pairs, define the conditions that were tested extensively. This represents a two level composite statistical design with duplicated center point (RP59 & RP70; Table 2). These conditions spanned a range of operating conditions from very dilute upflow, core annular flow, and approaching dense upflow. The global response of the riser is represented by the apparent solids holdup or pressure drop in the riser, considering that the gas friction was insignificant and that the solids shear is negligible in the riser, Tables 1 and 3. The riser pressure drop is superimposed on a map of the operating regime in Figure 6. This apparent solids fraction, (1-ε), can be calculated using equation 9:

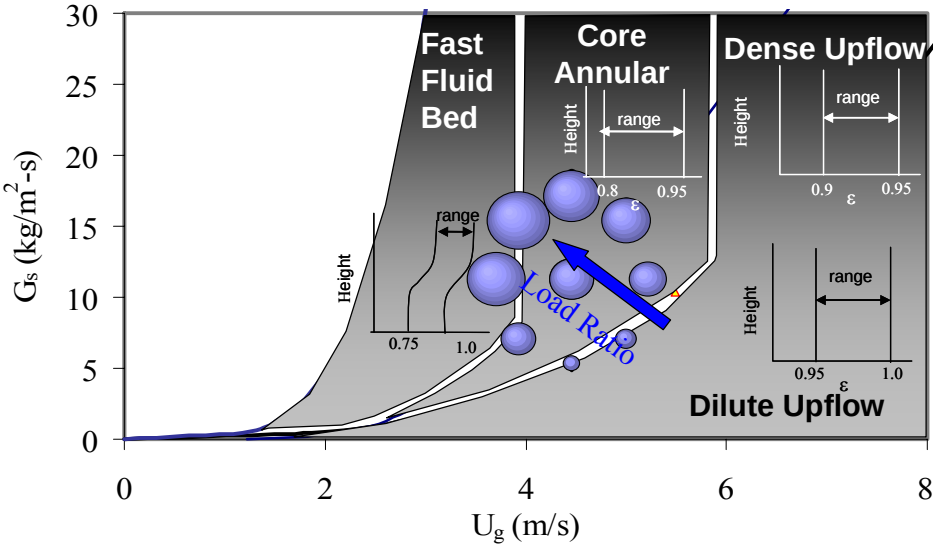

Figure 6. Test matrix with Cork in the CFB flow regimes.

$$(1-\varepsilon) = \Delta P/(\rho_s g H) \qquad \text{Equation 9}$$

The data contained in this paper are from the tests numbers reported in Table 2. Table 2 identifies the flow rates for each test condition and whether or not clusters were observed from the analysis. The axial distribution of the solids for all conditions was essentially uniform except relatively short (2-3 m) entrance and exit effects. In other words, the apparent solids fraction was not a function of height for each test and ranged between 0.016 and 0.113 for the test matrix.

Table 2 Test Matrix

Test #	Gas Velocity (m/s)	Solids flow rate (kg/hr)	Loading ratio (G_s/G_g)	(1-ε)
RP59	4.65	2722	1.56	0.051
RP64	4.65	4536	2.60	0.090
RP65	5.49	2722	1.32	0.037
RP66	5.24	4004	2.04	0.062
RP67	4.65	907	0.52	0.010
RP68	4.06	4004	2.63	0.113
RP69	5.24	1439	0.73	0.016
RP70	4.65	2722	1.56	0.049
RP71	4.06	1439	0.95	0.030
RP72	3.81	2722	1.90	0.095

Instantaneous void fractions in the LDV sample volume can be calculated for each adjacent pair of particles by meeting the following criteria: sufficiently fast data acquisition rate, small sample volume relative to the particle size, and avoiding obscuration of the sample volume by interfering particles (Breault et al. 2004b). The LDV system is set up to take data upon being triggered by an acceptable signal. The fastest data rate recorded between adjacent particles was 100kHz. The sample volume was taken assuming only 10% of the particle (effective diameter) needs to be within the Doppler interference pattern to trigger a signal. The width of the volume was taken as twice the effective particle diameter; the height was distance traversed by the particle moving at the measured velocity, v_p; and the depth of the sample volume was the length of the Doppler pattern plus twice the effective particle diameter. Samples taken immediately at the wall avoid obscuration by interfering particles. The instantaneous voidage is portrayed over the sampling time for the relatively dense case (RP68) in Figure 7. The average voidage near the wall for this case is 0.739 which was somewhat lower than the average as presented in Table 2 as expected.

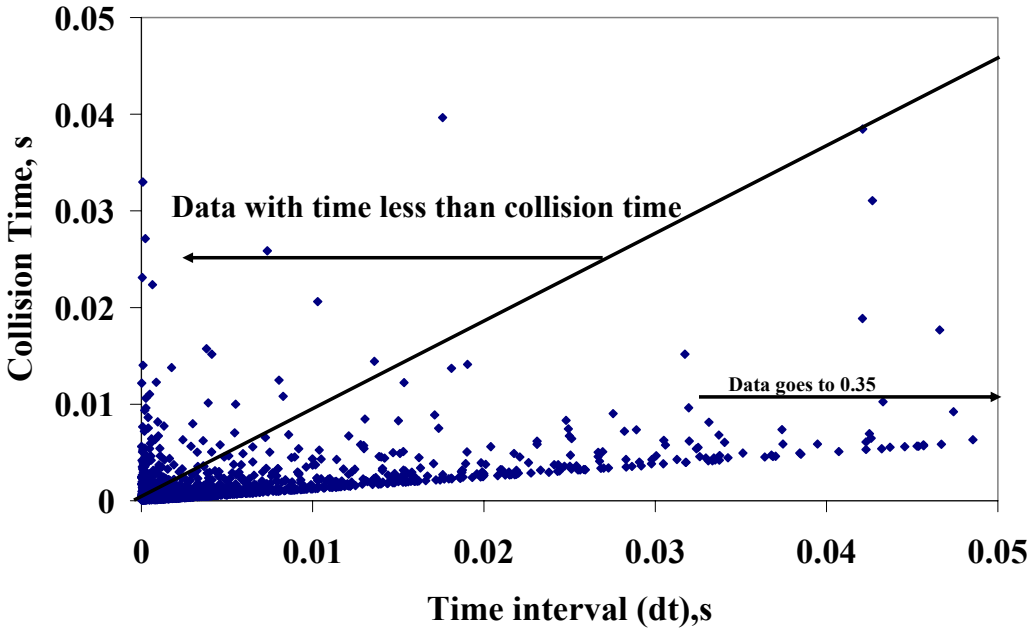

Figure 7 Collision time for adjacent 800 μm particles near the wall for RP68.

The distribution of voidages for this run is presented in Figure 8. In this case almost 25% of the solids have a void fraction similar to a minimally fluidized bed. Nearly 25% of the solids were in very dilute condition with a void fraction greater than 0.975. The voidage distribution drops off smoothly from this value until it reaches the step 0.375. This is indicative of the voidage in the dispersed phase has a continuous functionality where the material in the minimally fluidized state is the cluster phase.

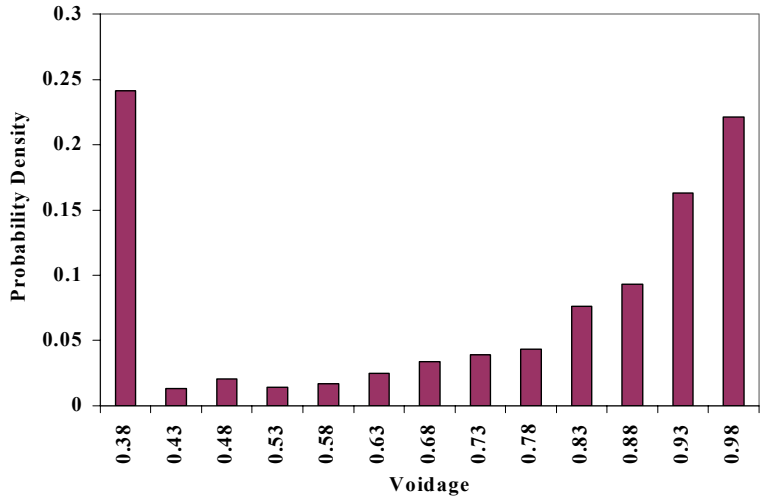

Figure 8 Frequency distribution for void fractions near wall for RP68.

Once the instantaneous solids fraction was determined for each set of adjacent particles a collision time was calculated using equation 7. The richest data set characterized was RP68. The collision times are shown in Figure 9 over the shortest range of time intervals. The data set continues up to time intervals of 0.035 s. In this data set 530 data points $t < t_c$, these were then used to calculate granular temperature. Of these data points 318 points were in clusters as defined by Breault et al. (2004a or b). The mean granular temperature for clusters was 0.03 $(m/s)^2$, much lower than the mean overall granular temperature 0.088 $(m/s)^2$. The mean granular temperature in the dispersed phase, i.e. excluding clusters, was even higher having a value of 0.10 $(m/s)^2$.

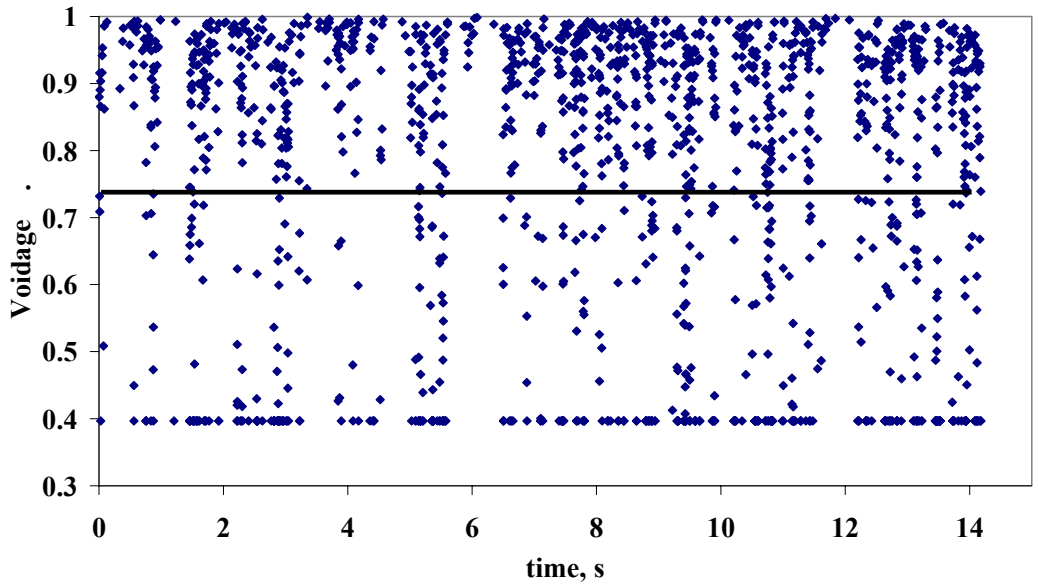

Figure 9. Voidage at the wall for RP68 as measured from LDV data over the sampling time.

In order to test the sensitivity to particle size distribution, the values for the granular temperature were also calculated using d_p=500 μm to determine the collision times. The result was the mean value of Θ for clusters was unchanged, and that for the dispersed phase was only 0.0015 lower than Θ determined using d_p=800 μm. This can be considered a measure of the uncertainty due to using an average particle size to determine the collision time.

The mean turbulent kinetic energy, the velocity fluctuations for data in which the time interval was greater than t_p (equation 9), was 0.206 $(m/s)^2$. This was significantly higher than the mean granular temperature for even the dispersed phase.

The dependence of both granular temperature and turbulent kinetic energy on solid fraction is presented in Figure 10. The data points represent a running average over 50 particles having similar solids fractions for the TKE measurements where the data set was richer and over 10 particles having similar solids fractions for granular temperature

where the data was sparser. Both temperature and turbulent kinetic energy follow the same trend, decreasing with increasing solids fraction. This data follows the same general trend derived theoretically and measured experimentally by Gidaspow and Huilin (1998) and Neri and Gidaspow (2004) for FCC in their cases with higher solids fractions. The mean granular temperature reached a maximum of 0.5 $(m/s)^2$ near a solid fraction of 0.015, but this drops to a level of 0.01 $(m/s)^2$ for more densely loaded flows. The mean granular temperature measured even at low solids fractions was typically at a level of 0.04 $(m/s)^2$. The granular temperature was about an order of magnitude lower than the turbulent kinetic energy.

MFIX simulations of the same riser, sampling location, and operating conditions (RP68) were performed using cork particles. Granular temperature was readily calculated using an algebraic model (Syamlal,). Granular temperature data were taken every 0.1 seconds during steady state. These data are also presented on Figure 10. This algebraic model was found to be somewhat higher than the measured granular temperature, particularly for the lower solids loadings. The algebraic model calculated an asymptotic level at higher solids fractions approaching the granular temperature of the limit at minimum fluidization. The algebraic model in MFIX was 5 times higher than these measurements at solid fractions of about 5%. The two deviated further at lower solids fractions. On the other hand these calculated values were similar to the measured turbulent kinetic energy values.

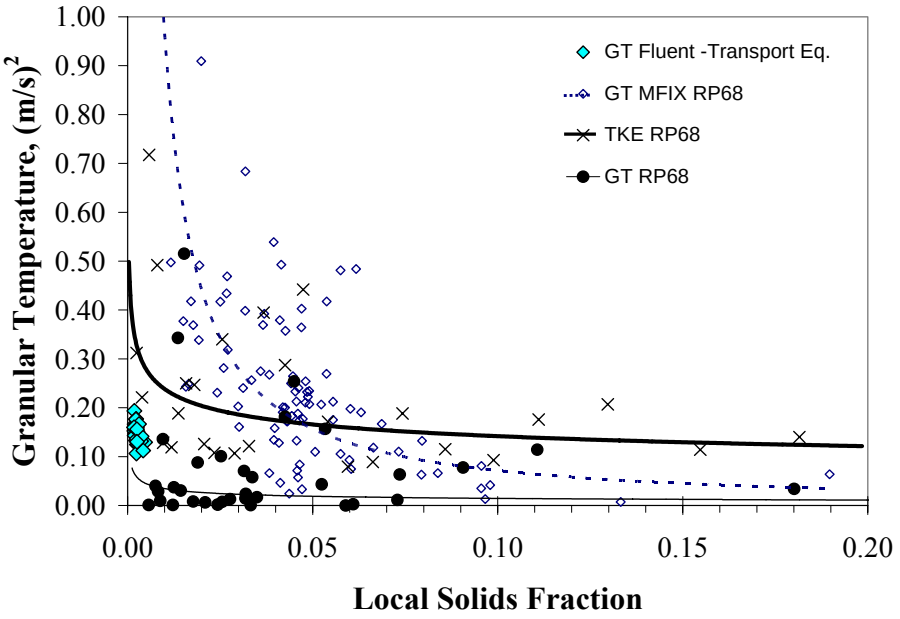

Figure 10 Measured granular temperature for RP68 compared to TKE , MFIX , and Fluent simulations.

Granular temperature was also simulated using Fluent using the transport equations, for a more dilute test case (RP69). In this case the solids fraction was very dilute; the range of solids fractions attained near the wall was only between 0.15% and 0.5%. The value of Θ

was less than 0.2 $(m/s)^2$ approaching an asymptotic level of about 0.12 $(m/s)^2$, and as expected, Θ was inversely related to $(1-\varepsilon)^2$. The granular data taken in RP68 appeared to approach these simulated values although few data existed for such dilute local solids fractions. Clearly the measured granular temperatures were of comparable magnitude to these simulations performed with Fluent using the transport equations to determine the granular temperature.

Theory indicates that granular temperature is inversely related to the square root of the solids concentration (Gidaspow and Huilin, 1998). This was supported by the measurements here. An extension of this theory in the very dilute case would have predicted a direct dependence between Θ and $\varepsilon^{2/3}$; however, there was no evidence that the granular temperature dropped as the solids fraction approached zero. This was not observed in the measurements nor the Fluent simulations which approached very small solids fractions.

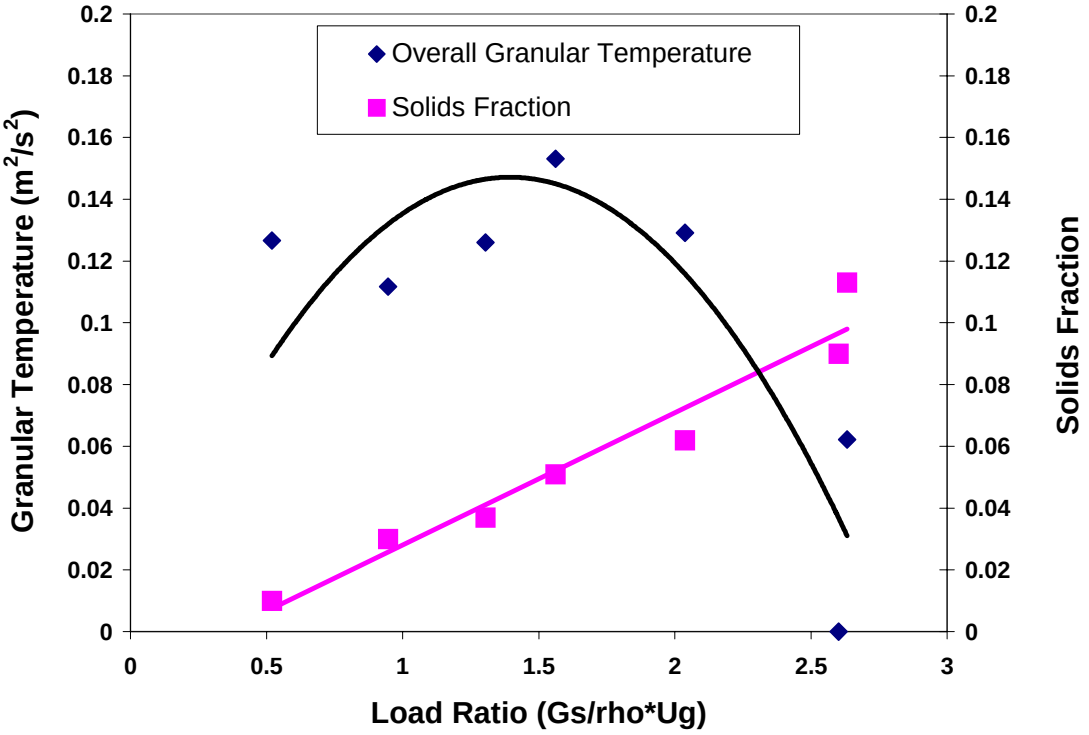

Figure 11 Mean local void fraction and granular temperature near the wall as a function of the riser load ratio.

The overall granular temperature was measured for the data in all 10 RP test cases. The mean granular temperature and the mean solids fraction near the wall for these cases are presented in Figure 11 as a function of the load ratio, i.e. solids flux/gas flux. The error bars on the granular temperature data reflects the range of data, in particular the 25 and 75 percentile readings for each. As the load ratio increased the solids fraction near the

wall decreased reflecting the greater concentration of clusters moving down in this core annular regime. The granular temperature remained relatively flat over this range of conditions displaying a slight tendency to increase in the mid range data sets. The lowest load ratio was the only case producing an average positive velocity near the wall, and the particles were nearly all in the dispersed phase. Beyond that the number of clusters increased with load ratio. It is hypothesized that the granular temperature increased with solids fraction initially particularly in the region where clusters were be destroyed or torn apart at a rate comparable to their formation. This is the range of conditions in which the voidage changed least with load ratio. As the load ratio the void fraction changed at a greater rate with increased load ratio. This may be caused by the cluster formation rate overwhelming the cluster destruction rate, thus a much larger proportion of the solids resided in clusters of significantly increasingly lower granular temperature.

Summary

In Summary, theory indicates that granular temperature is inversely related to the square root of the solids concentration (Gidaspow and Huilin, 1998). This was supported by the measurements here. An extension of this theory in the very dilute case would have predicted a direct dependence between Θ and $\varepsilon^{2/3}$; however, there was no evidence that the granular temperature dropped as the solids fraction approached zero. This was not observed in the measurements nor the Fluent simulations which approached very small solids fractions.

References

Gidaspow, D. and Huilin, L. (1998) Equations of state and readila distribution functions of FCC particles in a CFB, *AIChE Journal,* 44(2), 279-293

Tartan, M. and Gidaspow, D. (2004) Measurement of granular temperature and stresses in risers, *AIChE Journal,* 50(8), 1760-1775

Neri, A. and Gidaspow D. (2000) Riser hydrodynamics: simulation using kinetic theory, *AIChE Journal,* 46 (1), 52-66

P. Pandey, R. Turton, P. Yue, L.J. Shadle (2004) Non-intrusive particle motion studies in the near-wall region of a pilot-scale circulating fluidized bed, *Industrial & Engineering Chemistry Research,* 43(18), 5582-5592

J. C. Ludlow, L.J. Shadle, M. Syamlal (2002) Method to continuously monitor Solids Circulation Rate, in: J. R. Grace, J. Zhu, H. de Lasa (Ed.), Circulating Fluidized Bed Technology VII, Canadian Society of Chemical Engineering, Ottawa, Canada, 2002, p. 513-520.

L. J. Shadle, E. R. Monazam, and J. S. Mei (2002) Characterization of Operating Flow

Regimes In a Cold Flow, in: J. R. Grace, J. Zhu, H. de Lasa (Ed.), Circulating Fluidized Bed Technology VII, Canadian Society of Chemical Engineering, Ottawa, Canada, 2002, p. 255-262.

(Ghordzoe et al., 2001).

Stevenson, Warren H. 1979. A Historical Review of Laser Velocimetry, in Laser Velocimetry and Particle Sizing, pp 1-12, H. Doyle Thompson and Warren H. Stevenson, ed., Hemisphere Publication Corporation, Washington, New York, and London.

(Ainley).

P. Pandey, R. Turton, P. Yue, L.J. Shadle (2004) Non-intrusive particle motion studies in the near-wall region of a pilot-scale circulating fluidized bed, *Industrial & Engineering Chemistry Research,* 43(18), 5582-5592

J. C. Ludlow, L.J. Shadle, M. Syamlal (2002) Method to continuously monitor Solids Circulation Rate, J. R. Grace, J. Zhu, H. de Lasa (Ed.), *Circulating Fluidized Bed Technology VII*, Ottawa, Canada, 2002, p. 513-520.

L. J. Shadle, E. R. Monazam, and J. S. Mei (2002) Characterization of Operating Flow Regimes In a Cold Flow, J. R. Grace, J. Zhu, H. de Lasa (Ed.), *Circulating Fluidized Bed Technology VII*, Ottawa, Canada, 2002, p. 255-262.

Breault, R. W., Ludlow, J. C. and Yue, P. C., "Cluster Particle Number and Granular Temperature of Cork Particles at the Wall in the Riser of a CFB", Powder Technology **149**, 68-77 (Breault 2005)

Breault, R. W., Ludlow, J. C., Yue, P. C. and Shadle, L. J., "Granular Temperature of Cork Particles in the Riser of a CFB", Submitted for publication, Powder Technology 09/04 (Breault 2004b)

Syamlal, M., "MFIX Document Numerical Technique", Department of Energy Report DOE/MC31346-5824, Jan. 1998